Mechanistic First-Principles and Kinetic Modelling Studies of Upgrading of Oxygenates on Single-Atom Alloy Catalysts



Weitian Li

Lady Margaret Hall

University of Oxford

A thesis submitted in fulfilment of the requirements for the degree of Doctor of Philosophy in Engineering Science

Hilary Term 2026

Abstract

Decarbonizing the global energy system while meeting growing demand requires scalable, low-carbon routes to hydrogen (H_2) production. Liquid oxygenates derived from renewable carbon streams, notably methanol (CH_3OH) and formic acid (HCOOH), are attractive H carriers, but their practical deployment depends on catalysts that combine high activity, selectivity, and resistance to deactivation. This thesis develops a multi-scale modelling framework to understand and design single-atom alloy (SAA) catalysts for hydrogen production from small oxygenates. Density functional theory (DFT) is used to quantify adsorption thermodynamics and elementary reaction barriers on SAA catalysts, comprising coinage-metal hosts doped with isolated transition-metal atoms, while graph-theoretical kinetic Monte Carlo (GT-KMC) simulations are employed to connect microscopic energetics to macroscopic observables under temperature-programmed conditions, explicitly accounting for site populations, diffusion, lateral interactions, and coverage effects.

Three projects are presented. First, a broad DFT screening study across multiple host–dopant combinations (Cu, Ag, Au hosts with Ni, Pd, Pt, Rh dopants) elucidates how SAAs tune oxygenate adsorption and reactivity for methanol dehydrogenation and C–O coupling chemistry relevant to renewable fuels and chemicals. Thermochemical scaling (TCS) and Brønsted–Evans–Polanyi (BEP) analyses reveal that SAAs can deviate from monometallic trends,

achieving comparatively weak product binding while maintaining low activation barriers, thereby identifying compositions with improved catalytical activity and selectivity for key bond-activation and coupling steps.

Second, reactivity trends for HCOOH decomposition on Cu-based SAAs are resolved by focusing on the experimentally consistent dehydrogenation pathway in which bidentate formate (HCOO) C–H scission governs carbon dioxide (CO_2) and H_2 evolution. DFT-calculated energies and forces, combined with harmonic transition state theory, are used to identify dopant-dependent transition-state structures and establish an activity ordering across PdCu, PtCu, NiCu, and RhCu SAAs. A descriptor-based interpretation emerges in which carbon monoxide (CO) formation energy on the dopant linearly correlates with the HCOO C–H activation barrier on SAAs.

Third, the thesis addresses CO poisoning by introducing the concept of secondary single-atom sites as CO scavengers on two-dopant SAA surfaces. DFT-derived CO diffusion and desorption energetics, integrated into GT-KMC, demonstrate how CO redistribution can kinetically trap and release active sites and rationalize experimentally observed double-peak CO_2 features. The combined DFT-KMC workflow provides mechanistic and design principles for tailoring SAA compositions to promote H_2 evolution while mitigating deactivation, thereby advancing predictive catalyst design for H_2 production.

Acknowledgements

I would like to express my deepest gratitude to my advisor, Michail, for his unwavering support and guidance throughout my PhD. His encouragement has inspired me to pursue a career in academia. I am also very grateful to Romain for his valuable insights and for always being available for helpful discussions. In addition, I would like to thank Charlie Sykes and Yicheng Wang at Tufts University for their experimental perspective and practical guidance, which helped shape the research presented in this thesis. I also thank all group members for their helpful discussions. Finally, I am deeply grateful to my family, who have always wanted the best for me and have shown me endless love and support.

Declaration of the Use of Published and Unpublished Work

Parts of this thesis (Chapter 3-5) are based on research outputs produced by the author during DPhil studies at the University of Oxford, including work that is published, submitted, or currently under peer review, as well as raw data in preparation for submission. Wherever such prior work is incorporated, the relevant manuscript or publication is clearly identified and cited. For manuscripts under review or otherwise unpublished, the thesis cites the work as an unpublished manuscript (or manuscript under review) and, where appropriate, provides the journal name and the date/status at the time of submission of this thesis.

All material drawn from these outputs has been substantially rewritten and integrated into the thesis to ensure a coherent narrative while preserving the underlying scientific content. Any figures, tables, or data reproduced from published sources are included in accordance with applicable copyright and reuse permissions.

More specifically, Chapter 3 of this thesis is based in part on the author's published work in ACS Catalysis (ACS Catal. 2023, 13 (24), 15851–15868)[1], and the relevant material has been rewritten and integrated into the thesis with appropriate citation. In addition, Chapters 4 and 5 of this thesis incorporate data derived from the author's own contributions to two research manuscripts

produced during the course of the DPhil: (i) Breaking Established Reactivity Trends with Single-Atom Alloys (under review at Nature Catalysis, submitted 7 February 2025)[2] and (ii) Secondary Single-Atom Sites in Single-Atom Alloy Surfaces Enhance Reactivity by Scavenging CO (manuscript in preparation for submission to Nature Chemistry)[3]. The relevant sections in Projects 2 and 3 have been substantially rewritten, restructured, and integrated to form a coherent thesis narrative and to avoid textual duplication. All related manuscripts are cited at the appropriate points.

The material reproduced in Chapters 4 and 5 corresponds specifically to the computational/theoretical work carried out by the author (including DFT calculations, kinetic Monte Carlo (KMC) modelling, and associated mechanistic analysis and interpretation). Any results originating from collaborators (e.g., experimental measurements) are included only where necessary for context and comparison and are clearly attributed.

Table of Contents

Abstract ..... **I**

Acknowledgements ..... **III**

Declaration of the Use of Published and Unpublished Work ..... **IV**

Abbreviation Lists ..... **XII**

List of Figures and Tables ..... **XV**

Chapter 1 Background Knowledge and Overview **1**

1.1 Introduction 1

1.2 Attractive Feedstocks for H_2 Production 3

1.3 An Overview of Heterogeneous Catalysis 4

1.4 Principles and Descriptors Used in Catalytic Performance 6

1.4.1 The Sabatier Principle in Heterogeneous Catalysis 6

1.4.2 BEP and TCS Relationships 9

1.5 An Introduction to the SAA 11

1.5.1 The definition of the SAA 11

1.5.2 Key Properties of SAAs 12

1.6 Conclusion 16

Chapter 2 Methodology and Research Approach **18**

2.1 Introduction 18

2.2 An Introduction to the Schrödinger Equation 19

2.3 Born-Oppenheimer Approximation 20

2.4 The Development of the Hartree-Fock Equation 23

2.5 The Development of DFT 27
2.6 Exchange Correlation Functional 31
2.7 Periodic Boundary Conditions and Bloch's Theory 34
2.8 Pseudopotential Approximation 38
2.9 Solving the KS Equations 39
2.10 Electronic Structure Analysis 40
2.10.1 DOS Analysis 40
2.10.2 PDOS Analysis 41
2.10.3 COOP and COHP Analysis 43
2.11 Structural Optimization 45
2.11.1 Quasi-Newton Method 46
2.11.2 CG Method 48
2.12 Transition State Searching Method 49
2.12.1 EB Methods for Obtaining Reaction Paths 50
2.12.2 Dimer Method 53
2.13 Frequency Calculations 55
2.14 DFT Related Software 57
2.15 Energy Definitions Used in this Thesis 59
2.15.1 Formation Energy 59
2.15.2 Activation Energy and Reaction Energy 60
2.16 Mesoscopic Simulations of Reaction Kinetics 61
2.17 An Introduction to On-lattice KMC Simulation 65

2.17.1 The Importance of On-Lattice KMC 65
2.17.2 An Introduction to Master Equation 67
2.17.3 Principles of On-Lattice KMC Simulation 70
2.18 Acquiring Rate Constant via TST 72
2.19 Coverage-Dependent Correction to the Activation Energy 76
2.20 An Introduction to CE 78
2.21 Overview of KMC Algorithms 79
2.21.1 An Introduction to the First-Reaction Method 80
2.21.2 On-lattice KMC Simulation Procedure 81
2.21.3 Accelerating GT-KMC Simulations to Prevent Stiffness 84
2.21.4 An Introduction to Zacros 86
2.22 Conclusion 88
Chapter 3 Elucidating the Reactivity of Oxygenates on SAA Catalysts .. 90
3.1 Introduction 90
3.2 Computational Setups and Research Process 91
3.2.1 Computational Setups 91
3.3 Results and Discussion 93
3.3.1 Adsorption Configurations and Energies 93
3.3.1.1 Preferable Surface Configurations of Each Fragment 94
3.3.1.2 Formation Energy Comparisons and TCS Relationships 98
3.3.2 Catalytically Relevant Bond Coupling/Dissociation Reactions 105
3.3.2.1 C-H Activation in CH_3OH 106

3.3.2.2 O-H Activation in CH_3OH 110
3.3.2.3 C-H Activation in CH_3O 112
3.3.2.4 C-H Activation in CH_2OH 116
3.3.2.5 C-O Coupling between CH_3O and CH_3 122
3.3.3 Comparing Catalytic Activities between SAAs and Pure Metals 129
3.3.3.1 C-H and O-H Bond Scission Reactions 130
3.3.3.2 C-O Coupling between CH_3O and CH_3 134
3.3.4 BEP Relationships 136
3.4 Conclusion 142
Chapter 4 Reactivity Trends in Cu-Based SAA for HCOOH Decomposition 145
4.1 Introduction 145
4.2 Methodology 147
4.2.1 DFT Calculation 147
4.2.2 KMC Simulation 149
4.3 Results and Discussion 150
4.3.1 Experimental TPD results on HCOOH Decomposition 150
4.3.2 DFT Investigations of the HCOO C-H Activation Pathway 152
4.3.3 CO Formation Energy as Activity Descriptor for C-H Activation 160
4.3.4 KMC Simulations of HCOO Dissociation on SAAs 166

4.3.4.1 TPD Spectra of H_2 and CO_2 Desorption on SAAs 166

4.3.4.2 The Effect of Residual H* for Decomposition of HCOO. 171

4.3.5 Effect of van der Waals Corrections 175

4.4 Conclusion 178

Chapter 5 Secondary Dopants Boost SAA Reactivity by Scavenging CO 180

5.1 Introduction 180

5.2 Methodology 181

5.2.1 DFT Calculations 181

5.2.2 KMC Simulation 182

5.2.2.1 Cu-based Bimetallic SAAs 182

5.2.2.2 Cu-based TD-SAAs 183

5.3. Results and Discussion 184

5.3.1 Experimental TPD Results 184

5.3.2 Mechanistic Studies of CO Desorption on SAAs 186

5.3.3 Initial Distribution of CO on TD-SAA Surfaces 189

5.3.4 The Temperature of CO Diffusion on each TD-SAA Surface .. 196

5.3.5 HCOO Dissociation on TD-SAA Surfaces with Pre-existing CO 201

5.3.6 Effect of Residual CO on on HCOO Dissociation 206

5.4 Conclusion 208

Closing Statement and Future Perspectives 211

Appendix A **217**

Appendix B **230**

References **241**

Abbreviation List

H_2: Hydrogen

CH_3OH: Methanol

HCOOH: Formic Acid

SAA: Single-Atom Alloy

DFT: Density Functional Theory

GT-KMC: Graph-Theoretical Kinetic Monte Carlo

TCS: Thermochemical Scaling

BEP: Brønsted–Evans–Polanyi

HCOO: Formate

CO_2: Carbon Dioxide

CO: Carbon Monoxide

KMC: Kinetic Monte Carlo

RDS: Rate-Determining Step

CI-NEB: Climbing-Image Nudged Elastic Band

TST: Transition State Theory

PES: Potential Energy Surface

SCF: Self-Consistent Field

KS: Kohn-Sham

LDA: Local Density Approximation

GGA: Generalized Gradient Approximation

RPBE: Revised Perdew-Burke-Ernzerhof

PBE: Perdew-Burke-Ernzerhof

USPP: Ultra-Soft pseudopotential

PAW: Projector Augmented-Wave

DOS: The Density of States

PDOS: Projected Density of States

COOP: Crystal Orbital Overlap Population

COHP: Crystal Orbital Hamilton Population

CG: Conjugate Gradient

RMM-DIIS: Residual Minimization Method with Direct Inversion in the Iterative Subspace

MEP: Minimum Energy Path

EB: Elastic Band

NEB: Nudged Elastic Band

VASP: Vienna Ab Initio Simulation Package

VESTA: Visualized Electronic Structural Analysis

MD: Molecular Dynamics

TOF: Turn-Over Frequency

CE: Cluster Expansion

ECI: Effective Cluster Interaction

CH_2O: Formaldehyde

CH_3O: Methoxy

CH_2OH: Hydroxymethyl

CH_3OCH_2: Methoxymethyl

CH_3OCH_3: Dimethyl Ether

TPD: Temperature-Programmed Desorption

TD-SAA: Two-Dopant SAA

GM: Graph Multiplicity

R^2: Coefficients of Determination

MAE: Mean Absolute Errors

List of Figures

Figure 1. 1 Illustration of the Sabatier principle as a volcano activity plot. The catalytic activity for a reaction is optimized when the catalyst binds substrates at an intermediate strength. 7

Figure 1. 2 Surface structure of a four-layer SAA (111) surface. The dopant metal is displayed in blue and the host metal in yellow. 11

Figure 1. 3 A schematic of BEP plots for C-H bond dissociation. The blue, yellow and red dots in the figure represent the transition metals, host metals and the SAA, respectively. 14

Figure 2. 1 Side view of a supercell structure model used for surface calculation. 34

Figure 2. 2 An illustration of a potential energy surface. Regions A and B represent the initial state and final state, respectively. The dashed line marks the boundary between different states. The black solid lines represent energy contour lines. 64

Figure 2. 3 Part of a lattice used for a KMC simulation of the RhCu(100) catalytic surface. Top and four-fold hollow sites are represented by circles and squires, respectively. 66

Figure 2. 4 Flowchart of a commonly used on-lattice KMC algorithm. 82

Figure 3. 1 The figure shows the typical fcc(111) surface structures of pure metal (left) and SAA fcc(111) (right) and different sites. Cu is displayed in brown, Pd in green. 93

Figure 3. 2 DFT-optimized structures for (a) the CH_3O intermediate on Ag(111), (b) the CH_2OH intermediate on Pd(111), (c) the CH_3OCH_3 intermediate on Cu(111), and (d) the CH_2OCH_3 intermediate on Au(111). Pd in green, Cu in orange, Au in gold, Ag in silver, C in black, O in red, and H in white in the figure. 95

Figure 3. 3 Front views of DFT-optimized structures for the CH_2O intermediates on (a) Au(111) and (b) Pd(111). Top views of DFT-optimized structures for the CH_2O intermediates on (c) Au(111) and (d) Pd(111). Pd in green, Au in gold, C in black, O in red, and H in white in the figure. 95

Figure 3. 4 DFT-optimized structures for: (a) the OH and CH_3O intermediates and (b) the CH_2OH and CH_3OCH_2 intermediates on Rh/Ag(111). (c) the H_2O and CH_3OH and (d) H_2O and CH_3OCH_3 intermediates on Rh/Ag(111) and Pt/Ag(111). (e) the OH and CH_3O intermediates on Rh/Au(111) and Pd/Au(111). (f) the CH_2OH and CH_3OCH_2 intermediates, (g) H_2O and CH_3OH intermediates, and (h) H_2O and CH_3OCH_3 intermediates on Rh/Ag(111). (i) the OH and CH_3O intermediates and (j) the CH_2OH and CH_3OCH_2 intermediates on Pt/Cu(111). (k) the H_2O and CH_3OH and (l) H_2O and CH_3OCH_3 intermediates on Rh/Cu(111) and Pt/Cu(111). The arrows indicate replacement of fragments, e.g. the H atom of the OH is replaced with a CH_3 in (a). 96

Figure 3. 5 TCS relations of the formation energy E_f corresponding to fragments of (a) CH_3O vs OH, (b) CH_3OCH_2 vs CH_2OH, (c) CH_3OH vs H_2O, (d) CH_3OCH_3 vs H_2O bound in the most stable adsorption site on pure metals (blue) and SAAs (red). Adsorbates on SAAs were bound to their most stable dopant site. Corresponding linear regression fitting parameters and error analysis are given in the Table A3 in Appendix A. 99

Figure 3. 6 Two biomass reforming related reaction pathways for (a) the decomposition of CH_3OH and (b) the synthesis of CH_3OCH_3 on the different surfaces considered in this work. 105

Figure 3. 7 Initial states (left), transition states (middle), and final states (right) for C−H dissociation in CH_3OH on Pd/Ag(111) and Pt/Ag(111) SAAs for the “d-CH_3OH” (top) and “h-CH_3OH” (bottom) dissociation pathways. A five-layer slab was used in these calculations along with a *p*(4×4) unit cell. Only a portion of the cell is shown for clarity. 107

Figure 3. 8 Initial states (left), transition states (middle), and final states (right) for O−H dissociation in CH3OH on Pd/Au(111) and Pt/Cu(111) SAAs for the “d-CH_3OH” (top) and “h-CH_3OH” (bottom) dissociation pathways. A five-layer slab was used in these calculations along with a *p*(4×4) unit cell. Only a portion of the cell is shown for clarity. 111

Figure 3. 9 Initial states (left), transition states (middle), and final states (right) for O−H dissociation in CH_3O on Pt/Cu(111), Ni/Ag(111), and Pt/Au(111) SAAs for the “d-CH_3O” (top) and “h-CH_3O” (middle and bottom) dissociation pathways. A five-layer slab was used in these calculations along with a *p*(4×4) unit cell. Only a portion of the cell is shown for clarity. 113

Figure 3. 10 Initial states (left), transition states (middle), and final states (right) for CH_2OH O−H dissociation on Pt/Cu(111) and Pd/Au(111) SAAs for the “d-CH_2OH” (top) and “h-CH_2OH” (bottom) dissociation pathways. A five-layer slab was used in these calculations along with a *p*(4×4) unit cell. Only a portion of the cell is shown for clarity. 117

Figure 3. 11 Energy barriers for (a) the d-CH_2OH and (b) the h-CH_2OH reaction pathways. The dark gray, dark yellow, and brown bars show the activation energy on SAAs, while the light gray, yellow, and pink bars represent the energy required for moving CH_2OH binding to dopant top sites to host sites. The numbers on the top of the light gray, yellow, and pink bars represent the apparent activation energies on SAAs. The circle, triangle, and square represent the activation energy on Ag(111), Au(111), and Cu(111), respectively. Three datapoints are missing as we were not able to find a transition state for the corresponding pathway for Pd/Au, Pt/Au and Rh/Au. Reaction energies of these pathways can be found in Table A7 in Appendix A..... 120

Figure 3. 12 Initial states (left), transition states (middle), and final states (right) for C-O coupling between CH_3 and CH_3O on Ni/Ag(111) (Group 1 SAA) for the "d-CH_3O" (top) and "h-CH_3O" (bottom) dissociation pathways. A five-layer slab was used in these calculations along with a *p*(4×4) unit cell. Only a portion of the cell is shown for clarity. Activation energies and reaction energies for Group 1 SAAs and pure metals can be found in Table A8 in Appendix A. 125
Figure 3. 13 Initial states (left), transition states (middle), and final states (right) for C-O coupling between CH_3 and CH_3O on Ni/Au(111) (Group 2 SAA) for the "d-CH_3O" (top) and "h-CH_3O" (bottom) dissociation pathways. A five-layer slab was used in these calculations along with a *p*(4×4) unit cell. Only a portion of the cell is shown for clarity. Activation energies and reaction energies for Group 2 SAAs and pure metals can be found in Table A9 in Appendix A. 126
Figure 3. 14 Energy profiles of d-CH_3O and h-CH_3O pathways for C-O coupling on a Group 1 SAA: (a) Pd/Ag, as well as the following Group 2 SAAs: (b) Ni/Ag(111), (c) Ni/Au(111), (d) Pt/Au(111), (e) Rh/Au(111), and (e) Pt/Cu(111). 128

Figure 3. 15 Heatmap charts of the transition state formation energy differences ($\Delta EF, dTS$) for the following dehydrogenations: (a) CH_3OH C-H activation, (b) CH_2OH O-H activation, (c) CH_3OH O-H activation, and (d) CH_3O C-H activation for Cu-, Ag- and Au-based SAAs. For each SAA, $\Delta EF, dTS$ is calculated as the formation energy of the lower-energy transition state (between the d- and h-pathways) minus the formation energy of the transition state in the corresponding pure dopant metal. 131

Figure 3. 16 Heatmap charts of the transition state formation energy differences ($\Delta EF, hTS$) for the following dehydrogenations: (a) CH_3OH C-H activation, (b) CH_2OH O-H activation, (c) CH_3OH O-H activation, and (d) CH_3O C-H activation for Cu-, Ag- and Au-based SAAs. For each SAA, $\Delta EFTS$ is calculated as the formation energy of the lower-energy transition state (between the d- and h-pathways) minus the energy of the corresponding pure host metal. 132

Figure 3. 17 Heatmap charts of the transition state formation energy differences ($\Delta EF, dTS$) for (a) CH_3OCH_2 and (b) CH_3OCH_3 intermediate formation for Cu-, Ag- and Au-based SAAs. For each SAA, $\Delta EF, dTS$ is calculated as the formation energy of the transition state minus the energy of the corresponding pure dopant metal. 135

Figure 3. 18 Heatmap charts of the transition state formation energy differences ($\Delta EF, hTS$) for (a) CH_3OCH_2 and (b) CH_3OCH_3 intermediate formation for Cu-, Ag- and Au-based SAAs. For each SAA, $\Delta EF, hTS$ is calculated as the formation energy of the transition state minus the energy of the corresponding pure host metal. 135

Figure 3. 19 BEP relationships for (a) C-H activation in CH_3OH, (b) O-H activation in CH_3OH, (c) C-H activation in CH_3O, and (d) O-H activation in CH_2OH on pure metal (111) surfaces (blue) and SAA (111) surfaces (red). The plots show the activation energy as a function of the reaction energy. Linear fits are drawn for each reaction on each surface type. Corresponding linear regression fitting parameters and error analysis are given in Table A11. 137

Figure 3. 20 Energies of transition versus initial states for the O-H activation in CH_2OH. A linear regression fit is only drawn for pure metals (blue). Red and orange circles indicate d-CH_2OH and h-CH_2OH pathways on SAAs, respectively. Formation energies can be found in Table A10 in Appendix A. 139

Figure 3. 21 (a) BEP relationships for h-pathway occurring on Group 1 SAAs and pure metals (111) surfaces. (b) BEP relationships for d-pathway occurring on all kinds of SAA and pure metals (111) surfaces. The plots show the activation energy as a function of the reaction energy. Linear fits are drawn for each reaction on each surface type. Corresponding linear regression fitting parameters and error analysis are given in Table A12 in Appendix A. 141

Figure 4. 1 Side and top view of a typical fcc(100) surface structures of RhCu SAA and its different sites. Cu is displayed in brown, Rh in blue. 148
Figure 4. 2 Part of a typical SAA fcc(100) surface used for KMC simulation. Host and dopant top sites are represented by orange and light blue dots, respectively. Host hollow sites and dopant-host-mixed hollow sites are shown in red and blue squares, respectively. The numbers in this figure are used to define energy patterns in Table B1 in Appendix B. 149
Figure 4. 3 TPD profiles for HCOOH decomposition on Cu(100) and Cu-based SAAs. (A) H_2 (black) and CO_2 (red) signals recorded after dosing HCOOH on Cu(100), PdCu(100), PtCu(100), NiCu(100), and RhCu(100), followed by linear heating. (B) Corresponding isotopic experiment using DCOOH, showing H_2 (black) and D_2 (blue) evolution. 151

Figure 4. 4 Geometries and energetics for $HCOO^{**}$ dissociation on various SAAs. A) The following $HCOO^{**}$ binding geometries are shown from left to right: di-σ (top-top) on dopant-host sites, proximal di-σ on host-host sites, transition state for C-H scission, final state with chemisorbed CO_2 ($CO_2^{*}{}_c$), final state with physisorbed CO_2 ($CO_2^{*}{}_p$), and state after CO_2 desorption. A five-layer slab *p*(4 × 4) unit cell was used in these calculations and only a portion of the cell is shown for clarity. B) Reaction profiles with zero-point energy corrections for the C-H activation step on Cu and Cu-based SAAs. The adsorption energy of $HCOO^{**}$ on pure Cu was chosen as a reference state and the minimum energy pathways are shown. 153

Figure 4. 5 Configurations of “parallel-lying” transition state (A) and “stood-up” transition state (B). The investigated O atoms are marked with red arrows in these figures. COHP of dopant-C bonding (C) and dopant-O bonding (D) of HCOO** adsorbed at dopant sites in Cu-based SAAs. The grey dashed lines mark the Fermi level, serving as the energy boundary separating occupied states (below) from unoccupied states (above). 156

Figure 4. 6 A) BEP relationships for C–H activation in HCOO** on pure metal (blue) and SAA (red) (100) surfaces. The plots show the activation energy as a function of the reaction energy. B) TCS relations of the formation energy E_f corresponding to fragments of H* vs CO* bound in the most stable adsorption site on SAAs with low atomic size mismatch (red) and all SAAs (grey). 161

Figure 4. 7 Geometries and energetics for $HCOO^{**}$ dissociation on various pure metals. A) The following $HCOO^{**}$ binding geometries of are shown from left to right: di-σ (top-top) configurations, transition state for C-H scission, final state with chemisorbed CO_2 ($CO_2^{*}{}_c$), final state with physisorbed CO_2 ($CO_2^{*}{}_p$), and state after CO_2 desorption. B) Reaction profiles with zero-point energy corrections for the C-H activation step on pure metals. The adsorption energy of $HCOO^{**}$ on pure Cu was chosen as a reference state and the minimum energy pathways are shown. 163

Figure 4. 8 Atom size mismatch for different SAAs. Orange bars indicate SAAs with large size mismatch. Note that the formation energies of H^{*} and CO^{*} on these SAAs obviously deviate from the expected linear correlation. Red bars indicate SAAs with small size mismatch. 165

Figure 4. 9 (A) The simulated TPD spectra of H_2 and CO_2 desorption on lattices. The simulated TPD spectra of H_2 (black line) and CO_2 (red line) desorption on lattices, with the arrows indicating experimentally observed peak temperatures. (B) a bar chart showing the percentage of HCOO** dissociation on dopant versus host sites. These results are obtained from simulations using activation energies calculated by DFT. 168

Figure 4. 10 KMC simulated HCOOH* dissociation processes starting with σ_H = σ_{HCOO} = 0.1 on Cu and Cu-based SAA surfaces. A) Simulated TPD spectra of H_2 (black line) and CO_2 (red line) desorption on lattices, with the arrows indicating experimentally observed peak temperatures. B) Bar chart showing the percentage of HCOO** dissociation on dopant sites. These results are obtained from simulations using the modified C-H activation energies, originally calculated by DFT and subsequently increased by 0.2 eV. 169
Figure 4. 11 Bar charts showing the percentage of H_2 formed and desorbed from dopant versus host sites according to the KMC simulation (A) without and (B) with the 0.2 eV correction, respectively. 170
Figure 4. 12 Coverages of H* (black) and percentage of HCOO** consumed (red) on the RhCu(100) surface as functions of temperature for (A) without and (B) with 0.2 eV correction, respectively. The orange region shows the temperature range for HCOO** C-H activation. 173
Figure 4. 13 The simulated TPD spectra of CO_2 desorption starting with σ_{H^*} = 0.1 excess H* (blue), without pre-existing H* (red), and with hypothetical fast H_2 desorption (black) on (A) RhCu(100) and (B) NiCu(100) lattices. To simulate a scenario where H* produces H_2* and desorbs from the surface rapidly (black), the dissociation reactions for KMC simulations on both dopant and host sites have been altered to ensure that no H* is generated (HCOO** → CO_2*). Note that the simulations in this figure do not include the 0.2 eV correction to the energetics obtained from the GGA functional. 174

Figure 4. 14 Geometries and energetics for formate dissociation on various SAA systems calculated using optB86b-vdw functional. A) The following geometries of formate are shown from left to right: bound to the dopant-host di-σ site, bound to the host-host di-σ site, transition state for C-H scission, final state with chemisorbed CO_2 ($CO_2^*{}_c$), final state with physisorbed CO_2 ($CO_2^*{}_p$), and state after CO_2 desorption. A five-layer slab was used in these calculations along with a p(4 × 4) unit cell. Only a portion of the cell is shown for clarity. B) Reaction profiles with zero-point energy corrections for the C-H activation reaction on Cu and Cu-based SAAs. Only the minimum energy paths are considered in each case. 176

Figure 4. 15 KMC-simulated $HCOO^{**}$ dissociation processes starting with $\sigma_H = \sigma_{HCOO} = 0.1$ on Cu and Cu-based SAA surfaces. A) Simulated TPD spectra of H_2 (black line) and CO_2 (red line) desorption on lattices, with the arrows indicating experimentally observed peak temperatures. B) Bar chart showing the percentage of $HCOO^{**}$ dissociation on dopant sites. These results are obtained from simulations using the modified C-H activation energies, originally calculated by DFT with the optB86b-vdw functional and subsequently increased by 0.2 eV. 177

Figure 5. 1 (A) A typical TD-SAA fcc(100) surface used for KMC simulation in this work, including two parts of TD-SAA for1st (B) and 2nd (C) dopant region. Host, 1st and 2nd dopant top sites are represented by red, blue, and blue dots, respectively. Host hollow sites and 1st and 2nd dopant-host-mixed hollow sites are shown in orange, light blue, and light green squares, respectively. The numbers in this figure are used to define energy patterns in Table S2.....183
Figure 5. 2 TPD spectra of CO_2 evolution from HCOOH* decomposition on RhCu, RhNiCu, RhPtCu, and RhPdCu. Each surface was exposed to 0.1 L of HCOOH at 90 K. 185
Figure 5. 3 (A) Reaction profiles with zero-point energy corrections for the CO* diffusion and desorption steps on Cu and Cu-based bimetallic SAAs. The adsorption energy of CO^* on pure Cu was chosen as a reference state. Note that the transition states whose barrier are lower than 0.01 eV are not shown in this figure. Instead, their initial and final states are connected by dashed lines. (B) the TPD of CO from bimetallic SAAs. CO* adsorbate are only seeded on the dopant sites at the beginning of the simulation. Solid lines represent CO* desorbed from host sites after a diffusion, and dotted lines represent CO* directly desorbing from dopant sites. The black arrow shows the experimental TPD peak. 187

Figure 5. 4 KMC results for clean surfaces under low CO* pressure (1×10^{-10} bar) at 100 K on each TD-SAA and on RhCu SAA. (A) Time evolution of the number of CO* on Rh sites. The arrows indicate (i) the first time at which CO* fully covers Rh sites on RhCu and (ii) 3000 s. (B) Percentage of CO* adsorbed on each site type for each catalyst. Red, blue, and light-blue bars correspond to CO* adsorbed on Cu, Rh, and the secondary dopant (Ni, Pt, or Pd), respectively. The bar chart shows the time immediately after all the dopant site have been blocked. Note that the percentages are computed once Rh and the secondary-dopant sites are fully covered. The model surface contains 10,000 Cu sites, of which 50 are replaced by the secondary dopant and 7 by Rh. Each KMC simulation is repeated 20 times, and results are averaged. 190
Figure 5. 5 CO* coverage on Rh site profiles with respect to number of pre-existing CO* on the Cu sites at 100 K after (A) 1 s and (B) 86400 s, and at 150 K after (C) 1 s and (D) 86400 s on each TD-SAA. The coverage is normalized with respect to the number of surface Rh atoms, and thus, the maximum coverage is 100 %, when all hollow sites are covered. Each KMC simulation is repeated 20 times, and the results are averaged. 192
Figure 5. 6 Reaction occurrence statistics of the KMC model after 86400 s at different temperatures: (a) 100 and (b) 150 K. The red and orange bars represent CO* diffusion between Cu and Rh. The blue and light blue bars represent CO* diffusion between Cu and the secondary dopants. Each KMC simulation is repeated 20 times, and results are averaged. 192

Figure 5. 7 Parity plot of the coverage of CO* on Rh versus coverage of CO* on the secondary dopant at 100 K after 86,400 s. The black, red, and blue dot represent RhNiCu, RhPdCu, and RhPtCu respectively. The black labels indicate the numbers of CO* adsorbate molecules on Cu at the beginning of the simulations. The coverage is normalized with respect to number of surface Rh and secondary dopant atoms, respectively. 194

Figure 5. 8 CO* (solid) and H* (dot) coverages (normalized with respect to number of top and mixed hollow Rh sites, respectively) on Rh site profiles with respect to temperature without (A) and with (B) 1000 pre-existing H* on RhPtCu; and without (C) and with (D) 1000 pre-existing H* on RhNiCu. The black, red, blue, green, and purple dash and dot lines represent, respectively, the results with 20 %, 40 %, 60 %, 80 %, and 100 % CO* occupancies (normalized with respect to Pt/Ni sites) set on the Pt/Ni sites before simulations start. The green region indicates the time window when the CO* starts to diffuse from Pt site to Rh site. Each trajectory is the average of three KMC runs to simulate diffusion and desorption of H* and CO*. 197

Figure 5. 9 CO* (solid) and H* (dot) coverages (normalized with respect to number of top and mixed hollow Rh sites, respectively) on Rh site profiles with respect to temperature without (A) and with (B) 1000 pre-exist H* on RhPdCu. Panels (C) and (D) are enlarged views of the temperature ranges highlighted in (A) and (B), respectively. The black, red, blue, green, and purple dash and dot lines represent the 20 %, 40 %, 60 %, 80 %, and 100 % CO* (normalized with respect to Pd sites) are set on Pd site before simulations start, respectively. The green region indicates the time window when the CO* adsorbates start to diffuse from Pd site to Rh site. Each trajectory is the average of three KMC runs to simulate diffusion and desorption of H* and CO*. 199
Figure 5. 10 KMC simulated HCOO** dissociation processes starting with coverage of HCOO** and H* equals to 10 % (coverage respective to total 10,000 sites) on RhPtCu surfaces with different coverage of CO*, including 0 %, 20 %, 40 %, 60 %, 80 %, and 100 % (coverage respective to 70 Pt sites), initially set on the secondary dopants. (A) Simulated TPD spectra of CO_2 desorption on Rh (blue line), Pt (black line), and Cu (red line) desorption on lattices. Dashed vertical lines differentiate the temperature regimes where CO* desorption is dominated by the primary dopant (Rh) vs. the other sites (Pt and Cu). (B) Bar chart showing the percentage of HCOO** dissociation on Rh (blue), Pt (black), and Cu (red) sites. Each trajectory is the average of three KMC runs to simulate HCOO** dissociation and desorption of CO_2*..... 201

Figure 5. 11 KMC simulated HCOO** dissociation processes starting with coverage of HCOO** and H* equals to 10 % (coverage respective to total 10,000 sites) on RhNiCu surfaces with different coverage of CO*, including 0 %, 20 %, 40 %, 60 %, 80 %, and 100 % (coverage respective to 70 Ni sites), initially set on the secondary dopants. (A) Simulated TPD spectra of CO_2 desorption on Rh (blue line), Ni (black line), and Cu (red line) desorption on lattices. Dashed vertical lines differentiate the temperature regimes where CO* desorption is dominated by the primary dopant (Rh) vs. the other sites (Ni and Cu). (B) Bar chart showing the percentage of HCOO** dissociation on Rh (blue), Ni (black), and Cu (red) sites. Each trajectory is the average of three KMC runs to simulate HCOO** dissociation and desorption of CO_2*.....204
Figure 5. 12 KMC simulated HCOO** dissociation processes starting with coverage of HCOO** and H* equals to 10 % (coverage respective to total 10,000 sites) on RhPdCu surfaces with different coverage of CO*, including 0 %, 20 %, 40 %, 60 %, 80 %, and 100 % (coverage respective to 70 Pd sites), initially set on the secondary dopants. (A) Simulated TPD spectra of CO_2 desorption on Rh (blue line), Pd (black line), and Cu (red line) desorption on lattices. Dashed vertical lines differentiate the temperature regimes where CO* desorption is dominated by the primary dopant (Rh) vs. the other sites (Pd and Cu). (B) Bar chart showing the percentage of HCOO** dissociation on Rh (blue), Pd (black), and Cu (red) sites. Each trajectory is the average of three KMC runs to simulate HCOO** dissociation and desorption of CO_2*.....205

Figure 5. 13 CO* (solid) coverages (normalized with respect to number of top and mixed hollow Rh sites, respectively) on Rh site and percentage of HCOO** (dot) on the surface profiles with respect to temperature on (A) RhNiCu and (B) RhPtCu. The black, red, blue, green, and purple dash and dot lines represent the 20 %, 40 %, 60 %, 80 %, and 100 % CO* (normalized with respect to secondary dopant top sites) are set on secondary dopant sites before simulations start, respectively. Dashed vertical lines differentiate the temperature regimes where CO* desorption is dominated by the primary dopant (Rh) vs. the other sites (Pd and Cu). Each trajectory is the average of three KMC runs to simulate HCOO** dissociation. 207

Figure A 1 Transition state of C-O coupling h-CH_3O pathway on Ni/Au(111). Distance between the lowest H atom in CH_3 and the dopant atom ($D_{H\text{-}dopant}$) and distance between the C atom in CH_3 and the dopant atom ($D_{C\text{-}dopant}$) are shown in the black and the red arrow, respectively. 229

Figure B 1 (A) A typical TD-SAA fcc(100) surface used for KMC simulation in this work, including two parts of TD-SAA for the 1st (B) and 2nd (C) dopant region. Host, 1st and 2nd dopant top sites are represented by red, blue, and blue dots, respectively. Host hollow sites and 1st and 2nd dopant-host-mixed hollow sites are shown in orange, light blue, and light green squares, respectively. The numbers in this figure are used to define energy patterns in Table B1 in Appendix B. 230
Figure B 2 Microscopic processes that could occur on the main lattice during the KMC simulation in Chapter 4 and Chapter 5. Top sites of Rh, Ni, Pt, Pd, and Cu atoms of TD-SAA(100) are shown as blue, light blue, green, light green, and red circles, respectively. Hollow sites of Rh, Ni, Pt, Pd, and Cu atoms of TD-SAA(100) are shown as blue, light blue, green, light green, and red squires, respectively. Events (a) and (b) are HCOO** dissociations to CO* adsorbates, events (c) - (e) are HCOO** dissociations to CO gas molecules. 230

Figure B 3 Microscopic processes that could occur on the main lattice during the KMC simulation. Top sites of Rh, Ni, Pt, Pd, and Cu atoms of TD-SAA(100) are shown as blue, light blue, green, light green, and red circles, respectively. Hollow sites of Rh, Ni, Pt, Pd, and Cu atoms of TD-SAA(100) are shown as blue, light blue, green, light green, and red squires, respectively. Events (a) - (c) are H_2* formations via neighboring hollow sites, events (c) - (e) are H_2* formations via diagonal hollow sites. Events (g) and (h) are gas phase H_2 formations via neighboring hollow sites, events (i) and (j) are gas phase H_2 formations via diagonal hollow sites.....231
Figure B 4 Microscopic processes that could occur on the main lattice during the KMC simulation. Top sites of Rh, Ni, Pt, Pd, and Cu atoms of TD-SAA(100) are shown as blue, light blue, green, light green, and red circles, respectively. Hollow sites of Rh, Ni, Pt, Pd, and Cu atoms of TD-SAA(100) are shown as blue, light blue, green, light green, and red squires, respectively. Events (a) - (c) are H_2* desorption. Events (d) and (e) are CO_2* desorption. Events (f) - (j) are CO* desorption. 231
Figure B 5 Microscopic processes that could occur on the main lattice during the KMC simulation. Top sites of Rh, Ni, Pt, Pd, and Cu atoms of TD-SAA(100) are shown as blue, light blue, green, light green, and red circles, respectively. Hollow sites of Rh, Ni, Pt, Pd, and Cu atoms of TD-SAA(100) are shown as blue, light blue, green, light green, and red squires, respectively. Events (a) - (e) are H* diffusions. Events (f) - (j) are CO* diffusions. 232

Figure B 6 Microscopic processes that could occur on the main lattice during the KMC simulation. Top sites of Rh, Ni, Pt, Pd, and Cu atoms of TD-SAA(100) are shown as blue, light blue, green, light green, and red circles, respectively. Hollow sites of Rh, Ni, Pt, Pd, and Cu atoms of TD-SAA(100) are shown as blue, light blue, green, light green, and red squires, respectively. Events (a) - (e) are HCOO** translation diffusions.....232
Figure B 7 Microscopic processes that could occur on the main lattice during the KMC simulation. Top sites of Rh, Ni, Pt, Pd, and Cu atoms of TD-SAA(100) are shown as blue, light blue, green, light green, and red circles, respectively. Asterisk indicates the sites must be empty for the diffusion step to occur. Hollow sites of Rh, Ni, Pt, Pd, and Cu atoms of TD-SAA(100) are shown as blue, light blue, green, light green, and red squires, respectively. Events (a) - (i) are HCOO** rotation diffusions. 233

List of Tables

Table A 1 Optimized lattice constants from DFT using OptB86b-vdW for FCC Cu, Ag, Au, Ni, Pd, Pt and Rh. The lattice constants are found by performing total energy minimization at various FCC unit cell volumes (a=b=c, α=β=γ=90°), fitting the resulting energies and volumes to the Murnaghan equation of state and finding the minimum thereof. 217

Table A 2 Formation energies (E_F) of fragments adsorbed to the most favored (lowest energy) adsorption site on pure metal and SAA (111) surfaces, as computed by DFT. Values of E_F are relative to CH_4(g), H_2(g), and CO_2(g) as given by Eq. (2.51) in the main text. 218

Table A 3 TCS for species 1 (x-axis) and species 2 (y-axis) adsorbed in their most favored adsorption sites on pure metals and SAAs (Fig. 3.5 in main text). Linear Regression parameters (slope, a, and intercept, b in eV) are given in addition to coefficients of determination (R^2) and mean absolute errors in eV (MAE). Results of Student's T-test (to determine if the slopes and intercepts of pure metal and SAA TCS relations are different) are given for 90 % and 99 % confidence intervals as "Yes" or "No" for different and not different, respectively. Details of calculation methods can be found in the work of Darby et al.[59] ... 219

Table A 4 Activation energies (Ea) and reaction energies (ΔE_{Rxn}) for the h-CH_3OH and the d-CH_3OH C-H dissociation reaction pathways on pure metal (blue) and SAA (red) surfaces. Preferable pathway in the table is defined as the pathway with lower absolute energy of the transition state. The energy differences of ΔE_{Tot}^{IS} and ΔE_{Tot}^{TS} are calculated by the activation energy of h-pathway minus that of the d-pathway and the reaction energy of h-CH_3OH pathway minus that of the d-CH_3OH pathway, respectively. Double dash means that we were not able to find a transition state for the corresponding pathway. 220

Table A 5 Activation energies (Ea) and reaction energies (ΔE_{Rxn}) for the h-CH_3OH and the d-CH_3OH O-H dissociation reaction pathways on pure metal (blue) and SAA (red) surfaces. The “preferable pathway” in this table is defined as the pathway with the lower absolute energy of the transition state. Energy differences of ΔE_{Tot}^{IS} and ΔE_{Tot}^{TS} are calculated by the activation energy of h-pathway minus that of the d-pathway and the reaction energy of h-CH_3OH pathway minus that of the d-CH_3OH pathway, respectively. Double dash means that we were not able to find a transition state for the corresponding pathway. 221

Table A 6 Activation energies (Ea) and reaction energies (ΔE_{Rxn}) for the h-CH_3O and the d-CH_3O C-H dissociation reaction pathways on pure metal (blue) and SAA (red) surfaces. Preferable pathway in the table is defined as the pathway with lower absolute energy of the transition state. The energy differences of ΔE^{IS}_{Tot} and ΔE^{TS}_{Tot} are calculated by the activation energy of h-pathway minus that of the d-pathway and the reaction energy of h-CH_3OH pathway minus that of the d-CH_3OH pathway, respectively. Double dash means that we were not able to find a transition state for the corresponding pathway. 222
Table A 7 Activation energies (Ea) and reaction energies (ΔE_{Rxn}) for the h-CH_2OH and the d-CH_2OH O-H dissociation reaction pathways on pure metal (blue) and SAA (red) surfaces. Preferable pathway in the table is defined as the pathway with lower absolute energy of the transition state. The energy differences of ΔE^{IS}_{Tot} and ΔE^{TS}_{Tot} are calculated by the activation energy of h-pathway minus that of the d-pathway and the reaction energy of h-CH_3OH pathway minus that of the d-CH_3OH pathway, respectively. Double dash means that we were not able to find a transition state for the corresponding pathway. 223

Table A 8 Activation energies (Ea) and reaction energies (ΔE_{Rxn}) for the h-CH_3O and the d-CH_3O C-O coupling reaction pathways on Group 1 pure metal (blue) and SAA (red) surfaces. Preferable pathway in the table is defined as the pathway with lower absolute energy of the transition state. Energy differences of ΔE_{Tot}^{IS} and ΔE_{Tot}^{TS} are calculated by the activation energy of h-pathway minus that of the d-pathway and the reaction energy of h-CH_3OH pathway minus that of the d-CH_3OH pathway, respectively. Double dash means that we were not able to find a transition state for the corresponding pathway. 224
Table A 9 Activation energies (Ea) and reaction energies (ΔE_{Rxn}) for the h-CH_3O and the d-CH_3O C-O coupling reaction pathways on Group 2 pure metal (blue) and SAA (red) surfaces. Preferable pathway in the table is defined as the pathway with lower absolute energy of the transition state. The energy differences of ΔE_{Tot}^{IS} and ΔE_{Tot}^{TS} are calculated by the activation energy of h-pathway minus that of the d-pathway and the reaction energy of h-CH_3OH pathway minus that of the d-CH_3OH pathway, respectively. Double dash means that we were not able to find a transition state for the corresponding pathway. 225
Table A 10 Formation energies of initial states ($E_{F,ini}$), transition states ($E_{F,tra}$), and final states ($E_{F,fin}$) of C-O coupling on pure metal and SAA (111) surfaces, as computed by DFT. Values of E_F are relative to CH_4(g), H_2(g), and CO_2(g) as given by Eq. (2.51) in the main text. Double dash means that we were not able to find a transition state for the corresponding pathway. 226

Table A 11 Formation energies of initial states ($E_{F,ini}$), transition states ($E_{F,tra}$), and final states ($E_{F,fin}$) of CH_2OH O-H activation on pure metal and SAA (111) surfaces, as computed by DFT. Values of E_F are relative to $CH_4(g)$, $H_2(g)$, and $CO_2(g)$ as given by Eq. (2.51) in the main text. Double dash means that we were not able to find a transition state for the corresponding pathway. 227

Table A 12 Linear regression slopes (a), intercepts (b, in eV), R^2 and MAE in eV for the BEP relationship for six reactions; C-H and O-H activation of CH_3OH, C-H activation of CH_3O, C-H activation of CH_2OH, C-O coupling between CH_3 and CH_3O. Data is given for these reactions on pure metal (111) surfaces (blue), SAA (111) surfaces (red) and globally (black). Results of Student's T-test (to determine if the slopes and intercepts of pure metal and SAA BEP relations are different) are given for 90 % confidence intervals as "Yes" or "No" for different and not different, respectively. 228

Table A 13 Distance between the lowest H atom in CH_3 and the dopant atom ($D_{H\text{-}dopant}$) and distance between the C atom in CH_3 and the dopant atom ($D_{C\text{-}dopant}$) on the slab for Group 1 SAAs (blue) and Group 2 SAAs (red) in transition states of C-O coupling h-CH_3O pathway. 229

Table B 1 ECI parameters and their graph multiplicities (GM). This table shows which clusters were used in the cluster expansion of each investigated alloy, along with the corresponding ECI and GM. The positions of occupied adsorption sites are shown in Figure B1. The double dashes indicate that the specific cluster was not used in this case. ‘N/A’ indicates that the given configuration is unstable, so large ECIs (3.0 eV) are used to avoid the occurrence of that configuration. The ECIs are given in eV and include zero-point energy corrections. 234
Table B 2 Key elementary steps related to the HCOO dissociation mechanism on TD-SAA lattices. The frequency of initial, transition, and final states for each step are shown in the table, and blue frequencies indicate gas phase molecules. Forward energy barrier represents the reaction energy of a given elementary step from co-adsorbates. The energies are given in eV and include zero-point energy corrections. Since the partial pressures of CO_2 and H_2 are 0 bar during the reaction, no adsorption of these species will occur. 236
Table B 3 Peak temperatures of HCOO** dissociation TPD spectra obtained from simulations (before and after modifying the C-H activation barriers), experiments, and their deviations. The temperature begins at 100 K with 1000 H* and 1000 HCOO** on the lattice and ends at 550 K, with a ramp rate of 2 K/s. Positive deviations are indicated in blue and negative deviations in red. 240

Objectives and Thesis Outline

The objectives of this thesis are organized into three consecutive stages. First, DFT calculations are performed to construct complete reaction energy profiles for hydrogen formation from oxygenates (mainly CH_3OH and HCOOH) on SAA surfaces, including the identification of key intermediates and transition states and the evaluation of reaction and activation energies. Second, the resulting energetics are analyzed to extract general catalytic trends for SAAs by establishing BEP relationships and TCS correlations, thereby enabling descriptor-based interpretation of activity and selectivity across different host–dopant combinations. Third, KMC simulations are carried out using the DFT-derived parameters with lateral-interaction effects to connect atomistic kinetics with macroscopic behavior under relevant conditions to bridge the gap between static energetics and experimentally observable reactivity. The remainder of the thesis is organized as follows.

Chapter 1 establishes the background and conceptual framework for the remainder of the thesis. It motivates H_2 production by highlighting oxygenate feedstocks as practical and scalable hydrogen sources, reviews the fundamentals of heterogeneous catalysis, and summarizes key descriptors, including the Sabatier principle, BEP relationships, and TCS. The chapter further introduces SAAs as a promising catalyst.

Chapter 2 details the theoretical and computational framework used in Chapters 3–5, covering DFT, electronic-structure analysis, structural optimization methods, and transition-state searching. It then introduces GT-KMC as the kinetic modelling methodology adopted in this thesis, including the master-equation formalism, transition-state theory, coverage-dependent corrections, and the cluster expansion.

Chapter 3 investigate reaction and activation energetics for two representative elementary processes: (i) the decomposition of CH_3OH to CH_2O and (ii) C–O coupling between CH_3 and CH_3O. By interpreting the computed energetics using TCS and BEP relationships, we identify SAA compositions that retain relatively weak product adsorption while still exhibiting low kinetic barriers.

Chapter 4 focuses on investigating activity trends on copper-based SAAs for formic acid decomposition, combining DFT and KMC to interpret experimental TPD trends, elucidate the HCOO C–H activation pathway and assess the impact of residual H* as well as van der Waals corrections.

Chapter 5 explores the role of secondary single-atom sites in two-dopant SAA surfaces, demonstrating how such sites can enhance reactivity by scavenging CO and altering diffusion, adsorption distributions, and HCOO dissociation behavior under CO-rich conditions.

Summary and Closing Statement consolidates the main conclusions, highlights the broader implications for catalyst design, and proposes directions for future research, with supporting material provided in the appendices.

Chapter 1 Background Knowledge and Overview

1.1 Introduction

Global energy demand remains exceptionally large, and its scale presents a fundamental challenge for deep decarbonization. According to the 2025 Statistical Review of World Energy, the Energy Institute documents that total global energy supply rose by about 2% to a new high of ~592 EJ last year, highlighting that energy services must be delivered while reducing greenhouse-gas emissions.[4] In parallel, the International Energy Agency reports that global H_2 demand increased to almost 100 Mt in 2024, reflecting the continued importance of H_2 in industry and the growing interest in low-emissions fossil fuel alternatives.[5]

Realizing efficient H_2 production depends on applying catalysts that enable efficient H_2 release from attractive hydrogen carriers, such as CH_3OH and HCOOH, with high activity, selectivity and stability.[6, 7] Recent estimates place the 2004 value of the global catalyst market at roughly US$24.5 billion,[8] which includes a major contribution from high value precious metal catalysts, commonly based on platinum-group metals such as Pt, Pd, Rh, Ir, and Ru.[9, 10]

Catalysts can operate in homogeneous or heterogeneous systems.[11, 12] While homogeneous catalysis may offer high intrinsic activity, large scale deployment often faces practical challenges associated with catalyst separation and

recycling.[12, 13] In contrast, heterogeneous catalysts, typically solids interacting with gas/liquid-phase reactants and products, are widely preferred due to their operational robustness, ease of separation, and compatibility with continuous processing.[11, 13]

Among heterogeneous catalysts, active transition metals and their alloys play a central role across refining, petrochemicals, and emerging low carbon processes. Among them, a novel kind of heterogeneous transition metal alloy catalysts, called SAAs[1, 14-16], is formed by doping isolated transition metal dopants to coinage metal hosts. These SAAs can inherit both high activity and selectivity from their monometallic counterparts, while maintaining high stability.

This thesis focuses on screening and investigating SAAs with different metallic combinations on H_2 production from CH_3OH and HCOOH feedstock. In this work, we combine atomistic calculations based on density functional approximations with stochastic kinetic simulations to bridge microscopic elementary steps and macroscopic observables. Specifically, DFT[17-19] is used to quantify adsorption thermodynamics and elementary reaction barriers for key intermediates relevant to H_2 production from small oxygenates on SAAs. These energetics are then embedded into KMC simulations to explicitly account for site populations, diffusion-driven site competition, coverage effects, and lateral interactions under temperature-programmed conditions.[20-26]

The remainder of this chapter introduces the key concepts that underpin heterogeneous catalysis. These concepts are used to rationalize and predict the behavior of transition metal heterogeneous catalysts and are referred to throughout this thesis. We then provide a background on SAAs, which serve as the central catalyst platform throughout this thesis.

1.2 Attractive Feedstocks for H_2 Production

Among liquid oxygenates, CH_3OH and HCOOH are widely considered practical molecules for demand H_2 generation, because they combine high H content with well-established production, storage, and transport infrastructure.[27-29] In addition, both molecules can be sourced from low-carbon carbon streams, such as renewable carbon or biomass-derived routes. Therefore, these two chemicals can be integrated into circular-carbon strategies coupled with low-emission upstream processes.[30-32]

CH_3OH is a particularly attractive hydrogen carrier due to its high volumetric energy density and mature supply chain. It can be converted to H_2 via catalytic reforming or dehydrogenation pathways.[27-29] From a catalytic perspective, methanol conversion offers a well-defined set of elementary steps, including O–H or C–H activation and subsequent dehydrogenation, making it a useful model system for theoretically screening the activity of the catalysts.[27-29] In addition,

HCOOH, is also appealing because it can release H_2 under relatively mild conditions through dehydrogenation to H_2, CO, and CO_2. Importantly, HCOOH is also frequently discussed as a liquid organic H carrier, since its decomposition can be tuned toward CO-free H_2 when appropriate catalysts are used.[32, 33]

Despite these advantages, both systems pose nontrivial catalytic challenges that motivate atomistic studies. H_2 production rates and selectivity depend on competing elementary steps, coverage effects, and the availability of active sites, while CO poisoning (from background CO or side chemistry) can deactivate the active sites on catalysts.[34, 35]

1.3 An Overview of Heterogeneous Catalysis

Heterogeneous catalysis underpins a large portion of industrial chemical manufacturing processes by enabling reactions to proceed at practical temperatures and pressures.[36-38] By providing a reaction pathway with lower effective activation barriers, a catalyst can increase conversion rates, carry out the reaction at milder conditions, such as lower temperature and pressure, and improve overall process economics.[39, 40] The choice of catalyst is critical in achieving these goals. An effective catalyst should deliver high reaction rates (activity), maintain performance over extended operation (stability), and favor the formation of desired products (selectivity).[29]

A heterogeneous catalytic cycle can be decomposed into a sequence of microscopic steps occurring on the surface. Typical processes involve adsorption of reactants, surface diffusion, bond-breaking and bond-forming reactions among adsorbed intermediates, and desorption of products.[39, 40] The macroscopic rate and selectivity observed experimentally are emergent outcomes of several elements. Energy barriers of elementary steps, adsorption energies, and local surface environments collectively determine which pathways dominate and how rapidly the product is generated.[39-42] Because catalytic mechanisms often comprise many competing routes, and surface coverages and local environments evolve dynamically during operation, it is frequently challenging to identify the key factors that control performance.[39, 41]

Experimentally, this complexity creates a fundamental limitation. Measurements often report net rates, apparent activation energies, and overall selectivity, while the underlying distribution of surface configuration and the mechanism of elementary steps remain hidden. As a result, catalyst development has relied heavily on empiricism and trial-and-error method approaches.[40, 41] Figuring out the reaction mechanism involved in a specific catalytic process, e.g., catalytic dissociation of CH_3OH and HCOOH over SAAs requires approaches that can link molecular scale chemistry to macroscopic observables.[41, 42]

At the atomistic level, quantum chemistry calculations, such as DFT, can quantify adsorption energies, reaction energies, and activation barriers on well-defined surface models, thereby providing a consistent basis for comparing different materials.[17-19] To connect elementary step energetics to measurable kinetics, kinetic modelling methods such as microkinetic modeling and KMC simulations are widely used. These approaches translate rate constants of elementary processes into turnover frequencies, enabling evaluation of surface states under realistic conditions.[20-26] For the projects presented in this thesis, we employ DFT and KMC methods to investigate the reaction mechanisms of different catalytic systems.

1.4 Principles and Descriptors Used in Catalytic Performance

1.4.1 The Sabatier Principle in Heterogeneous Catalysis

The dependence of catalytic activity on the strength of catalyst–adsorbate interactions is often rationalized using the Sabatier principle, originally proposed by Paul Sabatier in the early twentieth century.[43, 44] In its simplest form, the principle states that an effective catalyst must interact with reactants neither too weakly nor too strongly.[43, 44] Adsorption must be sufficiently favorable to populate reactive intermediates on the surface, but not so strong that intermediates and products become immobilized and block active sites.[44]

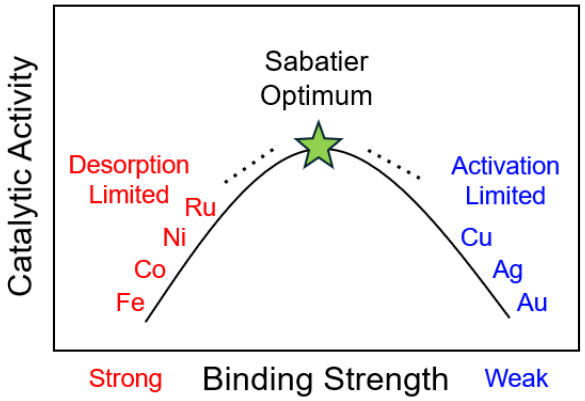


Figure 1. 1 Illustration of the Sabatier principle as a volcano activity plot. The catalytic activity for a reaction is optimized when the catalyst binds substrates at an intermediate strength.

This balance naturally leads to the volcano-shaped relationship frequently observed when catalytic performance is plotted against a measure of binding strength (Fig. 1.1).[44, 45] On the weak binding side of a volcano, the surface struggles to activate or retain reactants, so reaction rates are limited by low surface coverage or high energy barriers.[44, 46] On the strong binding side, the catalyst binds species so tightly that product desorption and surface regeneration become slow, and the surface may become poisoned by strongly adsorbed adsorbates.[44, 46] Note that overly strong binding can promote further conversion of the products on the surface, thereby decreasing selectivity.[44, 46] Maximum activity is typically found near an intermediate interaction region where both activation and desorption are kinetically accessible.[44, 45]

The Sabatier principle is fundamentally conceptual unless “binding strength” is defined precisely and connected to measurable or computable quantities.[44]

Real catalytic networks involve many elementary steps and multiple intermediates, so the relevant “binding strength” is rarely a single number.[44, 46] In addition, the performance optimum depends on other elements, such as temperature, pressure, surface structure, coverage effects, and competitive adsorption.[41, 42, 44] Consequently, the Sabatier principle alone does not directly predict which catalyst will be best; it instead motivates a systematic search for materials whose surface energetics strike the appropriate balance for the rate-determining steps (RDS).[42, 44]

The practical use of Sabatier’s idea became significantly more prominent with the rise of electronic structure calculation methods, for example DFT.[42, 46] DFT makes it possible to compute adsorption energies and reaction energetics for families of catalysts.[42, 46] By surveying multiple catalysts, researchers can identify trends and correlations according to a given reaction.[42, 44, 46] While DFT provides adsorption energies and elementary step energetics, kinetic modeling approaches, such as KMC can explicitly resolve the time evolution of surface coverages.[25, 41] This is particularly important for accurately characterizing catalyst performance on the strong binding side of a volcano plot (Fig. 1.1), where surface poisoning and further conversion of products can strongly influence the observed activity and selectivity.[25, 41]

1.4.2 BEP and TCS Relationships

The name Brønsted–Evans–Polanyi (BEP) relationship reflects Brønsted's earlier contribution to linear free-energy relationships, which linked reaction rates to thermodynamic quantities such as equilibrium constants, and the later formulation by Evans and Polanyi of a linear correlation between activation energy and reaction energy discovered later in 1938:[47]

$$E_a = E_0 + \omega \Delta H \tag{1.1}$$

where E_a is activation energy, ΔH is the enthalpy of reaction, and ω is proximity factor ranging from 0 to 1. In 2001, Logadottir et al.[48] justified the applicability of the BEP relationship in heterogeneous catalysis.[48] They discovered that the dissociation of nitrogen (N_2) on the surface of various transition metals indeed follows a BEP relationship, indicating that the relationship could be used to predict the reactivity trends of solid transition metals. One year later, Michaelides et al.[49] extended the BEP relationships to a large number of other common heterogeneously catalyzed elementary steps including O-H bond breaking, C-C bond breaking, adsorption dehydrogenation, CO_2 decomposition, hydrocarbon cracking reactions and diatomic cracking reactions on many transition metal surfaces such as Cu(111), Ru(111), Ru(001), and Pd(111), etc.[49] They calculated the energies of the initial, final and transition states of these reactions using DFT and computed the activation energies and

reaction energies which were then used to build the BEP relationships. In 2004, Bligaard and Nørskov established a relationship between reaction rate and dissociation adsorption energy via combining the reaction kinetic model and the BEP relation.[50] Additionally, they created a database in which the DFT approach was used to determine the chemisorption energies of a variety of simple gas molecules on different transition metal surfaces.

Pedersen et al. discovered a novel linear relationship, which is called TCS, between the adsorption energies of similar adsorbates in 2007.[51] They also built relationships between adsorption energies of NH_x, SH_x, CH_x, and hydroxy (OH) and those of the C, N, O, or S atom on various transition metal surfaces, respectively. Their results showed that these adsorption energies correlated linearly and the scaling constants γ only depended on x.

$$\Delta E_{ads}^{AH_x} = \gamma_x \Delta E_{ads}^{A} + \varepsilon \qquad (1.2)$$

where A represents C, N, O, and S. This work demonstrates that the TCS relationship can play an important role in estimating the adsorption energy of similar adsorbates on solid surfaces. The above works paved the way for establishing the methodology of building BEP and other related relationships to evaluate the performance of heterogeneous catalysts. Although these studies mainly focused on pure metals, the methodologies are transferable to

investigations of catalytic effects on various other materials including the more recently explored SAAs.

1.5 An Introduction to the SAA

1.5.1 The definition of the SAA

To satisfy the strict requirements of catalysts for H production from oxygenates, such as poison resistance, high selectivity, and low temperature activity, some preliminary studies have shown that SAAs are novel materials that could potentially function as catalysts for this purpose.[1, 14-16] SAAs are highly diluted bimetallic alloys where a reactive metal is dispersed in a less reactive host.[1, 14-16] Fig. 1.2 shows the structure of a SAA surface.

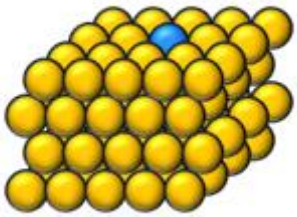


Figure 1. 2 Surface structure of a four-layer SAA (111) surface. The dopant metal is displayed in blue and the host metal in yellow.

SAAs as novel catalysts, exhibit many profound advantages, such as high selectivity, high catalytic activity, and poisoning resistance.[1, 14-16] This dilute architecture creates isolated dopant sites embedded in a host-dominated surface, which underpins several distinctive catalytic advantages discussed below.

1.5.2 Key Properties of SAAs

Recent work has revealed that SAAs possess distinctive electronic characteristics, often exhibiting a narrow band consisting of d-states near the Fermi level that provides a powerful handle for modulating adsorbate binding. Moreover, careful selection of the host–dopant metal pair enables deliberate tuning of the SAA electronic structure, allowing activity and selectivity to be optimized for specific catalytic reactions. In addition, the noble metal atoms that are predominant on the surfaces of SAAs can also make it resistant to poisoning and lead to improved catalyst lifetimes.

As mentioned in Section 5.1, the surface of a SAA is formed by the dispersion of transition metal atoms on the surface of noble metals at extremely high dilutions. Some transition metal atoms on the surface can provide more active sites than pure noble hosts, which explains why SAAs usually have higher activities than those pure host metals. Boucher et al.[52] found that the activity of catalysts can be dramatically increased, even if only less than 1 (at)% active metal atoms were introduced into the pure host metal. Additional surface-science studies from the Sykes group showed that isolated Pd atoms in a Cu surface substantially lower the barriers for H_2 desorption and enable highly selective hydrogenations (e.g., styrene and acetylene) compared with pure Cu or Pd.[53] Similarly, γ-Al_2O_3-supported Pt/Cu SAAs with <1 Pt atom per 100 Cu

atoms exhibited high activity and selectivity for 1,3-butadiene hydrogenation to butene under mild conditions.[54]

Besides, as the surfaces of pure transition metals have the potential to bind adsorbates strongly, the latter may be difficult to desorb from surfaces. In this case, adsorbates are prone to performing side reactions, thereby reducing the selectivity of the catalysts. However, SAAs have the potential to maintain high selectivity. Lucci et al.[54] found that SAAs have high hydrogenation selectivity due to the extremely low H_2 dissociation barrier offered by dopant-host sites. Shan et al.[55] found the Pt/Cu SAA had outstanding selectivity when used to dehydrogenate CH_3OH, while the Ni/Cu SAA could effectively catalyze the dehydrogenation of C_2H_5OH by facilitating C-H bond cleavage without breaking the O-H bond. Beyond hydrogenation, Pt/Cu SAAs were also shown to be highly selective for formic acid dehydrogenation (suppressing the CO-forming dehydration pathway), further illustrating that single-atom dilution can enhance performance while reducing precious-metal usage.[56]

Some products may also poison the catalysts via strongly adsorbing to the catalyst's surface and blocking its active sites. However, the noble metal atoms that are predominant on the surfaces of SAAs can significantly weaken the interaction between their surfaces and most kinds of strongly bound adsorbates and thus increase the selectivity of the catalyst as well as extend its life

expectancy. Liu et al.[57] investigated the relationship between CO poisoning resistance of Pt/Cu SAA and the atomic ratio of Pt/Cu. They identified the optimal atomic ratio of Pt/Cu to be 1:125. Besides, the dispersed dopant atoms can also increase the possibility of adsorbates spillover onto host-dopant sites, where selective reaction can easily take place. As the spillover pathway on SAAs can also be controlled, the selective poisoning of the dopant can be seen as a means of controlling the spillover pathway. Marcinkowski et al.[58] discovered and named the "molecular cork effect," which enabled the trapping of higher-energy H atoms on the SAA surface by blocking the sites for H atom desorption from the SAA surface with CO.

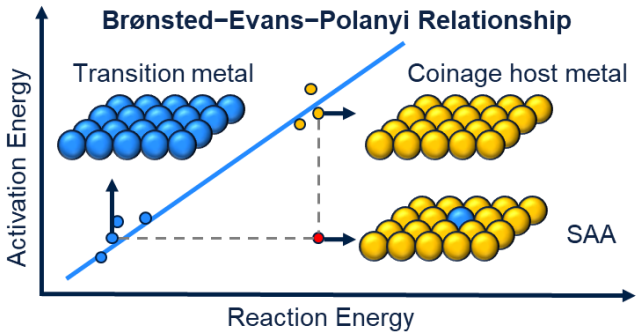


Figure 1. 3 A schematic of BEP plots for C-H bond dissociation. The blue, yellow and red dots in the figure represent the transition metals, host metals and the SAA, respectively.

One of the unique advantages of SAAs as catalysts is the fact that they have the potential to break the BEP relationship followed by pure metals. This was first demonstrated in 2018 by Darby et al.[59, 60] who performed DFT calculations on SAAs and then carried out comparisons with pure metals. Their findings

suggested that SAAs might easily diverge from a linear relationship, thereby enhancing the catalyst's performance (Fig. 1.3).

This deviation arises because the activation barrier and reaction energy can be governed by different local environments in SAAs. The bond-activation step often occurs directly at the isolated dopant atom, allowing the transition state to inherit the favorable activation properties of the dopant metal. In contrast, the final-state intermediates are not necessarily stabilized on the same dopant site; they may spill over onto the host surface or bind at mixed dopant–host sites. As a result, the final state can be destabilized relative to that on the pure dopant metal, giving a higher reaction energy while retaining a low activation barrier. This decoupling of transition-state stabilization from final-state binding enables SAAs to deviate from, or even break, the conventional BEP relationship followed by monometallic surfaces.[59, 60] That work also revealed the reasons for the deviation of SAAs and how to identify suitable SAA catalysts for various reactions based on this characteristic.

In conclusion, the combination of highly active transition-metal dopant atoms and the comparatively weak binding on coinage-metal host surfaces enables SAAs to achieve both high activity and high selectivity. The highly dilute dopant site can, in some cases, lead to deviations from conventional BEP trends, while also improving tolerance to poisoning and extending catalyst lifetimes. From

the above research, we conclude the specific bimetallic SAAs combinations may preferentially catalyze certain reactions of interest. This conclusion also means that finding the most suitable catalyst is an arduous task that can be facilitated by adopting computational methods, which provide fundamental insight and thus guide catalyst development efforts.

1.6 Conclusion

This chapter has provided the background and conceptual framework required for the remainder of the thesis. It first outlined the motivation for H_2 production and introduced representative oxygenates feedstocks that are attractive for producing H_2 under practical and scalable conditions.

The fundamentals of heterogeneous catalysis were then reviewed, emphasizing how adsorption, surface intermediates, and elementary reaction steps collectively determine activity and selectivity. Building on this foundation, the chapter discussed widely used principles and descriptors for catalytic performance, including the Sabatier principle, the BEP relationship and thermochemical linear scaling relations that connect reaction energetics with kinetic barriers.

The chapter then introduced SAAs as an emerging catalyst that can combine the advantageous features of dilute active sites with inert hosts thereby

acquiring both high activity and high selectivity. Key concepts relevant to SAAs were summarized, including how isolated dopant atoms modify adsorption and reaction energetics relative to pure metals, and how these effects can benefit oxygenate upgrading. In this thesis, we use the DFT-KMC framework[1-3] to investigate the catalytic performance of SAAs and compare them with pure metals. These two methods (DFT and KMC) are discussed in the next chapter.

Chapter 2 Methodology and Research Approach

2.1 Introduction

This chapter presents the theoretical framework adopted throughout this thesis to investigate catalytic reactivity on SAA surfaces. The aim is to establish a consistent workflow that connects electronic structure calculations with kinetic modelling, enabling mechanistic insight and quantitative predictions across the case studies discussed in Chapters 3–5. To this end, the chapter first introduces the DFT approach, including the development of the formalism, exchange–correlation functionals, periodic boundary conditions and the Bloch's theorem, pseudopotentials, and practical algorithms for solving the Schrödinger equations. Methods for electronic-structure analysis are then described to support the interpretation of bonding and reactivity, followed by the procedures used for structural optimization and transition-state location, including climbing-image nudged elastic band (CI-NEB), the dimer method, and vibrational frequency calculations for validating stationary points.

It then introduces the KMC framework from first principles, starting from the master equation progressing to transition state theory (TST) and the derivation of rate expressions. Key extensions required for realistic surface kinetics, such as coverage-dependent barrier corrections and cluster expansion representations of lateral interactions, are also discussed. Finally, the chapter reviews major KMC algorithms and presents the GT-KMC strategy, which is

used later to bridge the gap between atomistic energetics and experimentally observable catalytic behavior.

2.2 An Introduction to the Schrödinger Equation

The formation or breaking of bonds is due to the re-distribution of electrons around nuclei and the motion of the latter. Since both nuclei and electrons are quantum particles, their behavior is governed by the time-dependent Schrodinger equation which gives us the time evolution of the wavefunction (a function that encodes the complete information of the quantum state) for physical and chemical systems.

$$i\hbar \frac{\partial \Psi_{tot}(\boldsymbol{r}_1 \cdots \boldsymbol{r}_N, \boldsymbol{R}_1 \cdots \boldsymbol{R}_n, t)}{\partial t} = \widehat{H}_{tot} \Psi_{tot}(\boldsymbol{r}_1 \cdots \boldsymbol{r}_N, \boldsymbol{R}_1 \cdots \boldsymbol{R}_n, t) \qquad (2.1)$$

Where $\widehat{H}_{tot}$ is the Hamiltonian operator corresponding to the total energy of that system. Ψ_{tot} is the wavefunction of all particles including both nuclei and electrons, $\boldsymbol{R}_i$ and $\boldsymbol{r}_j$ are the coordinates of the i-th nuclei and the j-th electron, and n and N being the total number of nuclei and electrons, respectively. If the Hamiltonian is time-independent, the energy does not change with time. Therefore, we can use the time-independent Schrödinger equation (mentioned as Schrödinger equation in the following text) to obtain the energy eigenvalues of the system:

$$\widehat{H}_{tot}\Psi_{tot}(\boldsymbol{r}_1 \cdots \boldsymbol{r}_N, \boldsymbol{R}_1 \cdots \boldsymbol{R}_n) = E_{tot}\Psi_{tot}(\boldsymbol{r}_1 \cdots \boldsymbol{r}_N, \boldsymbol{R}_1 \cdots \boldsymbol{R}_n) \qquad (2.2)$$

where E_{tot} is the total energy of the system. The unknown of the Schrödinger equation is the wavefunction, which is a complex function in a $(3 \times N + 3 \times n)$–dimensional space ($n$ and N being the number of nuclei and electrons, respectively). Thereby, solving such equations for complex systems with many atoms is difficult.

2.3 Born-Oppenheimer Approximation

Obtaining approximate solutions to Schrödinger equations for complex systems has attracted increasing interest over the last century. To solve this problem, several approximations and mathematical methodologies have been proposed. Among them, the Born-Oppenheimer approximation reduces the dimension of the Schrödinger equation (Eq. (2.2)).[61] Due to the significant mass difference between electrons and atomic nuclei (the mass of a proton is approximately 1836 times that of an electron), the speeds of the latter are negligible compared to those of electrons, which means that wavefunction of electrons can instantly adapt to the dynamics of nuclei so that the motion of electrons can be decoupled from the nuclei. In this case, the electronic motion can be solved at fixed nuclear geometry. This allows an approximate separation of electronic and nuclear degrees of freedom.

$$\Psi_{tot}(\boldsymbol{r}_1 \cdots \boldsymbol{r}_N, \boldsymbol{R}_1 \cdots \boldsymbol{R}_n) \approx \Psi(\boldsymbol{r}_1 \cdots \boldsymbol{r}_N)\Psi_I(\boldsymbol{R}_1 \cdots \boldsymbol{R}_n) \tag{2.3}$$

where Ψ and Ψ_I are the wavefunctions of electrons and nuclei, respectively. In this case, one can decompose the full-particle Schrödinger equation (Eq. (2.2)) into a Schrödinger equation for the electrons (Eq. (2.4)) and a Schrödinger equation for the nuclei (Eq. (2.5)).

$$\hat{H}\Psi(\boldsymbol{r}_1 \cdots \boldsymbol{r}_N) = E\Psi(\boldsymbol{r}_1 \cdots \boldsymbol{r}_N) \tag{2.4}$$

$$\hat{H}_{II}\Psi_I(\boldsymbol{R}_1 \cdots \boldsymbol{R}_n) = E_{tot}\Psi_I(\boldsymbol{R}_1 \cdots \boldsymbol{R}_n) \tag{2.5}$$

where $\hat{H}$ and $\hat{H}_{II}$ are the Hamiltonian operators corresponding to the energy of electrons and nuclei, and E is the total energy of the electrons. In practice, nuclei are typically approximated as classical particles, so their dynamics are obtained by integrating Newton's equations of motion (which will be discussed in Section 2.8 in this Chapter). Note that motion is governed not only by the mutual Coulomb repulsion between nuclei, but also by the force arising from the potential created by the surrounding electronic density. For a particular system, the electronic Schrödinger equation is first solved by assuming the position of each nucleus is fixed, followed by solving the nuclei Schrödinger equation (Eq. (2.6)).

$$\left[-\frac{1}{2}\sum_{i=1}^{n}\frac{1}{M_i}\nabla_i^2 + E_{II} + E(\boldsymbol{R}_1 \cdots \boldsymbol{R}_n)\right]\Psi_I = E_{tot}\Psi_I$$

$$[-\frac{1}{2}\sum_{i=1}^{n}\frac{1}{M_i}\nabla_i^2 + \sum_{i>j}^{n}\frac{Z_i Z_j}{|\boldsymbol{R}_i - \boldsymbol{R}_j|} + E(\boldsymbol{R}_1 \cdots \boldsymbol{R}_n)]\Psi_I = E_{tot}\Psi_I \qquad (2.6)$$

where M_i and Z_i are the mass and the nuclear charge of the i-th nuclei, respectively. Note that the formulas in this thesis use atomic units, namely: $4\pi\varepsilon_0 = e = \frac{h}{2\pi} = m_e = 1$. In this Born–Oppenheimer nuclear Schrödinger equation, the Hamiltonian inside the brackets consists of three contributions: the first term is the nuclear kinetic-energy operator; the second term E_{II} is the nucleus–nucleus (internuclear) Coulomb repulsion energy, which originates from Coulombic repulsions among themselves; and $E(\boldsymbol{R}_1 \cdots \boldsymbol{R}_n)$ is the electronic energy obtained by solving the electronic Schrödinger equation at fixed nuclear positions, acting as an effective potential for nuclear motion. The eigenvalue E_{tot} is the total energy associated with the nuclear wavefunction Ψ_I. This quantity $E(\boldsymbol{R}_1 \cdots \boldsymbol{R}_n)$ defines the PES, namely the electronic energy as a function of nuclear geometry. The PES provides the forces on nuclei via its gradients and therefore governs molecular structures.

Therefore, under the Born–Oppenheimer approximation, the central problem is reduced to obtaining the electronic energy $E(\boldsymbol{R}_1 \cdots \boldsymbol{R}_n)$ efficiently and accurately as a function of nuclear geometry. This is the starting point for most electronic structure methods discussed in the following sections. The problem

we are facing now is how to solve the electron Schrödinger equation efficiently.[61]

2.4 The Development of the Hartree-Fock Equation

Although the dynamics of electrons and nuclei can be decoupled, thereby needing to solve lower dimensional equation for each type of particle, there are still several challenges that make solution difficult. For electrons models, the Schrödinger equation has a form of:

$$\left[-\frac{1}{2}\sum_{i=1}^{N}\nabla_i^2+\sum_{i=1}^{N}V(r_i)+\sum_{i=1}^{N}\sum_{j<i}U(r_i,r_j)\right]\Psi=E\Psi \tag{2.7}$$

$$\langle\Psi|\hat{H}|\Psi\rangle=E \tag{2.8}$$

where E is the total energy of the electrons, Ψ is the wavefunction of all electrons, r_i is the coordinates of the ith electron, and N is the number of electrons. The three terms in the brackets from left to right represent the sum of the kinetic energies of every electron, V is the potential energy due to attractive forces between each electron and the nuclei, and U is the potential energy due to repulsive forces between different electrons.

The third term of the Schrödinger equation (Eq. (2.7)) represents interactions between electrons, which makes the equation difficult to solve. To address this issue, a new type of approximation was proposed by Slater et al.[62], which is

called the mean-field approximation. This approximation assumes that each electron in the system can be seen as moving in an average potential field generated by other electrons, indicating that the energy of each electron only depends on its own distribution in space. In this case, the Schrödinger equation can now be decoupled into a set of single-electron wavefunctions. With the help of the mean-field approximation, the wavefunction of all electrons can be approximated via single electron wavefunctions, called orbitals. Hartree products were first proposed to approximate the wavefunction of all electrons, constructed by simply multiplying spatial orbitals:

$$\Psi = \varphi_1(r_1)\varphi_2(r_2)\varphi_3(r_3)\cdots\varphi_i(r_i)\cdots\varphi_N(r_N) \tag{2.9}$$

where $\varphi_i(r_i)$ represents the orbital of the ith electron in the system. However, the wavefunction of a single electron contains not only a spatial part $\varphi(r)$ but also a spin part $\chi(\omega)$. Due to the indistinguishability of electrons and the antisymmetric nature of the wavefunction, which is linked to Pauli's exclusion principle[63], Slater proposed a new way to represent the wavefunction of all electrons via spin orbitals ψ, which is known as the Slater determinant.[62]

$$\Psi = \frac{1}{\sqrt{N!}}\begin{vmatrix} \psi_1(x_1) & \psi_1(x_2) & \cdots & \psi_1(x_N) \\ \psi_2(x_1) & \psi_2(x_2) & \cdots & \psi_2(x_N) \\ \vdots & \vdots & \ddots & \vdots \\ \psi_N(x_1) & \psi_N(x_2) & \cdots & \psi_N(x_N) \end{vmatrix} \tag{2.10}$$

$$\psi_i(x_j) = \varphi_i(r_j)\chi_i(\omega_j) \tag{2.11}$$

where $\varphi_i(r_j)$ and $\chi_i(\omega_j)$ is the spital part and the spin part of the single electron wavefunction, respectively.

After substituting the wavefunction from Eq. (2.10) into Eq. (2.7), the method of Lagrange multipliers was used to find the minimum of the energy E. The problem then becomes equivalent to solving a set of i coupled equations; one representative equation is given below.

$$\hat{F}\varphi_i(r_i) = \varepsilon_i\varphi_i(r_i) = \left[-\frac{1}{2}\nabla^2 + V(r_i) + \sum_j^N \int dr_j \frac{|\varphi_j(r_j)|^2}{|r_i - r_j|} - \frac{1}{2}\sum_j^N \int dr_j \frac{\varphi_j^*(r_j)\varphi_i(r_j)}{|r_i - r_j|}\right]\varphi_j(r_i) \quad (2.12)$$

Eq. (2.12) is also called Hartree-Fock equation, where ε_i represents the Hartree-Fock energy of the ith electron in the system, $\varphi_i(r_i)$ is the spatial wavefunction of the i-th electron, and $\hat{F}$ is called the Fock operator.[62, 64-66] The first two terms represent the kinetic energy of the ith electron and the potential energy due to the attraction between nuclei and the ith electron. The third term accounts for the Coulomb repulsion between the ith electron and every other electron, while the fourth term evaluates the so-called “exchange effects” resulting from the anti-symmetry of the electronic wavefunctions. The equation (1.5) can be solved via the self-consistent field (SCF) method.[64, 67] Wavefunctions of each electron are first given an initial guess followed by

calculating the three operators in Eq. (2.12). The Hartree-Fock equation can then be used to update $\varphi_1 \cdots \varphi_N$ and their Hartree-Fock energies again to finish the first iteration step. These iteration steps are then stopped when the equation is self-consistent.[62, 66]

However, the Hartree–Fock mean-field approximation does not fully account for electron correlation. It includes exchange effects between electrons with the same spin through the antisymmetric of the wavefunction, but neglects dynamic Coulomb correlation associated with the instantaneous repulsion between electrons. This effect causing a lower real energy than that calculated from Hartree-Fock equation. The correlation energy is defined as the difference between the exact electron energy and the Hartree-Fock energy.[68]

$$E_c = E_{exact} - E_{HF} \tag{2.13}$$

Additionally, calculating the Fock operator in Eq. (2.12) is still computationally expensive.[66, 67] As a result, new approaches are required to simultaneously improve efficiency and accuracy by reducing the computational cost and incorporating electron–electron correlation effects neglected in the Hartree–Fock approximation.[69]

2.5 The Development of DFT

In 1964, Hohenberg and Kohn first proposed the Kohn-Hohenberg theorems justifying that the ground state energy of a system can in principle be expressed via the electron density $n(\boldsymbol{r})$, which can be calculated by the following equation:[69]

$$n(r) = N \int |\Psi(\boldsymbol{r}, \boldsymbol{r}_2, \cdots, \boldsymbol{r}_N)|^2 d\boldsymbol{r}_2 \cdots d\boldsymbol{r}_N \tag{2.14}$$

where $\Psi(\boldsymbol{r}_1, \cdots, \boldsymbol{r}_N)$ is multi-electron wavefunction of the system. The ground-state energy of a many-electron system can be written as a functional of the electron density, $E_g[n(\boldsymbol{r})]$.[70] In addition, the electron density that minimizes this energy functional is the ground state density, and the corresponding minimum value is the ground state energy.[70] If we neglect the ion–ion interaction term E_{II} discussed in the Section 2.3, the ground state energy of a system can be written as:

$$\begin{aligned} E_g[n] &= \min_n (T[n] + V_{ext}[n] + V_{ee}[n]) \\ &= \min_n \left(T[n] + \int v_{ext}(\boldsymbol{r}) n(\boldsymbol{r}) d\boldsymbol{r} + V_{ee}[n] \right) \end{aligned} \tag{2.15}$$

Here, $n(\boldsymbol{r})$ is the electron density, $T[n]$ is the kinetic energy functional of the interacting system, $v_{ext}(\boldsymbol{r})$ is the energy associated with the external potential acting on the electrons, and $V_{ee}[n]$ is the electron–electron interaction energy

functional.[70-72] In this way, determining the ground state energy becomes a problem of minimizing the functional with respect to electron density $n(\boldsymbol{r})$.[70-72]

However, explicit density-functional expressions for $T[n]$ and $V_{ee}[n]$ are not available in general, and obtaining accurate values requires nontrivial approximations and computational procedures.[69, 71, 72] Although the kinetic energy can be written in terms of the many electron wavefunction $\Psi(\boldsymbol{r}_1, \cdots, \boldsymbol{r}_N)$, obtaining Ψ for an interacting system is itself highly nontrivial. To address this issue, Kohn and Sham introduced an auxiliary noninteracting reference system Φ that reproduces the same electron density as the interacting system and used it to define an approximate kinetic energy T_s.[69] As the system is noninteracting, we can write the electronic density as:

$$n(\boldsymbol{r}) = N \int |\Phi(\boldsymbol{r}, \boldsymbol{r}_2 \cdots, \boldsymbol{r}_N)|^2 d\boldsymbol{r}_2 \cdots d\boldsymbol{r}_N = \sum_{i=1}^{N} |\varphi_i(\boldsymbol{r})|^2 \tag{2.16}$$

$$T_s = -\frac{1}{2}\langle \Phi | \nabla^2 | \Phi \rangle = -\frac{1}{2} \sum_{i}^{occ} \langle \varphi_i | \nabla^2 | \varphi_i \rangle \tag{2.17}$$

We define $\varphi_i(\boldsymbol{r})$ in this auxiliary system as the Kohn–Sham (KS) orbitals.[69] T_s is the kinetic energy of the noninteracting reference system. In practice, T_s often provides a useful approximation to the true interacting kinetic energy functional $T[n]$.[69] For the electron–electron interaction term $V_{ee}[n]$, we first decompose it as

$$
\begin{aligned}
V_{ee}[n] &= J[n] + E_x[n] + E_c[n] \\
&= (J_{pair}[n] + J_{self}[n]) + E_x[n] + E_c[n] \\
&= \frac{1}{2}\int \frac{n(\boldsymbol{r})n(\boldsymbol{r}')}{|\boldsymbol{r}-\boldsymbol{r}'|}dr + E_x[n] + E_c[n]
\end{aligned} \tag{2.18}
$$

Here, the Hartree (classical Coulomb) term $J[n]$ is straightforward to evaluate, whereas the exchange energy $E_x[n]$ and the correlation energy $E_c[n]$ generally do not have simple explicit expressions.[69, 70] Note that the Hartree energy contains an unphysical self-interaction term $J_{self}[n]$, which is then cancelled by the exchange functional $E_x[n]$. Substituting this decomposition into the total energy functional gives

$$
\begin{aligned}
E_g[n] &= \min_n (T[n] + V_{ext}[n] + V_{ee}[n]) \\
&= \min_{\Phi\to n}(T_s[\Phi] + V_{ext}[n] + J[n] + ((T[n]-T_s) + E_x[n] + E_c[n])) \\
&= \min_{\Phi\to n}\left(-\frac{1}{2}\langle\Phi|\nabla^2|\Phi\rangle + V_{ext}[n] + J[n] + E_{xc}[n]\right)
\end{aligned} \tag{2.19}
$$

The exchange–correlation functional $E_{xc}[n]$ consists of four contributions: exchange energy $E_x[n]$, correlation energy $E_c[n]$, the self-interaction term in the Hartree energy $J_{self}[n]$, and the kinetic energy correction $(T[n]-T_s)$ between the interacting system and the noninteracting KS reference system.[69, 70] The KS reference system can be viewed as the noninteracting system Φ that reproduces the target density $n(\boldsymbol{r})$ while having the minimum noninteracting kinetic energy.[69, 71] We can then apply the variational principle to Eq. (2.19), leading to a set of single-particle equations[69];

the Schrödinger equation for each electron can thus be written in the following form:

$$\left[\frac{\delta T_{ref}[n(\boldsymbol{r})]}{\delta n(\boldsymbol{r})} + V_{ext}(\boldsymbol{r}) + \frac{\delta J[n(\boldsymbol{r})]}{\delta n(\boldsymbol{r})} + \frac{\delta E_{xc}[n(\boldsymbol{r})]}{\delta n(\boldsymbol{r})}\right]\varphi_i = \varepsilon_i \varphi_i$$

$$\left[-\frac{1}{2}\nabla^2 + V_{ext}(\boldsymbol{r}) + v_{Hartree}(\boldsymbol{r}) + v_{xc}(\boldsymbol{r})\right]\varphi_i = \varepsilon_i \varphi_i \qquad (2.20)$$

Here $V_{ext}(\boldsymbol{r})$ is the external potential, and $v_{xc}(\boldsymbol{r})$ is the exchange–correlation potential. Eq. (2.20) is known as KS equation. In the KS framework, the effective "one-electron" operator is determined by the electron density $n(\boldsymbol{r})$, so the many-electron interacting problem is mapped onto a set of single particle equations that can be solved self-consistently.

The total energy can be expressed in terms of the KS eigenvalues as

$$E_g[n(\boldsymbol{r})] = \sum_i^{occ} \varepsilon_i - J[n(\boldsymbol{r})] - \int v_{xc}(\boldsymbol{r}) n(\boldsymbol{r})\, d\boldsymbol{r} + E_{xc}[n(\boldsymbol{r})] + E_{II} \qquad (2.21)$$

Eq. (2.21) relates the sum of the single-particle eigenvalues $\sum_i^{occ} \varepsilon_i$ of the auxiliary noninteracting system to the total energy. Each Kohn–Sham eigenvalue ε_i contains the expectation value of the Hartree potential $v_{Hartree}(\boldsymbol{r})$. Therefore, simply summing all occupied eigenvalues would count the electron–electron Coulomb interaction twice, and one must subtract the

Hartree energy $J[n(\boldsymbol{r})]$ to correct this double counting. Similarly, the eigenvalues also include the term $\int v_{xc}(\boldsymbol{r})n(\boldsymbol{r})\,d\boldsymbol{r}$, which is generally not equal to the exchange–correlation energy functional $E_{xc}[n(\boldsymbol{r})]$. Hence, one subtracts $\int v_{xc}(\boldsymbol{r})n(\boldsymbol{r})\,d\boldsymbol{r}$ and adds back $E_{xc}[n(\boldsymbol{r})]$. Finally, adding the ion–ion (nucleus–nucleus) interaction energy E_{II} gives the total energy of the system E_g. The accuracy of the overall calculation depends on identifying a reasonable approximation of the exchange-correlation functional $V_{xc}(r)$.[73]

2.6 Exchange Correlation Functional

Numerous exchange–correlation functionals have been developed for different classes of systems, ranging from non-empirical, constraint-based forms derived from exact conditions to semi-empirical parameterizations fitted to thermochemical and/or benchmark electronic-structure data.[74] The local-density approximation (LDA) is one of the simplest approximations that assumes the exchange correlation functional is an expression of solely the electron density:

$$E_{xc}^{LDA}[n] = E_x^{LDA}[n] + E_c^{LDA}[n] = C\int n^{\frac{3}{4}}(r)\,dr + E_c^{LDA}[n] \qquad (2.22)$$

where the exchange correlation functional $E_{xc}^{LDA}[n]$ is composed of two parts, namely the exchange functional $E_x^{LDA}[n]$ and the correlation functional $E_c^{LDA}[n]$, which are only related with the electron density. Note that, although

the exchange functional normally has a fixed expression, the correlation functional may have a variety of distinct forms.[75, 76]

Because the LDA considers merely the effect of electron density on the exchange correlation functional, it may result in large inaccuracies when evaluating the energy of complicated multielectron systems. To solve this problem, the generalized gradient approximation (GGA) was proposed.[77] According to the GGA, the exchange correlation functional is related not only to the electron density itself, but also to the gradient thereof at each point:

$$E_{xc}^{GGA}[n] = E_{x}^{GGA}[n] + E_{c}^{GGA}[n] = \int n(r)\epsilon_{xc}^{GGA}(n(r), |\nabla n(r)|)\, dr \qquad (2.23)$$

where ϵ_{xc} represents the energy per electron. As a result, a correction term that includes the electron density gradient is introduced in both the exchange and the correlation functionals. Most common GGA exchange-correlation functionals includes Becke[78], B86[79], P86[80], and LG[81].

The exchange-correlation functional can be further improved by introducing the second derivative of the electron density as an additional correction term. These exchange correlation functionals are called meta-GGA functionals.[82] Additionally, hybrid functionals incorporate a fraction of Hartree–Fock exchange into a density-functional framework, typically mixing it with semi-local DFT

exchange and using a chosen correlation functional, with the mixing coefficients often determined empirically.[79, 83]

The exchange correlation functional used in the research discussed in this thesis is the optB86b-vdW and Revised Perdew–Burke–Ernzerhof (RPBE) functional.[84, 85] According to optB86b-vdW, the exchange part of the functional belongs to the GGA functional, which is improved based on the B86b functional[86] to make the functional more suitable for multi-electronic systems by including a term that accounts for van der Waals interactions.[84, 87] The resulting improved accuracy of this functional is particularly useful for our research, because groups such as CH_3 and CH_3O rely on van der Waals forces to adsorb on the surface of the alloy.

Another exchange–correlation functional used in this thesis for electronic structure calculations is the RPBE functional.[85] In addition, RPBE is a GGA that revises the exchange part of the original Perdew–Burke–Ernzerhof (PBE) functional,[88] and was specifically designed to improve adsorption energetics for atoms and molecules on transition-metal surfaces by reducing the systematic over-binding often observed with standard GGAs.[85] This improved description of chemisorption and surface energetics is particularly relevant to the present work, where adsorbates interact with alloy surfaces through a balance of short-range bonding and weaker dispersion contributions.

2.7 Periodic Boundary Conditions and Bloch's Theory

DFT proposes an efficient approach for solving the multi-electron Schrödinger equation on systems with a finite number of atoms. However, if DFT is applied to analyze adsorption/desorption or other chemical processes on metal surfaces, an additional issue must be first resolved – how to build a reasonable model? To eliminate the influence of boundary effects of the surfaces, the solid surface is frequently treated as an infinite plane, which complicates model construction.[89] To solve this problem, periodic boundary conditions are utilized to approximate an infinite system by perfectly tiling an infinite number of identical small blocks, referred to as supercells, along three dimensions.[89, 90] An example structure of a supercell is shown in Figure 2.1.[89]

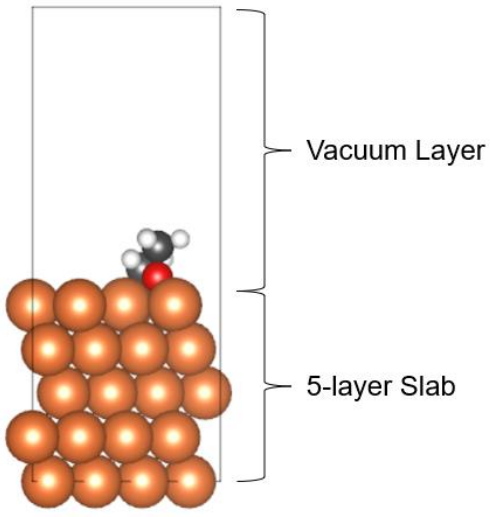


Figure 2. 1 Side view of a supercell structure model used for surface calculation.

In order to avoid interactions between a slab and its images due to the periodic

boundary conditions along the z-axis, a thick enough vacuum layer should be built in the supercell (Fig. 2.1).[89, 91] After imposing periodic boundary conditions on the supercell containing a finite number of atoms, the properties of large-scale systems can be described accurately.[89]

Bloch's theorem is used to describe the electron wavefunctions of a supercell.[92] The theorem states that the wavefunction of an electron in a periodic potential field can be expressed as the product of a periodic function $u_k(\boldsymbol{r})$ with the same periodicity at that of the potential and a plane wave:[92]

$$\varphi_k(\boldsymbol{r}) = \exp(i\boldsymbol{k}\cdot\boldsymbol{r})\, u_k(\boldsymbol{r}) \tag{2.24}$$

where $u_k(\boldsymbol{r})$ is periodic amplitude function, $\boldsymbol{k}$ is a vector in reciprocal space (wavevector), $\boldsymbol{r}$ is a vector in real space (the spatial variable). In practice, we restrict the wavevector to the first Brillouin zone (namely the Wigner–Seitz cell of the reciprocal lattice, which contains all inequivalent $\boldsymbol{k}$-points and therefore provides a unique representation of Bloch states); the resulting $\boldsymbol{k}$ is called the reduced wavevector. For a wavevector that lies outside the first Brillouin zone, one can always fold it back into the first Brillouin zone by adding a reciprocal lattice vector $\boldsymbol{G}$. After using plane wave functions as the basis to expand the above periodic function $u_k(\boldsymbol{r})$, Eq. (2.25) can be acquired:

$$\varphi_{n,\boldsymbol{k}}(\boldsymbol{r}) = \sum_{\boldsymbol{G}} c_{n,\boldsymbol{G}} \exp[i(\boldsymbol{k}+\boldsymbol{G})\cdot\boldsymbol{r}] \tag{2.25}$$

where the index n is the band index, labeling the different eigenstates (energy bands) obtained for the same $\boldsymbol{k}$-point when solving the KS equations; for each $\boldsymbol{k}$, n orders the corresponding eigenvalues (bands) from low to high energy. The reciprocal lattice vector $\boldsymbol{G}$ is defined as

$$\boldsymbol{G} = n_1\boldsymbol{b_1} + n_2\boldsymbol{b_2} + n_3\boldsymbol{b_3}; (n \in Z) \tag{2.26}$$

where $\boldsymbol{b_i}$ is the lattice vector of supercell in reciprocal space. There are still two difficulties that need to be overcome. The first problem is that many important quantities, such as the charge density $n(\boldsymbol{r})$, require integration over the first Brillouin zone.

$$n(\boldsymbol{r}) = \frac{V_{cell}}{(2\pi)^3}\sum_{n}^{occ}\int_{IBZ} f(n,\boldsymbol{k})\left|\varphi_{n,\boldsymbol{k}}(\boldsymbol{r})\right|^2 d\boldsymbol{k} \tag{2.27}$$

where V_{cell} is the volume of a cell in real space, $f(n,\boldsymbol{k})$ is the distribution of electrons indicating the number of electrons that occupy the state $\{n,\boldsymbol{k}\}$. However, in the thermodynamic limit, $\boldsymbol{k}$ is a continuous variable, so the Brillouin-zone integral cannot be evaluated analytically. In this case, we can use mathematical methods to acquire the approximate value of the integral via a

weighted sum over a discrete set (grid) of particular $\boldsymbol{k}$ points:[89]

$$\int_{IBZ} f(n,\boldsymbol{k}) \left|\varphi_{n,\boldsymbol{k}}(\boldsymbol{r})\right|^2 d\boldsymbol{k} \approx \sum_{\boldsymbol{k}} \omega_{\boldsymbol{k}} f(n,\boldsymbol{k}) \left|\varphi_{n,\boldsymbol{k}}(\boldsymbol{r})\right|^2 \tag{2.28}$$

One of the most common approaches to find a reasonable k-point grid is by using the method proposed by Monkhorst and Pack.[89] To get an accurate estimation of the integral, a large enough density of $\boldsymbol{k}$ points in the Brillouin zone must be sampled. However, a higher k-point density also increases the computational time, thereby decreasing the calculation efficiency.

Secondly, the sum of Eq. (2.28) involves an infinite number of terms for any point $\boldsymbol{k}$ in the reciprocal space, which makes the equation impossible to solve numerically. Therefore, we need to truncate the expansion and introduce a cut-off energy E_{cut}. The kinetic energy E_k of one plane wave can be easily calculated:

$$E_{\boldsymbol{k}} = \frac{h}{2m}|\boldsymbol{k}+\boldsymbol{G}|^2 < E_{cut} \tag{2.29}$$

where E_{cut} is the cut-off energy.[89] The role of the cut-off energy is to discard all terms with higher kinetic energy than the cut-off. Increasing the cut-off energy can improve the accuracy of the calculation but also increases the time required for the calculation. It is very important to find a reasonable cut-off

energy for a given system to balance the error and computational efficiency. The pseudopotential approximation introduced in the next chapter can be applied to reduce the cut-off energy to a reasonable value.[93, 94]

2.8 Pseudopotential Approximation

Although core electrons usually make only a small contribution to chemical bonding and can often be treated together with the nuclei as an ionic core, they still affect valence electrons through Coulomb screening through the orthogonality constraint between valence and core states. If one solves the electronic wavefunctions using an all-electron potential, all orbitals must be orthogonal to each other (indicating that the valence orbitals must remain orthogonal to the core orbitals) and experience a very strong Coulomb attraction near the nuclei. As a result, the wavefunctions vary rapidly in the vicinity of the nuclei (exhibiting multiple nodes and strong oscillations). In a plane-wave basis, accurately representing such rapid variations requires a very high kinetic-energy cutoff, meaning a large number of plane waves, which is computationally expensive.[89]

Therefore, it would be better to replace the true valence–core electron interaction by an effective potential that is smoothened near the nuclei. This makes the valence-electron wavefunctions much smoother within the core region and thus significantly reduces the required plane-wave cutoff. Meanwhile,

a good representation should reproduce the all-electron results outside the core region, match the all-electron valence eigenvalues for the chosen reference configuration, and possess a certain degree of transferability. The hypothetical smoothed potential is referred to as the pseudopotential, and the approximation is called the pseudopotential approximation. Before solving the KS equation, the actual potential generated by the nucleus and core electrons of each atom is replaced by the pseudopotential thereof to reduce the cut-off energy required in the expansion of Eq. (2.28) without changing the energy of valance electrons. Hard pseudopotentials demand a greater cut-off energy, whereas soft pseudopotentials require a lower cut-off energy.[95]

The ultra-soft pseudopotential (USPP) model proposed by David Vanderbilt in 1990 flattens the wavefunction around the nucleus and further reduces the required cut-off energy, thereby enhancing the calculation efficiency.[93] However, because USPPs include a large number of empirical parameters, only a handful pseudopotentials of atoms have been gathered and tested. Later, the projector augmented-wave (PAW) method proposed by Blöchl and improved by Kresse and Joubert makes up for this shortcoming and has become a widespread method.[96]

2.9 Solving the KS Equations

Periodic DFT calculations are generally performed through two coupled loops,

namely the electronic step and the ionic step.[18, 97] An electronic step can be viewed as solving the KS equations via SCF once according to Eq. (2.30),[18, 69]

$$\hat{H}_{\boldsymbol{k}}\varphi_{\boldsymbol{k}}(\boldsymbol{r}) = \varepsilon_{\boldsymbol{k}}\hat{S}_{\boldsymbol{k}}\varphi_{\boldsymbol{k}}(\boldsymbol{r}) \tag{2.30}$$

After obtaining a set of KS orbitals $\{\varphi_i(\boldsymbol{r})\}$, one reconstructs the electron density $n(\boldsymbol{r})$ via Eq. (2.27) from them and uses the updated density to rebuild the Hamiltonian operator $\hat{H}_{\boldsymbol{k}}$.[18, 69] The KS equations are then solved again with this new Hamiltonian to produce an updated set of orbitals. This procedure is iterated until self-consistency is reached. This is called the SCF method.[18, 66] Once the electronic loop converges and the total energy of the system is obtained, the atomic structure is optimized by adjusting the ionic coordinates (Eq. (2.6)).[18, 97]

2.10 Electronic Structure Analysis

2.10.1 DOS Analysis

In a periodic crystal, the discrete energy levels of isolated atoms broaden into energy bands.[98] To quantitatively describe how these bands are distributed along the energy axis, the electronic states need to be counted statistically. The density of states (DOS) is used to analyze the electronic band structure of the system.[98] The DOS gives the number of available quantum states per unit energy interval that can be occupied by electrons. For a three-dimensional periodic system, the total DOS can be written as[98]

$$DOS(E) = \frac{1}{V_{BZ}} \sum_{n} \int_{BZ} \delta(E - \varepsilon_{n\boldsymbol{k}})\, d^3\boldsymbol{k} \tag{2.31}$$

where V_{BZ} is the volume of the first Brillouin zone, $\varepsilon_{n\boldsymbol{k}}$ is the eigenenergy of the n-th band at the wave vector $\boldsymbol{k}$, and $\delta(\cdot)$ is the Dirac delta function. In calculations, the Brillouin zone integral is approximated numerically using a finite set of $\boldsymbol{k}$-points.[99] The delta function is commonly replaced by a broadened function with finite width, such as Gaussian quadrature, or the integral is evaluated using the tetrahedron method, yielding a smooth DOS curve.[100, 101] One typically performs a SCF calculation to obtain a converged charge density and then carries out a non-self-consistent calculation on a denser $\boldsymbol{k}$-point mesh to collect $\varepsilon_n(\boldsymbol{k})$ and compute the DOS.[18, 97]

The DOS describes how many electronic states are available for occupation at each energy, providing a direct link between the band structure and macroscopic properties. By examining the DOS near the Fermi level E_F, one can differentiate between metallic, semiconducting, and insulating.[89, 98]

2.10.2 PDOS Analysis

The projected density of states (PDOS) resolves contributions from specific atomic orbitals $\phi_{a,i}(\boldsymbol{r})$ (where a labels a specific atom and i denotes the orbital quantum numbers $\{l, m, n\}$), allowing one to identify which atoms or

orbitals dominate the valence-band maximum, conduction-band minimum, or characteristic DOS peaks. This orbital resolved DOS spectra is widely used to interpret chemical bonding and hybridization, and electronic structure changes associated with adsorption and activation in catalytic processes. To analyze the contributions from specific elements or orbitals, the PDOS can be calculated and plotted.[18, 96, 102]

PDOS decomposes the states around a given energy E according to their contributions from specific atoms, elements, or atomic orbitals. A common approach is to expand each KS wavefunction $\varphi_{n,\boldsymbol{k}}(\boldsymbol{r})$ in a selected set of localized basis atom-centered orbitals of a particular atom.[96, 102] For a given KS eigenstate with band energy $\varepsilon_{n\boldsymbol{k}}$, the wavefunction can be expanded in an atomic orbital Bloch-sum basis $\{\phi_{a,i,\boldsymbol{k}}(\boldsymbol{r})\}_{a,i}$, yielding expansion coefficients $c_{n,\boldsymbol{k}}^{a,i}$. Note that these localized bases should be formed as Bloch-summed local functions $\phi_{a,i,\boldsymbol{k}}$,[102]

$$\varphi_{n,\boldsymbol{k}}(\boldsymbol{r}) = \sum_{a,i} c_{n,\boldsymbol{k}}^{a,i} \left|\phi_{a,i,\boldsymbol{k}}(\boldsymbol{r})\right\rangle \tag{2.32}$$

$$\phi_{a,i,\boldsymbol{k}}(\boldsymbol{r}) = \frac{1}{\sqrt{N}} \sum_{\boldsymbol{R}} e^{i\boldsymbol{k}\cdot\boldsymbol{R}}\, \phi_{a,i}(\boldsymbol{r}-\boldsymbol{R}) \tag{2.33}$$

Because the atomic-orbital Bloch-sum basis functions $\phi_{a,i,\boldsymbol{k}}(\boldsymbol{r})$ are generally non-orthogonal, an overlap matrix $\boldsymbol{S}_{ai,a'i'} = \left\langle \phi_{a,i,\boldsymbol{k}}(\boldsymbol{r}) \middle| \phi_{a',i',\boldsymbol{k}}(\boldsymbol{r}) \right\rangle$ must be

introduced.[103] The orbital-resolved PDOS can then be written as[103]

$$PDOS_{a,i}(E)$$
$$= \frac{1}{V_{BZ}} \sum_{n} \int_{BZ} Re\left[c_{n,\boldsymbol{k}}^{a,i\,*} \sum_{a',i'} c_{n,\boldsymbol{k}}^{a',i'} \langle \phi_{a,i,\boldsymbol{k}}(\boldsymbol{r}) | \phi_{a',i',\boldsymbol{k}}(\boldsymbol{r}) \rangle \right] \delta(E - \varepsilon_{n\boldsymbol{k}})\, d^3\boldsymbol{k}$$
$$= \frac{1}{V_{BZ}} \sum_{n} \int_{BZ} Re\left[c_{n,\boldsymbol{k}}^{a,i\,*} \sum_{a',i'} c_{n,\boldsymbol{k}}^{a',i'} \boldsymbol{S}_{ai,a'i'} \right] \delta(E - \varepsilon_{n\boldsymbol{k}})\, d^3\boldsymbol{k} \qquad (2.34)$$

Note that the DOS obtained from PAW-based plane-wave DFT calculations mainly counts the valence KS states, i.e., those electrons treated explicitly as valence electrons in the PAW dataset.[96, 102, 103]

2.10.3 COOP and COHP Analysis

Crystal orbital overlap population (COOP) and crystal orbital Hamilton population (COHP) are energy-resolved tools for quantitatively analyzing the interactions between selected pairs of orbitals in periodic systems.[104, 105] The COOP between two orbitals a_1 and a_2 is obtained by weighting the overlap-matrix element $\langle \phi_{a_1,i_1,\boldsymbol{k}} | \phi_{a_2,i_2,\boldsymbol{k}} \rangle$ with the corresponding weight $c_{n,\boldsymbol{k}}^{a_1,i_1\,*} c_{n,\boldsymbol{k}}^{a_2,i_2}$, and then integrating over the Brillouin zone with an energy filter $\delta(E - \varepsilon_{n\boldsymbol{k}})$.[104, 105] This yields the orbital-resolved overlap interaction at energy E,

$$COOP_{a_1 i_1, a_2 i_2}(E)$$

$$= \frac{1}{V_{BZ}} \sum_{n} \int_{BZ} Re\left[{c_{n,\boldsymbol{k}}^{a_1,i_1}}^{*} c_{n,\boldsymbol{k}}^{a_2,i_2} \langle \phi_{a_1,i_1,\boldsymbol{k}} | \phi_{a_2,i_2,\boldsymbol{k}} \rangle \right] \delta(E - \varepsilon_{n\boldsymbol{k}})\, d^3\boldsymbol{k}$$

$$= \frac{1}{V_{BZ}} \sum_{n} \int_{BZ} Re\left[{c_{n,\boldsymbol{k}}^{a_1,i_1}}^{*} c_{n,\boldsymbol{k}}^{a_2,i_2} \boldsymbol{S}_{a_1 i_1, a_2 i_2, \boldsymbol{k}} \right] \delta(E - \varepsilon_{n\boldsymbol{k}})\, d^3\boldsymbol{k} \quad (2.35)$$

In COHP, the overlap-matrix element is replaced by the Hamiltonian matrix element, yielding a quantity that is more directly related to energetic contributions.[105] To compute the COHP, the DFT Hamiltonian operator is first applied in the atomic orbital Bloch-sum basis. The Hamiltonian matrix element between the two orbitals, $\langle \phi_{a_1,i_1,\boldsymbol{k}} | \widehat{H} | \phi_{a_2,i_2,\boldsymbol{k}} \rangle$, is then weighted by the coefficient cross term ${c_{n,\boldsymbol{k}}^{a_1,i_1}}^{*} c_{n,\boldsymbol{k}}^{a_2,i_2}$ and integrated over the Brillouin zone with the energy filter $\delta\big(E - \varepsilon_n(\boldsymbol{k})\big)$:[105]

$$COHP_{a_1 i_1, a_2 i_2}(E)$$

$$= \frac{1}{V_{BZ}} \sum_{n} \int_{BZ} Re\left[{c_{n,\boldsymbol{k}}^{a_1,i_1}}^{*} c_{n,\boldsymbol{k}}^{a_2,i_2} \langle \phi_{a_1,i_1,\boldsymbol{k}} | \widehat{H} | \phi_{a_2,i_2,\boldsymbol{k}} \rangle \right] \delta\big(E - \varepsilon_n(\boldsymbol{k})\big)\, d^3\boldsymbol{k}$$

$$\frac{1}{V_{BZ}} \sum_{n} \int_{BZ} Re\left[{c_{n,\boldsymbol{k}}^{a_1,i_1}}^{*} c_{n,\boldsymbol{k}}^{a_2,i_2} \boldsymbol{H}_{a_1 i_1, a_2 i_2, \boldsymbol{k}} \right] \delta\big(E - \varepsilon_n(\boldsymbol{k})\big)\, d^3\boldsymbol{k} \quad (2.36)$$

$$ICOHP_{a_1 i_1, a_2 i_2}(E) = \int_{-\infty}^{E_f} COHP_{a_1 i_1, a_2 i_2}(E) dE \quad (2.37)$$

The quantity $-ICOHP$ is commonly used as a bond strength indicator. A more negative ICOHP typically implies stronger bonding interactions between the corresponding atomic pair.[105]

2.11 Structural Optimization

To perform a thorough analysis of reaction barriers and mechanisms, the molecular configurations and energies of the initial, final, and transition states must be investigated.[106-108] Although the energy of a particular structure can be estimated using DFT, it is essential to verify that the initial and final states correspond to local minima on the PES, while the transition state corresponds to a first-order saddle point. Therefore, structural optimization is carried out to remove residual forces to locate local minima on the PES (defined in Section 2.3).[69]

The process of identifying a stable configuration that minimizes the total energy with respect to the position of the nuclei in each supercell is called structural optimization.[18, 97] It is a key step in determining initial and final states of a chemical reaction. Therefore, the structural optimization problem can be seen as finding a local minimum of the function $E(\boldsymbol{R})$, where is E the total energy of the supercell and $\boldsymbol{R}$ is a 3N-dimensional variable that contains the coordinates of all relaxed atoms.[97]

In quantum chemistry, structure optimization is typically performed by first constructing a quadratic approximation to the potential energy surface.[109, 110] This is obtained by carrying out a second-order Taylor expansion of the energy function $E(\boldsymbol{R})$ about the reference geometry $\boldsymbol{R} = \boldsymbol{R}_0$,

$$E(\boldsymbol{R}_0 + \Delta\boldsymbol{R}) \approx E(\boldsymbol{R}_0) + \left(\nabla E|_{\boldsymbol{R}_0}\right)^T \Delta\boldsymbol{R} + \frac{1}{2}\Delta\boldsymbol{R}^T\left(\nabla^2 E|_{\boldsymbol{R}_0}\right)\Delta\boldsymbol{R}$$
$$= E(\boldsymbol{R}_0) + (-\mathbf{F})^T\Delta\boldsymbol{R} + \frac{1}{2}\Delta\boldsymbol{R}^T\mathbf{H}_{Hessian}\Delta\boldsymbol{R} \quad (2.38)$$

Here, $\mathbf{F}$ is the negative gradient of the energy with dimension $3N$.[110, 111] Its components correspond to the forces acting on each atom along the x, y, and z directions for each atom. The second derivative $\mathbf{H}_{Hessian}$ is a $(3N) \times (3N)$ matrix of force constants, commonly referred to as the Hessian matrix.[109, 111] Two common techniques for locating the minimum are the quasi-Newton method and the conjugate-gradient (CG) method.[110]

2.11.1 Quasi-Newton Method

Although Newton's approach was initially intended as a general method of solving non-linear equations, it may also can be used as an optimization method[110], as the derivative (or generally gradient) at a fixed point of a function is zero. It is worth highlighting that the fixed point need not be a minimum; Newton's method can converge to a maximum or a saddle point (for a multidimensional function). The iterative formula is[110]:

$$\boldsymbol{R}^i = \boldsymbol{R}^{i-1} + \frac{E'\left(\boldsymbol{R}^{i-1}\right)}{E''(\boldsymbol{R}^{i-1})} = \boldsymbol{R}^{i-1} + \mathbf{H}_{Hessian}^{-1} \times \mathbf{F}\left(\boldsymbol{R}^{i-1}\right) \quad (2.39)$$

where $\boldsymbol{R}^i$ is coordinates of nuclei acquired in i-th step, $\boldsymbol{B}$ is a square matrix

composed of all the second-order partial derivatives of the energy function $E(\boldsymbol{R})$, called Hessian matrix. However, because computing the inverse of the Hessian matrix takes a long time, various approximations are frequently utilized to construct estimated matrixes in place of the Hessian matrix.[110] These methods are called quasi-Newton methods.[110, 112]

The Residual Minimization Method with Direct Inversion in the Iterative Subspace (RMM-DIIS) method, which can be viewed as a quasi-Newton approach, is one of the most used structural optimization methods.[18, 97, 110] The RMM-DIIS method replaces $\mathbf{H}_{Hessian}^{-1}$ with an approximation that is updated from a small history of previous steps. In this way, the method determines a new direction using curvature information accumulated over several past iterations, without explicitly forming the Hessian each time. Specifically, the force residuals $\boldsymbol{r}$ (calculated from Eq. (2.40)) from multiple recent steps are combined to construct an improved update direction, achieving faster convergence than purely gradient-based updates at a much lower cost than full Newton steps.

$$\boldsymbol{r}^i = -\nabla E(\boldsymbol{R}^i) \tag{2.40}$$

In summary, the main purpose of the quasi-Newton approach is to reduce the computational cost by replacing the explicit Hessian with an approximate matrix

constructed from the gradients (forces) accumulated during the recent m iterative process, $\boldsymbol{r}^i \cdots \boldsymbol{r}^{i-m}$.[110, 113]

2.11.2 CG Method

Another widely used approach is the CG method.[110, 114] Compared with Newton-type methods, CG can be regarded as an improved steepest descent scheme: it does not require the Hessian matrix and uses only the energy and first derivatives (forces/gradients).[110] In the steepest-descent method, the geometry is updated along the current descent direction (negative gradient), i.e.,

$$\boldsymbol{R}^{i+1} = \boldsymbol{R}^i + \alpha\left(-\nabla E\left(\boldsymbol{R}^i\right)\right) = \boldsymbol{R}^i + \alpha\left(\boldsymbol{F}(\boldsymbol{R}^i)\right) \tag{2.41}$$

where $\boldsymbol{F}(\boldsymbol{R}^i)$ denotes the force vector and α is the step length.[110] Unlike steepest descent, CG constructs a new search direction that combines the current force with the previous search direction, so that successive directions are conjugate with respect to the Hessian.[110, 114] On a quadratic energy surface, this property can significantly reduce the number of iterations. In each iteration, the minimum is obtained by performing a line search along the current conjugate direction $\boldsymbol{p}^i$:[110, 115]

$$\boldsymbol{R}^{i+1} = \boldsymbol{R}^i + \alpha\boldsymbol{p}^i = \begin{cases} \boldsymbol{R}^i + \alpha\left(\boldsymbol{F}\left(\boldsymbol{R}^i\right)\right); i = 1 \\ \boldsymbol{R}^i + \alpha\left(\boldsymbol{F}\left(\boldsymbol{R}^i\right) + \beta\boldsymbol{p}^{i-1}\right); i > 1 \end{cases} \tag{2.42}$$

$$\beta = \frac{\boldsymbol{F}(\boldsymbol{R}^i)^T \boldsymbol{F}(\boldsymbol{R}^i)}{\boldsymbol{F}(\boldsymbol{R}^{i-1})^T \boldsymbol{F}(\boldsymbol{R}^{i-1})} \tag{2.43}$$

The step length α is typically determined by a one-dimensional line search and combined with a maximum displacement constraint to ensure numerical stability.[97, 110, 115] In the first iteration, the search direction is usually chosen as the steepest descent direction, while in subsequent iterations the new search direction is constructed to be conjugate to the previous one.[110, 114, 116] Because the CG method is relatively sensitive to numerical noise in the forces, sufficiently strict electronic convergence is required to fully benefit from its fast convergence.[97, 110]

Compared to the CG method, the DIIS approach exhibits faster convergence rate and is more effective in locating the nearest stationary point on the potential energy surface, whereas the CG method is slower but has a larger chance of discovering the local minimum.[18, 66, 110] In this project, the CG method is utilized to optimize the structure of the initial and final states of a reaction, while the quasi-Newton method is only used to refine the transition states searched by the dimer or CI-NEB method described in the following section.

2.12 Transition State Searching

For a given reaction, the transition state can be defined as a dividing hyperplane that separates the initial and final states. In practice, it is often approximated by

the first-order saddle point along the minimum energy path (MEP).[117] The MEP connects the reactant and product minima while minimizing the potential energy in all directions perpendicular to the path. Along this path, the highest point is a first-order saddle point that serves as the practical proxy for the transition state geometry.[118]

Although the initial and final states can be determined using the approach outlined in Section 7, locating the transition state is challenging because it is a first-order saddle point with a typically small basin of attraction. While Newton-type methods can in principle converge to saddle points, direct optimization using quasi-Newton algorithms is often not robust without a suitable initial guess.[117] However, by employing dedicated search methods for saddle points in molecular modelling software, the structure and energy of the transition state can be determined theoretically to analyze the mechanism of chemical reactions and thus compare the catalytic performance of various catalysts.[106-108]

2.12.1 EB Methods for Obtaining Reaction Paths

The CI-NEB method originates from the early elastic band (EB) approach, in which the reaction pathway is discretized by interpolation into a chain of intermediate structures between the initial and final states, called images.[106, 107, 119] During the calculation, neighboring images are connected by fictitious

springs, and each image is optimized on the true potential energy surface to obtain the MEP.[106, 119] In the original EB scheme, the force acting on image i is

$$\boldsymbol{F}_i^{EB} = -\nabla E\left(\boldsymbol{R}^i\right) + \boldsymbol{F}_i^{spring} = \boldsymbol{F}\left(\boldsymbol{R}^i\right) + \boldsymbol{F}_i^{spring} \tag{2.44}$$

However, the original EB method suffers from a major drawback: it is highly sensitive to the choice of the spring constant k.[119] If k is chosen too large, the spring forces can drive the band away from the MEP (also called the cutting corners effect), leading to deviations from the MEP.[106, 119] On the other hand, if k is too small, the images tend to slide toward the energy minima near the initial and final states, so that the transition region cannot be described effectively.[106, 119]

To address these issues, the nudged elastic band (NEB) method was proposed.[119] NEB "nudges" the total force by projecting out the undesired components. Only the spring force component along the MEP tangent is retained, while all the true force components perpendicular to the path are kept. This decoupling enables stable convergence to the MEP. The NEB force on image i can be written as

$$\boldsymbol{F}_i^{NEB} = -\nabla E\left(\boldsymbol{R}^i\right)_{i,\perp path} + \boldsymbol{F}_{i,\parallel path}^{spring} = \boldsymbol{F}\left(\boldsymbol{R}^i\right)_{i,\perp path} + \boldsymbol{F}_{i,\parallel path}^{spring} \tag{2.45}$$

In general, NEB yields a set of images along the MEP rather than locating the transition state directly. A more common approach for searching for transition states is the recently developed CI-NEB method which improved the NEB method.[107] During the optimization, one of the interpolation states will climb to the first-order saddle point automatically to obtain a more accurate transition state configuration.

In the CI-NEB scheme, once a standard NEB calculation has provided an approximate MEP, the spring force of the image with the highest energy is then removed.[107] The image is driven uphill along the path tangent by reversing the tangential component of the true force $\boldsymbol{F}(\boldsymbol{R}^{max})_{\parallel path}$ and optimized independently so that it converges to the saddle point.[107] The corresponding force expression is

$$\begin{aligned} \boldsymbol{F}^{CI-NEB} &= -\nabla E(\boldsymbol{R}^{max})_{\perp path} + \nabla E(\boldsymbol{R}^{max})_{\parallel path} \\ &= \boldsymbol{F}(\boldsymbol{R}^{max})_{\perp path} - \boldsymbol{F}(\boldsymbol{R}^{max})_{\parallel path} \end{aligned} \tag{2.46}$$

CI-NEB has the ability to converge directly to the first-order saddle point rather than merely sampling the minimum-energy path.[107] As a result, CI-NEB typically yields a more accurate transition state geometry and barrier instead of just a state near the transition state.[107]

2.12.2 Dimer Method

Another frequently used approach for optimizing transition states is the dimer method, which was introduced in 1999 by Henkelman and Jonsson.[108] Compared to CI-NEB, the dimer method requires an initial guess of the transition state's configuration and a vector that describes the direction of the unstable vibrational mode along the reaction coordinate.[108]

During the dimer search, the algorithm first forms a dimer from the initial guess by generating two nearly identical geometries separated by a small displacement along the estimated unstable vibrational direction.[108] The dimer structure is used to locate a saddle point; each iteration mainly consists of the following steps. First, the search plane is defined to search for the minimum curvature. Secondly, within the current search plane, the direction of minimum curvature is identified, and the dimer is rotated toward that direction. Finally, we translate the dimer with modified forces based on potential energy surface the minimum curvature direction.[108]

According to the first step, let the forces acting on the two dimer endpoints A and B be $\boldsymbol{F}_A$ and $\boldsymbol{F}_B$, respectively, and let the unit vector along the dimer axis be $\boldsymbol{D}^{\parallel}$.[108] Denoting the unit vector along this perpendicular direction by $\boldsymbol{D}^{\perp}$, the search plane is then defined as $span\{\boldsymbol{D}^{\parallel}, \boldsymbol{D}^{\perp}\}$.[108] Because the minimum curvature direction within this plane corresponds to the direction where the

torque vanishes, the rotation angle can be determined using a Newton procedure.[108] In practice, more sophisticated schemes, such as the improved Newton method and the CG procedure, are often employed to determine a more accurate rotation angle, mitigating the tendency of the simple Newton step to overestimate the required rotation.[108]

After that, the forces at the dimer endpoints after the rotation, $\boldsymbol{F}_A^{**}$ and $\boldsymbol{F}_B^{**}$, are calculated. The component of the force along the current dimer direction is reversed, while the components perpendicular to the dimer direction are kept unchanged. The dimer is then translated according to the resulting effective force $\boldsymbol{F}^{Dimer}$ and the coordinates are updated. The effective force components for the dimer translation can be written as[108]

$$\begin{cases} \boldsymbol{F}^{\perp,Dimer} = \dfrac{1}{2}(\boldsymbol{F}_A^{**,\perp} + \boldsymbol{F}_B^{**,\perp}) \\ \boldsymbol{F}^{\parallel,Dimer} = -\dfrac{1}{2}\left(\boldsymbol{F}_A^{**,\parallel} + \boldsymbol{F}_B^{**,\parallel}\right) \end{cases} \tag{2.47}$$

Although the dimer method has the potential to further improve the computational efficiency by avoiding optimizing multiple structures simultaneously (like CI-NEB), it requires a reasonable initial guess of the transition state and a reasonable unstable mode.[107, 108] Therefore this method is typically used when the general information of a reasonable approximation of the transition state can be deduced.[108]

We employed both approaches in this research project to determine the transition state.[107, 108] When the structure of the transition state cannot be deduced from available information, the CI-NEB approach was used to locate the transition state.[107] On the other hand, if the transition state structure can be obtained by analogy with the known transition state structure, the dimer method was applied to save computation time.[108]

2.13 Frequency Calculations

Verification of a transition state typically requires a vibrational frequency calculation.[97, 117] The frequency calculation is usually based on the harmonic approximation.[97, 120] Small displacements are applied to the optimized structure to construct the mass weighted Hessian matrix, which is then diagonalized to obtain the vibrational eigenfrequencies and normal modes.[120, 121] According to Newton's equation of motion, the generalized eigenvalue problem for the angular frequencies ω can be written as[120]

$$\mathbf{H}_{Hessian}\mathbf{A} = \boldsymbol{M}\omega^2\mathbf{A} \tag{2.48}$$

where $\mathbf{H}_{Hessian}$ is the force constant (Hessian) matrix, $\boldsymbol{M}$ is the mass matrix, and $\mathbf{A}$ contains the vibrational eigenvectors (normal modes).[120, 121] The force constant matrix $\mathbf{H}_{Hessian}$ is commonly obtained by finite differences. Near the

equilibrium geometry, a small displacement $\pm\Delta x$ is applied along each atomic degree of freedom, and single point calculations are performed to obtain the corresponding forces.[120, 121] The second derivatives of the energy are then approximated by numerical derivatives of the forces, yielding the Hessian matrix,[120, 121]

$$\mathbf{H}_{Hessian,ij} = -\frac{\boldsymbol{\partial F}_i}{\boldsymbol{\partial R}_j} \approx -\frac{\boldsymbol{F}_i(\boldsymbol{R}_j + \Delta x) - \boldsymbol{F}_i(\boldsymbol{R}_j - \Delta x)}{2\Delta x} \tag{2.49}$$

The resulting Hessian is then weighted to $\mathbf{D}_{ij}$ to transform the problem into a standard eigenvalue equation,[97]

$$\mathbf{D}_{ij} = \frac{\mathbf{H}_{Hessian,ij}}{\sqrt{m_{a(i)} m_{b(j)}}} \tag{2.50}$$

Here, $m_{a(i)}$ denotes the mass of the atom a associated with the vibrational degree of freedom i. Diagonalizing the mass weighted matrix $\mathbf{D}$ yields eigenvalues λ_i, from which the angular frequencies are obtained as $\omega_i = \sqrt{\lambda_i}$.[120]

The number of imaginary frequencies is commonly used to characterize the nature of a stationary point.[117] A stable local minimum should have no imaginary frequencies, whereas a first-order transition state should exhibit exactly one

imaginary frequency corresponding to the reaction coordinate.[117] This indicates that the structure is a maximum along that vibrational mode and a minimum along all other directions.[117] To confirm that the located transition state indeed connects the desired reactant and product, the corresponding normal mode often needs to be visualized to verify the direction of motion.[117] In this work, all transition states were validated by such vibrational analyses to ensure that the ideal transition states were obtained.[117, 120]

2.14 DFT Related Software

For the DFT and structural optimization we used Vienna Ab Initio Simulation Package (VASP), which implements the approaches discussed in the previous Sections 2.1-13.[18, 97] VASP is being widely applied to investigate heterogeneous chemical reactions, due to its fast operation and high accuracy. It was developed by Prof. G. Kresse and co-workers at the University of Vienna. It employs the PAW method and an efficient iterative diagonalization framework, which makes it well suited for accurate electronic structure calculations and geometry optimizations of periodic systems.[96, 102]

Transition state searches and reaction path calculations were carried out using the VTST tools interfaced with VASP (developed by the Henkelman and Jónsson groups). In particular, the CI-NEB method and the dimer method were employed to determine MEP and locate first-order saddle points.[107, 108] Post-

processing analyses of chemical bonding were performed using LOBSTER, developed by Maintz et al, which reconstructs local orbital information from VASP wavefunctions and enables the calculation of COHP/ICOHP for quantifying bond interactions in periodic systems.[105, 122, 123]

The initial model of the supercell structure in our calculations was established in the Materials Studio software, which is a molecular modeling and quantum chemical calculation software developed by DS BIOVIA. In addition, the Atomic Simulation Environment, developed by Larsen et al**,** was also employed to build and manipulate atomic structures, generate input files, and perform routine model preparation tasks, such as supercell construction and atom substitutions.[124]

Then, Visualized Electronic Structural Analysis (VESTA), developed by Momma et al, a three-dimensional visualization software, was used to transfer the file format form ".xsd" generated by MS to POSCAR which can be used in VASP.[125, 126] All figures of crystal structures in thesis are also represented by VESTA. Jmol, developed primarily by Hanson, was additionally used to visualize vibrational normal modes and to inspect the displacement directions associated with imaginary frequencies.[126]

2.15 Energy Definitions Used in this Thesis

2.15.1 Formation Energy

To investigate the preferable sites of adsorbates and the reaction mechanism on different SAAs, energy landscapes for adsorption and subsequent surface intermediates need to be constructed. This requires a consistent, well-defined reference state for every intermediate so that formation energies can be compared. Therefore, a set of reference species was defined, including the clean surface and selected gas phase species. The energies of the clean surface and the reference species were first computed using VASP, followed by calculating formation energies for other adsorbates using the following equations[1]:

$$E_F = E_{DFT}^{C+A} - E_F^A - E_{DFT}^C \tag{2.51}$$

where E_F is the formation energy, E_{DFT}^{C+A} is the DFT energy of catalyst and adsorbate, E_{DFT}^C is the DFT energy of the catalyst, and E_F^A is the formation energy of adsorbates calculated by a linear combination of gas phase molecules. For example, if gas phase CH_4, H_2, and CO_2 are chosen as the reference states, the formation energy of adsorbates CH_3 and CH_3O are calculated by Eqs. (2.52 and 2.53).

$$E_F^{CH_3} = E_{DFT}^{CH_4} - 0.5E_{DFT}^{H_2} \tag{2.52}$$

$$E_F^{CH_3O} = 0.5E_{DFT}^{CO_2} + 0.5E_{DFT}^{CH_4} + 0.5E_{DFT}^{H_2} \quad (2.53)$$

where $E_F^{CH_3}$ and $E_F^{CH_3O}$ are the formation energies of CH_3 and CH_3O calculated by a linear combination of DFT energies of gas phase molecules $E_{DFT}^{CH_4}$, $E_{DFT}^{CO_2}$, and $E_{DFT}^{H_2}$.[1]

2.15.2 Activation Energy and Reaction Energy

Surface configurations corresponding to the initial states and final states were generated by constructing initial guesses of adsorption geometries and subsequently relaxing them to local minima. The most relevant initial and final states were then selected based on their relative stability and chemical plausibility along the intended elementary step. Transition states for the reactions of interest were located using the CI-NEB method, and further refined/validated with the dimer method as implemented in VASP with the VTST tools interface.[107, 108] Activation energies and reaction energies for the reactions were calculated by the following equations.

$$\Delta E = E^{FS} - E^{IS} \quad (2.54)$$

$$E_a = E^{TS} - E^{IS} \quad (2.55)$$

where ΔE is the reaction energy, E_a is the activation energy, E^{FS} is the energy of the final state, E^{IS} is the energy of the initial state and E^{TS} is the

energy of the transition state. Catalysts should generally exhibit low activation energies for elementary steps towards the desired products.

2.16 Mesoscopic Simulations of Reaction Kinetics

In the previous sections, the energetics of the elementary steps were established by DFT, including the relative stability of adsorbed intermediates and the kinetic barriers between them. However, an energy landscape alone does not directly determine the overall catalytic performance, because experimentally relevant observables—such as turnover frequency, selectivity, and surface coverages—are governed by the rates of competing elementary events rather than by energies themselves. To bridge this gap, the computed thermodynamic quantities must be translated into rate constants k for each elementary step, which then serve as inputs to mesoscale kinetic simulations (e.g., KMC) to propagate the surface reaction network in time. In this context, activation barriers provide the key link from DFT energetics to kinetics by determining k through an Arrhenius relationship, as described below.

The temperature dependence of an elementary reaction rate is commonly described by the Arrhenius equation.[127, 128]

$$k = Aexp\left(-\frac{E_a}{k_B T}\right) \tag{2.56}$$

where k is the rate constant, A is the pre-exponential factor, E_a is the activation energy, k_B is the Boltzmann constant, and T is the temperature. This expression shows that the rate depends exponentially on the activation barrier. At a fixed temperature, a larger E_a leads to a smaller k, whereas lowering E_a increases k and accelerates the elementary step.

Ideally, DFT provides the energies of the initial state, transition state, and final state for each elementary step. From these quantities, the rate constants of individual events can be estimated and used to compare the intrinsic kinetics of competing pathways.[25, 128] However, heterogeneous catalysis under realistic conditions is a collective and dynamic phenomenon. Macroscopic conversion and selectivity arise from an enormous number of various elementary events occurring on the surface per unit time. The frequency of these events is governed not only by the intrinsic activation barriers, but also by the external reaction conditions (temperature, pressure, and gas-phase composition) and by the evolving state of the catalytic surface itself, such as surface coverages, lateral interactions, and the availability of specific site types.[129-131] Consequently, analyzing barriers with the Arrhenius equation alone is often insufficient to identify the RDS in complex catalytic systems.[25, 131] This motivates mesoscale kinetic modelling approaches, such as KMC, which can account for these collective effects and explicitly simulate the coupled surface reaction network over time.

Kinetic simulation frameworks can resolve the time evolution of the surface state under given conditions from atomic energetics.[132, 133] To accurately simulate the motion of molecules on a catalyst, the molecular dynamics (MD) approach can be employed, by which a force field is used to compute atomic forces and velocities at each time step, followed by updating atomic positions.[134] However, during conventional MD simulations, atomistic trajectories are dominated by fast vibrational motions (typically femtoseconds), whereas chemical reactions correspond to barrier-crossing events that occur much more rarely and often on much longer timescales.[135, 136] This pronounced separation of timescales makes it unlikely for reactive events to be observed within the limited simulation time accessible to standard MD. Consequently, practical MD simulations are typically restricted to relatively small surface models and short trajectories, primarily due to the high computational cost of resolving atomic motion over extended times.[135] For simulations focusing on reaction kinetics on large surfaces and longtime scales, a coarse-grained model is required.[41, 132] Thus, approaches such as microkinetic modeling and KMC have been invented to simulate macroscopic observables, such as turn-over frequencies (TOFs), selectivity, and coverages, thereby capturing the behavior of large-scale catalyst surfaces.[41, 137, 138]

The coarse graining procedure partitions the potential energy surface into a set

of basins, each treated as a discrete configuration. Each basin is labelled by a representative structure at its local minimum, i.e., the relaxed stable adsorbate/surface geometry associated with that basin.[139-141] For the potential energy surface of a single reaction (Fig. 2.2), region A is the initial state and region B is the final state.

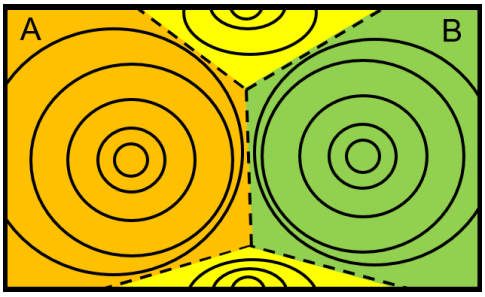


Figure 2. 2 An illustration of a potential energy surface. Regions A and B represent the initial state and final state, respectively. The dashed line marks the boundary between different states. The black solid lines represent energy contour lines.

In heterogeneous catalysis, the surface can host a very large number of possible adsorbed configurations, arising from different adsorbates, adsorption sites, and local environments.[25, 132, 137] To make such problems tractable, a coarse-grained description is commonly adopted. Instead of following continuous atomic vibrations as in MD, each state of the system is represented by a set of discrete stable surface configurations (local minima on the potential energy surface).[25, 132, 137] The dynamics are then described as transitions between these minima, where each transition corresponds to an elementary event such as adsorption, desorption, diffusion, or a surface reaction step.[21, 41, 142] By focusing on these rare (compared to atomic vibrations) but chemically relevant events, coarse-grained models avoid spending most of the

computational effort on fast vibrational motions and can access much longer timescales than atomistic MD.[41, 135] Many approaches such as Langmuir-Hinshelwood models, Sabatier analysis, mean-field microkinetic modeling, and on-lattice KMC modeling make use of this coarse-graining idea.[41, 44, 132, 143] Since this thesis focuses on on-lattice KMC simulations, we will mainly introduce the on-lattice KMC approach below.

2.17 An Introduction to On-lattice KMC Simulation

2.17.1 The Importance of On-Lattice KMC

Many heterogeneous catalysis mechanisms depend on specific spatial arrangements of adsorbates.[24, 144] For example, consider a surface reaction $A^* + B^* \rightarrow AB_{(g)}$ in which reactants A^* and B^* form a gaseous product.[24, 144] If A^* and B^* must diffuse and become sufficiently close on the surface to react, diffusion can strongly influence the overall rate and may even become the RDS.[137, 144] To capture such spatial effects, it is necessary to adopt a modelling approach that relies on explicitly tracking where species reside on the surface and how they migrate between sites. On-lattice KMC is therefore well suited for this purpose, as it naturally represents the catalytic surface as a network of discrete adsorption sites and explicitly simulates stochastic reaction and diffusion events on that lattice.[41, 144]

On-lattice KMC simulates a continuous time random walk on a discrete state

space.[20, 94] Each reaction event is assumed to happen instantaneously after a waiting time, which is a continuous random variable, hence the continuous-time process. The catalytic surface is represented as a lattice and the state space is this discrete space of configurations (lattice site occupations).[41, 144] More specifically, a KMC lattice, representing the catalytic surface, consists of different types of sites arranged on a network, where each site connects to a set of neighboring sites (Fig. 2.3).[22, 144] The system state is therefore specified by the lattice occupancy.[24, 144]

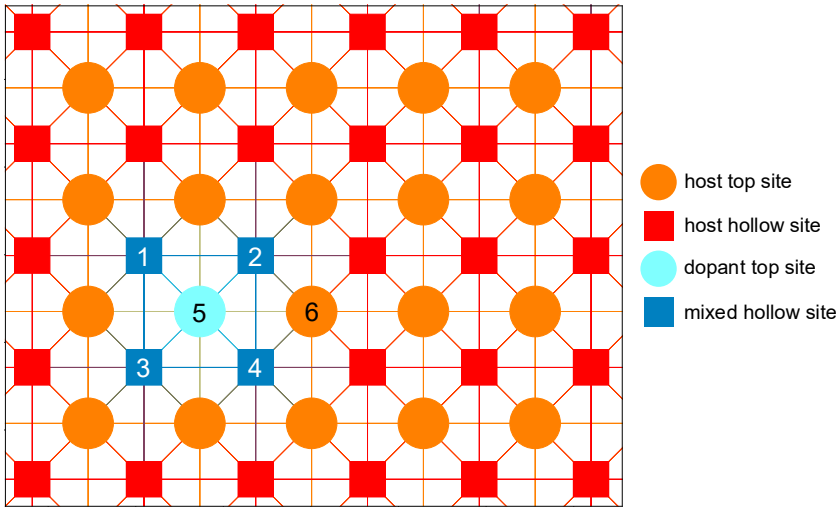


Figure 2. 3 Part of a lattice used for a KMC simulation of the RhCu(100) catalytic surface. Top and four-fold hollow sites are represented by circles and squires, respectively.

By explicitly simulating the evolution of lattice occupation patterns, on-lattice KMC can account for the spatial configuration of species in the system.[24, 41, 144] This state definition enables on-lattice KMC to represent surface configurations and their evolution accurately.[137, 144]

2.17.2 An Introduction to Master Equation

Realizations of such random walks are captured by master equations, which describe the time evolution of state probabilities for a stochastic process among discrete states.[145, 146] A prerequisite for applying the master equation on chemical processes is to assume that the reactions are memoryless (giving rise to a so-called Markovian process).[145, 146] In practice, this relies on two features of chemical reactions. First, the time required to cross the transition state is extremely short compared with the residence time in stable reactant or product basins. Second, the excess kinetic energy along the reaction coordinate is rapidly dissipated after the transition state is crossed.[147, 148] Under these assumptions, the system quickly loses memory of the previous event, and its dynamics can be described by the master equation,[145, 146]

$$\frac{dP_i}{dt} = \sum_j \left[W_{ij}P_j - W_{ji}P_i\right] \tag{2.57}$$

where P_i is the probability of finding the system in state i at time t. The transition rate (or propensity) W_{ij} denotes the probability per unit time for a transition from state j to state i. The first term on the right-hand side, $\sum_j W_{ij}P_j$, represents the inflow into state i from all other states j.[145, 146] The second term, $-\sum_j W_{ji}P_i$, represents the outflow from state i to all other states and therefore enters with a minus sign. The master equation thus forms a set of coupled

ordinary differential equations which can also be written in matrix form.[145, 146]

$$\dot{\boldsymbol{P}} = \boldsymbol{W}\boldsymbol{P}; \boldsymbol{W}_{ij} = \begin{cases} W_{ij}, & i \neq j \\ -\sum_{i} W_{ij}, & i = j \end{cases} \tag{2.58}$$

Here, $\boldsymbol{W}$ is the transition-rate matrix that tabulates all propensities.[145, 146, 149] Note that the diagonal term contains all the net outflow rate from the corresponding state (Eq. (2.58)).

In addition, the detailed balance condition is a constraint that the transition probabilities need to satisfy, so that the simulation is thermodynamically valid/consistent. [146, 149] For any pair of states i and j,

$$WijP_j^{eq} = WjiP_i^{eq} \tag{2.59}$$

where P_i^{eq} is the equilibrium probability of finding the system in state i.[146, 150, 151]

Eq. (2.59) implies: (i) for every elementary process $i \rightarrow j$, there exists a reverse process $j \rightarrow i$; and (ii) at thermodynamic equilibrium, the average number of transitions per unit time from $i \rightarrow j$ equals that from $j \rightarrow i$.[146, 152] This constraint (also called microscopic reversibility) must be respected when defining rate

constants to make sure the microscopic reversibility all the time during the simulation. As a result of this constraint, at equilibrium, the state probabilities follow the Boltzmann distribution,[150, 151]

$$P_i^{eq} \propto \exp\left(-\frac{F_i}{k_B T}\right) \tag{2.60}$$

where F_i is the free energy of state i. Therefore, from Eq. (2.60) the rate constants must satisfy

$$\frac{Wij}{Wji} = \exp\left(-\frac{F_i - F_j}{k_B T}\right) \tag{2.61}$$

For the $A^* + B^* \rightarrow AB_{(g)}$ example mentioned in Section 2.17.1, we can determine where reactants adsorb on the surface.[25, 93, 144] By inspecting neighboring sites, we can decide whether A^* and B^* are sufficiently close to react.[24, 144] In this way, diffusion is treated as an explicit elementary event with its own diffusion rate, so that diffusion enters the master equation and becomes part of the KMC trajectory.[21, 142, 144] Consequently, the number of possible states grows scaling exponentially with the number of sites, making a direct solution of the master equations prohibitively difficult.[144] In this situation, instead of solving an astronomical number of coupled differential equations, we resort to KMC sampling.[142, 144]

2.17.3 Principles of On-Lattice KMC Simulation

In a common sampling procedure, starting from a given initial state, we construct the distribution of “waiting times” based on the propensities of all possible elementary events.[21, 22, 142] Random numbers are then drawn to determine the time increment to the next event.[21, 142] The system is subsequently updated to the new surface state. Because the random numbers are used to sample event times and event identities according to the underlying propensities, the law of large numbers ensures that, after sufficiently many events, the simulated trajectories yield macroscopic observables consistent with the statistics.[20, 142, 146]

Constructing the waiting time distribution for each elementary event is crucial in KMC.[21, 142] Derived from the master equation and the definition of the survival probability, the cumulative distribution function of the waiting time τ of event R_{ji} is

$$F(\tau) = 1 - \exp\left(-\int_0^{\tau} W_{ji}(t)\, dt\right) \tag{2.62}$$

Accordingly, the probability density function for the occurrence time τ of event R_{ji} is

$$f(\tau) = \frac{dF(\tau)}{d\tau} = \mathrm{W}_{ji}(\tau) \cdot \exp\left(-\int_0^{\tau} W_{ji}\,(t)dt\right) \tag{2.63}$$

In practice, random numbers u drawn from the uniform distribution on $(0,1)$ are used to sample waiting times via inverse transform sampling. For a time-independent W_{ji}, the cumulative distribution function is[146]

$$F(\tau) = 1 - \exp\left(-\int_0^{\tau} W_{ji}\,dt\right) = u; u{\sim}(0,1)$$

$$\tau = -\frac{1}{W_{ji}}\ln\,(1-u) \tag{2.64}$$

If the propensity is time-dependent, and the current time is t_0, the waiting time τ is obtained by solving:[153, 154]

$$1 - \exp\left(-\int_{t_0}^{t_0+\tau} W_{ji}(t)\,dt\right) = u; u{\sim}(0,1) \tag{2.65}$$

The waiting time τ is obtained by solving Eq. (2.65).[153, 154] Therefore, once the propensity W_{ji} for an elementary event R_{ji} is known, we can sample the time interval τ until that event occurs.[21, 142, 155] The next key step in performing KMC is thus to determine the propensities for all possible events under a given system state.[154, 155] In practice, propensities are computed from rate constants via TST.[128, 156]

2.18 Acquiring Rate Constant via TST

In catalytic systems, it is often more convenient to work with a rate constant k_{TST} rather than a state transfer propensity W_{ji}.[128] The propensity W_{ji} refers to the rate of a particular event occurring at a specific location, causing the lattice occupation changes from i to j, whereas the rate constant k_{TST} is used to define an intrinsic parameter that is shared by a kind of elementary steps.[41, 144] In other words, for a given pattern of reactants defining the initial state, the rate constant $k_{TST,i}$ of a given elementary step i quantifies the probability per unit time of reaching the final state.[128]

Rate constants k_{TST} are commonly determined using TST. The key assumption of TST is that the reactants and the transition state ensemble are in quasi-equilibrium along the reaction coordinate.[128] Assuming that, upon the occurrence of the elementary event p, $A^* + B^* \rightarrow AB_{(g)}$, the lattice-occupation state changes from i to j. Derived from TST, the rate constant of process p can be calculated by[128]

$$k_{TST,p} = W_{ji} = \frac{k_B T}{h} \cdot \frac{Q^*}{Q_A Q_B} \tag{2.66}$$

Here, $k_{TST,p}$ is the TST rate constant of elementary process p, and W_{ji} is the corresponding site-specific propensity for the system to evolve from lattice-occupation state i to state j when process p occurs at a given location. k_B

is the Boltzmann constant, T is the temperature, and h is Planck's constant. Q_A and Q_B are the single-particle partition functions of the reactant adsorbates A^* and B^* in the initial state, and Q^* is the single-particle partition function of the transition state, with the vibrational mode along the MEP removed.[128, 157] If we separate the potential energy contribution from the partition functions, the TST rate constant can be expressed in a form that is readily evaluated using DFT energies and frequencies,[128]

$$k_{TST} = \frac{k_B T}{h} \cdot \frac{Q^*}{Q_A Q_B} = \frac{k_B T}{h} \cdot \frac{q^*}{q_A q_B} \cdot \exp\left(-\frac{E_{TS} - E_{IS}}{k_B T}\right) = \frac{k_B T}{h} \cdot \frac{q^*}{q_A q_B} \cdot \exp\left(-\frac{E_a}{k_B T}\right) \quad (2.67)$$

where E_{IS} and E_{TS} are the DFT energies of the initial state and transition state, respectively, and E_a is the activation energy if the given elementary step.[128] The corresponding quantities q_A, q_B, and q^* denote the same single-event partition functions with the potential-energy contribution factored out. The single species partition functions are written as:[158]

$$q_A = q_{tran,A} q_{rot,A} q_{vib,A}$$
$$q^* = q^*_{tran} q^*_{rot} q^*_{vib} \quad (2.68)$$

where q_A is the single-event partition function of gas-phase species A, expressed as the product of its translational, rotational, and vibrational contributions. Here, $q_{tran,A} q_{rot,A} q_{vib,A}$ denote the translational, rotational, and

vibrational partition functions of A, respectively. Likewise, q^* is the single-event partition function of the transition state, where $q^*_{tran}q^*_{rot}q^*_{vib}$ are the corresponding contributions for the transition-state configuration with the vibrational mode along the MEP removed.

For elementary surface reactions involving only adsorbates, such as $A^* + B^* \rightarrow C^*$, translational and rotational motions are treated as additional vibrational modes within the harmonic approximation.[133, 158] In this case, the TST expression reduces to

$$k_{TST}^{surface,fwd} = \frac{k_B T}{h} \cdot \frac{q^*}{q_A q_B} \cdot \exp\left(-\frac{E_{TS} - E_{IS}}{k_B T}\right) = \frac{k_B T}{h} \cdot \frac{q^*_{vib}}{q_{vib,A} q_{vib,B}} \cdot \exp\left(-\frac{E_a}{k_B T}\right) \quad (2.69)$$

$$k_{TST}^{surface,bwd} = \frac{k_B T}{h} \cdot \frac{q^*_{vib}}{q_{vib,C}} \cdot \exp\left(-\frac{E_a - \Delta E}{k_B T}\right) \quad (2.70)$$

For elementary steps involving gas-phase molecules, such as adsorption $A_{(g)} \rightarrow A^*$, the rate expression should retain the translational and rotational contributions of the gas phase species.[158] Elementary steps involving gas phase species additionally depends on the gas pressure above catalyst surface. the forward and backward adsorption rate constant can be written as[128, 159]:

$$k_{TST}^{act-ads,fwd} = \frac{k_B T}{h} \cdot \frac{q_{vib}^*}{q_{2D-tran,A} q_{vib,A} q_{rot,A}} \cdot \frac{p_A S_{at}}{\sqrt{2\pi m_A k_B T}} \cdot \exp\left(-\frac{E_a}{k_B T}\right)$$

$$q_{2D-tran,A} = q_{tran,x\in S_{at},A} q_{tran,y\in S_{at},A} \quad (2.71)$$

$$k_{TST}^{act-ads,bwd} = \frac{k_B T}{h} \cdot \frac{q_{vib}^*}{q_{vib,A^*}} \cdot \exp\left(-\frac{E_a - E_{ads}}{k_B T}\right) \quad (2.72)$$

where S_{at} is the area of the active adsorption site. In Eq. (2.71), $q_{tran,x\in S_{at},A}$ and $q_{tran,y\in S_{at},A}$ are the two one-dimensional translational partition functions of the incident gas-phase species A parallel to the surface, restricted to the active adsorption area S_{at} (along the x and y directions, respectively).

Similarly, for an Eley-Riedel reaction involving gas-phase molecules of the type $A_{(g)} + B^* \rightarrow C^*$, the rate is given as:

$$k_{TST}^{ER,fwd} = \frac{k_B T}{h} \cdot \frac{q_{vib}^*}{q_{2D-tran,A} q_{rot,A} q_{vib,A} q_{vib,B}} \cdot \frac{p_A S_{at}}{\sqrt{2\pi m_A k_B T}} \cdot \exp\left(-\frac{E_a}{k_B T}\right)$$

$$q_{2D-tran,A} = q_{tran,x\in S_{at},A} q_{tran,y\in S_{at},A} \quad (2.73)$$

$$k_{TST}^{ER,bwd} = \frac{k_B T}{h} \cdot \frac{q_{vib}^*}{q_{vib,C^*}} \cdot \exp\left(-\frac{E_a - \Delta E}{k_B T}\right) \quad (2.74)$$

where $k_{TST}^{ER,fwd}$ and $k_{TST}^{ER,bwd}$ are the TST rate constants for the forward and backward Eley–Rideal elementary step, respectively. Eqs. (2.69–2.74) were used to parameterize the KMC simulations reported in Chapters 4 and 5.

2.19 Coverage-Dependent Correction to the Activation Energy

Adsorbates on a catalyst surface can interact with one another through attractive or repulsive lateral interactions.[41, 160] As a result, the activation energy of an elementary step depends not only on the intrinsic energetics of the isolated initial state and transition state, but also on how co-adsorbates (often referred to as spectators) stabilize or destabilize the initial, transition, and final state.[161, 162] Because spectators may interact differently with the initial (or final) state and transition state, lateral interactions can shift the effective barrier by preferentially stabilizing one state relative to the other.[161, 162] For example, in an association reaction $A^* + B^* \rightarrow AB_{(g)}$, repulsive interactions between the reactants and surrounding spectators can destabilize the crowded adsorbed reactant configuration more than the transition state, thereby lowering the activation barrier and accelerating the formation of the gas-phase product.

A common rationalization is provided by BEP relationships, which posit an approximately linear correlation between changes in reaction energetics ΔE induced by spectators and the corresponding change in the activation barrier.[47, 50] One may write

$$\frac{E_a(\sigma)-E_a^0}{\Delta E(\sigma)-\Delta E^0} = \frac{E_a(\sigma)-E_a^0}{(E_{tot,FS}(\sigma) - E_{tot,IS}(\sigma))-\Delta E^0} = \omega \qquad (2.75)$$

where σ denotes the surface configuration or local environment, $\Delta E(\sigma)$ is the

reaction energy under local environment σ, and the superscript "0" refers to the no spectator (also called zero-limit coverage) condition.[47, 50] The parameter ω is the BEP slope.

Therefore, to evaluate the barrier of a given elementary step under a specific local configuration, we require the corresponding configuration and its energetic contributions.[41, 160] If the total energies difference between the final and initial states under local configuration σ can be computed as $\Delta E(\sigma)$, the forward and backward activation barrier can be corrected as[47, 50]

$$E_a^{fwd}(\sigma) = \max\left(0, \Delta E(\sigma), E_a^{0,fwd} + \omega(\Delta E(\sigma) - \Delta E^0)\right) \quad (2.76)$$

$$E_a^{bwd}(\sigma) = \max\left(0, -\Delta E(\sigma), E_a^{0,bwd} + (1-\omega)(\Delta E(\sigma) - \Delta E^0)\right) \quad (2.77)$$

Note that interaction contributions that are unchanged before and after the reaction (such as spectator–spectator interactions) cancel when forming $\Delta E(\sigma) = E_{FS}(\sigma) - E_{IS}(\sigma)$.[160, 162] Thus, only the change in the interaction between spectators and the reactants/products affects the coverage-dependent correction to the barrier.[162] In this context, it is crucial to evaluate the total energy on the surface during the KMC simulation to keep updating $\Delta E(\sigma)$.[41, 144, 160]

2.20 An Introduction to CE

In on-lattice KMC, the rates of elementary events depend on the local adsorbate environment through lateral interactions. To evaluate these environment-dependent energetics efficiently during the simulation, one needs a fast but accurate model for the total energy of the adsorbate layer across arbitrary coverages and local configurations. Cluster expansion (CE) is a method for representing the total energy of an adsorbate covered lattice system, as a systematic expansion over clusters.[163] With CE, one can build an energy model that predicts energies for arbitrary coverages and local environments.[164] CE assumes that the energy of a configuration σ can be written as a linear combination of contributions from clusters (from single sites, pairs, triplets, etc.), characterized by effective cluster interactions (ECIs):[163, 165]

$$E_{tot}(\sigma) = J_0 + \sum_{i}^{N_{site}} J_i \sigma_i + \sum_{i}^{N_{site}} \sum_{j>i}^{N_{site}} J_{ij} \sigma_i \sigma_j + \sum_{i}^{N_{site}} \sum_{j>i}^{N_{site}} \sum_{k>j}^{N_{site}} J_{ijk} \sigma_i \sigma_j \sigma_k + \cdots \quad (2.78)$$

Here, σ specifies which species occupies each lattice site, and J denotes the ECIs in the CE.[163, 165] In practice, DFT energies are computed for a limited set of representative configurations and used to fit the ECIs.[164] The fitted CE can then be used to efficiently evaluate energies for arbitrary coverages and arrangements without additional DFT calculations.[164] Because KMC simulations typically require large lattices and extensive sampling, it is impractical to include all interactions explicitly.[41] Instead, one selects m

representative configurations usually from first principles calculations to fit n ECIs ($m \geq n$) and then uses the resulting CE to compute the lattice energy before performing KMC simulations.[41]

After obtaining the fitted ECIs, one can use the subgraph-isomorphism algorithm to automatically scan the simulated lattice and count the occurrences of each interaction cluster.[26, 160, 166, 167] The current total lattice energy can then be evaluated as

$$E_{tot}(\sigma) = \sum_{k=1}^{N_{pattern}} \frac{NCI_k}{GM_k} ECI_k \tag{2.79}$$

Here, NCI_k is the raw number of matches of pattern k identified by the pattern search on the lattice, and GM_k is the graph multiplicity of pattern k.[26, 167] Because pattern search method, such as subgraph isomorphism, can visit the same match multiple times when starting from different nodes, we divide the raw count NCI_k by GM_k to avoid overcounting redundant matches.[166, 168]

2.21 Overview of KMC Algorithms

A variety of KMC algorithms have been developed, including both on-lattice and off-lattice variants.[23, 169] Well-mixed off-lattice KMC has limited use in surface science and is more commonly applied to reactor problems.[20, 142] In contrast, surface KMC simulations typically employ spatially resolved, lattice-based

descriptions.[22, 115, 144, 169] Here, we briefly introduce the first-reaction method, which were used to perform the KMC simulations reported in Chapters 4 and 5.

2.21.1 An Introduction to the First-Reaction Method

The basic idea of the first-reaction method is that the next executed event is the one that occurs earliest in time.[142] Accordingly, at each KMC step one generates a waiting time τ_i for every possible process and computes its tentative firing time t_i.[142] The event with the smallest tentative time is then selected and executed.[142] Mathematically, one assigns[142]

$$t_i = t_{curr} + \tau_i \tag{2.80}$$

$$t_{next} = \min\{t_1, t_2, \cdots, t_i, \cdots, t_N\} \tag{2.81}$$

Because the method considers only currently realizable events, it is rejection-free.[142] Its main cost is that each KMC step requires generating and comparing many random firing times.[23] In large systems with many possible transitions, this computational overhead can significantly reduce efficiency.[23]

To reduce the computational cost, one can adopt a time reuse strategy.[155, 170] If a previously generated process i is unaffected by the last executed event, its scheduled random time t_i can be retained without resampling until one of the following occurs: (i) the process itself is executed; (ii) an event consumes its

reactants; or (iii) the local environment of the reactants is perturbed resulting rate constant modified by lateral interactions.[153, 155] More advanced bookkeeping and data structures are necessary to further track event dependencies, enabling efficient invalidation and updating of event lists, rate constants, and waiting times.[153, 155, 170] The on-lattice KMC simulation procedure introduced in the following sector is based on the first-reaction method.

2.21.2 On-lattice KMC Simulation Procedure

In on-lattice KMC, the overall simulation procedure can be divided into two stages, namely the preparatory phase and the main KMC loop (Fig. 2.4). The preparatory phase is executed prior to the onset of the main loop, involving first constructing the lattice representation (including site types, connectivity and occupation conditions) of the catalytic surface. The preparatory process defines all the patterns of reactants and products for each elementary step together with their rate constants, before moving into the main KMC loop.[26, 160, 167, 171-173]

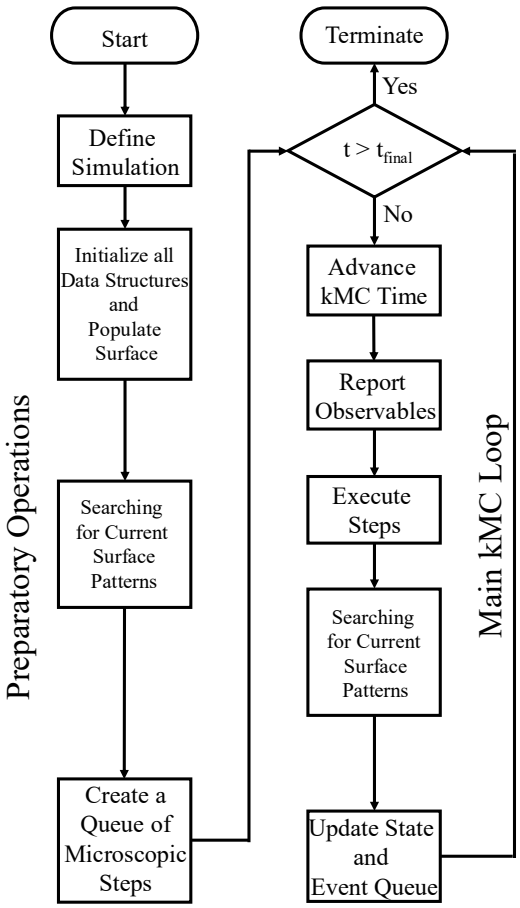


Figure 2. 4 Flowchart of a commonly used on-lattice KMC algorithm.

The main KMC loop (using first-reaction method) proceeds by first identifying the next reaction event to occur, then executing the corresponding elementary step by removing the reactants and placing the products onto the surface. Following this, the algorithm then identifies any newly enabled reaction patterns resulting from the updated surface configuration, and the event queue is accordingly updated. This identification process is performed each time the surface is modified, and it continues until the simulation time exceeds the predefined termination criterion. A more detailed on-lattice KMC process used to perform the on-lattice KMC simulations reported in Chapters 4 and 5 is

shown below.[26, 160, 167, 171-173]

1. Initialize the surface model. Define the catalyst surface defined at the outset and construct the main lattice graph. the initial and final state patterns of each elementary reaction, and the ECI patterns. Compute the activation energies in zero coverage limit (no spectators) and reaction energies for all reactions.

2. Compute the initial surface total energy. Search the main lattice for the relevant ECI patterns and evaluate the total energy of the initial surface using Eq. (2.79).

3. Enumerate realizable events and assign tentative firing times.

3.0. For the i-th reaction pattern ($i = 1$, if it is not assigned yet), search the main lattice for matching patterns of its initial state. If all patterns have been searched, move to step 4. For the match found here:

3.1. Evaluate the energy change for this match. Temporarily remove the reactants and place the products on the surface. Recompute the total surface energy using Eq. (2.79).

3.2. Update the activation barrier and rate. Compute the activation energy change induced by the total energy difference and evaluate the rate constant using the corrected activation energy expressions (Eqs. (2.76 and 2.77)).

3.3. Sample an occurrence time. Draw a random number and compute

the tentative occurrence time for this event using Eq. (2.65). Store the result in the event time list.

3.4. Restore the surface and continue searching. Restore the original surface configuration and continue searching for additional matches of the current pattern. If no further matches are found, go back to step 3.0 and start to search for the pattern of the $(i+1)$-th initial state.

4. Execute the next event and update the system. Select the smallest time in the event time list and execute the corresponding reaction for this KMC step. Update the surface occupancy, the total energy, and the simulation time. For the simple case where event time is not reused, clear the time list.

5. Checking the termination criterion. If the current time is smaller than the defined end time, return to step 3.0 and search from the 1st pattern; otherwise, stop the simulation.

2.21.3 Accelerating GT-KMC Simulations to Prevent Stiffness

Stiffness is a persistent computational bottleneck in KMC because catalytic models often contain events spanning vastly different time scales.[169, 174] Rapid processes (e.g., surface diffusion) may fire orders of magnitude more frequently than rare chemical transformations, leading to prohibitively long simulations.[169, 174] Numerous acceleration schemes have therefore been proposed, though all of which are approximate and ideally introduce small errors.[169, 175] Consequently, the modeler must apply such schemes with care, quantify the

associated errors, and verify that the accelerated simulation preserves the relevant kinetics (e.g., rates, coverages, and selectivity trends) without distorting the underlying dynamics.

One of the classical early methods, the τ-leap method, advances time in finite increments and executes multiple events per step by assuming populations remain nearly constant within each leap.[176, 177] However, this assumption breaks down on microscopic lattices with strong spatial heterogeneity.[169] Other methods pre-partition the network into fast and slow subsets, integrating the fast subset deterministically while sampling slow events stochastically, but this requires reliable a priori time-scale separation and can fail when regimes change.[178-181]

More flexible on-the-fly strategies detect quasi-equilibrated dynamics during the simulation.[169, 182, 183] Accelerated superbasin KMC identifies rapidly interconverting state and downscales related internal rates to escape superbasins sooner, though sampling large superbasins can be expensive in realistic models.[144, 184] Channel-based scaling operates at the level of reaction channels instead of individual states.[182, 185] According to this method, fast, equilibrated channels are downscaled and then reset after non-equilibrated events, but frequent resets reduce efficiency in long transients or non-stationary processes. Refinements that condition channels on local environments improve

accuracy but greatly increase channel bookkeeping.[182, 185, 186] “Downscaling-only” variants avoid resets yet can lose accuracy when time scales evolve.[183, 186] Recent work introduced error-aware, adaptive downscaling for well-mixed KMC by testing candidate scaling factors and selecting those that balance speed and error, although extension to lattice KMC remains nontrivial due to spatial correlations.[183, 186]

Prats et al.[186] proposed a novel channel-based scaling algorithm designed to be robust and broadly applicable to surface chemistry KMC models with many reaction channels, multiple site types, strong lateral interactions, and transient conditions. The method detects fast, quasi-equilibrated channels based on event statistics and adjusts their rate constants through controlled upscaling and downscaling, overcoming key limitations of earlier strategies.[183, 186]

2.21.4 An Introduction to Zacros

The KMC simulations in this thesis were conducted using the GT-KMC framework as implemented in Zacros (version 3.02), developed by Stamatakis and co-workers.[26, 160, 167, 171-173] In GT-KMC, the catalytic surface is represented as a lattice graph and reactions are encoded as graph-based patterns, which allows events to be defined in terms of local connectivity and site types.[26] In the following two paragraphs, we will describe how a catalytic surface is represented as a lattice in on-lattice KMC simulations in Zacros.[26]

The first step is to discretize the catalytic surface into a set of adsorption sites, based on the locations where adsorbates bind stably. Each site is assigned to a site type. For example, the (111) surface of an fcc metal can be represented by a lattice with four site types: top, bridge, fcc-hollow, and hcp-hollow. Different site types can exhibit distinct properties, for instance, the same species may bind with different strengths and display different reactivity depending on the site type. After defining the site types and their spatial arrangement, the lattice geometry and the current lattice state are stored. The lattice state records the occupancy of each site.[26]

In on-lattice KMC, it is not sufficient to specify only the occupancy of each site; the connectivity between sites must also be defined.[26, 144] This is because event realizability is typically determined by the local geometric environment rather than by an isolated site.[144, 169] For example, diffusion corresponds to a hop from one site to a neighboring site. Without an explicit neighbor list to record channels, diffusion cannot be formulated as an elementary event.[144, 169] Likewise, many surface reactions involve two or more sites, such as Langmuir–Hinshelwood surface reactions.[26, 144] Their realizability depends on whether reactants occupy a neighboring pair of sites, as well as on the associated site types.[26, 144] Connectivity therefore determines which reactant pairs can be enumerated.[26, 169]

During the simulation, Zacros identifies realizable events via subgraph-isomorphism searches on the current lattice configuration (covering both reaction patterns and lateral-interaction motifs), assigns event rates based on the corresponding kinetic parameters, and advances the system in time by executing one event at a time using the first reaction method.[26, 142, 160, 167] In Zacros, reaction energies and activation barriers required for these kinetic parameters are obtained from CEs and BEP relationships following the general workflow illustrated in Fig. (2.4). This formulation is particularly convenient for surface reaction networks with multiple site types, complex local environments, and lateral interactions, enabling efficient and consistent treatment of local configuration dependencies.[26, 144, 160]

2.22 Conclusion

In summary, this chapter has established the theoretical basis and computational software used in the remainder of the thesis. The DFT framework, together with electronic-structure analyses, structural optimization protocols, and transition-state searching methods, provides reliable access to adsorption structures, reaction pathways, and activation energetics on periodic catalyst surfaces (Sections 2.1-14 in this chapter). Section 2.15 in this chapter also set out a consistent set of energy definitions that enables direct comparison of thermochemistry across different SAA compositions and reaction families.

Beyond static energetics, the discussion of kinetic modelling approaches (Sections 16-21 in this chapter) elucidated the technicalities of capturing surface reactivity and introduced practical strategies to incorporate essential many-body effects, including coverage dependence and lateral interactions via cluster expansion. By reviewing KMC algorithms, the chapter provides the methodological bridge from elementary step energetics to time dependent, catalytic behavior. These methods collectively underpin the mechanistic analyses and reactivity trend studies presented in Chapters 4–5, where DFT-derived parameters are integrated with GT-KMC simulations to interpret experiments and identify design principles for SAA catalysts.

Chapter 3 Elucidating the Reactivity of Oxygenates on SAA Catalysts

3.1 Introduction

Introducing isolated transition metal atoms into coinage metal catalysts to form SAAs is a powerful strategy for boosting both activity and selectivity relative to the corresponding pure metals.[1, 14-16] In these materials, the atomically dispersed dopants serve as reactive centers that can promote bond activation and coupling steps that are otherwise sluggish on the host.

Here, we computationally examine a series of SAAs spanning multiple host–dopant pairs (Ni, Pd, Pt, and Rh doped into Cu(111), Ag(111), and Au(111)) with a focus on oxygenate chemicals that are pertinent to biomass-derived feedstocks. Using DFT,[17-19, 97] we evaluate the relative stability of key adsorbed intermediates by calculating formation energies for species, including CH_3, formaldehyde (CH_2O), methoxy(CH_3O), hydroxymethyl (CH_2OH), CH_3OH, methoxymethyl (CH_3OCH_2), and dimethyl ether (CH_3OCH_3) on each SAA surface.[1]

We then determine reaction and activation energetics for the following two systems: (i) the decomposition of CH_3OH to CH_2O and (ii) the coupling between CH_3 and CH_3O. CH_3OH, which can be produced from biomass-derived syngas, can generate surface H* atoms upon dissociation; these H* atoms may

subsequently recombine and desorb as H_2, offering a potential route to renewable hydrogen. Likewise, CH_3OH fragments, including CH_3 and CH_3O, can undergo coupling to form CH_3OCH_3, which is widely regarded as a clean fuel and useful chemical.[1]

By interpreting calculated energy results through TCS and BEP trends, we identify cases where SAAs can maintain comparatively weak adsorption for the products while still delivering low kinetic barriers.[42, 47-51, 187, 188] Such behavior suggests that selected SAA compositions may outperform their monometallic counterparts for crucial oxygenate-conversion steps. Overall, this study provides mechanistic guidance for the design of SAA catalysts aimed at cleaner, more sustainable routes to fuels and chemicals as part of the broader shift from fossil to renewable resources.[1]

3.2 Computational Setups and Research Process

3.2.1 Computational Setups

In this project, DFT calculations were performed using VASP 5.4.1.[17-19, 97] The OptB86b-vdW van der Waals exchange–correlation functional was chosen to improve the description of dispersion interactions, which are expected to contribute significantly to the adsorption and stabilization of key surface species (e.g., CH_2O, CH_3OH, and CH_3OCH_3) on catalytic surfaces in the heterogeneous systems considered in this chapter.[84, 87, 189, 190] PAW potentials are used to

alleviate computational efficiency challenges caused by core electrons.[96, 102] For valence electron expansion, the cutoff energy is set to 400 eV. When optimizing surface configurations, the convergence criterion for the energy at each ionic step is set to 10^{-7} eV, and for geometry optimization, we require the Hellmann−Feynmann forces on all free atoms to be lower than 0.01 eV/Å. To achieve a high computational accuracy, the Brillouin zone is sampled with a 9 × 9 × 1 Monkhorst-Pack k-point grid. Stable structures are identified by the CG method. Transition states are searched by CI-NEB method or the dimer method before refining them with the quasi-Newton method.[106, 107] Frequency tests are then applied to validate these states by ensuring each transition state only has one imaginary frequency along the MEP. To verify the initial and final states of each transition state, the normalised vector of the unstable mode was multiplied by 0.3 and added to (or subtracted by) the validated transition state thereby creating stretched (perturbed) structures, which then were optimized by the CG method to verify that they converge to the original initial and final states. After that, TCS and BEP relationships were built to compare the energy barriers and energy requirements of the coupling steps on different SAAs.[47-51]

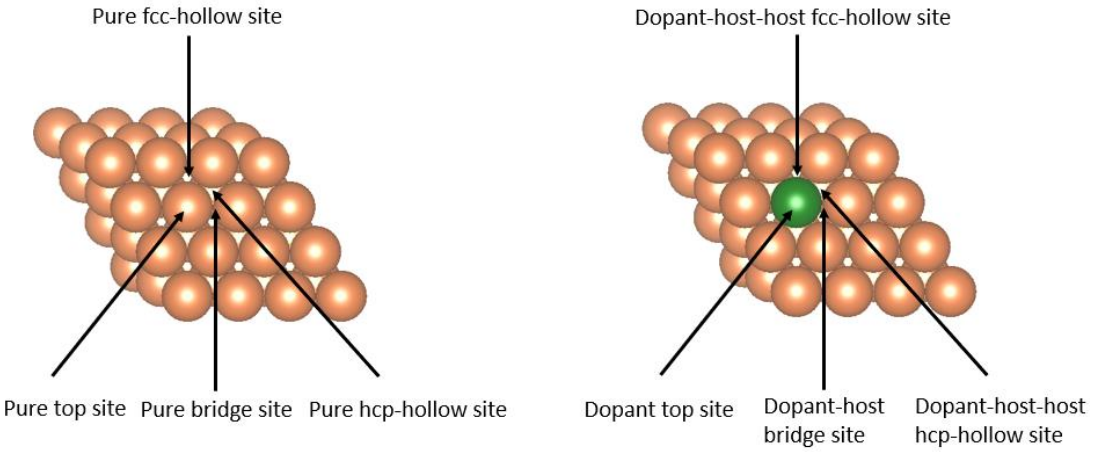


Figure 3. 1 The figure shows the typical fcc(111) surface structures of pure metal (left) and SAA fcc(111) (right) and different sites. Cu is displayed in brown, Pd in green.

MS was used to build 5-layer *p*(4 × 4) supercell models with top three layers relaxed and bottom two layers fixed to simulate fcc(111) surfaces for Au & Au-based SAAs, Ag & Ag-based SAAs, Cu & Cu-based SAAs, Ni, Rh, Pt, and Pd catalysts. Every supercell has a 14 Å vacuum layer to avoid the interaction between periodic images along this direction.[191] An example of surface structures for a pure metal (Cu) and a SAA (Pd/Cu) is given in Fig. 3.1, where the dopant metal atom is displayed in green and the host metal atom in brown. Four kinds of sites for the SAA and pure metal are shown in the figure. The lattice constants are shown in Table A1 in Appendix A.

3.3 Results and Discussion

3.3.1 Adsorption Configurations and Energies

We first investigate the adsorption geometries and energies of simple organic oxygenates including CH_3OH, CH_3O, CH_3OCH_3, CH_3OCH_2, CH_2OH, and CH_2O, as well as inorganic fragments H_2O and OH, on the surface of pure metals and

SAAs. The results of formation energies are shown in Table A2 in Appendix A. The formation energies were then used to compare the stability of the adsorbates on various SAAs and pure metals.

3.3.1.1 Preferable Surface Configurations of Each Fragment

On monometallic transition metal surfaces, H_2O, CH_3OH, CH_2OH, CH_3OCH_2 and CH_3OCH_3 preferentially occupy top sites, whereas CH_3O and OH are more stable on fcc-hollow sites of the host surfaces (Fig. 3.2). In contrast, CH_2O exhibits more diverse adsorption configurations. On Au(111) and Ag(111), CH_2O resides relatively far from the surface with its molecular plane approximately parallel to the surface.[192, 193] For the other pure metals considered, CH_2O adopts a more strongly bound configuration in which the carbon atom coordinates to a surface top site, while the oxygen atom simultaneously interacts with a neighboring bridge site, consistent with prior reports (Fig. 3.3).[194-198]

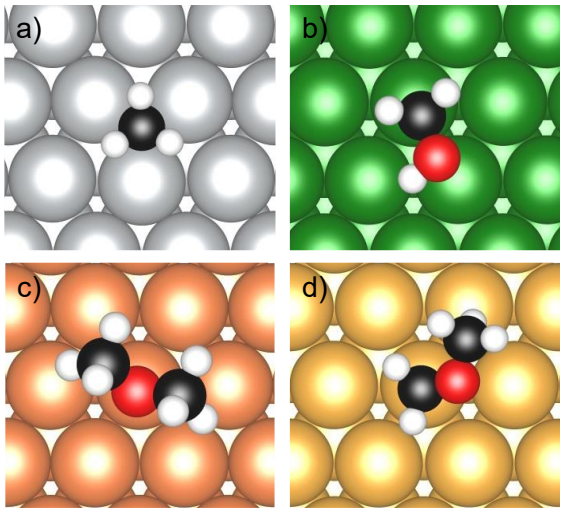


Figure 3. 2 DFT-optimized structures for (a) the CH_3O intermediate on Ag(111), (b) the CH_2OH intermediate on Pd(111), (c) the CH_3OCH_3 intermediate on Cu(111), and (d) the CH_2OCH_3 intermediate on Au(111). Pd in green, Cu in orange, Au in gold, Ag in silver, C in black, O in red, and H in white in the figure.

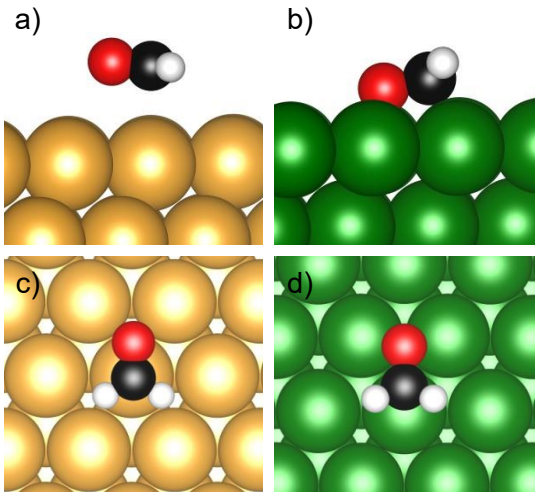


Figure 3. 3 Front views of DFT-optimized structures for the CH_2O intermediates on (a) Au(111) and (b) Pd(111). Top views of DFT-optimized structures for the CH_2O intermediates on (c) Au(111) and (d) Pd(111). Pd in green, Au in gold, C in black, O in red, and H in white in the figure.

On SAAs, CH_3O most often binds through the O atom at mixed fcc-hollow sites involving the host and dopant atoms, with two notable exceptions: on Pt/Au(111) and Rh/Au(111) the top site becomes the preferred adsorption motif, giving the lowest formation energies (Fig. 3.4a, e, and i). A similar trend is observed for

OH, which generally follows the same site preference as CH_3O and shows the same exceptions on Pt/Au(111) and Rh/Au(111) (Fig. 3.4e).

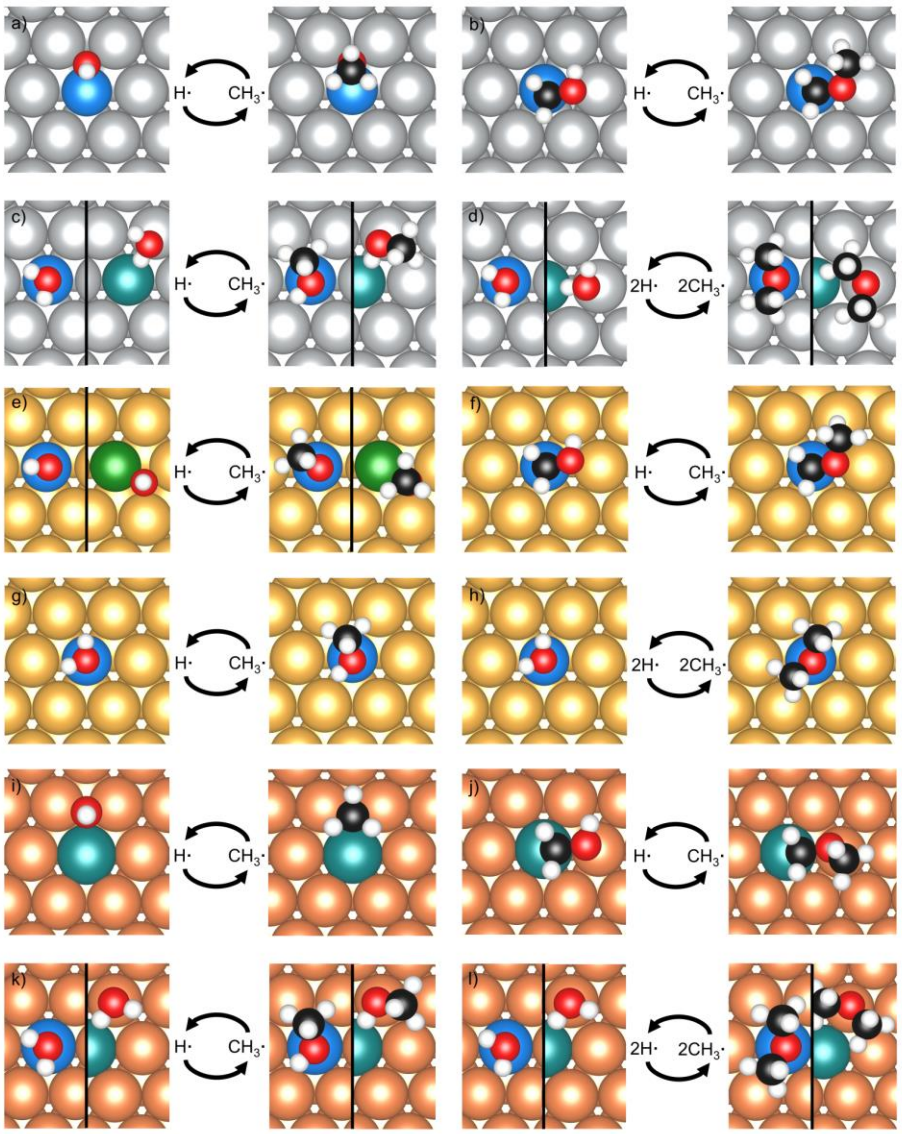


Figure 3. 4 DFT-optimized structures for: (a) the OH and CH_3O intermediates and (b) the CH_2OH and CH_3OCH_2 intermediates on Rh/Ag(111). (c) the H_2O and CH_3OH and (d) H_2O and CH_3OCH_3 intermediates on Rh/Ag(111) and Pt/Ag(111). (e) the OH and CH_3O intermediates on Rh/Au(111) and Pd/Au(111). (f) the CH_2OH and CH_3OCH_2 intermediates, (g) H_2O and CH_3OH intermediates, and (h) H_2O and CH_3OCH_3 intermediates on Rh/Ag(111). (i) the OH and CH_3O intermediates and (j) the CH_2OH and CH_3OCH_2 intermediates on Pt/Cu(111). (k) the H_2O and CH_3OH and (l) H_2O and CH_3OCH_3 intermediates on Rh/Cu(111) and Pt/Cu(111). The arrows indicate replacement of fragments, e.g. the H atom of the OH is replaced with a CH_3 in (a).

For CH_3OCH_2 and CH_2OH, adsorption is consistently favored at the dopant top site across all SAAs. In these configurations, the C atom adopts an sp^3 like coordination and directly bonds to the dopant atom (Fig. 3.4b, f, and j). Likewise, H_2O, CH_3OH (Fig. 3.4c, g, and k), and CH_3OCH_3 (Fig. 3.4d, h, and i) predominantly bind via their oxygen atom at the dopant top site. Exceptions arise for Pt/Ag(111), Pt/Cu(111), and Pd/Cu(111), where H_2O and CH_3OH preferentially adsorb on the top site of the nearest host atom rather than directly on the dopant (Fig. 3.4c and k). Similarly, CH_3OCH_3 favors adsorption on nearby host atoms for Pt/Ag(111) and Pt/Cu(111) (Fig. 3.4d and i). One plausible explanation is that the dopant atoms in Pt/Ag(111), Pt/Cu(111), and Pd/Cu(111) carry comparatively large negative charges (−0.61, −0.45, and −0.30 e, respectively), which disfavors close approach of adsorbates whose O atoms are also negatively polarized, thereby shifting the preference toward adjacent host sites (Fig. 3.4c, d, k, and i).[199] It should be noted that the atomic charges reported in Ref. 99 were obtained from Bader charge analysis.

Additionally, CH_2O displays more diverse binding configurations. On Pd/Au(111), Rh/Au(111), Ni/Au(111), Ni/Ag(111), and Rh/Ag(111), it adsorbs at the dopant top site with both C and O interacting with the dopant, whereas for the remaining SAAs the C binds to the dopant top site and the O interacts with a neighboring host bridge site. Overall, the adsorption preferences of the species examined here are consistent with simple valency arguments: closed-

shell Lewis bases and fragments with a single dangling bond tend to bind on the dopant top site, while fragments with two or three dangling bonds are stabilized on shared dopant–host bridge or dopant–host–host hollow sites, respectively. This is in line with the rules proposed by Michaelides and Hu.[200] In the following section, we compare formation energies for all adsorbates at their most stable binding sites.

3.3.1.2 Formation Energy Comparisons and TCS Relationships

The formation energies of all adsorbates at their most stable binding sites are summarized in Table A2 in Appendix A. Overall, the computed results show that closed-shell molecules are only weakly affected by introducing a transition metal dopant into Cu, Ag, or Au hosts. In contrast, the open-shell fragments, including CH_3O, OH, CH_3OCH_2, and CH_2OH exhibit a much broader spread in formation energies across the different surfaces, with a total variation of roughly 1.4 eV (Fig. 3.5a,b). By comparison, the formation energies of H_2O, CH_3OH, and CH_3OCH_3 vary by less than 0.50 eV among the surfaces considered (Fig. 3.5c,d).

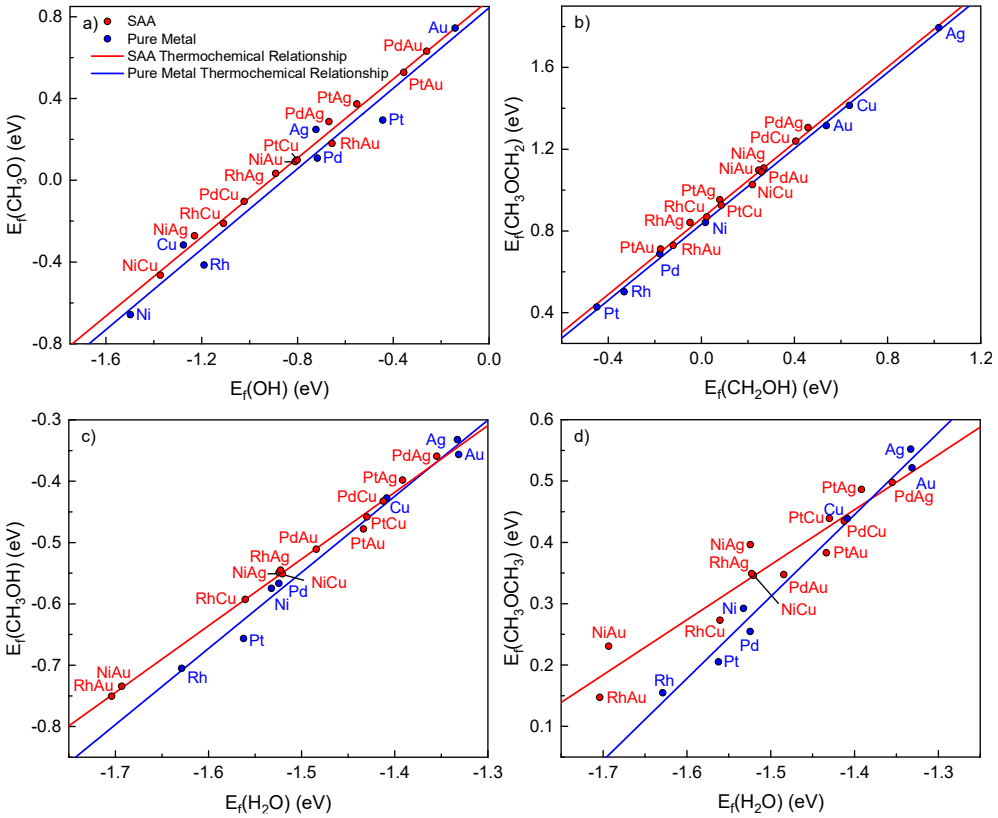


Figure 3. 5 TCS relations of the formation energy E_f corresponding to fragments of (a) CH_3O vs OH, (b) CH_3OCH_2 vs CH_2OH, (c) CH_3OH vs H_2O, (d) CH_3OCH_3 vs H_2O bound in the most stable adsorption site on pure metals (blue) and SAAs (red). Adsorbates on SAAs were bound to their most stable dopant site. Corresponding linear regression fitting parameters and error analysis are given in the Table A3 in Appendix A.

This contrast can be rationalized in terms of bonding character. closed-shell species (including CH_3OH, CH_2O, and CH_3OCH_3) typically bind through the O atom at dopant top sites on most SAAs, and their interaction with the surface remains relatively weak and less sensitive to the specific dopant. As the degree of saturation decreases, however, adsorbates tend to form stronger chemical bonds with the surface. In such cases, the covalent contribution becomes more important. The presence of a transition metal dopant, which can form stronger bonds with adsorbates than coinage metal hosts, leads to a substantially larger variation in stabilization across different SAA compositions.[199]

For most adsorbates, the formation energies computed on SAA surfaces fall between those obtained on the corresponding monometallic host and dopant surfaces, consistent with prior observations.[59] In general, adsorption on the pure coinage metal hosts is markedly less stabilizing, which manifests as higher formation energies, than on pure transition metals (Table A2 in Appendix A). This tendency is also apparent on SAAs. Adsorbates typically bind more strongly at, or in the vicinity of, the dopant atom than on the surrounding host lattice.

Notably, this intermediate behavior on SAAs can break down when the adsorption strengths on the pure host and pure dopant metals are already very similar. For instance, CH_3O on Pt/Ag(111) and Pd/Ag(111) is predicted to be less stable than on either of the two monometallic reference surfaces. This occurs because CH_3O has nearly the same formation energies on Pt(111), Pd(111), and Ag(111) (with differences < 0.15 eV), so introducing a dopant does not provide a clear thermodynamic advantage and can perturb the local binding environment (Fig. 3.5a).

A second notable exception is found for the closed-shell molecules H_2O, CH_3OH, and CH_3OCH_3. On Ni/Au(111) and Rh/Au(111), which feature the two most positively charged dopant atoms among the SAAs considered (0.32 and

0.12 e, respectively)[199], adsorption at the dopant site leads to higher stability than adsorption on the corresponding pure transition metal surfaces (Fig. 3.5c,d). This suggests that, for these O containing closed-shell species, electrostatic effects associated with strongly polarized dopant sites can outweigh the simple interpolation expected from monometallic references.

On monometallic metal surfaces, adsorption energies of related fragments often exhibit TCS, particularly when the species share similar binding patterns and local adsorption geometries.[42, 187, 188] Here, we extend this concept to SAAs by comparing the adsorption behavior of more complex oxygenate intermediates with that of simpler reference fragments obtained by replacing CH_3 groups with H (Fig. 3.4). This substitution provides a systematic way to isolate how the functional group (CH_3) influence stability across different SAA compositions. We employ TCS relationships to analyze correlations among formation energies of chemically similar adsorbates. Such correlations can be used to rationalize the stability of key organic intermediates (including CH_3OH, CH_3O, CH_3OCH_3, CH_3OCH_2, CH_2OH, and CH_2O) as well as inorganic fragments (including H_2O and OH) on the SAA surfaces considered in this work.

Based on their similar binding configuration, we first paired CH_3O and OH to examine whether their adsorption stabilities correlate on both pure metals and SAAs. We constructed TCS relationships between their formation energies (Fig.

3.5). The results reveal pronounced linear correlations for these two open-shell fragments on both material sets (pure metal R^2 = 0.967, SAA R^2 = 0.991). Likewise, CH_3OCH_2 and CH_2OH adsorbed at top sites also show strong linear scaling (pure metal R^2 = 0.999, SAA R^2 = 0.990) (Table A3 in Appendix A). These trends suggest that, for open-shell fragments, formation energies tend to scale linearly when the species occupy sites of the same type.

To assess whether the linear fits obtained for pure metals and SAAs are statistically distinguishable, we applied Student's *t*-tests to compare the slopes and intercepts of the corresponding regressions (Table A3 in Appendix A). For the OH and CH_3O pair, the fitted slopes and intercepts are statistically indistinguishable between pure metals and SAAs at the 90% confidence level. For the CH_2OH and CH_3OCH_2 relationship, the intercepts are statistically indistinguishable at the 99% confidence level but become significantly different at the 90% confidence level. Overall, these results indicate that scaling relations established on pure metals can, in many cases, provide useful predictions for the adsorption energies of more complex adsorbates on SAA surfaces. More generally, our calculations show that substituting H with CH_3 for open-shell adsorbates yields a new species whose formation energy remains well correlated with that of the parent adsorbate on both monometallic and SAA surfaces.

Turning to the closed-shell species, H_2O, CH_3OH, and CH_3OCH_3 adsorb predominantly at dopant top sites through the O lone pairs. As such, these molecules can be regarded as Lewis bases, interacting with the surface mainly by donating electron density. Here, we tested whether their formation energies obey TCS on both pure metals and SAAs (Fig. 3.5c,d). The computed formation energies of CH_3OH correlate strongly with those of H_2O (pure metal R^2 = 0.986, SAA R^2 = 0.995). A similar, though slightly weaker, correlation is observed between CH_3OCH_3 and H_2O (pure metal R^2 = 0.983, SAA R^2 = 0.912) (Table A3 in Appendix A). Overall, these results support the established view that closed-shell Lewis-base adsorbates exhibit robust scaling relationships when they bind in the same site type on a surface.

For the H_2O and CH_3OH pair, Student's *t*-tests indicate that the regressions obtained for pure metals and SAAs share statistically indistinguishable intercepts at the 90% confidence level. In contrast, for the H_2O and CH_3OCH_3 pair, both the intercepts and the slopes differ between pure metals and SAAs already at the same confidence level (Table A3 in Appendix A). We further find that the CH_3OH and CH_3OCH_3 scaling relations for pure metals and SAAs have statistically indistinguishable slopes and intercepts at 90% confidence. These comparisons suggest that a single ("universal") scaling relation can reasonably be used across both monometallic and SAA surfaces to estimate CH_3OH formation energies from those of H_2O, and CH_3OCH_3 formation energies from

those of CH_3OH. It can be found that these pairs indicating the adsorbates differ only by replacing one H atom with a CH_3 group. By contrast, a universal relation is not reliable for predicting CH_3OCH_3 directly from H_2O. Overall, this trend implies that, within the H_2O / CH_3OH / CH_3OCH_3 set, transferring a TCS relation from pure metals to SAAs becomes less accurate as the chemical and bonding similarity between the paired adsorbates decreases.

In contrast, the formation energies of CH_2O do not exhibit clear correlations with any of the fragments discussed above, which can be attributed to its distinct electronic character and its unique, often bidentate, adsorption motifs. One plausible explanation is that adsorbates acting primarily as electron density acceptors do not scale with those acting as electron density donors, even when they bind at the same site type. The TCS for donor adsorbates depends on the ability of each surface to accept electron density.[59, 201] The surface-accepting properties remain constant, irrespective of the adsorbate, and thus donor species formation energies are correlated with one another. As CH_2O adsorbs on the surface via one positively charged C atom and one negatively charged O atom, the adsorbate can both accept and donate density to the surface. As a result, its adsorption energetics reflect a mixture of donor and acceptor type interactions, and it is therefore unsurprising that CH_2O does not follow the same scaling relationships observed for conventional Lewis-base adsorbates.

3.3.2 Catalytically Relevant Bond Coupling/Dissociation Reactions

We next compute and compare the activation and reaction energies for a set of representative elementary steps involving the oxygenated fragments discussed above on both SAA and monometallic surfaces. From the many possible transformations, we focus on two model chemistries: (i) the initial decomposition step of CH_3O to CH_2O and (ii) the formation of CH_3OCH_3 via coupling between CH_3 and CH_3O. These two pathways serve as targeted probes of SAA catalytic performance for bond-activation and bond-coupling reactions relevant to oxygenate conversion (Fig. 3.6).

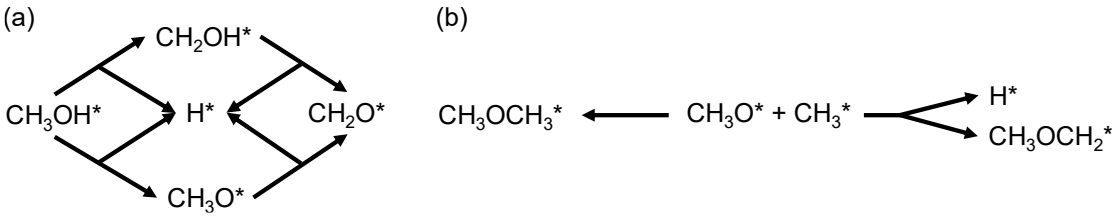


Figure 3. 6 Two biomass reforming related reaction pathways for (a) the decomposition of CH_3OH and (b) the synthesis of CH_3OCH_3 on the different surfaces considered in this work.

We examined elementary steps associated with methanol dissociation, including C–H activation in CH_3OH and CH_3O, as well as O–H activation in CH_3OH and CH_2OH (Fig. 3.6a). The mechanism and activation barriers of C–O coupling relevant to CH_3OCH_3 formation from CH_3 and CH_3O, were then investigated (Fig. 3.6b). By comparing DFT derived energetics across the different catalysts, we identify SAA compositions that are predicted to lower activation barriers and thereby facilitate oxygenate decomposition and coupling

pathways. Then, we investigate the catalysis of bond formation and scissions on SAAs to shed light on their mechanistic routes while comparing them to pure metals. Finally, we highlight a subset of SAAs with the most promising performance for experimental and practical exploration, followed by constructing BEP relationships for the reaction set considered on SAAs.

3.3.2.1 C-H Activation in CH_3OH

We first examined C–H bond dissociation in CH_3OH. As discussed in Section 3.1 from the computed CH_3OH formation energies, CH_3OH is generally more stable at dopant top sites on SAAs, except for Pd/Cu, Pt/Ag, and Pt/Cu, where adsorption at the nearest host top site is preferred. Accordingly, we considered two initial state configurations for C–H activation on each SAA. Based on the position of the CH_3OH adsorbates in the initial states, the two reaction pathways are referred as host-CH_3OH (h-CH_3OH) and dopant-CH_3OH (d-CH_3OH), respectively, (Fig. 3.7). Our calculations indicate that the d-CH_3OH pathway consistently yields lower-energy transition states for the CH_3OH initial dissociation step on all SAAs. In the following discussion, we focus on the pathway that gives the lowest transition state formation energy for each elementary step on each SAA surface.

At the beginning of dehydrogenation, CH_3OH is adsorbed at a dopant top site through the O atom. A surface-facing hydrogen is then abstracted, leading to

elongation of the targeted C–H bond. Because the C atom remains essentially sp^3 hybridized upon loss of H, the adsorption pattern shifts from O-bound to C-bound at the dopant top site, giving rise to a transition state geometry that resembles a CH_2OH-like configuration. Subsequently, the detached H atom transfers to and stabilizes at a nearby dopant–host–host hollow site on the SAA surface. By comparing the transition state geometries for the two pathways (h-CH_3OH versus d-CH_3OH), we infer that the d-CH_3OH pathway exhibits a higher barrier because the CH_2OH is less stably accommodated in the nearest host top site (Fig. 3.7).

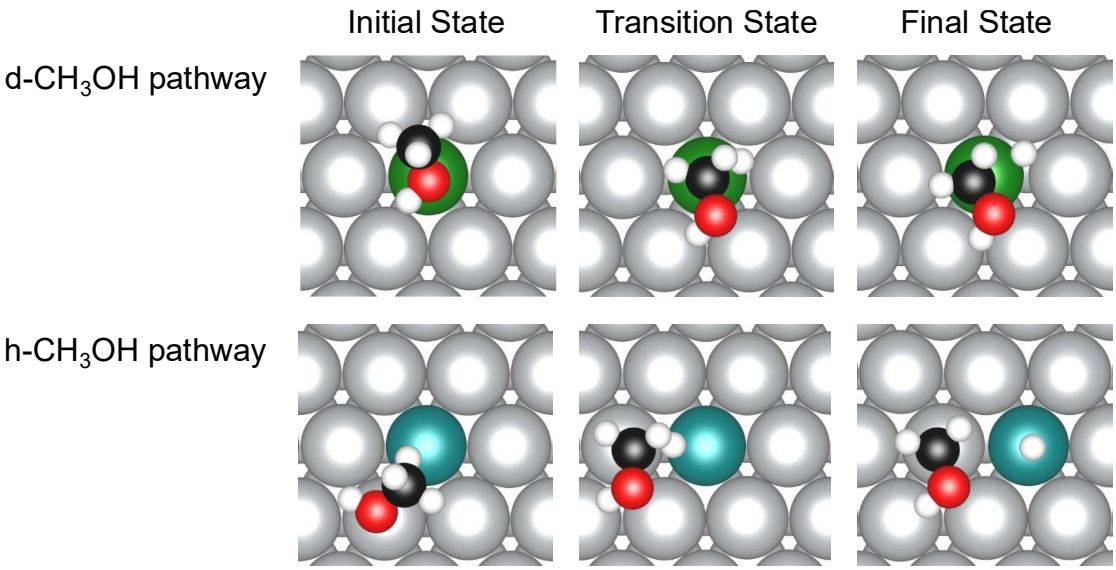


Figure 3. 7 Initial states (left), transition states (middle), and final states (right) for C−H dissociation in CH_3OH on Pd/Ag(111) and Pt/Ag(111) SAAs for the "d-CH_3OH" (top) and "h-CH_3OH" (bottom) dissociation pathways. A five-layer slab was used in these calculations along with a *p*(4×4) unit cell. Only a portion of the cell is shown for clarity.

We then compare the C–H activation barriers on SAAs and on the corresponding monometallic surfaces. For the coinage metals Ag(111),

Au(111), and Cu(111), the calculated C–H scission barriers are 1.91, 1.52, and 1.40 eV, respectively, whereas substantially lower barriers are obtained on the transition metals Ni(111), Pd(111), Pt(111), and Rh(111), with values of 0.78, 0.64, 0.63, and 0.67 eV, respectively (Table A4 in Appendix A). These results confirm that C–H activation is intrinsically more facile on transition metal surfaces than on coinage metal hosts, and they motivate the use of SAAs as a strategy to lower the high activation barriers characteristic of the host metals.

Our calculations indicate that introducing transition metal dopants into coinage metal hosts systematically lowers the C–H scission barriers relative to the corresponding pure host surfaces. The largest barrier reductions are obtained with Rh doping. The C–H activation barriers decrease to 0.59, 0.70, and 0.69 eV on Rh/Ag(111), Rh/Au(111), and Rh/Cu(111), respectively. These values are close to the barrier on pure Rh(111) (Table A4 in Appendix A). Pt dopants also substantially promote C–H activation, yielding barriers of 0.81, 0.78, and 0.88 eV on Pt/Ag(111), Pt/Au(111), and Pt/Cu(111), respectively. Ni-doped Ag(111), Au(111), and Cu(111) display similarly reduced barriers (0.94, 1.06, and 0.88 eV; Table A4 in Appendix A), although these remain higher than for the Rh and Pt doped SAAs. By contrast, Pd shows the weakest promotion effect, with C–H activation barriers of 1.10, 1.07, and 1.09 eV on Pd/Ag(111), Pd/Au(111), and Pd/Cu(111), respectively (Table A4 in Appendix A).

Relative to the corresponding pure hosts, the barrier decrease is most pronounced for Ag-based SAAs, where doping lowers the activation energy by more than 0.8 eV. The reductions are also substantial for Au and Cu hosts, exceeding ~0.5 eV and ~0.3 eV, respectively. Finally, we note that all activation energies reported in this section correspond to the d-CH_3OH pathways, which consistently yield lower transition state energies than the corresponding h-CH_3OH pathways for all the SAAs studied.

The reduced C–H scission barriers on SAAs relative to the pure host surfaces can be rationalized by examining the corresponding formation energies. Introducing a transition metal dopant stabilizes both the initial state and the transition state, but not to the same extent. The stabilization of the initial state arises primarily because CH_3OH binds at the dopant top site rather than on a host atom. As noted in Section 3.1.2, CH_3OH is a closed-shell adsorbate whose formation energy varies only modestly upon doping across the metal surfaces considered.

By contrast, the d-CH_3OH transition state geometry is “product-like”, indicating that the CH_2OH part of the transition state interacts with the dopant through the C atom. Consistent with the trends discussed in Section 3.1.2, CH_2OH experiences a much stronger stabilization when bound at the dopant top site compared to bound at the host. Moreover, the detached H atom is also

preferentially stabilized at a dopant–host–host hollow site, as reported previously by Darby et al.[59] Taken together, these effects imply that doping enhances the stabilization of the transition state more than that of the initial state, thereby lowering the activation barrier, which is consistent with the formation energy trends discussed in Section 3.1.2.

3.3.2.2 O-H Activation in CH_3OH

The same reasoning also helps to interpret the alternative pathways observed for elementary steps of CH_3OH O–H activation. As illustrated in Figure 3.8, two CH_3OH dissociation routes were considered and denoted as h-CH_3OH and d-CH_3OH pathway, corresponding to CH_3OH initially bound at a host or dopant site, respectively. Darby et al.[59] reported that the d-CH_3OH transition states are lower in formation energy than the h-CH_3OH ones on Ni/Au(111), Ni/Ag(111), Ni/Cu(111), Pd/Au(111), Rh/Au(111), and Rh/Ag(111), whereas the remaining SAAs favor the h-CH_3OH pathway. Using an independent computational setup, our results are consistent with this overall picture and additionally provide a complete comparison of both pathways across all SAAs investigated here (Table A5 in Appendix A). These findings indicate that the most stable initial adsorption configuration does not necessarily lead to the lowest energy transition state on a given SAA. This observation also suggests a mechanistic link between pathway preference and the relative stabilization of key intermediate CH_3O as discussed in Section 3.1.2.

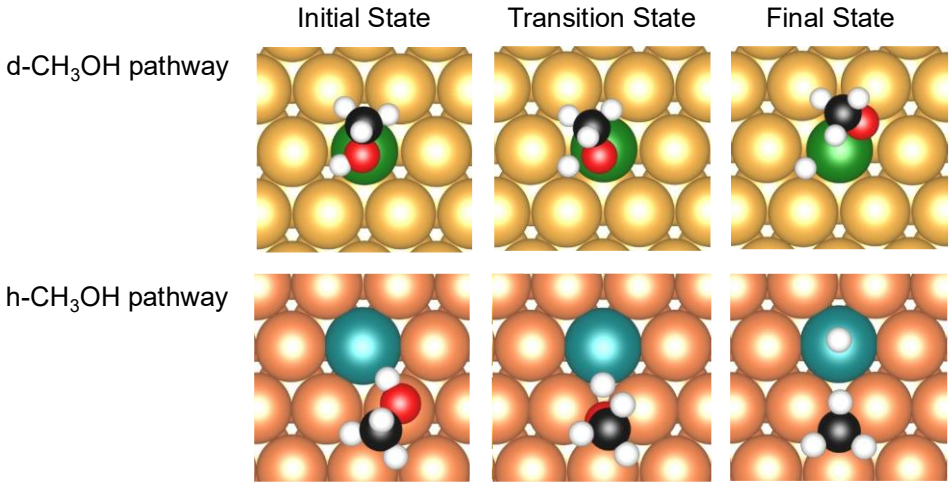


Figure 3. 8 Initial states (left), transition states (middle), and final states (right) for O−H dissociation in CH3OH on Pd/Au(111) and Pt/Cu(111) SAAs for the "d-CH_3OH" (top) and "h-CH_3OH" (bottom) dissociation pathways. A five-layer slab was used in these calculations along with a *p*(4×4) unit cell. Only a portion of the cell is shown for clarity.

More specifically, we find that the final state CH_3O always occupies a host hollow site along the h-CH_3OH pathway, whereas for the d-CH_3OH pathway it binds at a mixed hollow site that involves the dopant atom. This distinction is consistent with the CH_3O formation energy trends. For all SAAs that favor the d-CH_3OH route, including Ni/Au(111), Ni/Ag(111), Ni/Cu(111), Pd/Au(111), Rh/Au(111), and Rh/Ag(111), CH_3O is thermodynamically more stable when adsorbed at dopant-associated hollow sites. Consequently, the d-CH_3OH transition states, in which the CH_3O part resides close to the dopant, can be stabilized, contrary to the corresponding h-CH_3OH transition states.

For the remaining SAAs, except for Pt/Au(111), CH_3O instead prefers host sites over dopant associated sites, which aligns with the host trapped CH_3O-like

transition state and final state geometries along the h-CH_3OH pathway. A possible explanation for the Pt/Au(111) exception is that H adatoms preferentially occupy the dopant top site rather than a dopant–host–host hollow site, which can sterically disfavor CH_3O coordination near the dopant and thereby shift CH_3O toward a host site, as also discussed by Darby et al.[59]

3.3.2.3 C-H Activation in CH_3O

We then examined C–H bond cleavage in CH_3O for configurations in which CH_3O is bound either at a dopant top site or at a mixed dopant–host–host hollow site on SAAs. Like the C–H and O–H activation steps in CH_3OH, distinct initial adsorption configurations can lead to different reaction pathways. When CH_3O is adsorbed at the dopant top site, C–H activation proceeds at a neighboring host site. In contrast, when CH_3O occupies a dopant–host–host hollow site, the C–H bond can be activated at either the dopant atom or an adjacent host atom. In this situation, the pathway cannot be uniquely classified by the initial state alone; instead, we distinguish the two routes according to the site at which C–H cleavage occurs at dopant and host sites, denoting them as dopant-CH_3O (d-CH_3O) and host-CH_3O (h-CH_3O) pathways, respectively (Fig. 3.9).

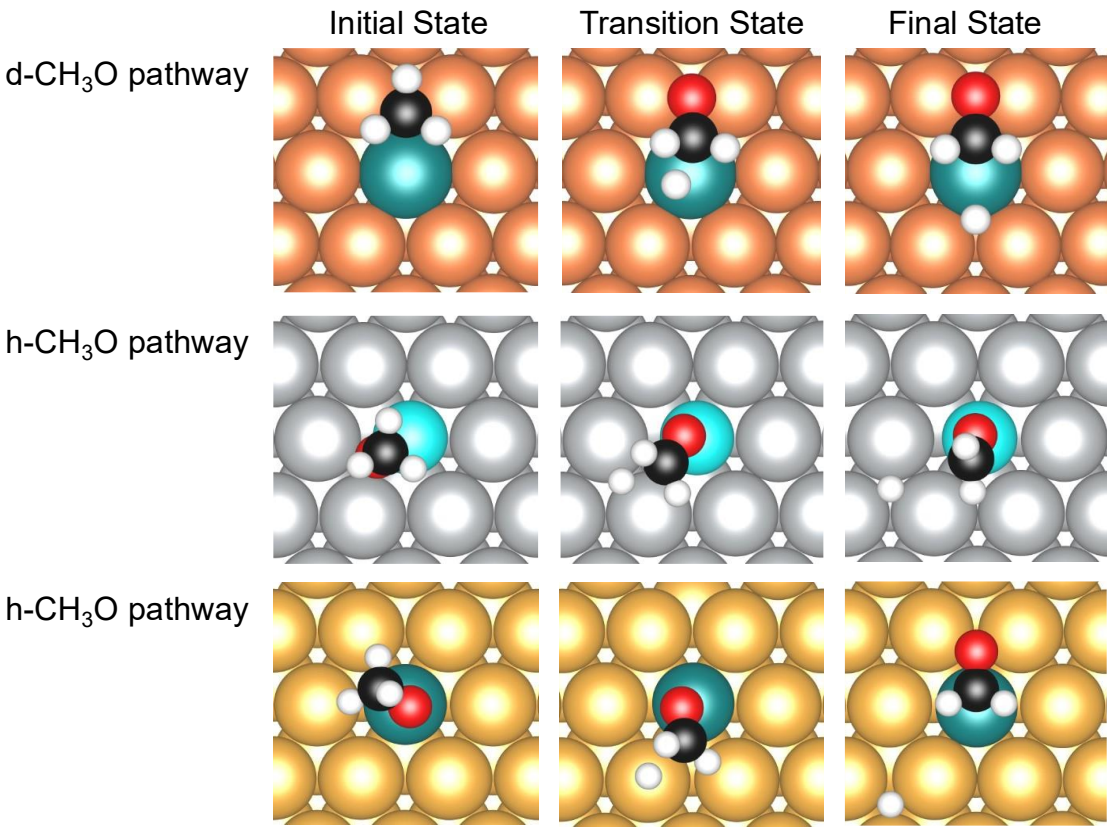


Figure 3. 9 Initial states (left), transition states (middle), and final states (right) for O−H dissociation in CH_3O on Pt/Cu(111), Ni/Ag(111), and Pt/Au(111) SAAs for the "d-CH_3O" (top) and "h-CH_3O" (middle and bottom) dissociation pathways. A five-layer slab was used in these calculations along with a *p*(4×4) unit cell. Only a portion of the cell is shown for clarity.

For most SAAs, the d-CH_3O route yields lower transition state formation energies than the corresponding h-CH_3O pathway. Two notable exceptions are Pt/Au(111) and Rh/Au(111) (Fig. 3.9). On these Au-based SAAs, C–H scission of CH_3O is found to occur exclusively at the nearest host site. Consistent with this behavior, the CH_3O formation energies show that, CH_3O is thermodynamically more stable when bound at the dopant top site rather than at a mixed dopant–host–host hollow site only on Pt/Au(111) and Rh/Au(111). Because the C–O axis in CH_3O is tilted relative to the surface normal in these

top bound geometries, the C atom can approach a neighboring host atom more closely, facilitating C–H activation on the host site (Fig. 3.9).

For the remaining SAAs, CH_3O typically begins the C–H activation step from a dopant–host–host hollow site, with the C–O axis oriented approximately perpendicular to the surface. As dissociation proceeds, the C atom approaches a nearby host atom and the O shifts from the hollow site toward an adjacent host bridge site, causing the C–O bond to gradually tilt toward the surface plane. In this geometry, a H atom is abstracted from the C with the cleavage event occurring near the dopant top site. After C–H scission, the detached H relaxes into a nearby dopant–host–host hollow site, while the resulting CH_2O species remains bound at a dopant-associated hollow site on the opposite side of the dopant (Fig. 3.9).

We also find that CH_3O adsorbed at mixed hollow sites can undergo C–H activation on a host atom for Ni/Ag, Ni/Cu, Pd/Ag, Pd/Cu, Pt/Cu, and Rh/Cu SAAs when the carbon tilts toward the host; however, these h-CH_3O routes are associated with higher barriers (Table A6 in Appendix A). In contrast to the behavior observed for C–H and O–H activation in CH_3OH, the lowest energy transition state for CH_3O C–H cleavage always corresponds to the most stable CH_3O adsorption configuration in the initial state. In the discussion below, we

focus on the pathway that yields the lowest transition state formation energy for each SAA surface.

On the monometallic transition metal surfaces, Pt(111) exhibits the lowest C–H activation barrier, at only 0.18 eV, followed by Pd(111), Rh(111), and Ni(111), with higher barriers of 0.57, 0.60, and 0.86 eV, respectively. In contrast, the coinage metals Ag(111) and Cu(111) show substantially larger activation energies, reaching 1.16 and 1.22 eV, respectively. An apparent exception is Au(111), for which the computed barrier is 0.76 eV, which is lower than that of Ni(111). This barrier is consistent with previous calculations by Réocreux et al.[202] The formation energy analysis offers a plausible explanation for this anomaly. Specifically, CH_3O is unusually unstable on Au(111), exhibiting an exceptionally high formation energy. This raises the energy of the initial state for the C–H activation step and, consequently, reduces the activation barrier relative to surfaces where the initial state is more strongly stabilized (Table A6 in Appendix A).

For the SAAs, Ni-, Pd-, Pt-, and Rh-doped Ag(111) exhibit CH_3O C–H activation barriers of 0.74, 0.78, 0.45, and 0.42 eV, respectively, while the corresponding values for the same dopants in Cu(111) are 0.76, 1.00, 0.73, and 0.56 eV (Table A6 in Appendix A). These results demonstrate that introducing transition metal dopants into Ag(111) and Cu(111) can markedly lower the C–H scission barriers

relative to the monometallic host surfaces. Consistent with the formation energy trends discussed above, both the initial and transition states are stabilized upon doping. However, the dopant-induced stabilization is more pronounced for the transition state than for the initial state. This differential stabilization reduces the activation energy and explains the improved kinetic accessibility of C–H activation on the SAA surfaces.

In contrast, Au-based SAAs show comparatively little change in the C–H activation barrier. Two factors may contribute to this behavior. First, C–H scission in CH_3O on Au(111) already proceeds with a relatively low barrier. The activation barrier is lower than that on Ni(111) and only modestly higher than that on Pt(111) and Rh(111) (by 0.16 and 0.19 eV relative to Pd(111) and Rh(111), respectively). This unusually low barrier on Au(111) is consistent with the high formation energy of CH_3O on Au(111), which indicates a destabilized initial state and thus a reduced activation energy. Second, for Pt/Au(111) and Rh/Au(111), C–H activation occurs predominantly on the nearest Au host atoms rather than at the dopant site. As a result, the transition state interacts less strongly with the dopant atom, limiting dopant-induced stabilization and leading to higher transition state energies than dopant-centered activation.

3.3.2.4 C-H Activation in CH_2OH

As discussed in Section 3.1.1, CH_2OH is generally most stable when adsorbed

at the dopant top site on each SAA. However, analogous to O–H scission in CH_3OH, the lowest barrier pathway does not necessarily originate from the thermodynamically most stable initial adsorption configuration. Less stable initial states can still lead to more stabilized transition states and thus more facile kinetics. To capture this effect, we investigated C–H activation in CH_2OH for multiple initial state geometries, considering activation occurring either at the nearest host atoms or directly at the dopant site on the SAA surface. We distinguish two pathways, namely host-CH_2OH (h-CH_2OH) and dopant-CH_2OH (d-CH_2OH), according to whether CH_2OH is initially bound at a host or dopant site (Fig. 3.10).

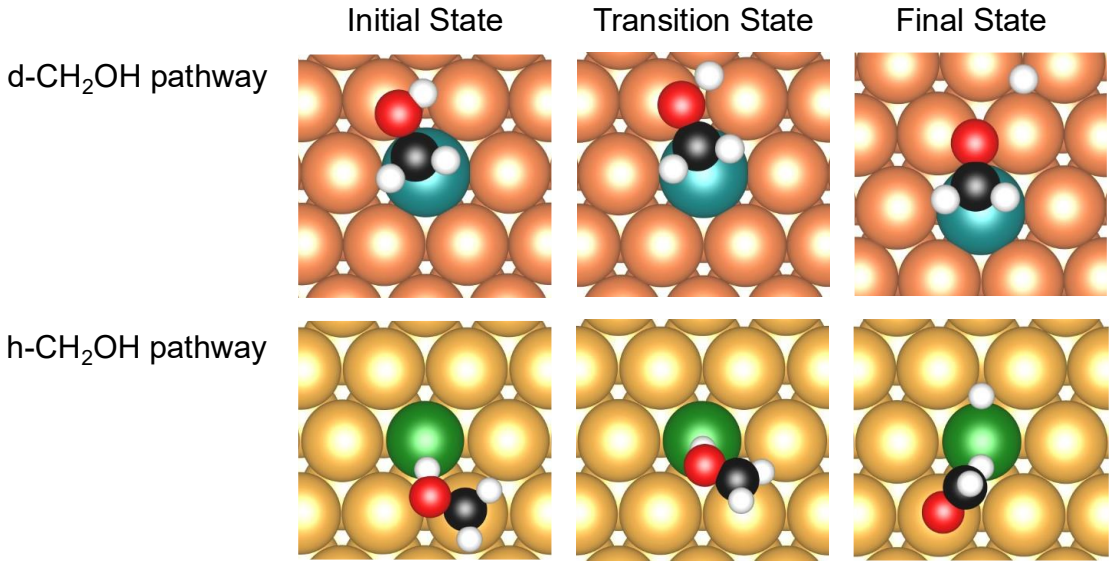


Figure 3. 10 Initial states (left), transition states (middle), and final states (right) for CH_2OH O−H dissociation on Pt/Cu(111) and Pd/Au(111) SAAs for the "d-CH_2OH" (top) and "h-CH_2OH" (bottom) dissociation pathways. A five-layer slab was used in these calculations along with a *p*(4×4) unit cell. Only a portion of the cell is shown for clarity.

In the d-CH_2OH pathway, CH_2OH first adsorbs at the dopant top site through the carbon atom, with the H and O atoms oriented toward the neighboring host region. This geometry positions the H close enough to a host atom to enable O–H cleavage at the host site. As the H atom in CH_2OH is abstracted and moves away from the CH_2OH fragment, the O–H bond breaks on the host atom. Following dissociation, the detached H relaxes into a nearby host hollow site, while the resulting CH_2O species remains bound at the dopant top site (Fig. 3.10).

In contrast, O–H cleavage proceeds via the h-CH_2OH pathway when CH_2OH initially binds at a host top site with the O–H bond oriented approximately parallel to the SAA surface. Along this route, the CH_2OH progressively rotates such that its molecular plane becomes nearly perpendicular to the metal surface. In the transition state, the hydroxyl hydrogen approaches the dopant atom, and the fragment adopts a geometry in which the H atom interacts directly with the dopant top site, where O–H activation takes place. After dissociation, the detached H remains bound at the dopant site, while the resulting CH_2O fragment binds at a nearby host top site (Fig. 3.10).

CH_2OH dissociation on the monometallic surfaces follows a mechanism that is broadly analogous to the d-CH_2OH pathway observed on SAAs. As expected, the transition metals exhibit lower O–H scission barriers than the coinage metal

hosts. Specifically, the calculated barriers on Ni(111), Pd(111), Pt(111), and Rh(111) are 0.65, 0.72, 0.64, and 0.71 eV, respectively, whereas Au(111), Ag(111), and Cu(111) exhibit higher values of 0.98, 0.87, and 0.94 eV (Fig. 3.11).

Across the SAAs, we find that O–H scission proceeds preferentially (with lower formation energy of transition states) via the d-CH_2OH pathway on Ni/Au, Ni/Cu, Pd/Cu, Pt/Cu, and Rh/Cu, with corresponding barriers of 1.05, 0.99, 0.90, 1.05, and 1.00 eV, respectively (Fig. 3.11). The remaining SAAs instead favor the h-CH_2OH route. When comparing apparent activation energies defined with respect to the most stable initial state, (see Section 2 for the Computational Details), Ag-based SAAs display higher values, namely 1.28 eV on Ni/Ag(111), 1.11 eV on Pd/Ag(111), 1.19 eV on Pt/Ag(111), and 1.40 eV on Rh/Ag(111), than the corresponding Au-based SAAs (1.04 eV on Pd/Au(111), 1.09 eV on Pt/Au(111), and 1.27 eV on Rh/Au(111)) with the same dopant (Fig. 3.11b).

As discussed in Section 3.1.1, CH_2OH is generally stabilized at dopant top sites, such that the d-CH_2OH pathway can proceed directly, with O–H scission occurring at a neighboring host atom. However, because the bond breaking involves a mixed dopant–host environment, the dopant does not stabilize the transition state as strongly as it stabilizes the transition state from the host bound initial state (h-CH_2OH pathway). Consequently, although the initial state formation energies are substantially lowered upon introducing a transition-

metal dopant, the corresponding transition states are affected to a lesser extent. This differential stabilization leads to larger activation energies on SAAs than on the pure host metals, consistent with our computed trends, with Pd/Cu(111) being the only notable exception (Fig. 3.11a).

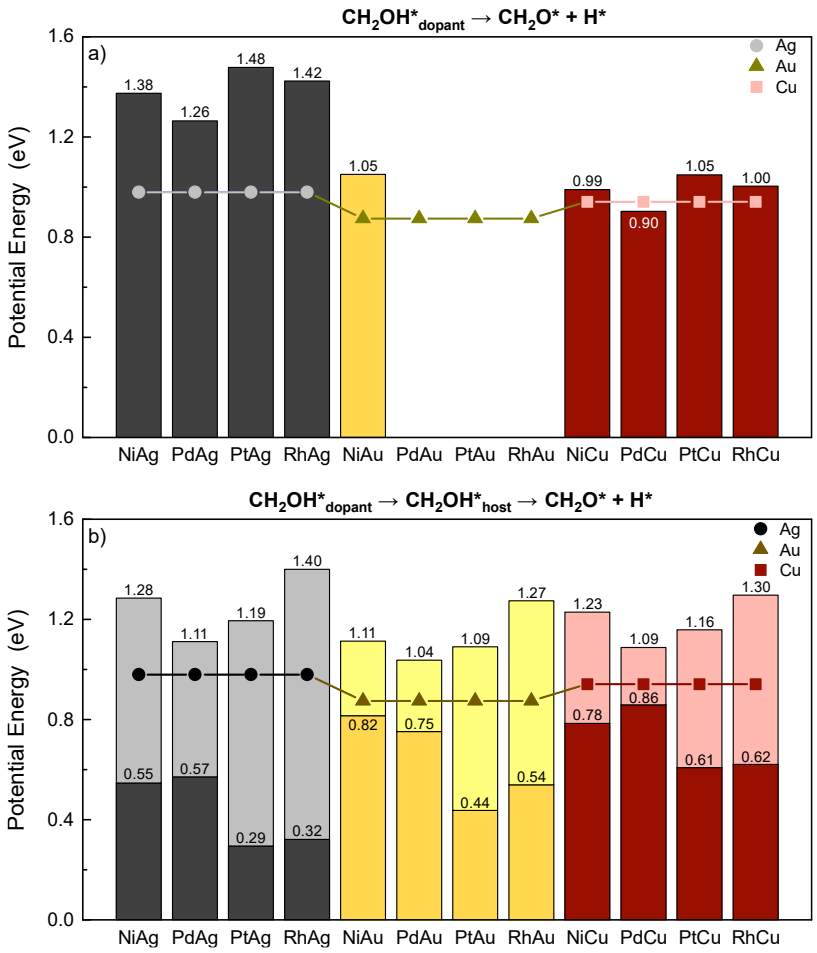


Figure 3. 11 Energy barriers for (a) the d-CH_2OH and (b) the h-CH_2OH reaction pathways. The dark gray, dark yellow, and brown bars show the activation energy on SAAs, while the light gray, yellow, and pink bars represent the energy required for moving CH_2OH binding to dopant top sites to host sites. The numbers on the top of the light gray, yellow, and pink bars represent the apparent activation energies on SAAs. The circle, triangle, and square represent the activation energy on Ag(111), Au(111), and Cu(111), respectively. Three datapoints are missing as we were not able to find a transition state for the corresponding pathway for Pd/Au, Pt/Au and Rh/Au. Reaction energies of these pathways can be found in Table A7 in Appendix A.

In addition, the apparent activation energies reported here for the d-CH_2OH pathway can be viewed as comprising two contributions: (i) the energetic cost associated with CH_2OH migrating from the dopant site to a host site, and (ii) the intrinsic barrier for the subsequent O-H bond activation step at the host reactive site. Unlike the other dehydrogenation reactions considered in this work, the choice of initial adsorption configuration plays a particularly important role because the energy difference between CH_2OH bound at the dopant top site and at a host top site is substantial, spanning 0.23–1.08 eV (Fig. 3.11b). One plausible explanation is that charge mixing between the transition metal dopant and the noble metal host is limited in these systems, such that the isolated dopant top site exhibits reactivity distinct from that of shared dopant–host–host hollow ensembles.[203-205]

Our results further indicate that, on several SAAs, the intrinsic barrier for the O-H bond activation step at the dopant site can be relatively low, whereas a substantial fraction of the apparent barrier arises from the prior diffusion of CH_2OH. For example, transferring CH_2OH from the dopant top site to a host site on Ni/Ag(111), Pt/Ag(111), and Rh/Ag(111) requires at least 0.73, 0.90, and 1.08 eV, respectively. Similarly, the corresponding migration penalties on Pt/Au(111), Rh/Au(111), and Rh/Cu(111) are at least 0.54, 0.73, and 0.68 eV. In these cases, the diffusion contribution accounts for more than half of the overall apparent barrier (Figure 3.11b).

This behavior reflects that isolated dopant atoms can strongly stabilize transition states when the bond scission occurs directly at the dopant, yet accessing the reactive configuration may require the adsorbate to diffuse between adsorption sites. Within the d-CH_2OH picture, dopant centered C–H cleavage benefits from significant transition state stabilization, while the initial state may be comparatively less stabilized because it often involves a more mixed adsorption configuration. Taken together, the h-CH_2OH and d-CH_2OH pathways highlight that SAAs can influence both initial and transition state energetics, and whether the overall barrier is reduced depends on the relative extent to which each state is stabilized.

3.3.2.5 C-O Coupling between CH_3O and CH_3

SAAs have been widely reported to deliver enhanced catalytic activity and selectivity relative to conventional monometallic catalysts.[8] Motivated by these advantages, we consider the formation of CH_3OCH_3, an industrially relevant molecule used as a fuel, refrigerant, and aerosol propellant, as a representative target reaction that may benefit from SAA catalysis. Accordingly, we investigate a set of SAAs spanning multiple host–dopant combinations—Ni, Pd, Pt, and Rh doped into Cu(111), Ag(111), and Au(111)—and evaluate their catalytic influence on the key C–O coupling step between CH_3O and CH_3.

To probe how dopant atoms influence C–O coupling, we constructed two distinct initial configurations for each SAA. In both cases, one reactant (CH_3 or CH_3O) was placed at its preferred dopant site, while the other was positioned at the nearest host site. We classify these initial states according to the location of CH_3O, denoting them as dopant-CH_3O (d-CH_3O) and host-CH_3O (h-CH_3O) geometries (Fig. 3.12).

A comparison of the corresponding formation energies shows that, for most SAAs, the h-CH_3O configuration is thermodynamically more stable, with two exceptions: Ni/Au(111) and Rh/Au(111), where the d-CH_3O geometry is favored. A plausible explanation is that the dopant atoms in Ni/Au and Rh/Au carry more positive charge than in the other SAAs. Because the O atom in CH_3O is strongly electronegative, adsorption on a positively polarized dopant site can strengthen the ionic component of the interaction, thereby stabilizing CH_3O at the dopant and leading to more stable d-CH_3O initial states in these systems.[199]

The C–O coupling reactions initiated from the d-CH_3O and h-CH_3O geometries are referred to as the d-CH_3O and h-CH_3O pathways, respectively. Our calculations indicate that CH_3 and CH_3O can couple through two competing elementary channels: one leading to the formation of adsorbed CH_3OCH_3, and another yielding CH_3OCH_2 accompanied by a surface H adatom. Which product

channel is favored depends on the initial adsorption configuration and on the specific SAA surfaces.

The SAAs considered here can be classified into two distinct groups based on the product channel observed in the C–O coupling chemistry. Group 1 SAAs include Pd/Au, Pd/Ag, Pd/Cu, and Pt/Cu. They can form CH_3OCH_3 via both d-CH_3O and h-CH_3O pathways (Fig. 3.12). In contrast, for Group 2 SAAs, including Ni/Au, Rh/Au, Pt/Au, Pt/Ag, Rh/Ag, Ni/Ag, Rh/Cu, and Ni/Cu, the dopant can additionally promote C–H activation of CH_3 along only the h-CH_3O pathway, leading to CH_3OCH_2 together with a surface H adatom (Fig. 3.12).

A similar separation is found for the monometallic reference surfaces. Au, Ag, Cu, and Pd do not cleave the C–H bond in CH_3 during the coupling process and therefore only form the CH_3OCH_3, whereas Ni, Pt, and Rh can facilitate C–H activation and yield CH_3OCH_2 plus H. Thus, the seven pure metals examined here can likewise be divided into two groups: Group 1 (Cu, Ag, Au, and Pd) and Group 2 (Ni, Pt, and Rh).

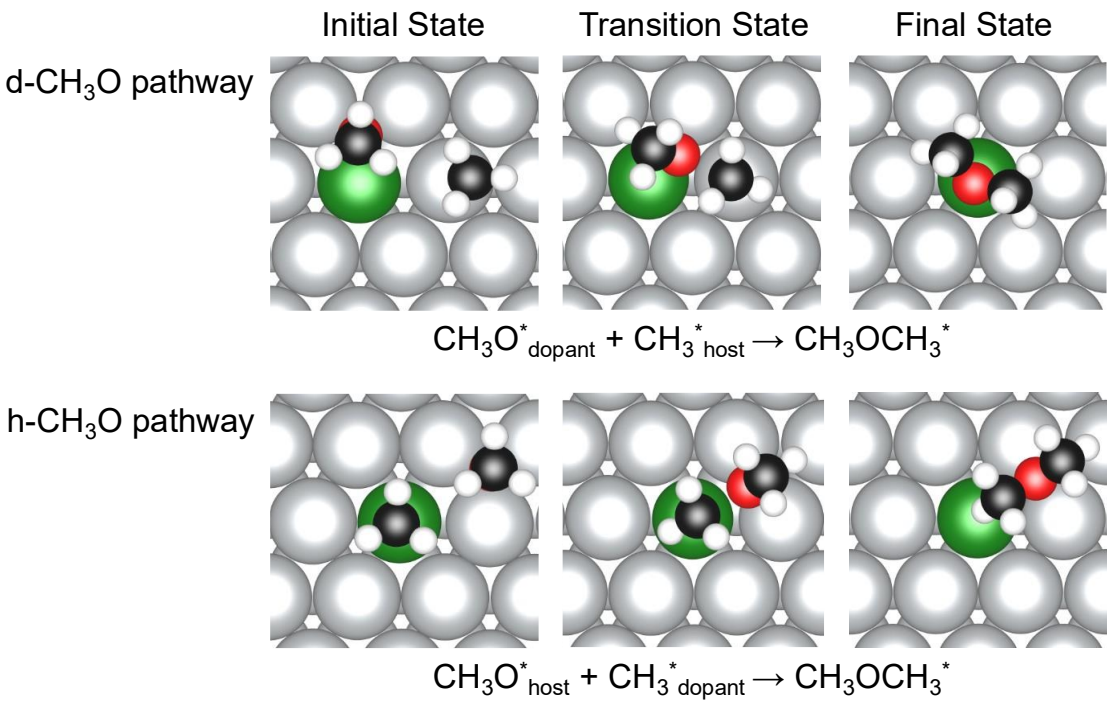


Figure 3. 12 Initial states (left), transition states (middle), and final states (right) for C-O coupling between CH_3 and CH_3O on Ni/Ag(111) (Group 1 SAA) for the "d-CH_3O" (top) and "h-CH_3O" (bottom) dissociation pathways. A five-layer slab was used in these calculations along with a *p*(4×4) unit cell. Only a portion of the cell is shown for clarity. Activation energies and reaction energies for Group 1 SAAs and pure metals can be found in Table A8 in Appendix A.

Our calculations indicate that, for Group 1 SAAs, formation of CH_3OCH_3 does not depend on whether the initial configuration is h-CH_3O or d-CH_3O (Fig. 3.12). At the onset of reaction, the CH_3O fragment migrates toward the CH_3 adsorbate. As the O approaches CH_3, the CH_3O C–O axis tilts away from its initial perpendicular orientation to the surface. Along the h-CH_3O pathway, C–O bond formation typically occurs first at a mixed hollow site, generating adsorbed CH_3OCH_3, which then relaxes and diffuses to a nearby host bridge site. Along the d-CH_3O pathway, the coupling step takes place at a dopant–host bridge site for Ni/Au(111), Pt/Au(111), and Rh/Au(111), whereas on the remaining SAAs it proceeds at the mixed hollow site (Figs. 3.12 and 3.13).

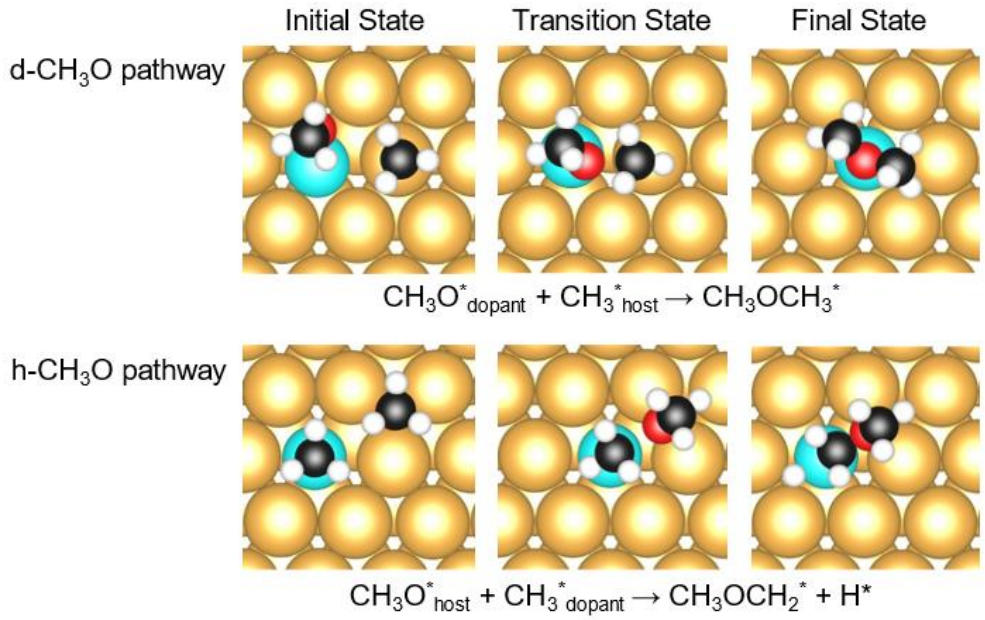


Figure 3. 13 Initial states (left), transition states (middle), and final states (right) for C-O coupling between CH_3 and CH_3O on Ni/Au(111) (Group 2 SAA) for the "d-CH_3O" (top) and "h-CH_3O" (bottom) dissociation pathways. A five-layer slab was used in these calculations along with a *p*(4×4) unit cell. Only a portion of the cell is shown for clarity. Activation energies and reaction energies for Group 2 SAAs and pure metals can be found in Table A9 in Appendix A.

For Group 2 SAAs, a concerted C–H cleavage can take place during the C–O coupling step only when the reaction starts from the h-CH_3O initial configuration (Fig. 3.13). In this channel, the dopant atom can facilitate activation of a C–H bond in the CH_3 fragment as the C–O bond forms, leading to CH_3OCH_2 together with a surface H adatom. By contrast, along the d-CH_3O pathway on Group 2 SAAs, the reaction proceeds only through the simple coupling route to yield adsorbed CH_3OCH_3, because the dopant sites in these systems cannot promote C–H scission for CH_3O.

A plausible explanation for the distinct reactivity patterns is that, in the coupling transition states, the CH_3 H atoms can approach the surface closely enough for concerted C–H activation to compete with simple C–O bond formation (Fig. 3.13). On Group 2 SAAs, the sp^3-hybridized C atom of CH_3 binds strongly to the dopant top site, making detachment of the C from the surface less favorable. Under these conditions, the carbon is more likely to maintain strong bonding to the transition metal dopant while the C–O bond is formed. In this case, one H must be detached to maintain the strong bonding between C and dopant atoms. In addition, the dopant–host–host hollow sites on Group 2 SAAs appear to stabilize H adatoms more effectively than those on Group 1 SAAs, which further promotes C–H cleavage in CH_3.[59] As a result, Group 2 dopants can open a lower-barrier pathway for the overall coupling event by abstracting H from CH_3 while keeping the carbon anchored at the dopant site during bond formation. Consistent with this interpretation, analysis of the transition state geometries shows that the CH_3 C sits farther from the dopant atom on Group 1 SAAs than on Group 2 SAAs (Table A13 in Appendix A), indicating weaker C–dopant interaction in Group 1 and a reduced tendency toward concerted C–H activation.

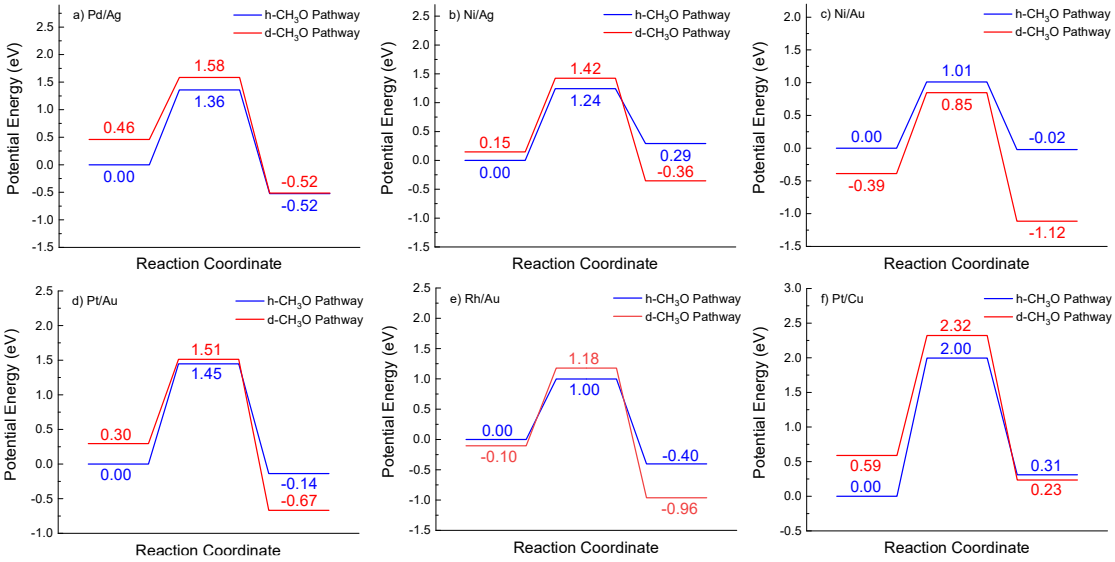


Figure 3. 14 Energy profiles of d-CH_3O and h-CH_3O pathways for C-O coupling on a Group 1 SAA: (a) Pd/Ag, as well as the following Group 2 SAAs: (b) Ni/Ag(111), (c) Ni/Au(111), (d) Pt/Au(111), (e) Rh/Au(111), and (e) Pt/Cu(111).

For Group 1 SAAs, the h-CH_3O pathway exhibits lower formation energies for both the initial state and the transition state than the corresponding d-CH_3O pathway, implying that the h-CH_3O route is thermodynamically and kinetically preferred on these surfaces (Fig. 3.14a,f). A similar trend is observed for Group 2 SAAs when comparing transition state formation energies. The h-CH_3O pathway yields the lower energy transition state for all systems examined, with the sole exception of Ni/Au(111) (Fig. 3.14b–e). To illustrate this behavior, we further compare the energy profiles of the h-CH_3O and d-CH_3O pathways on Ni/Ag(111) and Ni/Au(111) (Fig. 3.14b, c). Because CH_3O in the d-CH_3O transition state remains coordinated in the vicinity of the dopant, the anomalous preference observed for Ni/Au(111) may be attributed to the relatively high

positive charge localized on the Ni dopant, which strengthens CH_3O binding and stabilizes the corresponding transition state.

3.3.3 Comparing Catalytic Activities between SAAs and Pure Metals

To assess the potential advantages of SAAs for the reactions considered here, we compare their catalytic performance with that of the corresponding monometallic surfaces for both CH_3OH dehydrogenation and C–O coupling steps. Specifically, we evaluate differences in transition state formation energies between each SAA and its pure host and dopant reference metals.

It is worth noting that, although dopant metals in their pure form often exhibit lower energy barriers for dehydrogenation than SAAs, they can be poor choices in practice due to diminished selectivity and a greater propensity for poisoning and deactivation.[206, 207] Similarly, although many SAAs exhibit lower transition state formation energies than their monometallic host surfaces, their overall activity can still be constrained by the fact that the catalytic surface is dominated by host atoms, which typically exhibit higher intrinsic activation barriers compared to corresponding monometallic dopant surfaces.

On some monometallic surfaces, the activation energy referenced to the adsorbed initial state can appear deceptively low when the initial state itself is unusually high in energy (see Section 3.2.4). In such cases, the elementary

step may still be kinetically irrelevant in practice because adsorption and stabilization of the initial state is unfavorable, and the barrier referenced to that state can therefore be misleading. By contrast, transition state formation energies are referenced to a common baseline consisting of gas phase reference species and the clean surface and can be interpreted as an apparent kinetic metric from a consistent thermodynamic reference. Using transition state formation energies thus reduces the influence of initial state energy differences and enables a more meaningful comparison of catalytic activity trends across the SAA and pure metal surfaces considered here.

To precisely quantify how doping affects reactivity relative to the pure metals, we compute the transition state formation energy differences between each SAA and its corresponding pure metal surface. A negative energy difference $\Delta E_{F,h}^{TS}$ indicates that the SAA stabilizes the transition state more strongly than the pure metal, whereas a positive value implies the opposite trend.

3.3.3.1 C-H and O-H Bond Scission Reactions

For CH_2OH O–H activation, replacing pure dopant metals with SAAs leads to an increase in transition state formation energies of 0.54–1.07 eV. Similarly, for CH_3OH C–H activation, the intrinsic activity of Pd(111) and Pt(111) is expected to decrease upon alloying with coinage metal hosts, as the corresponding activation energies increase by 0.33–0.67 eV in the SAAs (Fig. 3.15a).

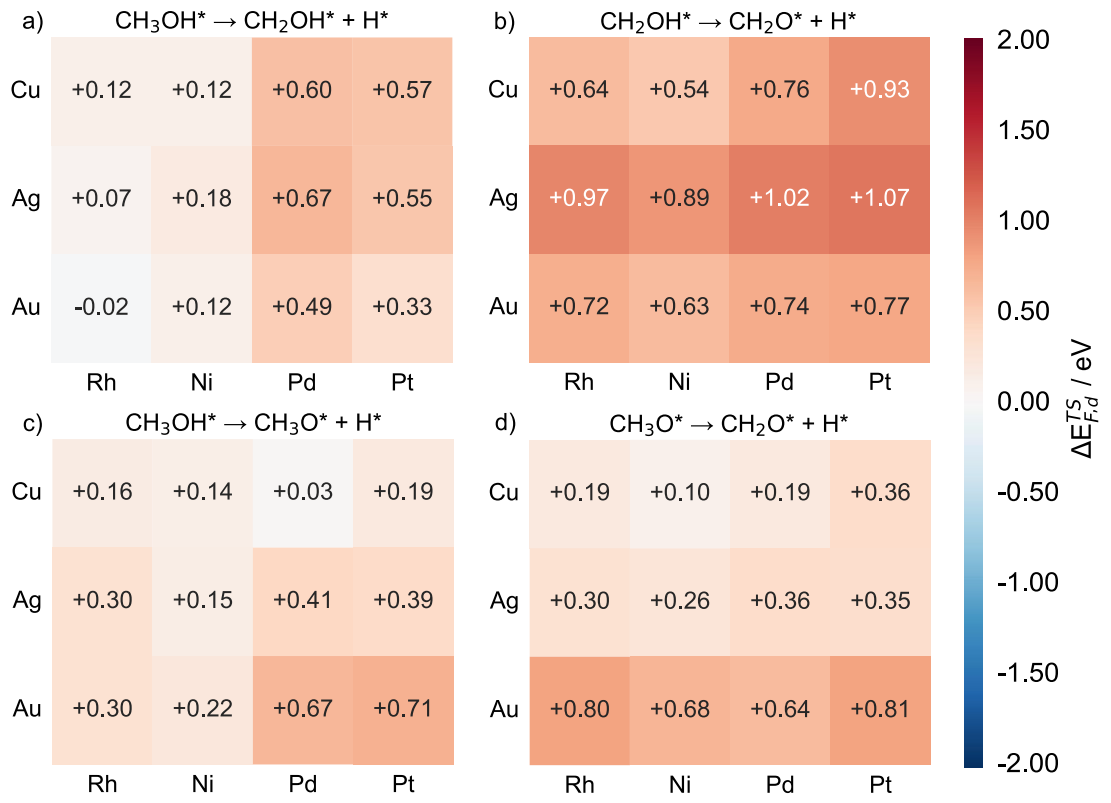


Figure 3. 15 Heatmap charts of the transition state formation energy differences ($\Delta E_{F,d}^{TS}$) for the following dehydrogenations: (a) CH_3OH C-H activation, (b) CH_2OH O-H activation, (c) CH_3OH O-H activation, and (d) CH_3O C-H activation for Cu-, Ag- and Au-based SAAs. For each SAA, $\Delta E_{F,d}^{TS}$ is calculated as the formation energy of the lower-energy transition state (between the d- and h-pathways) minus the formation energy of the transition state in the corresponding pure dopant metal.

For CH_3OH O–H activation and CH_3O C–H activation, the transition state formation energies on Au-based SAAs are also generally higher than those on the corresponding pure dopant surfaces (Fig. 3.15c,d). Notably, Rh/Au(111) and Pd/Cu(111) for CH_3OH C–H and O–H scission exhibit transition state energies that are comparable to those of their respective pure dopant metals. This suggests that isolated Rh and Pd atoms in Au and Cu hosts, respectively, can preserve much of the dopant's intrinsic ability to stabilize the relevant transition states.

It should be emphasized that extremely low barriers can promote over-dehydrogenation and increase the probability of catalyst poisoning and deactivation. This behavior was also observed in our earlier studies of Pt/Cu(111) and Rh/Cu(111).[206, 207] In this regard, alloying highly active dopants with more inert coinage metal hosts offers a practical advantage by moderating excessive reactivity, thereby helping to mitigate poisoning risks. This rationale motivates a direct comparison of the transition state formation energies on pure hosts versus SAAs, as summarized in Fig. 3.16, to quantify how the coinage-metal host tunes the reactivity of the active site.

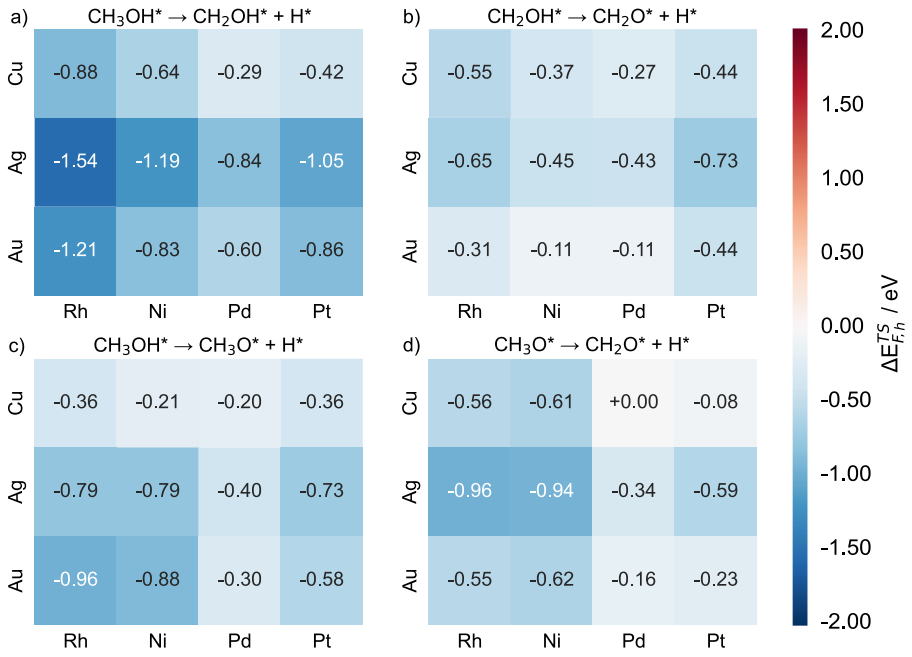


Figure 3. 16 Heatmap charts of the transition state formation energy differences ($\Delta E_{F,h}^{TS}$) for the following dehydrogenations: (a) CH_3OH C-H activation, (b) CH_2OH O-H activation, (c) CH_3OH O-H activation, and (d) CH_3O C-H activation for Cu-, Ag- and Au-based SAAs. For each SAA, ΔE_F^{TS} is calculated as the formation energy of the lower-energy transition state (between the d- and h-pathways) minus the energy of the corresponding pure host metal.

Our results show that the apparent barrier for CH_3OH C–H activation decreases most strongly for Ag(111) upon doping with an absolute reduction exceeding 0.8 eV, followed by Au(111). By contrast, introducing transition metal dopants has the smallest impact on enhancing the activity of Cu(111) for this step (Fig. 3.16a). When the intrinsic reactivity of the host surfaces is considered, this trend indicates that doping tends to provide the greatest relative benefit for hosts that are initially less active toward CH_3OH C–H activation. Among the dopants studied, Rh produces the largest decrease in the apparent barrier, followed by Pt and then Ni. In comparison, Pd doping yields the weakest reduction in the CH_3OH C–H activation barrier.

Turning to CH_2OH dehydrogenation, Ag(111) again emerges as the most responsive host to transition metal doping, followed by Cu(111) and then Au(111). In particular, Ni and Pd doping on Au(111) produces only marginal changes in the apparent barriers for this step (Fig. 3.16b). For the remaining dehydrogenation reactions, Pd consistently shows the smallest influence on the activation energies; this is especially evident for CH_3O C–H activation on Pd/Cu(111), where the apparent barrier is essentially unchanged upon doping (Fig. 3.16c,d).

Our results reveal that the extent to which doping lowers the activation barrier

is highly system dependent (Fig. 3.16). For instance, Rh doping on Ag(111) is predicted to decrease the apparent barrier for CH_3OH C–H activation by 1.54 eV, whereas Pd doping on Cu(111) reduces the barrier by only 0.29 eV (Fig. 3.16a). For CH_2OH O–H activation, Pt/Ag(111) stabilizes the transition state by 0.73 eV, representing an effect nearly seven times larger than that achieved by Ni or Pd doping on Au(111) for the same step. Overall, these comparisons illustrate that introducing a minute amount of a suitably chosen transition metal dopant into an inert host can yield SAAs with markedly improved catalytic activity relative to the pure host surfaces.

3.3.3.2 C-O Coupling between CH_3O and CH_3

Continuing with the C–O coupling reaction between CH_3O and CH_3, we find that the transition state formation energies on SAAs are generally higher than those on the corresponding pure dopant metals (Fig. 3.17). This indicates that C–O bond formation is, in principle, kinetically more facile on the monometallic transition metal surfaces. However, these pure dopant metals are not necessarily optimal catalysts for selective DME formation. In particular, Ni, Pt, and Rh tend to favor a concerted coupling pathway that includes C–H activation in CH_3O, which diverts reactivity away from the direct CH_3OCH_3 channel. Moreover, the pure transition metal surfaces also exhibit relatively low barriers for C–H scission in both CH_3 and CH_3O, which can further suppress the yield of CH_3OCH_3 by opening competing dehydrogenation routes.[59, 206, 207]

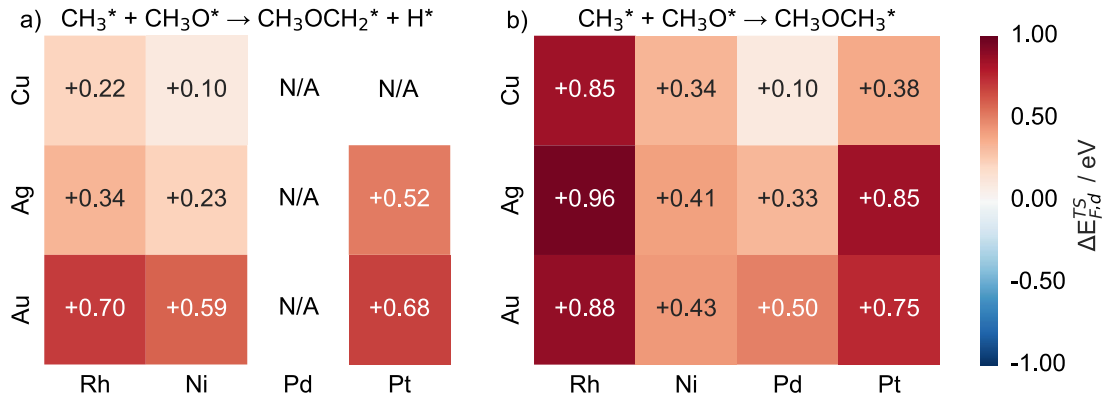


Figure 3. 17 Heatmap charts of the transition state formation energy differences ($\Delta E_{F,d}^{TS}$) for (a) CH_3OCH_2 and (b) CH_3OCH_3 intermediate formation for Cu-, Ag- and Au-based SAAs. For each SAA, $\Delta E_{F,d}^{TS}$ is calculated as the formation energy of the transition state minus the energy of the corresponding pure dopant metal.

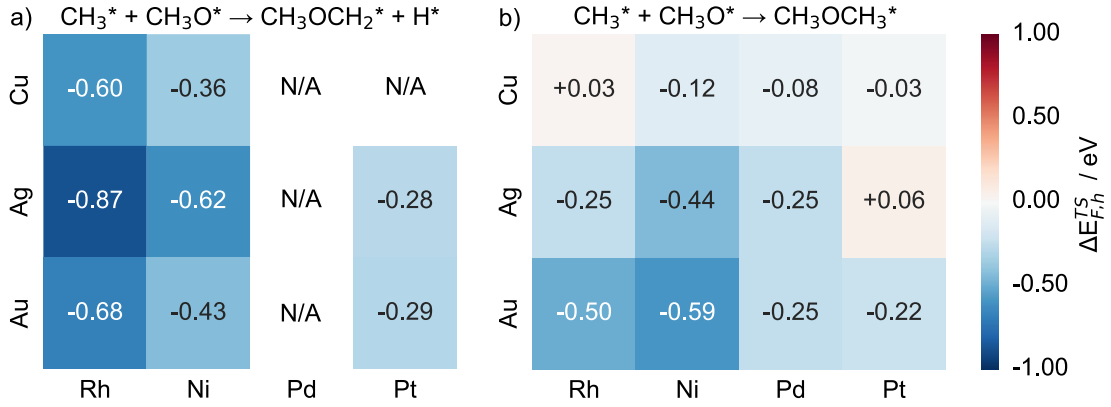


Figure 3. 18 Heatmap charts of the transition state formation energy differences ($\Delta E_{F,h}^{TS}$) for (a) CH_3OCH_2 and (b) CH_3OCH_3 intermediate formation for Cu-, Ag- and Au-based SAAs. For each SAA, $\Delta E_{F,h}^{TS}$ is calculated as the formation energy of the transition state minus the energy of the corresponding pure host metal.

Relative to the monometallic host surfaces, most SAAs exhibit lower transition state formation energies for the C–O coupling step, indicating that alloying coinage metal hosts with isolated transition metal dopants can stabilize the coupling transition state and thereby reduce the apparent activation barrier. Two notable exceptions are Pt/Ag(111) and Rh/Cu(111), for which this stabilization

is not observed (Fig. 3.18). The trends further suggest that Pd doping is more effective on Au(111) and Ag(111) than on Cu(111) in lowering the coupling barrier (Fig. 3.18b). In addition, the presence of transition metal dopants generally has an even stronger impact on reducing the apparent activation energies for the CH_3OCH_2-forming channel, with Ni/Au(111) being the main exception. Overall, these results point to Pd as a particularly promising dopant for designing SAAs that promote the selective formation of CH_3OCH_3. Compared with pure host metals, our results show that RhAg and NiAg have the potential to selectively catalyze CH_3OH dehydrogenation to CH_2O via CH_3O- and CH_2OH-path, respectively.

3.3.4 BEP Relationships

The BEP relationship describes an approximately linear dependence of the activation energy on the reaction energy for a given class of elementary steps, and is therefore widely used as a practical tool for estimating kinetic barriers and screening catalytic materials.[47-51] Here, we first construct BEP correlations for the bond cleavage steps in the CH_3OH dissociation network and compare the resulting trends across the reactions considered (Fig. 3.19).

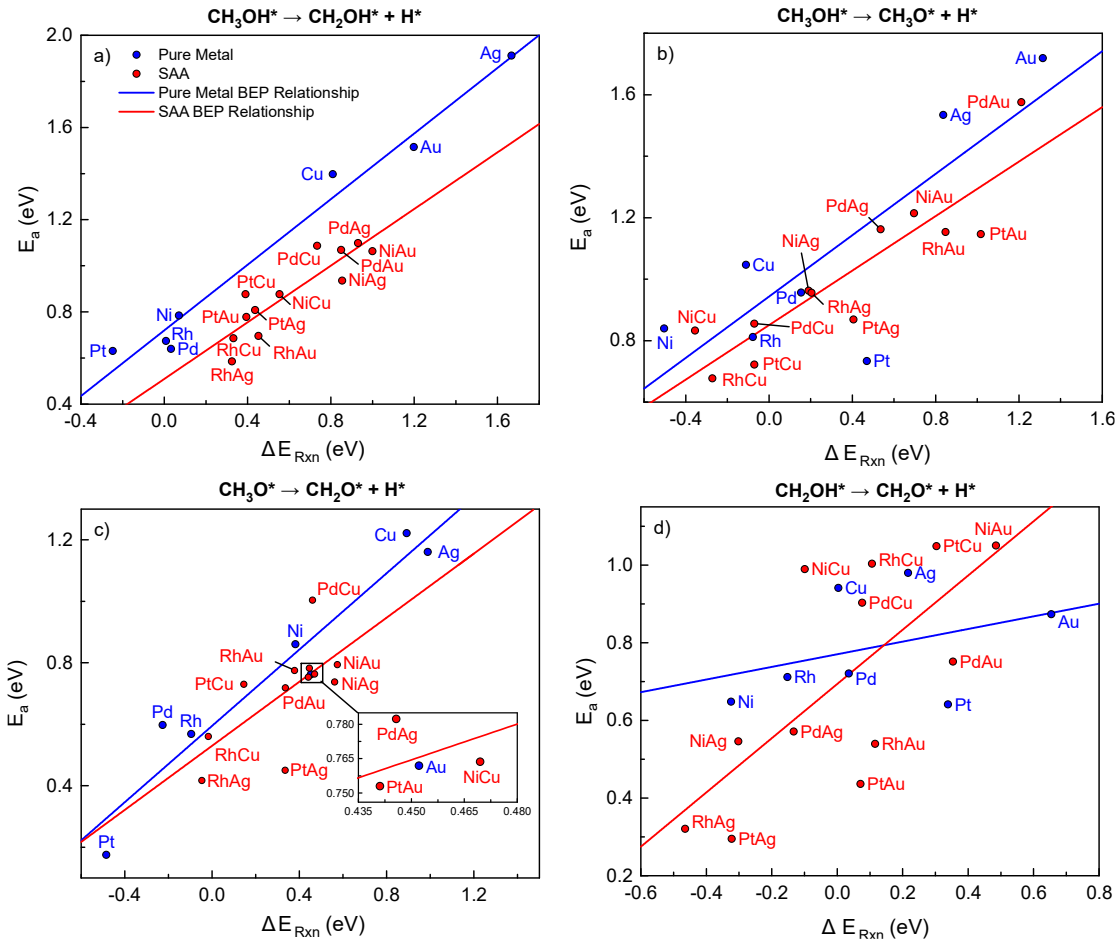


Figure 3. 19 BEP relationships for (a) C-H activation in CH_3OH, (b) O-H activation in CH_3OH, (c) C-H activation in CH_3O, and (d) O-H activation in CH_2OH on pure metal (111) surfaces (blue) and SAA (111) surfaces (red). The plots show the activation energy as a function of the reaction energy. Linear fits are drawn for each reaction on each surface type. Corresponding linear regression fitting parameters and error analysis are given in Table A11.

For the monometallic surfaces (blue markers/lines in Fig. 3.19), the BEP fits reproduce the activation reaction energy trends well for both CH_3OH scission and CH_3O C–H activation. Specifically, the regression statistics show R^2 = 0.979 with an MAE = 0.066 eV for C–H cleavage in CH_3OH, and R^2 = 0.928 with an MAE of 0.080 eV for H abstraction from CH_3O (Fig. 3.19a,c). In contrast, the O–H activation of CH_3OH exhibits a much weaker BEP trend on pure metals (R^2=0.658, MAE = 0.090 eV), which appears to be driven largely by Pt(111)

behaving as an outlier with an unusually high reaction energy (Fig. 3.19b). One possible origin of this deviation is the comparatively weak stabilization of the CH_3O on Pt(111). Among the monometallic surfaces considered, CH_3O has the second highest formation energy on Pt(111), consistent with reduced product stabilization and a more endothermic O–H cleavage step (Table A2 in Appendix A).

Turning to the SAA data set (red markers/lines in Fig. 3.19), the BEP regressions for CH_3OH C–H activation and CH_3OH O–H activation yield reasonably low prediction errors, with MAEs of 0.07 and 0.10 eV, respectively, and comparatively good linearity with R^2=0.756 and 0.780, respectively (Fig. 3.19a,b). In contrast, the BEP correlation for C–H scission in CH_3O is much weaker on SAAs, showing a poor linear fit (R^2=0.452) despite a similar MAE of 0.080 eV (Fig. 3.19c).

Over the range of reaction energies sampled in this work, the BEP lines derived for the SAAs lie consistently below the corresponding monometallic trends. This downward shift implies that, at comparable reaction energies, SAAs tend to exhibit lower activation energies than pure metal surfaces. In other words, SAAs can partially decouple adsorption strength and kinetics, offering the possibility of combining relatively weak binding with reduced barriers, thereby improving catalytic performance.

To assess whether the BEP relationships for SAAs and pure metals are statistically distinguishable for each elementary step, we applied Student's *t*-tests to compare the fitted slopes and intercepts. For the three dehydrogenation reactions discussed above, the slopes and intercepts of the monometallic and SAA BEP fits are not significantly different at the 90% confidence level, except for the intercept for CH_3OH C–H activation. Consequently, a single universal BEP relation appears appropriate for CH_3OH O–H scission and CH_3O C–H scission across both pure metals and SAAs, whereas CH_3OH C–H activation requires separate BEP parameterizations for the two material classes (Table A12 in Appendix A).

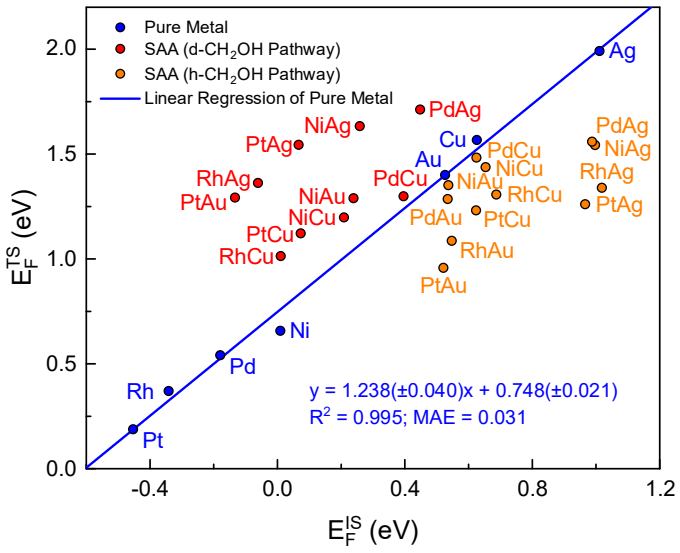


Figure 3. 20 Energies of transition versus initial states for the O-H activation in CH_2OH. A linear regression fit is only drawn for pure metals (blue). Red and orange circles indicate d-CH_2OH and h-CH_2OH pathways on SAAs, respectively. Formation energies can be found in Table A10 in Appendix A.

In contrast to the reactions discussed above, O–H activation in CH_2OH behaves very differently (Fig. 3.20d). The data are widely dispersed and neither the monometallic nor the SAA set exhibits a clear BEP trend (R^2=0.497, MAE = 0.024 eV for pure metals; R^2=0.141, MAE = 0.099 eV for SAAs). Notably, however, we observe a very strong linear relationship between the initial and final state energies for this step on pure metals (R^2=0.995; Fig. 3.20). This is consistent with the findings of Garćıa-Muelas and Lopez,[198] who also reported a poor BEP correlation for CH_2OH O–H activation on pure metals but showed that the correlation improves markedly when the initial state potential energy, rather than the reaction energy, is used as the descriptor.

As illustrated in Fig.3.20, the formation energies of CH_2OH adsorbed at host sites on SAAs are very close to those on the corresponding pure host metals (the orange SAA points lie almost directly below the blue monometallic points). In addition, the dopant atoms can provide additional stabilization of the transition state along the h-CH_2OH pathway, with an overall stabilizing capability that follows the trend Pt > Rh > Ni > Pd (with Ni/Au(111) as a notable exception, showing a higher transition state energy than Pd/Au(111)) (Fig. 3.20).

When CH_2OH binds directly to the dopant atom, the associated initial state energies are substantially reduced relative to the pure host references. Interestingly, only the Cu-based SAAs and Ni/Au(111) exhibit lower transition

state formation energies for the d-CH_2OH pathway than for the h-CH_2OH pathway. This suggests that, on other SAAs surfaces, the most effective activation environment is provided by the nearest host site, where the dopant induced stabilization of the transition state can be maximized (Fig. 3.20).

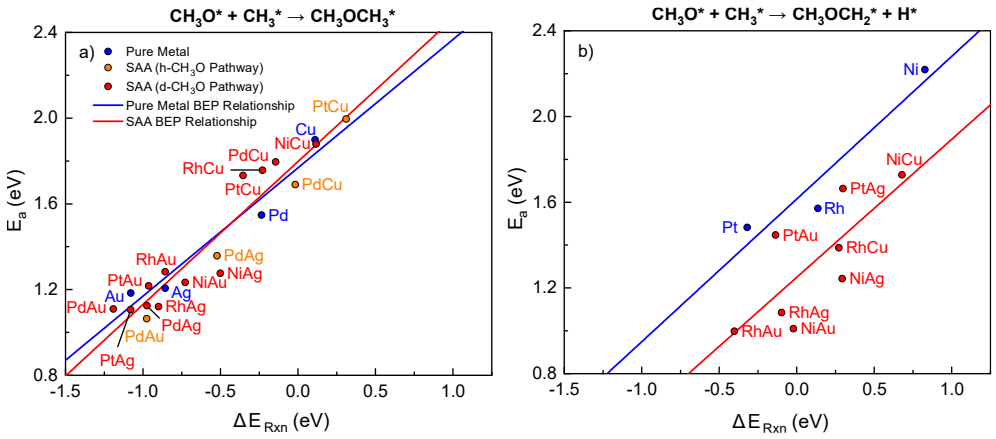


Figure 3. 21 (a) BEP relationships for h-pathway occurring on Group 1 SAAs and pure metals (111) surfaces. (b) BEP relationships for d-pathway occurring on all kinds of SAA and pure metals (111) surfaces. The plots show the activation energy as a function of the reaction energy. Linear fits are drawn for each reaction on each surface type. Corresponding linear regression fitting parameters and error analysis are given in Table A12 in Appendix A.

Finally, we constructed BEP relationships for the C–O coupling reaction by correlating reaction energies with activation energies for the h-CH_3O and d-CH_3O pathways on each SAA. For the h-CH_3O pathway, strong BEP linearity is obtained for both Group 1 SAAs and Group 1 monometallic (111) surfaces, with R^2=0.910 and 0.951, respectively (Fig. 3.21a). Student's *t*-tests were then used to assess whether the two regressions differ statistically. The results show that the BEP fits for Group 1 SAAs and pure metals have statistically indistinguishable slopes and intercepts at the 90% confidence level (Table A12

in Appendix A).

By contrast, the BEP fit for the h-CH_3O pathway on Group 2 SAAs is considerably weaker, with R^2=0.587 (Fig. 3.21b), indicating that the linear scaling observed for Group 1 catalysts is more robust than for Group 2. A plausible reason is that the h-CH_3O pathway on Group 2 SAAs can involve a concerted process in which C–O bond formation is coupled to C–H activation, introducing additional mechanistic complexity beyond a single bond forming event. Notably, the fitted BEP line for the Group 2 SAA data lies below the corresponding monometallic trend, implying that SAAs generally exhibit lower activation energies than pure metals at comparable reaction energies. This downward shift suggests that the coupled C–O coupling/dehydrogenation channel is kinetically more accessible on Group 2 SAAs.

3.4 Conclusion

In this study, we have conducted a thorough investigation of the catalytic performance of SAAs for pertinent reactions. DFT was used to first examine the adsorption behavior of simple oxygenated species (including CH_3OH, CH_3O, CH_3OCH_3, CH_3OCH_2, CH_2OH, CH_2O, H_2O, and OH), followed by investigating the mechanisms of several key elementary steps relevant to the biomass reforming, including decomposition of CH_3OH and the synthesis of CH_3OCH_3 on these catalysts. Finally, BEP relationships for these elementary steps on

pure metals and SAAs were developed to reveal the unique catalytic behavior of SAA materials.

The calculated adsorption energies indicate that for most of the adsorbates discussed in this study, the formation energies on the SAA surfaces lie between those of their monometallic components, except for Ni/Au(111) and Rh/Au(111). Moreover, the binding site preference of oxygenated organic adsorbates is generally determined by the number of dangling bonds in the adsorbate, thereby being subject to simple adsorption valency rules that are generally followed by pure metal surfaces. According to the TCS relations of the formation energy, we find that after replacing the H atom with CH_3, the formation energy of simple oxygenates, including CH_3O, CH_3OCH_2, CH_3OH, and CH_3OCH_3 exhibit a strong linear correlation with the formation energy of the original adsorbate (i.e., OH, CH_2OH, and H_2O) on both pure metals and SAAs.

Compared with pure host metals, our results show that RhAg and NiAg have the potential to selectively catalyze CH_3OH dehydrogenation to CH_2O via CH_3O- and CH_2OH-path, respectively. In addition, by comparing these activities, we determine that SAAs generally exhibit lower apparent activation energies than their pure host metals. Doping Ag(111) with Rh or Ni can significantly increase its activity for CH_3OH dehydrogenation to CH_2O. A concerted step that involves C-H activation in CH_3 and C-O coupling towards CH_3OCH_3 is found on

Ni-, Pt-, and Rh-doped SAAs. In this case, Pd/Au(111) has the lowest apparent activation energy for CH_3OCH_3 synthesis without breaking the C-H bond.

Finally, we built BEP relationships for the bond dissociations on SAAs and pure metals. For C-H and O-H scission in CH_3OH and C-H activation in CH_3O, the SAA BEP relations deviate from and lie below those of the pure metals. In this case, for a given reaction energy, the SAAs can exhibit broadly lower activation energies in comparison to the pure metal surfaces. On the other hand, no clear BEP linear relation is found for either SAAs or pure metals for O-H activation in CH_2OH. The BEP line of the concerted C-O coupling step lies below that of C-O coupling without C-H activation, indicating that Ni-, Pt-, and Rh-doped SAAs provide a lower energy pathway for the C-O coupling by activating the H atoms in CH_3 during the elementary step. Overall, SAAs can combine both weak binding and low activation energy, allowing for optimized catalytic performance.

The data presented in this article, along with our interpretations, will aid in the discovery and development of SAA materials that exhibit unique and exciting catalytic behavior for oxygenate chemistries relevant in the renewable energy and sustainability fields.

Chapter 4 Reactivity Trends in Cu-Based SAA for HCOOH Decomposition

4.1 Introduction

H_2 generation from biomass derived molecules is an attractive strategy for coupling renewable carbon with clean energy carriers.[6, 208] Among small oxygenates accessible from biomass processing, HCOOH is frequently discussed as a practical hydrogen carrier because it is liquid under ambient conditions, can be produced from renewable carbon streams and can, in principle, release H_2 under comparatively mild conditions.[6, 208, 209] Introducing isolated transition metal atoms into coinage metal catalysts to form SAAs is a powerful strategy for boosting both activity and selectivity relative to the corresponding pure metal catalysts.[15] In this project, we will use a combined DFT with KMC framework to investigate the HCOOH dissociation mechanism in copper-based SAAs for HCOOH decomposition.[25, 26, 56, 137, 210-213]

Understanding the catalytic trends of the dissociation of adsorbed HCOOH* species[1*] on Cu-based SAAs requires making a connection between the local environments of atomically dispersed dopants and the measurable reactivity under realistic conditions.[1, 15, 214] In the experiments, no additional CO production was detected beyond background CO, and O-H activation in

[1*] Asterisks denote adsorbed species, and the number of asterisks corresponds the number of dentates for a given adsorbate, e.g. bidentate HCOO would be denoted HCOO**.

HCOOH* occurs already at a very low temperature, indicating that O-H activation is not the RDS.[56] Consequently, this thesis focuses mainly on the HCOO** dehydrogenation step, which is relevant to the experiments, namely the C–H bond scission of adsorbed HCOO** to yield gas phase carbon dioxide CO_2 and surface H*.[214, 215] This focused mechanistic scope enables a clear, quantitative comparison of how isolated dopant atoms (Rh, Ni, Pt, Pd) embedded in Cu(100) modify the energetics of the C–H activation event and how those energetic changes translate into macroscopic behavior such as temperature-programmed desorption (TPD) features[1, 216].

To achieve this, DFT calculations are employed to map the minimum energy pathways for HCOO** C–H activation on Cu(100) and Cu-based SAAs, including the preferred adsorption sites of HCOO**, transition states for C–H cleavage, and final state configurations involving H* and weakly bound CO_2* prior to desorption.[107, 214] Our DFT analysis, reveals a key distinction between monometallic surfaces and single-atom alloys: unlike the pure metal series, the CO* adsorption (formation) energy on the dopant species can serve as an effective descriptor for the HCOO** decomposition barrier on the corresponding SAA.[59, 217] These DFT results also provide the energetic inputs, including adsorbate formation energies, co-adsorption energetics, and activation barriers, needed to parameterize a kinetic model.[25, 137, 218]

Because peak temperatures in TPD from experiments reflect not only a single barrier but also site availability, coverage evolution, and lateral interactions, the DFT energetics are further translated into kinetics using GT-KMC simulations in *Zacros*.[219, 220] The KMC model explicitly represents a large Cu(100) lattice with dilute dopant atoms, includes the elementary steps relevant to HCOO** dissociation and hydrogen evolution, and accounts for short range interactions involving H*.[25, 160] This combined DFT+KMC framework enables direct comparisons with experimental trends, thereby identifying which dopants most effectively promote HCOO** C–H activation.[137, 173]

4.2 Methodology

4.2.1 DFT Calculation

DFT calculations were carried out using the VASP version 5.4.1.[17-19, 97] The RPBE exchange-correlation functional was employed for the calculation of potential energies.[85] PAW potentials were used to efficiently model core electrons, and a cutoff energy of 400 eV was set for the expansion of the wavefunctions of valence electrons.[96, 102] During geometry optimization of surface species configurations, the convergence threshold for solving the electronic problem was fixed at 10^{-5} eV, and the convergence criterion for the ionic relaxation was applied on the Hellmann-Feynman forces on all free atoms, which were converged to values below 0.02 eV/Å. The Brillouin zone sampling utilized a 3 × 3 × 1 Monkhorst-Pack k-point grid. The CG method was used to

identify stable structures. Transition states were initially located using the dimer method and subsequently refined via the quasi-Newton method. Vibrational analyses were conducted to ensure each transition state had only one imaginary frequency.[106, 107] COHP analysis was then performed using LOBSTER, based on VASP calculations carried out with a 13 × 13 × 1 Monkhorst–Pack k-point mesh and symmetry switched off (ISYM = −1); the WAVECAR and related VASP output files were subsequently post-processed in LOBSTER.[105, 122, 221]

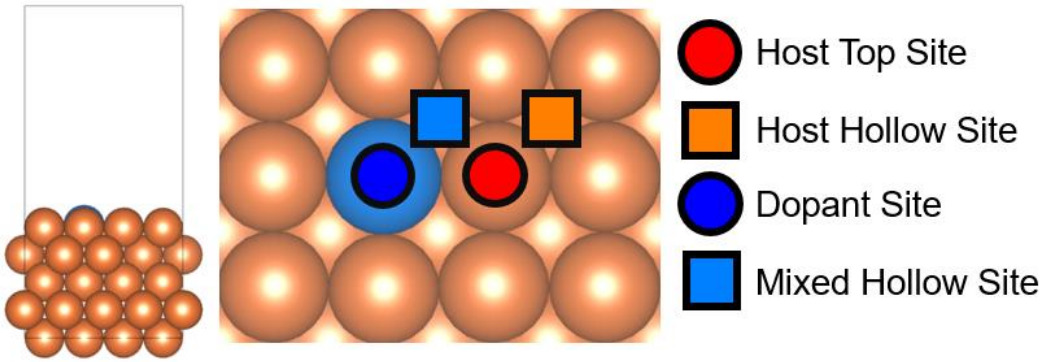


Figure 4. 1 Side and top view of a typical fcc(100) surface structures of RhCu SAA and its different sites. Cu is displayed in brown, Rh in blue.

A 5-layer p(4 × 4) supercell with the top two layers relaxed and the bottom three fixed was used to model fcc(100) surfaces for Cu and Cu-based SAAs (Fig. 4.1). Within each supercell a ~14 Å vacuum layer prevents interactions between periodic images along the direction vertical to the surface. The optimized lattice constant of bulk Cu, obtained using the same computational settings as described above with a denser 7 × 7 × 7 k-point mesh, is 2.60 Å.

4.2.2 KMC Simulation

The simulations of HCOO** dissociation on Cu and Cu-based SAAs were conducted using the GT-KMC framework as implemented in software Zacros (version 3.02) developed by Stamatakis and co-workers.[26, 160, 167, 171-173] In this study, simulations were conducted on a periodic (100) lattice capturing a surface with a total of 10,000 atoms. Each lattice contains 20,000 sites, including 10,000 top sites and 10,000 four-fold hollow sites. Among them, 70 out of 10,000 atoms were randomly chosen as the dopant atoms (including Rh, Ni, Pt, and Pd) to simulate 0.7% dopant coverage in Cu-based SAAs (Fig. 4.2).

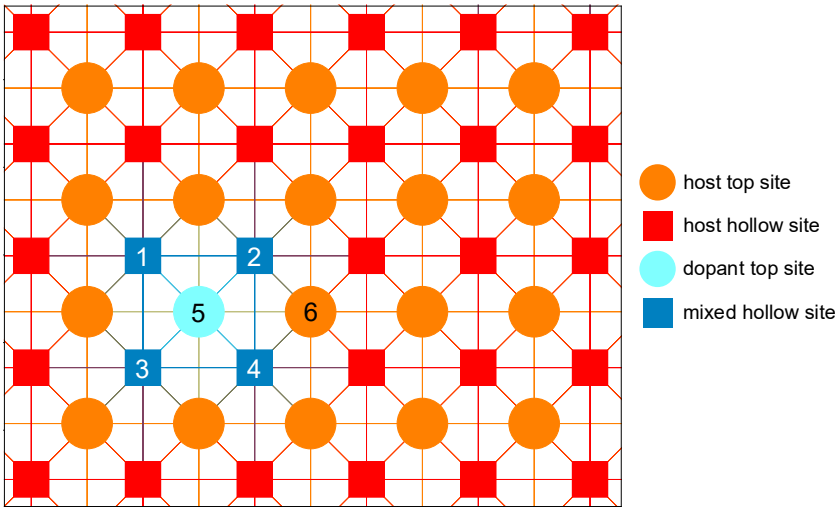


Figure 4. 2 Part of a typical SAA fcc(100) surface used for KMC simulation. Host and dopant top sites are represented by orange and light blue dots, respectively. Host hollow sites and dopant-host-mixed hollow sites are shown in red and blue squares, respectively. The numbers in this figure are used to define energy patterns in Table B1 in Appendix B.

At the initial state of the simulation, 1,000 H* and 1,000 HCOO** adsorbates are randomly seeded on hollow and top-top pairs of sites of the periodic surface,

respectively (HCOO** is treated as a di-σ bidentate species occupying two neighboring top sites).

Because H* preferentially occupies hollow sites located between neighboring top sites, it can influence nearby adsorbates via short-range lateral interactions. Accordingly, we included first nearest neighbor interactions between H* and all relevant adsorbates considered in this work. The corresponding interaction energy patterns and effective cluster interactions are summarized in Table B1 in Appendix B. The full set of elementary steps used in the KMC mode is listed in Table B2 in Appendix B. For each simulation, five independent KMC trajectories were performed, and the resulting spectra were averaged to obtain the final simulated TPD profiles.

4.3 Results and Discussion

4.3.1 Experimental TPD results on HCOOH Decomposition

To provide an experimental reference for the computational analysis, HCOOH* decomposition was examined by TPD on Cu(100) and a set of Cu-based single-atom alloys (SAAs), including PdCu(100), PtCu(100), NiCu(100), and RhCu(100). Note that the experiments in this section were performed by our collaborator Yicheng Wang in the E. C. H. Sykes group at Tufts University. In these samples, a dilute amount of dopant metal (0.7% of a monolayer) was deposited on Cu(100), the surface was cooled, exposed to a small dose of

HCOOH (0.1 L), and subsequently heated while monitoring H_2 (m/z = 2) and CO_2 (m/z = 44) signals. Two temperature regimes are relevant to HCOOH* reactivity, including a lower temperature signal (≈200–250 K) and a higher temperature signal, consistent with sequential surface dissociation in which early stage O–H activation forms surface HCOO**, followed by a higher-temperature C–H activation step that leads to CO_2 formation and hydrogen evolution (Figure 4.3a).[2]

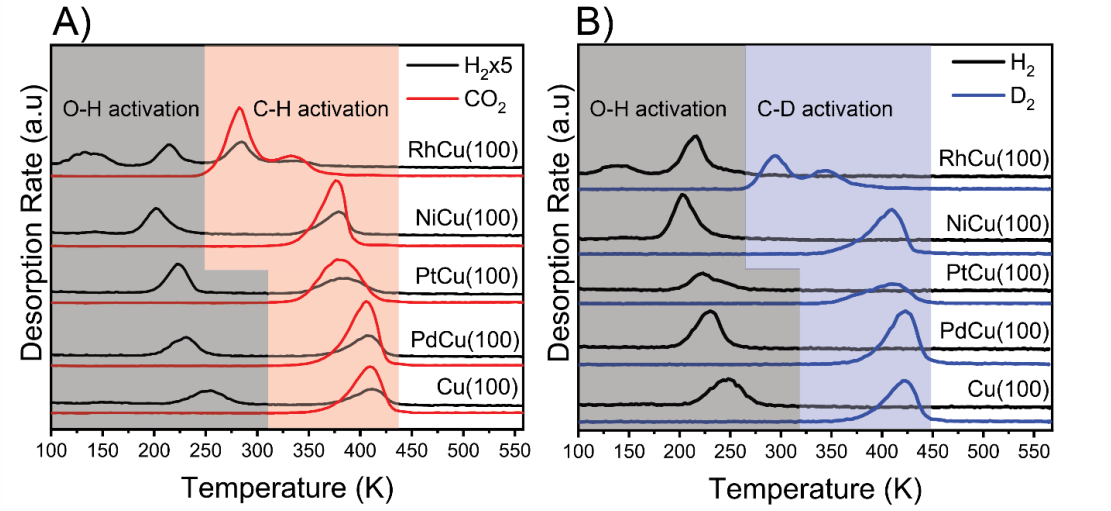


Figure 4. 3 TPD profiles for HCOOH decomposition on Cu(100) and Cu-based SAAs. (A) H_2 (black) and CO_2 (red) signals recorded after dosing HCOOH on Cu(100), PdCu(100), PtCu(100), NiCu(100), and RhCu(100), followed by linear heating. (B) Corresponding isotopic experiment using DCOOH, showing H_2 (black) and D_2 (blue) evolution.

Because molecular CO_2 is weakly bound on these metal surfaces and desorbs readily, the temperature at which CO_2 evolves in TPD primarily reflects the kinetics of the HCOO** C-H activation step rather than CO_2 desorption. The CO_2 evolution temperatures establish a clear reactivity ordering among the investigated surfaces: RhCu(100) > NiCu(100) > PtCu(100) > PdCu(100) >

Cu(100) (Figure 4.3A). Isotopic labeling experiments using deuterated formic acid further support this mechanistic assignment. The corresponding dehydrogenation signal shifts to higher temperature and reveals a distinct C–D activation regime, consistent with C–H cleavage being a key kinetically relevant step (Fig. 4.3B).[2]

These experimental trends are used in this thesis as quantitative benchmarks for the DFT-derived energetics and the subsequent KMC modeling of HCOO** C–H activation on Cu-based SAAs.

4.3.2 DFT Investigations of the HCOO C-H Activation Pathway

To rationalize the experimentally observed behavior at the atomistic level, we used DFT to map the dehydrogenation chemistry of HCOO** on Cu(100) and the selected Cu-based SAAs (including RhCu, NiCu, PtCu, and PdCu). Rather than considering only a single step, we enumerated several key steps along the conversion of HCOO** to gas phase CO_2. Several key configurations are calculated, including bidentate HCOO** bound either across a dopant–host pair or across two host sites, the corresponding transition states for C–H bond cleavage, and post-cleavage states consisting of H* co-adsorbed with CO_2* in both chemisorbed and physisorbed arrangements. We also considered the final state, CO_2(g) + H*, where CO_2 has entered the gas phase while H* remains adsorbed. In addition, subscripts “d-h” are used to label dopant and host

adsorption sites, respectively. For example, HCOO**$_{d–h}$ indicates a di-σ HCOO** species spanning a dopant–host pair. Based on these computed energies, energy diagrams were assembled to enable a direct comparison of C–H activation landscapes across the different SAA compositions (Fig. 4.4).

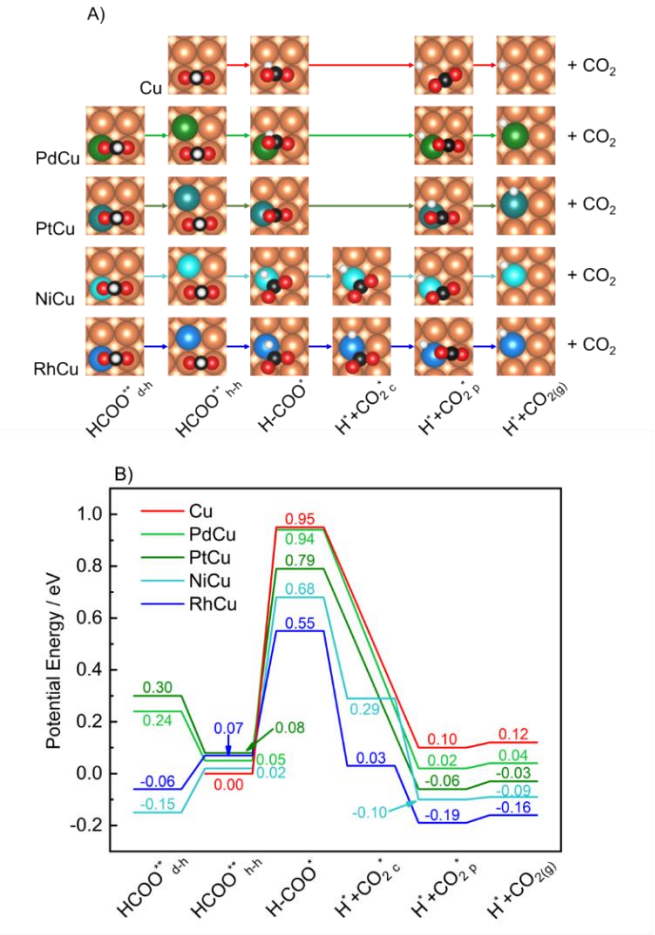


Figure 4. 4 Geometries and energetics for HCOO** dissociation on various SAAs. A) The following HCOO** binding geometries are shown from left to right: di-σ (top-top) on dopant-host sites, proximal di-σ on host-host sites, transition state for C-H scission, final state with chemisorbed CO_2 ($CO_2^*{}_c$), final state with physisorbed CO_2 ($CO_2^*{}_p$), and state after CO_2 desorption. A five-layer slab *p*(4 × 4) unit cell was used in these calculations and only a portion of the cell is shown for clarity. B) Reaction profiles with zero-point energy corrections for the C-H activation step on Cu and Cu-based SAAs. The adsorption energy of HCOO** on pure Cu was chosen as a reference state and the minimum energy pathways are shown.

We began by locating the lowest energy adsorption states of bidentate HCOO** on each surface by comparing computed potential energies. While HCOO** is well known to adopt a di-σ motif on Cu, our results show that the preferred adsorption configuration on Cu-based SAAs is dependent on the dopant atom, with stability shifting between dopant–host ($HCOO^{**}_{d-h}$) and host–host ($HCOO^{**}_{h-h}$) pairs of sites (Fig. 4.4A).[222] DFT results also indicate that Cu–Cu sites adjacent to the isolated dopant bind HCOO** slightly less strongly than Cu–Cu sites far from the dopant (Fig. 4.4A). Hereafter, we refer to these nearby Cu–Cu positions as proximal host sites, and to Cu–Cu sites in the pure Cu region as distal host sites. This weakening of the adsorption on proximal host sites is consistent with the “exclusion-zone” behavior previously reported for SAAs.[223]

Quantitatively, the formate adsorption energy on proximal host sites is higher than on distal ones by 0.07 eV for RhCu(100) and 0.02 eV for NiCu(100) (Fig. 4.4B). For these two alloys, the global minimum corresponds to a mixed dopant–host di-σ HCOO** ($HCOO^{**}_{d-h}$). However, since the C–H activation processes start with HCOO** positioned on a proximal Cu–Cu pair with dopant participation (Fig. 4.4), the adsorbate must first diffuse from $HCOO^{**}_{d-h}$ to the proximal $HCOO^{**}_{h-h}$ state. An uphill thermodynamic cost of 0.13 eV on RhCu(100) and 0.17 eV on NiCu(100) is thus incurred to escape the dopant–host “trap”. In contrast, PdCu(100) and PtCu(100) favor HCOO** adsorption on

distal Cu–Cu sites in the bidentate di-σ configuration; on these SAAs, binding at the mixed dopant–host sites is substantially weaker than at distal Cu sites by 0.30 eV (PdCu) and 0.24 eV (PtCu), respectively (Fig. 4.4B).

Our calculations indicate that HCOO** C–H cleavage proceeds through two distinct types of transition state motifs on Cu(100) and the Cu-based SAAs. Along the reaction coordinate, the bidentate HCOO** first reorients itself such that its molecular plane becomes approximately parallel to the surface (a ~90° tilt), positioning the hydrogen toward the isolated dopant. For RhCu(100) and NiCu(100), C–H activation occurs directly from this “parallel-lying” arrangement, yielding surface H* adatoms and CO_2* in an adsorbed state.

In contrast, on PtCu(100), PdCu(100), and Cu(100), the system continues to evolve beyond the parallel orientation. HCOO** undergoes an additional ~90° rotation about the one of the C–O axis, producing a **“**stood-up**”** geometry in which the molecular plane is roughly perpendicular to the surface and one O points away from the metal, while the H atom remains directed toward the dopant. COHP analysis supports a clear electronic distinction between these motifs. The parallel-lying structures display a stronger interaction between C and dopant than the stood-up transition states (Fig. 4.5).

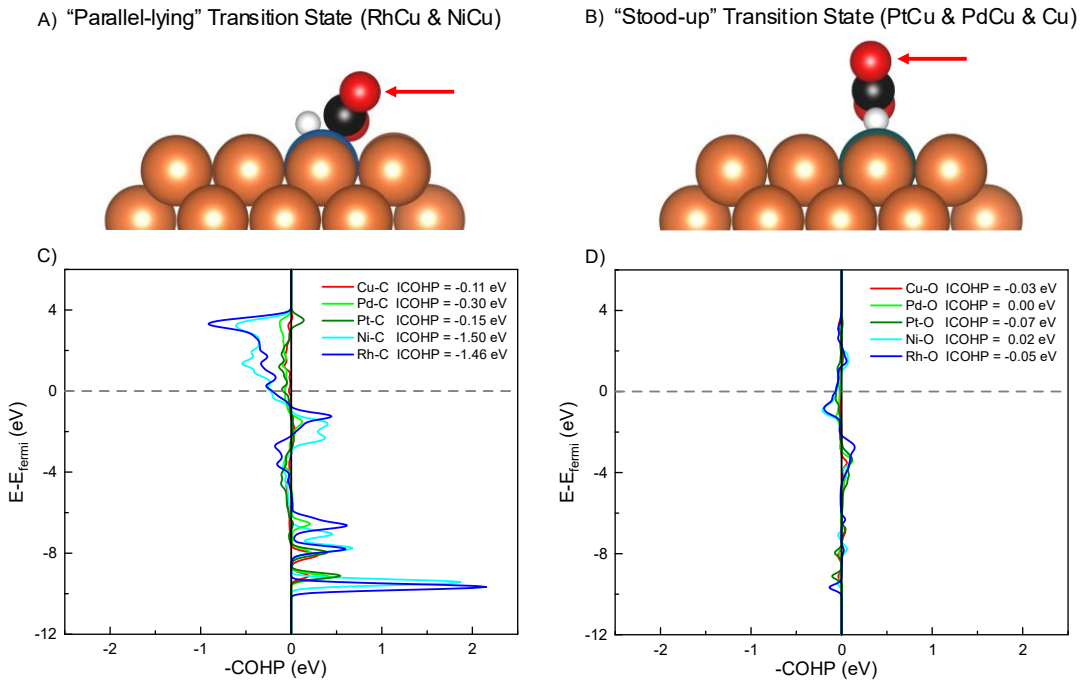


Figure 4. 5 Configurations of "parallel-lying" transition state (A) and "stood-up" transition state (B). The investigated O atoms are marked with red arrows in these figures. COHP of dopant-C bonding (C) and dopant-O bonding (D) of HCOO** adsorbed at dopant sites in Cu-based SAAs. The grey dashed lines mark the Fermi level, serving as the energy boundary separating occupied states (below) from unoccupied states (above).

To quantify how strongly the dopant interacts with the C and O atoms of the reacting HCOO** fragment, we analyzed COHP curves for the relevant bonds (Fig. 4.5).[105, 122, 221] Negative COHP contributions indicate bonding character, whereas positive values reflect antibonding interactions. We report the integrated COHP (ICOHP) evaluated up to the Fermi level; within this convention, more negative ICOHP values correspond to stronger net bonding.

As shown in Fig. 4.5A, the C–dopant interaction is substantially stronger on the alloys that proceed through the parallel-lying transition state motif, including

NiCu(100) and RhCu(100) exhibit ICOHP values of −1.50 eV and −1.46 eV, respectively. By comparison, surfaces associated with the stood-up transition state display much weaker C–dopant bonding, with ICOHP values of −0.15 eV for PtCu(100), −0.30 eV for PdCu(100), and −0.11 eV for Cu(100). This trend is consistent with a larger antibonding contribution in the C–dopant interaction when the system adopts the stood-up transition state geometry. In contrast, Fig. 4.5B indicates that O–dopant coupling is minor on all surfaces examined, with O–dopant ICOHP values below ~0.1 eV, confirming that these interactions are considerably weaker than the corresponding C–dopant bonds. The higher transition state energies on Cu(100), PdCu(100), and PtCu(100) can be interpreted as arising from the energetic cost of the additional rotation and partial loss of the stabilizing C–dopant interaction, leading to less stable C–H scission transition states in these cases (Fig. 4.4A).

For C–H bond cleavage from the di-σ HCOO** geometry located on proximal Cu–Cu pairs, the computed activation barriers decrease in the order: Cu (0.95 eV) > PdCu (0.89 eV) > PtCu (0.72 eV) > NiCu (0.66 eV) > RhCu (0.48 eV) (Fig. 4.4B). This ranking mirrors the experimental CO_2 TPD behavior, particularly the markedly lower CO_2 desorption temperature observed on RhCu, consistent with its substantially reduced C–H activation barrier.

A complication arises for NiCu(100) and RhCu(100) because the

thermodynamic minimum for HCOO** adsorption is not the proximal Cu–Cu configuration but a mixed dopant–host binding state. As a result, HCOO** must first migrate from the dopant associated site to a proximal Cu–Cu pair before entering the C–H scission pathway considered above. Incorporating this diffusion step increases the energetic demand for initiating decomposition on these two surfaces. When the most stable HCOO ** on each surface is taken as the reference initial state, the resulting overall C–H activation energies follow Cu (0.95 eV) > PdCu (0.94 eV) > NiCu (0.83 eV) > PtCu (0.79 eV) > RhCu (0.61 eV), where PdCu and PtCu reference the Cu–Cu-bound HCOO** minima, whereas NiCu and RhCu reference the dopant–host minima (Fig. 4.4B).

This trend for the activation barriers is different from the previously discussed one, based on the $HCOO^{**}_{h\text{-}h}$ configuration, with NiCu and PtCu changing places (Fig. 4.4B), and it is also different from the experimental results. Nevertheless, the separation between NiCu and PtCu is small (≈0.05 eV), suggesting that their TPD peak temperatures should be close and potentially indistinguishable within typical experimental resolution for CO_2 desorption, which is in line with the TPD experimental result.

Following C–H cleavage, the newly formed H* relocates to different favorable adsorption sites depending on the alloy composition: on PtCu(100) it preferentially occupies a dopant–host bridge position, whereas on the other

SAAs it gets stabilized in a mixed fourfold hollow site. The accompanying CO_2 product interacts only weakly with Cu(100), PtCu(100), and PdCu(100), remaining essentially linear and largely physiosorbed with minimal geometric perturbation. By contrast, on RhCu(100) and NiCu(100) the CO_2^* can transiently adopt a bent, chemisorbed structure with C–O–C angle ≈ 130° before relaxing toward a physiosorbed state (Fig. 4.4A), in agreement with earlier observations reported for (111) facets.[59, 60]

Importantly, the CO_2 adsorption pattern depends on the local hydrogen coverage. On RhCu and NiCu, when three or more H* adatoms populate neighboring hollow sites around a top site CO_2* species, the bent chemisorbed configuration does no longer exist and CO_2 becomes physiosorbed instead (Table B1). Using the proximal HCOO**$_{h–h}$ state as the reference, the reaction energy for forming H + CO_2* (physiosorbed) follows the sequence Cu (0.10 eV) > PdCu (−0.03 eV) > NiCu (−0.12 eV) > PtCu (−0.14 eV) > RhCu (−0.26 eV) (Fig. 4.4B), consistent with the trends discussed for the activation energetics. Finally, once CO_2* is in the physiosorbed state, desorption proceeds with only very small barriers on all SAAs, typically 0.01–0.03 eV (Fig. 4.4B).

Notably, the DFT-derived HCOO** dissociation energy barrier on SAAs ordering differs markedly from the activation energy trend reported for the corresponding pure metals (Pt(111) > Pd(111) > Rh(111) > Ni(111)).[16] This contrast highlights

that reactivity on SAAs cannot be inferred by simply transferring activity rankings from monometallic surfaces.

For pure metals, the established barrier ordering is generally consistent with BEP linear scaling behavior,[48-51] where increasingly exothermic reactions are often accompanied by reduced activation barriers. In pure metals, variations in the reaction energy are dominated by differences in the adsorption strength of HCOO** (in initial state) and H* (in final states), since HCOO** binding changes substantially across metals. The situation is fundamentally different on SAAs: the relevant C–H activation event occurs from di-σ $HCOO^{**}_{h–h}$ located on proximal Cu–Cu pairs, giving rise to closely comparable initial states across different dopant identities (Fig. 4.4B). Consequently, changes in the overall thermochemistry across SAAs are governed more strongly by the energetics of H* stabilization in final states than by differences in the HCOO**-involved initial state. Prior analyses have shown that adsorbed H* on SAAs can exhibit bonding characteristics similar to those found for CO* in SAA environments.[216] In the following section, we will discuss in more detail the relationship between CO* formation energy and the HCOO** C-H activation barrier on SAAs.

4.3.3 CO Formation Energy as Activity Descriptor for C-H Activation

DFT results show that the C–H activation barriers correlate linearly with the corresponding reaction energies for both monometallic surfaces and SAAs,

consistent with BEP relationship.[47-51] The fitted BEP relationships are strongly linear, with R^2 = 0.922 for the pure metal set and R^2 = 0.949 for the SAA set (Fig. 4.6A). A key distinction, however, is that on SAAs the bidentate HCOO** intermediate is predicted to diffuse from the dopant adsorption configurations onto nearby host-host (Cu–Cu) sites before C–H scission occurs. Once in this host proximal configuration, the isolated dopant can directly assist the C-H bond breaking event (Figs. 4.3A for SAAs and 4.7A for pure metals).

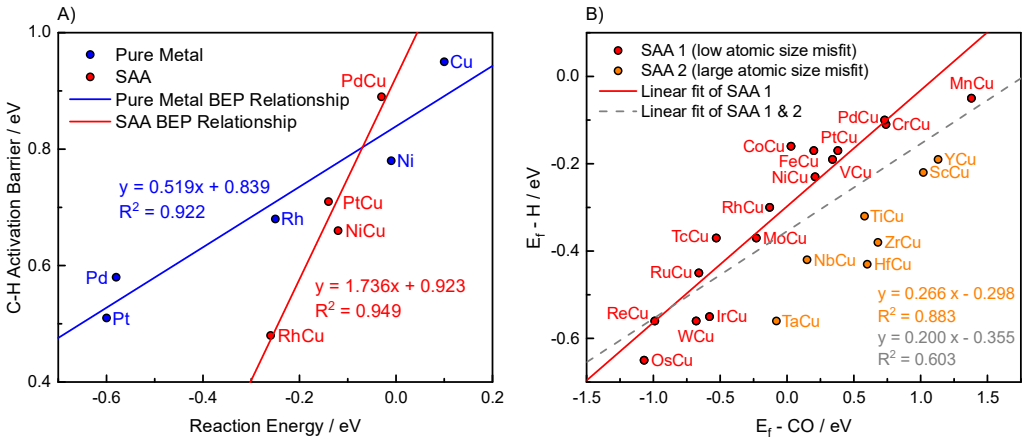


Figure 4. 6 A) BEP relationships for C–H activation in HCOO** on pure metal (blue) and SAA (red) (100) surfaces. The plots show the activation energy as a function of the reaction energy. B) TCS relations of the formation energy E_f corresponding to fragments of H* vs CO* bound in the most stable adsorption site on SAAs with low atomic size mismatch (red) and all SAAs (grey).

Prior work has shown that the vicinity of an isolated dopant in an SAA often forms an “exclusion-zone” environment in which adsorbates bind slightly less strongly than on the pristine host surface.[223] As a result, the reactant initial states relevant to HCOO** decomposition on different SAAs are energetically similar, because the HCOO** configurations reside on comparable proximal

host sites near the dopant. Under these similar initial state conditions, the linear BEP trend obtained for the SAA set implies that the C–H activation barrier varies approximately linearly with the reaction energy; equivalently, the barrier can be viewed as correlating with the formation energy of the products when the reactant reference is effectively fixed (Fig. 4.6A). In each of the systems considered, the product CO_2* in the final state is weakly bonded, so its contribution to the final state formation energy is small. Consequently, the potential energies of the final states are governed mainly by the stability of H*. Motivated by this observation, we further examine the formation energetics of H* and compare them with those of CO*.

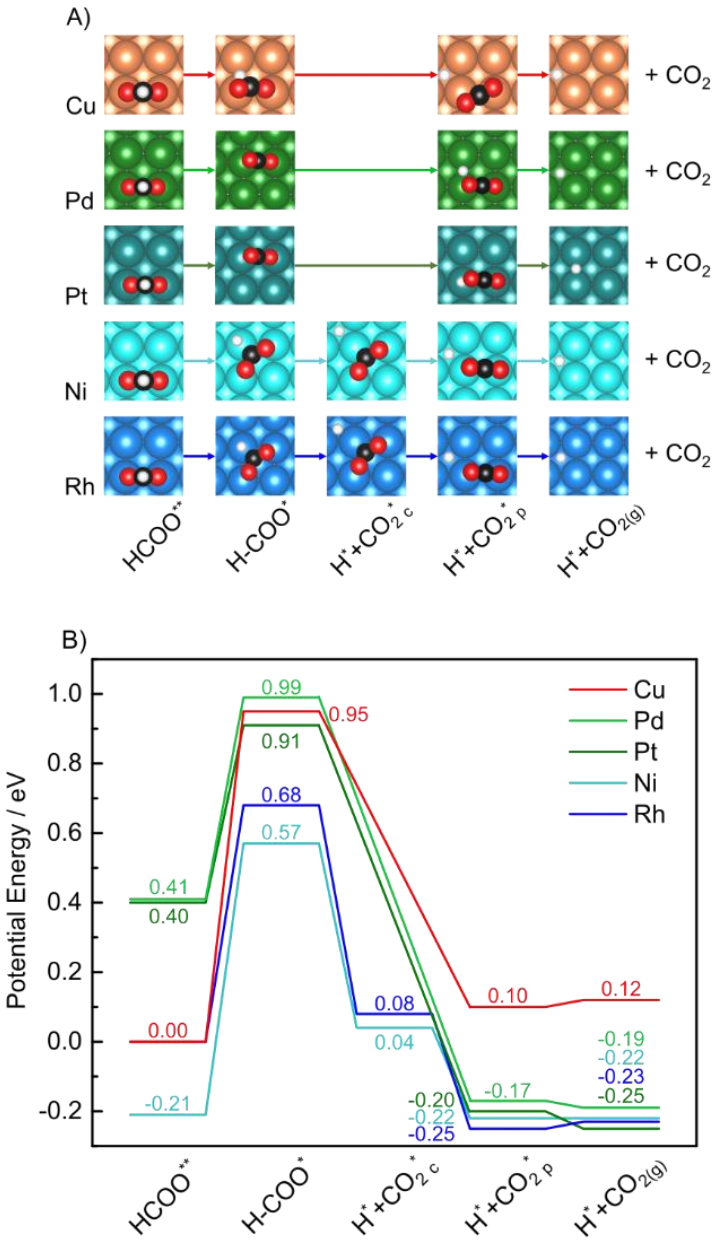


Figure 4. 7 Geometries and energetics for HCOO** dissociation on various pure metals. A) The following HCOO** binding geometries of are shown from left to right: di-σ (top-top) configurations, transition state for C-H scission, final state with chemisorbed CO_2 ($CO_2^*{}_c$), final state with physisorbed CO_2 ($CO_2^*{}_p$), and state after CO_2 desorption. B) Reaction profiles with zero-point energy corrections for the C-H activation step on pure metals. The adsorption energy of HCOO** on pure Cu was chosen as a reference state and the minimum energy pathways are shown.

We note that, for some SAAs, the formation energies of H* and CO* deviate from the expected linear correlation, leading to a relatively low overall

coefficient of determination (R^2 = 0.603, Fig. 4.6B). However, we also found these cases are mostly associated with dopants from the larger-sized transition metal atoms. In this work, we evaluate the atomic size mismatch between the host and dopant metals using Eq. (4.1) and find that SAAs with larger deviations generally exhibit a larger atomic size mismatch.[224] In this case, the linear relationship becomes stronger as we increase the atomic size mismatch criteria. For example, the R^2 is increased to 0.883 if we only consider SAA with lower than 10% mismatch (Fig. 4.6B).

$$\delta = \frac{2 \times |r_a - r_b|}{(r_a + r_b)} \times 100\ \% \qquad (4.1)$$

The deviation from the linear trend may arise from the following reason. Because H* on SAAs preferentially adsorbs at dopant-host-mixed hollow and bridge sites, its adsorption is jointly influenced by both the dopant atom and the Cu host. When the dopant atom is oversized and protrudes from the surface, it makes these “mixed sites” more dopant-dominated in terms of the local environment. This distortion can preferentially stabilizes H*. We therefore attribute these outliers to oversized dopants that protrude from the surface, which perturbs nearby H* adsorption on mixed sites and lowers its formation energy (Fig. 4.8).

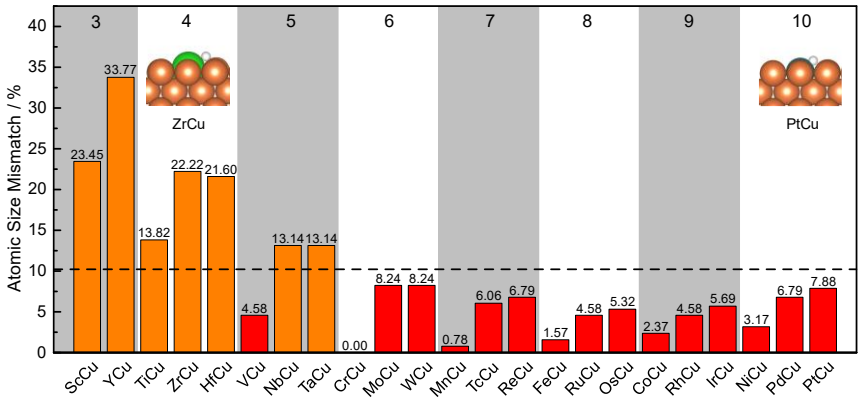


Figure 4. 8 Atom size mismatch for different SAAs. Orange bars indicate SAAs with large size mismatch. Note that the formation energies of H^* and CO^* on these SAAs obviously deviate from the expected linear correlation. Red bars indicate SAAs with small size mismatch.

For the pure metals examined here (with Pt, Rh, Ni, and Pd dopants), the final state formation energies span a much narrower range compared to initial states. Under these conditions, differences in the predicted barriers can be interpreted primarily as reflecting variations in the initial state, leading to an effective linear dependence of the barrier on the adsorption energy of HCOO** for dopant set.

For pure metals, extensive prior work has shown that the initial state (HCOO**) energetics do not follow a simple linear relation with respect to the adsorption energy of CO*.[51, 225, 226] More generally, linear scaling relations are most reliable when comparing adsorbates that interact with the surface through similar binding motifs and the same anchoring atoms. Because CO* and bidentate HCOO** attach to metals in fundamentally different ways, a robust scaling relation between their energetics is not expected. Moreover, on pure metals the final state energies can vary even more widely than in the subset considered

here, which further limits the universality of the CO* adsorption energy as a descriptor for the HCOO** C-H activation barriers. Taken together, these considerations indicate that CO* formation energy is not a suitable HCOO** dissociation activity descriptor for the pure metals.

4.3.4 KMC Simulations of HCOO Dissociation on SAAs

4.3.4.1 TPD Spectra of H_2 and CO_2 Desorption on SAAs

A simple way to relate experimental TPD measurements to kinetics is to apply the Redhead analysis, which estimates an activation energy from the peak desorption temperature, typically assuming a chosen pre-exponential factor and first order kinetics. Because it requires only the TPD peak position and the heating rate, Redhead-derived barriers are often used as a simple benchmark for comparing reactivity trends across surfaces or catalysts before moving to more detailed microkinetic treatments.

However, comparison between DFT-derived elementary step barriers and activation energies extracted from TPD via the Redhead method should be treated with caution. The Redhead approach assumes that a single rate-determining process controls the peak temperature, whereas real catalytic surfaces can exhibit multistep networks, competing channels, and coverage dependent behavior. In addition, the apparent desorption temperature can be shifted by site availability, evolving surface coverages, and lateral interactions,

none of which are captured by the Redhead analysis.[49, 57, 216]

To incorporate these effects and enable a more meaningful comparison with experiments, we employed the GT-KMC framework to explicitly simulate TPD spectra.[26] This framework provides a bridge from DFT energetics to experimentally measurable macroscopic TPD signals by accounting for the stochastic sequence of elementary events on a lattice, thereby connecting atomistic reaction energetics to the observed temperature-dependent product evolution.

In the SAA models, 70 of the 10,000 surface atoms were assigned as dopants at random, corresponding to a 0.7% dopant concentration in the Cu(100) layer. All KMC runs started from an initial temperature of 100 K to reflect the low temperature conditions prior to the temperature ramp. For TPD KMC simulations, defining an initial surface configuration that matches the experimental situation is essential. Experimentally, HCOOH* dissociates at a low temperature (≈100 K), whereas H–H recombination becomes significant only at higher temperatures (typically ~200 K). We therefore initialized the lattice with pre-formed HCOO** and H*, using equal starting coverages σ expressed as adsorbate to total surface atom ratios $\sigma_H = \sigma_{HCOO} = \frac{1000}{10000} = 10\%$.

KMC simulations based on the DFT energetics in Fig. 4.9 predict CO_2

desorption peak (black and red lines in Fig. 4.9A) that appear systematically at lower temperatures than those measured experimentally (arrows in Fig. 4.9A). For all SAAs except RhCu(100), the simulated CO_2 peaks are 67–81 K below experiment (Table B3 in Appendix B and Fig. 4.9).

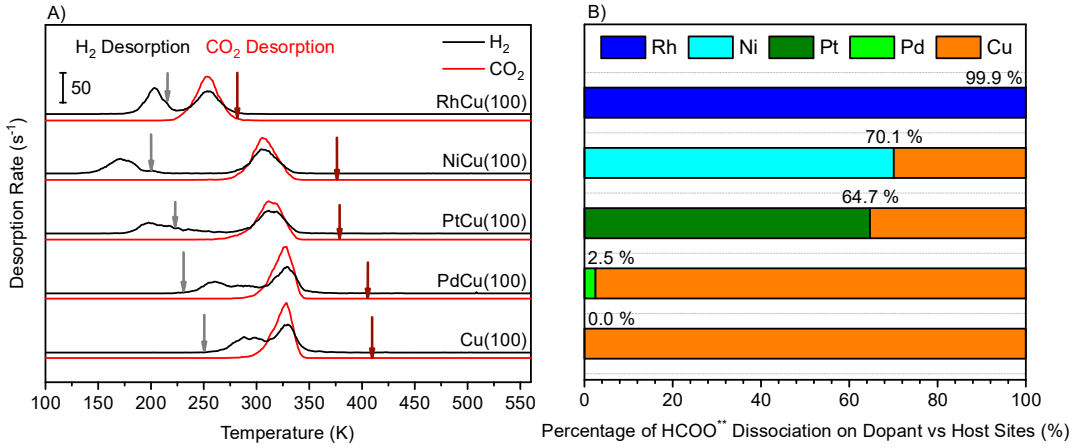


Figure 4. 9 (A) The simulated TPD spectra of H_2 and CO_2 desorption on lattices. The simulated TPD spectra of H_2 (black line) and CO_2 (red line) desorption on lattices, with the arrows indicating experimentally observed peak temperatures. (B) a bar chart showing the percentage of HCOO** dissociation on dopant versus host sites. These results are obtained from simulations using activation energies calculated by DFT.

This discrepancy is primarily due to errors caused by the GGA exchange-correlation functional for calculating C-H activation barriers in HCOO**, which can underestimate activation barriers for bond-breaking steps such as C–H scission in bidentate HCOO** due to self-interaction error.[227, 228] To mitigate this systematic bias, we apply a uniform +0.20 eV adjustment to the computed C–H activation barriers of HCOO** on every surface. With this correction, the discrepancy between simulated and experimental CO_2 peak temperatures is reduced to within ~35 K across the catalyst set (Fig. 4.10A).

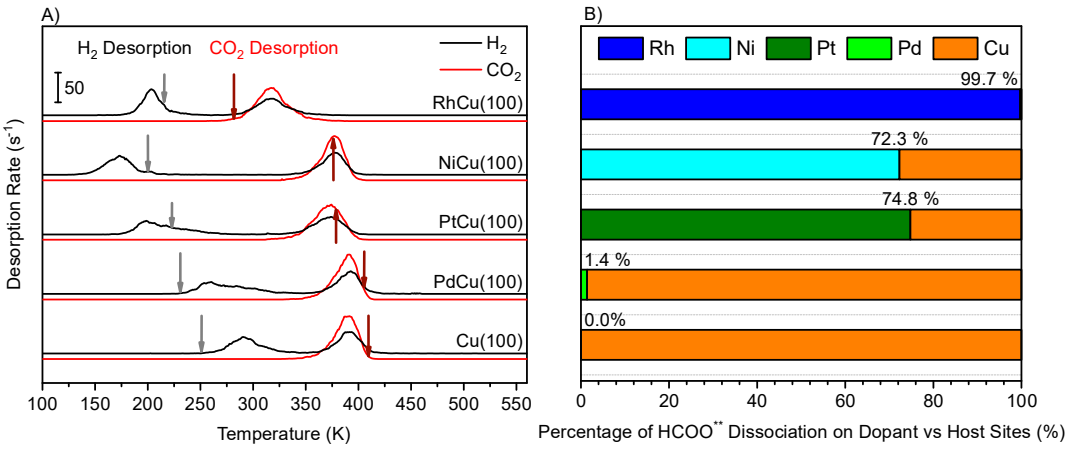


Figure 4. 10 KMC simulated HCOOH* dissociation processes starting with $\sigma_H = \sigma_{HCOO}$ = 0.1 on Cu and Cu-based SAA surfaces. A) Simulated TPD spectra of H_2 (black line) and CO_2 (red line) desorption on lattices, with the arrows indicating experimentally observed peak temperatures. B) Bar chart showing the percentage of HCOO** dissociation on dopant sites. These results are obtained from simulations using the modified C-H activation energies, originally calculated by DFT and subsequently increased by 0.2 eV.

Focusing on the H_2 signals first (black lines), the low-temperature peak shown in Fig. 4.10A represents the desorption of H_2 from the pre-exist H* on each surface. On Cu(100), this peak occurs at 287 K, which is at least 90 K higher compared to those of the SAAs (except for PdCu, where it is ~30 K higher), indicating that all the dopant atoms have the potential to catalyze H_2* associative desorption. The results of KMC simulations also indicate that most of the H_2 (>98%) forms on the dopant top sites for RhCu, NiCu, and PtCu, while for PdCu(100) only ~50% of the H_2 is produced from Pd (Fig. 4.11).

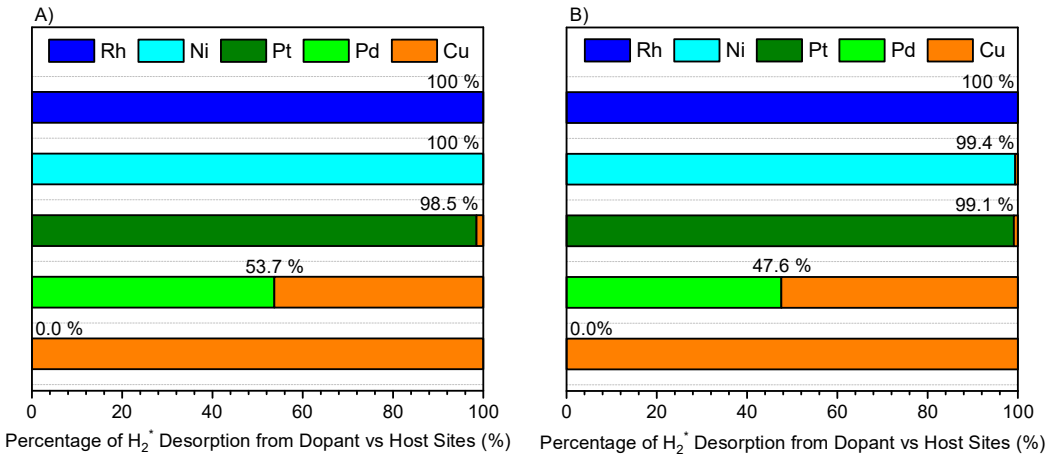


Figure 4. 11 Bar charts showing the percentage of H_2 formed and desorbed from dopant versus host sites according to the KMC simulation (A) without and (B) with the 0.2 eV correction, respectively.

This behavior can be traced to the comparatively large barrier for associative H_2* desorption at Pd top sites (0.68 eV), which is only 0.10 eV lower than the corresponding barrier on Cu(100). Thus, while Pd is intrinsically more active than Cu for H–H recombination, the scarcity of Pd sites in the dilute alloy surface relative to the overwhelming number of Cu sites indicates that a substantial fraction of H_2* still forms on the host. As a result, PdCu(100) shows an approximately even contribution of dopant versus host mediated H_2* production (Fig. 4.11).

Once the majority of surface H* has been removed via H_2* desorption, CO_2 production proceeds through HCOO** dissociation. The KMC simulations allow us to quantify where these C–H scission events occur, and the resulting dopant versus host site contributions for C-H scission are summarized in Fig. 4.10B. In general, a lower CO_2 peak temperature corresponds to a larger dopant site

share. For RhCu(100), C-H scission on dopant site dominates the chemistry, accounting for 99.7% of the HCOO** C–H activation events and giving a CO_2 peak at 318 K. By contrast, on PdCu(100) the decomposition occurs primarily on Cu host sites, which explains why PdCu(100) and Cu(100) display nearly indistinguishable CO_2 peak positions (≈390 K for both). For NiCu(100) and PtCu(100), the dopant contribution is intermediate and comparable. 72.3% and 74.8% of HCOO** species undergo C–H cleavage at Ni and Pt sites, respectively, consistent with their similar intrinsic C–H barriers (Fig. 4.10B). The dopant/host partitioning of C–H scission events follow the same ordering as the CO_2 evolution peak temperatures. This consistency indicates that C–H activation is the RDS for HCOO** decomposition across the investigated SAAs.

4.3.4.2 The Effect of Residual H* for Decomposition of HCOO

The observed barrier for HCOO** C–H cleavage is not just equal to the zero-coverage activation energy of this step. Because of lateral interactions between the reactant HCOO** and spectators, which appear in random configurations in the reaction neighborhood, there is a distribution of HCOO** C–H activation energies over the surface; thus, the barrier is subject to coverage effects. Such coverage effects can be incorporated in a simplified manner through a BEP scaling that relates changes in reaction energetics to changes in the corresponding activation barrier. Within this framework, the instantaneous HCOO** C-H activation rate is governed by (i) the zero-coverage limited DFT-

derived reference barrier for C–H activation and (ii) the H* coverage on mixed hollow sites, which controls both site availability and interaction strength. In the following, we examine how residual H* coverage reshapes the dominant reaction pathway and apparent kinetics on each SAA composition.

The KMC results indicate that NiCu(100) enters the HCOO** C–H scission temperature region with an essentially H* free surface. Because associative H_2* desorption occurs at a comparatively low temperature (~170 K) on NiCu, hydrogen produced during HCOO** decomposition is removed rapidly as H_2, leaving little residual H* to perturb subsequent C–H activation events. A similar situation applies to PtCu(100). Throughout the decomposition window, the H* population on mixed hollow sites remains modest (typically <25%), so lateral interaction effects on C–H cleavage are limited. For PdCu(100), HCOO** decomposition is dominated by the Cu host sites; consequently, occupation of mixed hollow sites is not a controlling factor, and variations in mixed site H* coverage do not substantially alter the overall reaction kinetics.

In contrast, on RhCu(100) the simulations with the uncorrected GGA energetics (without the +0.2 eV barrier adjustment) suggest that HCOO** C–H cleavage can begin while a substantial fraction of H_2 evolution is still ongoing. In this case, the onset of HCOO** dissociation overlaps with the H* removal stage, as illustrated in Fig. 4.12A. The dopant-host mixed hollow sites, which serve as

the binding location of H* generated during C-H dissociation, are partially occupied by pre-existing H* adatoms. When the HCOO** decomposition begins, the coverage of H* on mixed hollow sites is approximately 50%, followed by a gradual decrease to 0% as temperature increases (Fig. 4.12A).

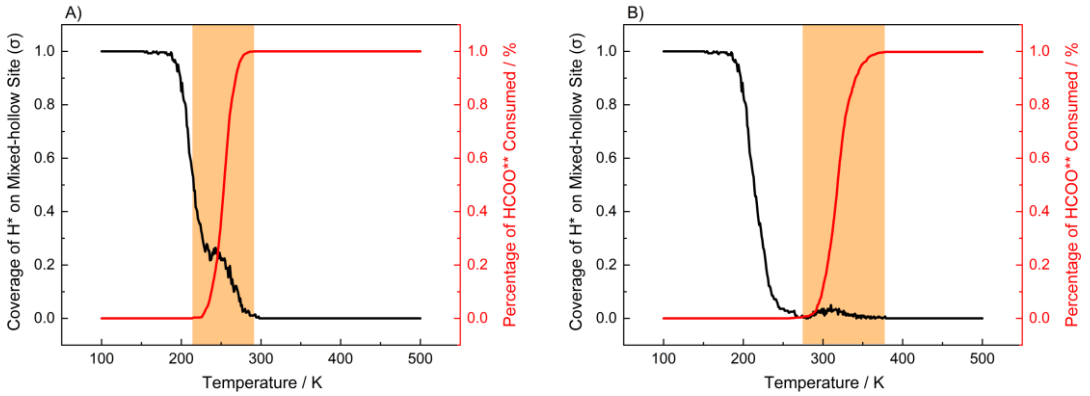


Figure 4. 12 Coverages of H* (black) and percentage of HCOO** consumed (red) on the RhCu(100) surface as functions of temperature for (A) without and (B) with 0.2 eV correction, respectively. The orange region shows the temperature range for HCOO** C-H activation.

Clearly, H* adatoms are not removed from the surface quickly enough, and thus C–H scission commences before the pre-adsorbed H* has fully recombined and desorbed as H_2. Residual H* therefore persists on the surface and preferentially occupies mixed hollow sites, effectively reducing the availability thereof. Under such conditions, repulsive lateral interactions between H* and CO_2* raise the potential energy of the final state, thereby increasing the effective barrier for C–H activation. Importantly, starting the simulation without pre-adsorbed H* does not eliminate this inhibitory effect, because H* generated during ongoing HCOO** decomposition can also populate hollow sites and reintroduce site

blocking, suppressing subsequent C–H scission events (Fig. 4.13A).

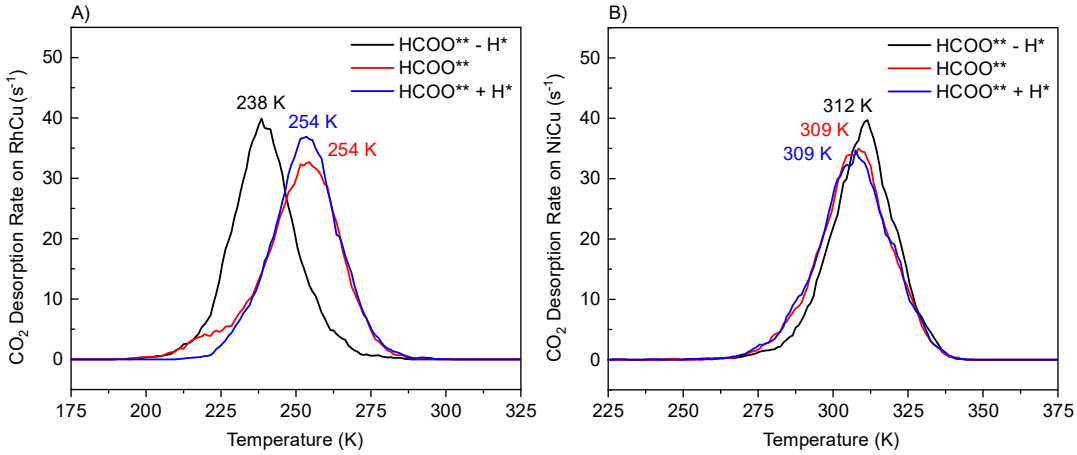


Figure 4. 13 The simulated TPD spectra of CO_2 desorption starting with σ_{H^*} = 0.1 excess H* (blue), without pre-existing H* (red), and with hypothetical fast H_2 desorption (black) on (A) RhCu(100) and (B) NiCu(100) lattices. To simulate a scenario where H* produces H_2* and desorbs from the surface rapidly (black), the dissociation reactions for KMC simulations on both dopant and host sites have been altered to ensure that no H* is generated (HCOO** → CO_2*). Note that the simulations in this figure do not include the 0.2 eV correction to the energetics obtained from the GGA functional.

This interpretation is corroborated by the three RhCu(100) KMC simulations shown in Fig. 4.13. The red trace corresponds to a run initialized without pre-existing H*; the blue trace includes an excess hydrogen coverage ($\sigma_{H^*} = 0.1$) at the start; and the black trace represents an idealized case in which H* formed during decomposition is removed immediately as H_2, implemented by modifying the dissociation steps so that no surface H* is produced (HCOO** → CO_2*).

The red and black curves overlap at early times because the surface is initially free of excess H*. As the reaction proceeds, however, H* accumulates in the simulation that produced the red curve, and the associated blocking effect

emerges, causing the red curve to drift toward the blue one. In the idealized rapid hydrogen removal limit (black), the CO_2 peak occurs ~13 K earlier than in the presence of pre-existing H*, directly demonstrating the inhibitory role of H* on the decomposition kinetics. These results further imply that catalyst performance could be enhanced if a faster pathway for H_2 release were available. By contrast, on NiCu(100) the peak positions in the three corresponding simulations remain nearly unchanged (Fig. 4.13B), consistent with the much lower H* coverage during the C–H activation regime on that surface.

4.3.5 Effect of van der Waals Corrections

Because this study hinges on relatively small energy differences among adsorption motifs and on correctly distinguishing physisorbed versus chemisorbed states, dispersion interactions are expected to contribute non-negligibly to the computed energetics. We therefore used the van der Waals corrected exchange–correlation functional optB86b-vdW to generate the energetic inputs for the KMC model, including stable and transition state formation energies.[84, 87, 189, 190] For the key step of C–H scission in HCOO**, optB86b-vdW yields the same qualitative ordering as RPBE, namely RhCu < NiCu < PtCu < PdCu < Cu (Fig. 4.14). Note that, similar with RPBE, to mitigate this systematic bias, we apply a uniform +0.2 eV adjustment to the computed C–H activation barriers of HCOO** on every surface. Consistent with this

agreement at the DFT level, KMC simulations parameterized with the optB86b-vdW dataset also reproduce the same reactivity trend (Fig. 4.15).

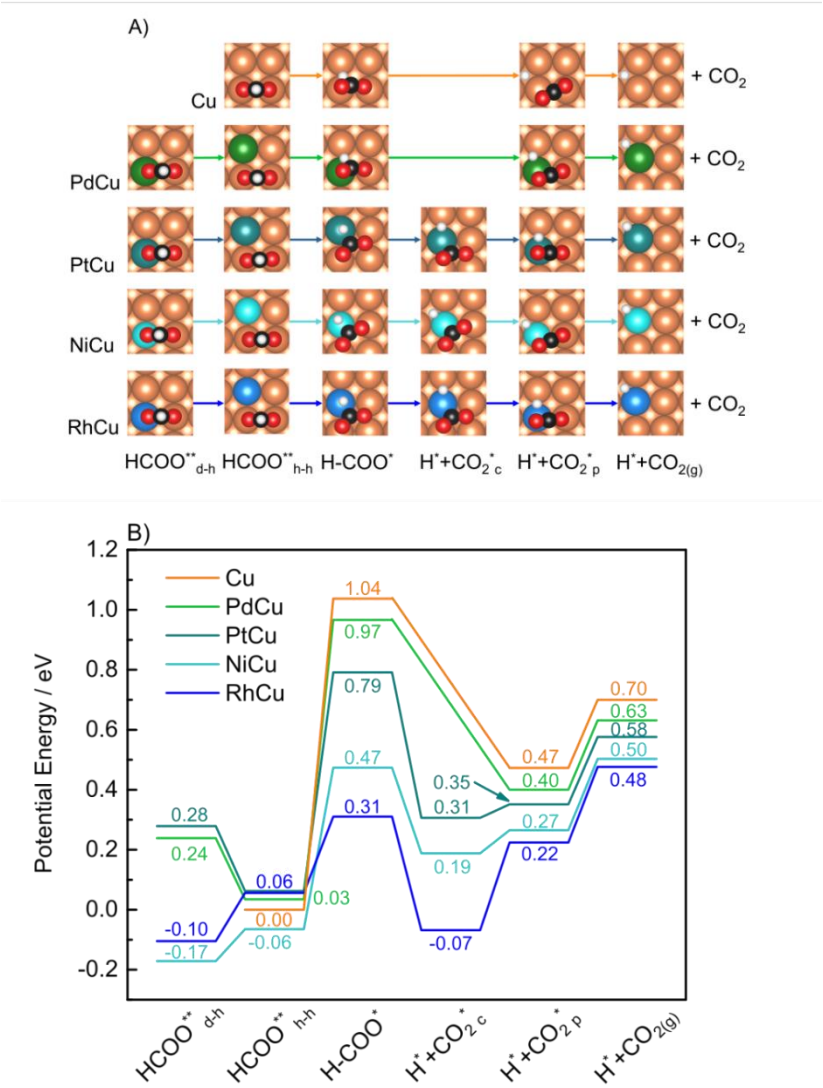


Figure 4. 14 Geometries and energetics for formate dissociation on various SAA systems calculated using optB86b-vdw functional. A) The following geometries of formate are shown from left to right: bound to the dopant-host di-σ site, bound to the host-host di-σ site, transition state for C-H scission, final state with chemisorbed CO_2 ($CO_2^*{}_c$), final state with physisorbed CO_2 ($CO_2^*{}_p$), and state after CO_2 desorption. A five-layer slab was used in these calculations along with a p(4 × 4) unit cell. Only a portion of the cell is shown for clarity. B) Reaction profiles with zero-point energy corrections for the C-H activation reaction on Cu and Cu-based SAAs. Only the minimum energy paths are considered in each case.

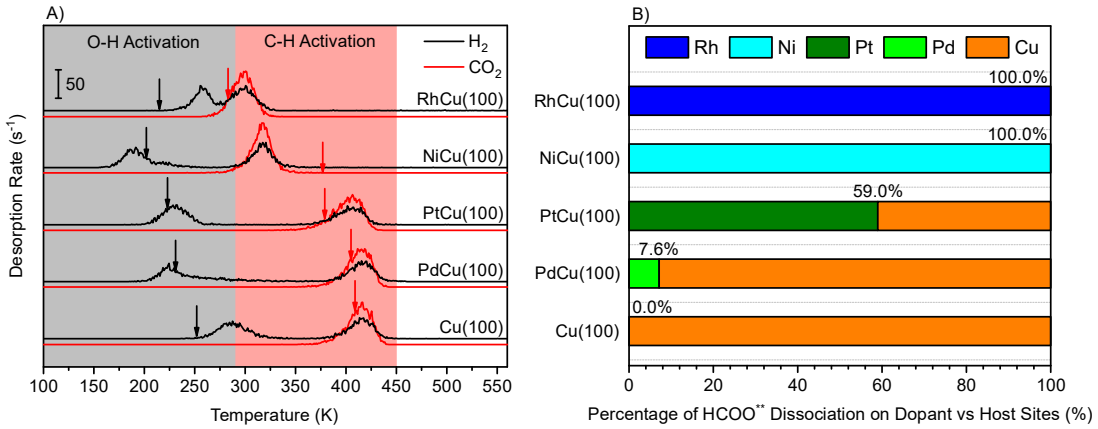


Figure 4. 15 KMC-simulated HCOO** dissociation processes starting with $\sigma_H = \sigma_{HCOO} = 0.1$ on Cu and Cu-based SAA surfaces. A) Simulated TPD spectra of H_2 (black line) and CO_2 (red line) desorption on lattices, with the arrows indicating experimentally observed peak temperatures. B) Bar chart showing the percentage of HCOO** dissociation on dopant sites. These results are obtained from simulations using the modified C-H activation energies, originally calculated by DFT with the optB86b-vdw functional and subsequently increased by 0.2 eV.

However, to ensure a consistent and physically meaningful description of HCOO decomposition on Cu-based SAAs, the RPBE functional was adopted in this work instead of optB86b-vdW. Although optB86b-vdW functional follows the trend calculated from RPBE and experimental results, our tests showed that it fails to reproduce the experimentally observed peak on NiCu. This suggests that, for HCOO** decomposition on NiCu, the optB86b-vdW functional does not provide a sufficiently reliable energetic description of the reaction network, even when the key barrier is altered. For this reason, RPBE was retained as the more appropriate functional for the present mechanistic and kinetic analysis.

4.4 Conclusion

This project established a picture for HCOO** decomposition to gas phase CO_2 and H_2 on Cu(100) and Cu-based SAAs with Rh, Ni, Pt, and Pd as the minority components (dopants). Guided by the experimental observation that no HCO/CO-formation channel is active under the relevant conditions, the study focused on the dehydrogenation of C–H activation in bidentate HCOO** governs CO_2 and H_2 evolution.

DFT calculations revealed that alloying at the single-atom limit reshapes both adsorption energies and transition state structures along the HCOO** dissociation pathway. Two distinct C–H scission transition state configurations were identified on SAAs: a parallel-lying geometry (favored on RhCu and NiCu) which exhibits strong C–dopant interaction, and a stood-up geometry (Cu, PdCu, PtCu) in which that interaction is weaker, consistent with COHP analysis. When C–H cleavage is referenced from the reactive proximal Cu–Cu configuration, the intrinsic barriers follow Cu > PdCu > PtCu > NiCu > RhCu, rationalizing the promoting effect of Rh and Ni on the HCOO** C–H activation.

In addition, the project provided a descriptor-level interpretation for SAAs. Because initial states for C–H activation are relatively similar across dopants (host-like proximal configurations), barrier variations are strongly influenced by final state energetics dominated by H* stability. In this regime, the CO*

formation energy on SAAs can serve as a practical descriptor for HCOO** decomposition barriers, whereas the same descriptor is not generally transferable to monometallic systems.

Finally, to bridge atomistic energetics with experimental observables, KMC simulations were performed using DFT formation energies, barriers, and short-range lateral interactions on large Cu(100) lattices with 0.7% randomly distributed dopants. KMC reproduced the experimentally observed activity ordering for CO_2 evolution and provided site resolved mechanistic evidence that C–H activation is the RDS across the SAA series. The simulations further showed that H* coverage can inhibit HCOO** decomposition through site blocking and lateral interactions (most prominently on RhCu when C–H scission overlaps with incomplete H_2 removal) while NiCu and PtCu remain comparatively insensitive due to low H* coverage during the C–H regime. Overall, the DFT+KMC workflow explains SAA reactivity trends and suggests that improving hydrogen removal can further enhance HCOO** to H_2 performance.

Chapter 5 Secondary Dopants Boost SAA Reactivity by Scavenging CO

5.1 Introduction

SAAs offer a powerful route to tune catalytic activity and selectivity by isolating reactive dopant atoms within a largely inert host.[15] In HCOOH decomposition on Cu-based SAAs, the RDS is C-H activation in HCOO**, followed by the evolution of CO_2 and H_2 evolution as discussed in Chapter 4.[2] A persistent limitation, however, is CO poisoning.[57] CO* can bind strongly to dopant sites and thus rapidly deactivate the active dopant top sites intended to promote C-H bond activation.[57, 223] It is therefore essential to understand how CO* migrates, and under what conditions it desorbs in the gas phase, especially when multiple dopant species coexist on SAAs.[15, 57, 59]

In this chapter, we develop a DFT + GT-KMC framework to connect atomistic energetics to experimentally observed TPD behavior and to establish the concept of secondary dopants as CO* “scavengers” that protect the active dopant site.[25, 26, 56, 137, 210-213] DFT is used to construct the potential energy landscape that involves elementary steps controlling CO* dynamics on Cu-based bimetallic SAAs (with Rh, Ni, Pt, and Pd as dopant metals), including diffusion between Cu sites, dopant–host diffusion steps, and CO* desorption. These calculations indicate that CO* diffusion barriers among Cu sites are small and that barriers for dopant–host diffusion steps can be seen as controlled by

the difference of the formation energies on the dopant and host sites. The relative stability of CO* on dopant sites of SAAs follows the trend: Rh > Ni > Pt > Pd, and CO* is least stabilized on the Cu host.

Next, we built lattice models for two-dopant SAAs (TD-SAAs), including RhNiCu, RhPtCu and RhPdCu, and performed KMC simulations to explicitly track CO* diffusion and desorption as a function of increasing temperature in a simulated TPD setup. We then used HCOO** decomposition to CO_2* as a chemically relevant probe reaction to validate how changes in the population of accessible active sites affect reactivity under CO* containing conditions on (100) surfaces of TD-SAAs. These simulations reproduce the experimentally observed "double-peak" feature in the CO_2 desorption signals, theoretically proving that the secondary dopant sites can act as CO* "scavengers" that protect an active Rh site. This insight suggests that deliberately introducing a secondary dopant can regulate CO* trapping and release, thereby offering a design principle for mitigating CO*-induced deactivation in SAA catalysts.

5.2 Methodology

5.2.1 DFT Calculations

All DFT calculations followed the same protocol reported in Chapter 4, Section 4.2.[2] In brief, computations were carried out using VASP 5.4.1 with the RPBE exchange–correlation functional and PAW pseudopotentials. A 400 eV energy

cutoff was applied to the plane wave basis.[17-19, 96, 97, 102] Surface models were represented by five-layer *p*(4×4) fcc(100) slabs, separated by approximately 14 Å of vacuum; the upper two layers were fully relaxed, while the bottom three layers were kept fixed. Brillouin-zone sampling was performed using a 3 × 3 × 1 Monkhorst–Pack k-point mesh. Self-consistent electronic iterations were converged to 10^{-5} eV, and structural optimizations were terminated when Hellmann–Feynman forces were below 0.02 eV $Å^{-1}$. Stable structures were identified by the CG method. Transition states were searched by the CI-NEB method or the dimer method before refining them with the quasi-Newton method.[106, 107] Frequency tests were then applied to validate these states by ensuring each transition state only has one imaginary frequency.

5.2.2 KMC Simulation

CO* diffusion and HCOO** decomposition on Cu-based bimetallic SAAs and TD-SAAs were simulated using the GT-KMC approach as implemented in *Zacros* v4.0, developed by Stamatakis and co-workers.[26, 160, 167, 171-173]

5.2.2.1 Cu-based Bimetallic SAAs

All SAA calculations were performed on a periodic fcc(100) lattice representing a surface containing 10,000 metal atoms (Fig. 5.1B-C). The corresponding lattice comprises 20,000 adsorption sites, namely 10,000 top sites and 10,000 fourfold hollow sites. To model dilute SAAs, 70 out of the 10,000 top sites

representing surface atoms were assigned as dopants (including Rh, Ni, Pt, or Pd) using random substitution, corresponding to a dopant concentration of 0.7% (Fig. 5.1B-C), while the other top sites were Cu host atoms.

5.2.2.2 Cu-based TD-SAAs

The TD-SAA simulations employed the same lattice size containing 10,000 metal atoms. Two dopant species were introduced by random substitution. Out of the 10,000 top sites representing metal atoms 7 were selected as the primary dopant (Rh, $\sigma = 0.07\%$), and 50 were selected as the secondary dopant (Ni, Pt, or Pd, $\sigma = 0.5\%$) (Fig. 5.1A), while the rest were Cu host atoms.

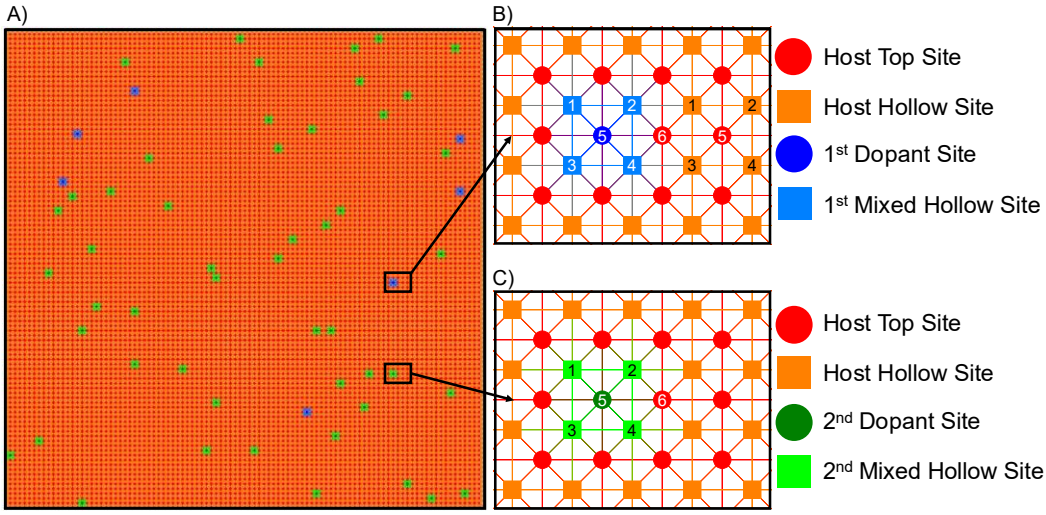


Figure 5. 1 (A) A typical TD-SAA fcc(100) surface used for KMC simulation in this work, including two parts of TD-SAA for1st (B) and 2nd (C) dopant region. Host, 1st and 2nd dopant top sites are represented by red, blue, and blue dots, respectively. Host hollow sites and 1st and 2nd dopant-host-mixed hollow sites are shown in orange, light blue, and light green squares, respectively. The numbers in this figure are used to define energy patterns in Table S2.

The corresponding energy patterns and ECIs are summarized in Table B1 in Appendix B.[2] The full set of elementary steps used in the KMC model is listed in Table B2 in Appendix B. For each simulation, three independent KMC trajectories were generated, and the resulting spectra were averaged to obtain the final simulated TPD profiles.

5.3 Results and Discussion

5.3.1 Experimental TPD Results

In Project 4, we investigated the decomposition behavior of HCOOH on a series of bimetallic SAAs.[2] When these bimetallic SAAs are extended to TD-SAAs containing two different dopant metals, an unusual double-peak feature emerges in the TPD profiles for HCOOH* decomposition on TD-SAAs (Fig. 5.2). Note that the experiments in this section were performed by our collaborator Yicheng Wang in the E. C. H. Sykes group at Tufts University.[3] Comparisons of the experimental TPD spectra of CO_2* evolution from HCOOH* were performed for a set of RhXCu(100) TD-SAAs, where the Rh and secondary dopant X (Pd, Pt, or Ni) loadings were held constant (0.07% Rh and 0.5% X). Under identical HCOOH* dosing and TPD conditions, a pronounced low temperature CO_2 signal (~283 K) was detected on RhNiCu(100) and RhPtCu(100), whereas RhPdCu(100) did not exhibit this low temperature peak (Fig. 5.2).[3]

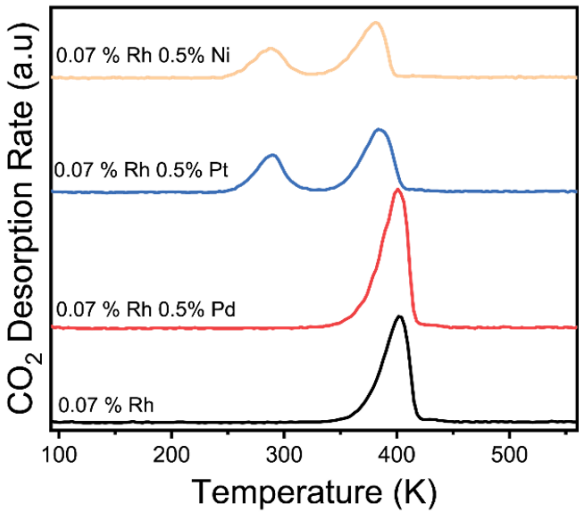


Figure 5. 2 TPD spectra of CO_2 evolution from HCOOH* decomposition on RhCu, RhNiCu, RhPtCu, and RhPdCu. Each surface was exposed to 0.1 L of HCOOH at 90 K.

The experimental TPD results indicate that CO_2 desorption ceases temporarily after ~300 K on RhNiCu and RhPtCu, and further CO_2 desorption (attributed to the decomposition of the remaining HCOOH*) is only observed when the temperature reaches ~500 K. In Chapter 4, we calculated the decomposition temperatures of HCOO** on bimetallic SAAs.[2] The two decomposition temperatures observed on TD-SAAs (i.e., 283 K and 374 K for RhNiCu) coincide with the HCOO** decomposition temperatures on two corresponding bimetallic SAAs (283 K and 377 K for RhCu and NiCu, respectively). In this case, it is reasonable to infer that Rh becomes deactivated upon heating for some reason, so that only a fraction of HCOO** is converted via Rh sites. As the temperature increases further, HCOO** enters the regime where it can be decomposed on the secondary dopant sites, giving rise to the second peak. Experimentally, background CO* is also known to be a common poisoning

impurity; we therefore hypothesize that CO*-induced deactivation of Rh is the primary origin of the shutdown of the catalytic activity of the Rh site and, ultimately, the observed double-peak behavior.[3]

Motivated by these measurements, the following section uses GT-KMC simulations to provide a molecular-level understanding of the double-peak behavior by explicitly tracking the redistribution of CO* adsorbates among the two types of dopant sites, as well as the host sites.

5.3.2 Mechanistic Studies of CO Desorption on SAAs

To elucidate the surface chemistry of CO* on TD-SAAs, we first carried out DFT calculations for the key elementary steps in which only CO* participates on bimetallic SAAs. The resulting energetics are used to construct the corresponding reaction energy profiles (Fig. 5.3A).

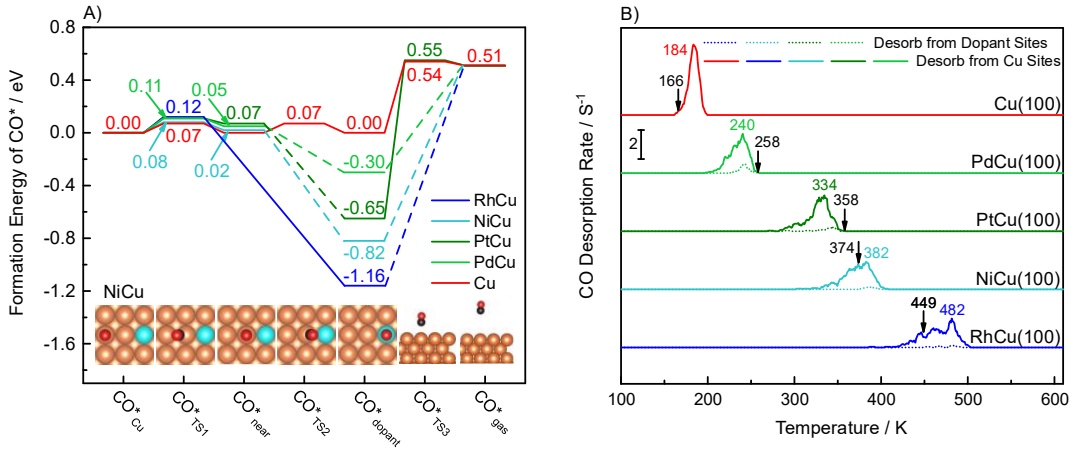


Figure 5. 3 (A) Reaction profiles with zero-point energy corrections for the CO* diffusion and desorption steps on Cu and Cu-based bimetallic SAAs. The adsorption energy of CO^* on pure Cu was chosen as a reference state. Note that the transition states whose barrier are lower than 0.01 eV are not shown in this figure. Instead, their initial and final states are connected by dashed lines. (B) the TPD of CO from bimetallic SAAs. CO* adsorbate are only seeded on the dopant sites at the beginning of the simulation. Solid lines represent CO* desorbed from host sites after a diffusion, and dotted lines represent CO* directly desorbing from dopant sites. The black arrow shows the experimental TPD peak.

To clarify how CO* desorbs from bimetallic SAAs, we first computed the diffusion and desorption energetics that define the CO* energy landscape (Fig. 5.3A). Because an "exclusion-zone"[223] region exists around the dopant, the reference pathway was initiated from third nearest neighbor host sites, ensuring that the DFT profile starts from a host-like environment and can fully consider effects stemming from the perturbed proximal region (Fig. 5.3A). The calculated barriers for Cu–Cu CO* diffusions in the dopant vicinity are uniformly small, with the corresponding transition states (CO^*_{TS1}) spanning only 0.07–0.12 eV. Likewise, host to dopant diffusion barriers (CO^*_{TS2}) are extremely low for all SAAs, typically ≤0.01 eV, indicating the barrier of this step is controlled by the difference of the CO* formation energy between dopant and host.

Thermodynamically, CO* stability on dopant top sites follows the formation energy ordering Rh > Ni > Pt > Pd, while CO* is least stabilized on the Cu host with the highest formation energy. For the CO* desorption step, the computed transition state energy is basically the same as the energy of gas-phase CO, so the reaction energy is a good approximation of the true activation barrier. The only deviations are PtCu and Cu, where small additional barriers of approximately 0.04 eV and 0.03 eV, respectively, are obtained for the desorption transition state (CO^*_{TS3}).

Using the DFT-derived energetic landscapes, we next carried out KMC simulations to identify the dominant CO* desorption pathway on each bimetallic SAA. To approximate the experimental dopant dilution, the lattice model contained 10,000 Cu host atoms with 70 dopant atoms, corresponding to a 0.7% dopant concentration. To emulate experiments in which CO is initially bound to dopant sites, we placed 70 CO* species exclusively on the dopant top sites at the start of the simulations.

As shown in Fig. 5.3B, the computed CO* desorption temperatures track the relative stability of CO* on the available sites. Importantly, CO* does not prefer to desorb directly from dopant sites. Instead, the majority of CO* first migrates from dopant sites onto the Cu host and then desorbs from the host sites (solid

curves in Fig. 5.3B). This behavior indicates that diffusion steps control the overall CO* removal kinetics on these SAAs. CO* desorption is limited by hops to adjacent host sites on the surface, which rationalizes the observed ordering in the desorption temperatures across the bimetallic alloys.

5.3.3 Initial Distribution of CO on TD-SAA Surfaces

To interpret the transient CO* behavior on TD-SAAs, it is first necessary to determine the initial site population at the onset of the temperature ramp. DFT indicates that CO* binds most strongly to Rh compared with the secondary dopants (Ni, Pt, or Pd). Further, we assume that the CO* coverage does not exceed the number of Rh sites and neglect the possibility of di- or multi-carbonyl formation; within these assumptions, the global thermodynamic minimum corresponds to CO* occupying essentially all Rh sites. In experiments, however, the system does not necessarily begin in this equilibrium configuration, as the CO* are introduced on the surface at low temperatures (~100 K).[3] In this case, CO* mobility is strongly hindered once trapped by any secondary dopant, so the surface can become kinetically trapped in metastable states. For this reason, the true initial CO* distribution must be established by additional KMC simulations that explicitly account for limited diffusion during the early stage of TPD progress.

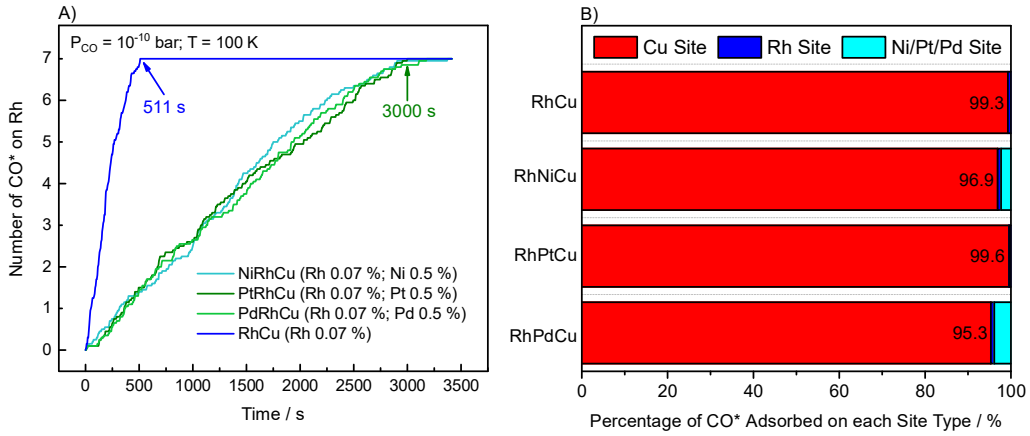


Figure 5. 4 KMC results for clean surfaces under low CO* pressure (1×10^{-10} bar) at 100 K on each TD-SAA and on RhCu SAA. (A) Time evolution of the number of CO* on Rh sites. The arrows indicate (i) the first time at which CO* fully covers Rh sites on RhCu and (ii) 3000 s. (B) Percentage of CO* adsorbed on each site type for each catalyst. Red, blue, and light-blue bars correspond to CO* adsorbed on Cu, Rh, and the secondary dopant (Ni, Pt, or Pd), respectively. The bar chart shows the time immediately after all the dopant site have been blocked. Note that the percentages are computed once Rh and the secondary-dopant sites are fully covered. The model surface contains 10,000 Cu sites, of which 50 are replaced by the secondary dopant and 7 by Rh. Each KMC simulation is repeated 20 times, and results are averaged.

To probe how CO* initially accumulates on these alloy surfaces, we carried out KMC simulations starting from clean SAA or TD-SAA lattices and fixing the temperature to a low value of 100 K, which is the initial temperature of the experimental TPD. The CO partial pressure was fixed to a low value of 10^{-10} bar, and only CO* adsorption and diffusion events were allowed (Fig. 5.4A). For the bimetallic RhCu (blue line), the simulations show that Rh sites become completely CO*-covered after roughly 511 s, indicating rapid loss of Rh-site availability. When a second dopant is introduced, the onset of full Rh site blocking is markedly delayed. Across the TD-SAA set, the time required to reach complete Rh site deactivation increases to approximately 3000 s at 100

K (Fig. 5.4A).

We next analyzed where adsorption occurs during this early stage (Fig. 5.4B). Most CO adsorption takes place on Cu host sites. Our calculation indicates that the propensity of CO adsorption on Cu ($k_{Cu}^{ads} = 1.95 \times 10^{-6} s^{-1}$) is similar to those on other dopant sites at 100 K ($k_{Rh}^{ads} = 6.40 \times 10^{-5} s^{-1}, k_{Ni}^{ads} = 1.74 \times 10^{-5} s^{-1}, k_{Pt}^{ads} = 5.73 \times 10^{-7} s^{-1}, k_{Pd}^{ads} = 2.58 \times 10^{-5} s^{-1}$) Although at 100 K the CO adsorption probability on Cu is nearly the same as that on dopant sites, the host sites dominate numerically (Cu : dopant > 200 : 1), the initial CO* population is still overwhelmingly Cu-based. On RhCu, CO* that lands on Cu migrates rapidly to the Rh trap, ultimately poisoning all Rh sites. For TD-SAAs, however, the CO* initially adsorbed on Cu can be trapped by the secondary dopant because multiple dopant sites are available. Additional KMC analysis is therefore needed to determine the preferred diffusion pathways and identify which dopant sites ultimately accumulate CO* during under transient conditions.

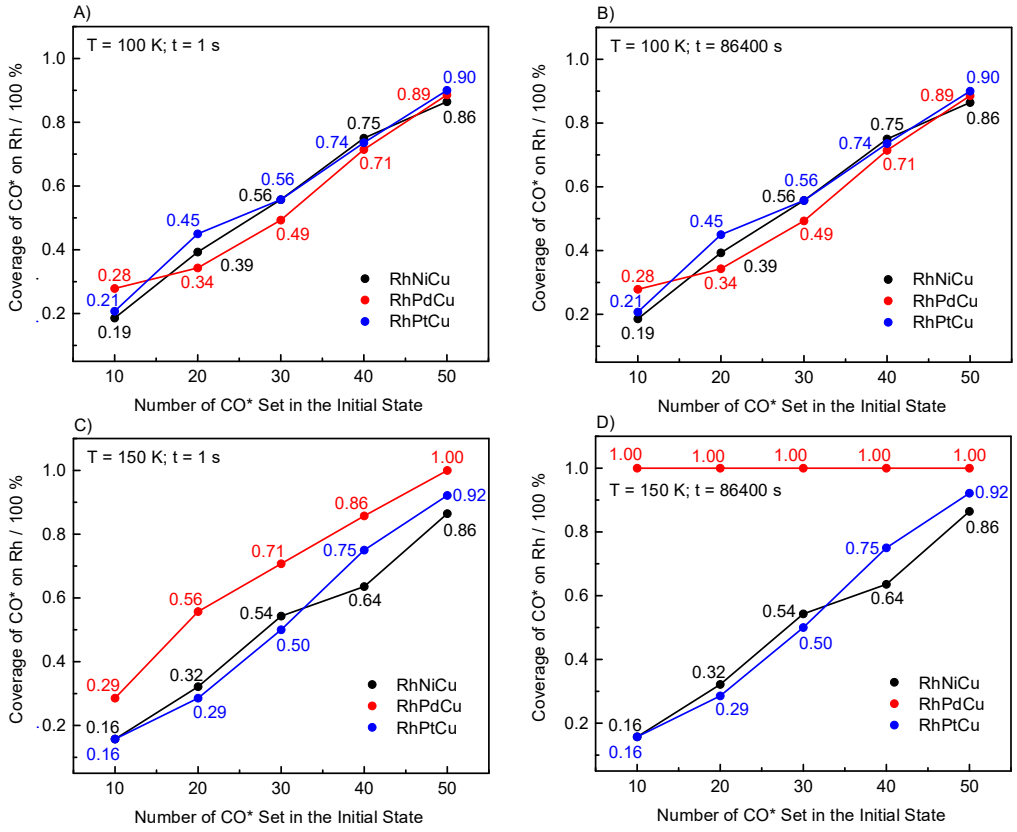


Figure 5. 5 CO* coverage on Rh site profiles with respect to number of pre-existing CO* on the Cu sites at 100 K after (A) 1 s and (B) 86400 s, and at 150 K after (C) 1 s and (D) 86400 s on each TD-SAA. The coverage is normalized with respect to the number of surface Rh atoms, and thus, the maximum coverage is 100 %, when all hollow sites are covered. Each KMC simulation is repeated 20 times, and the results are averaged.

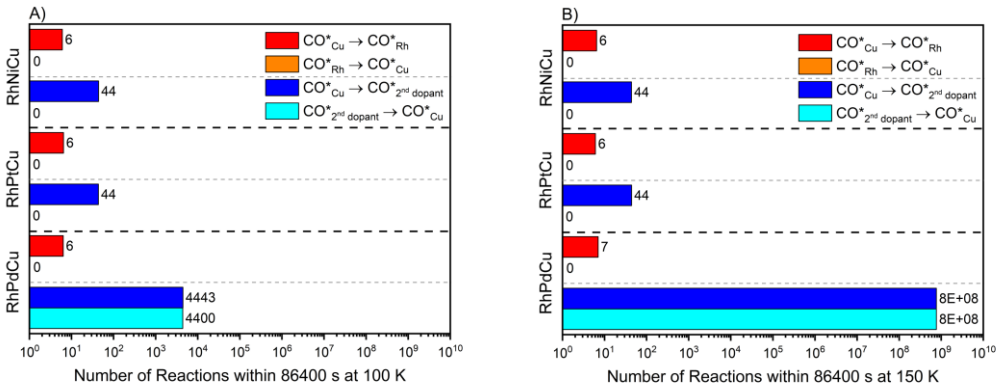


Figure 5. 6 Reaction occurrence statistics of the KMC model after 86400 s at different temperatures: (a) 100 and (b) 150 K. The red and orange bars represent CO* diffusion between Cu and Rh. The blue and light blue bars represent CO* diffusion between Cu and the secondary dopants. Each KMC simulation is repeated 20 times, and results are averaged.

To determine how CO* redistributes among dopants on TD-SAAs at low temperatures, we initialized the lattice by placing varying numbers of CO* randomly on Cu host sites only and then held the system to a fixed temperature of 100 K or 150 K for an extended period (1 day = 86,400 s of simulated time) without gas phase CO. Panels A and B of Fig. 5.5 report representative snapshots taken at 1 s and at 86,400 s for each condition. At 100 K, CO* initially residing on Cu can rapidly migrate to dopant sites and become trapped on both the Rh and the secondary dopant within the first second. Event auditing during the trajectories further shows that, on RhNiCu and RhPtCu, dopant-to-host back-diffusion does not occur even once over the full 24-hour simulation window (Fig. 5.6A).

Given the small host site diffusion barriers (Fig. 5.3A), CO* explores the host lattice efficiently until it encounters a dopant trap. Our calculations indicate that the propensities of CO diffusion between Cu sites ($k_{Cu}^{diff} = 8.83 \times 10^{7} s^{-1}$) are much higher than those from dopant sites to Cu ($k_{Rh}^{diff} = 1.27 \times 10^{-47} s^{-1}, k_{Ni}^{diff} = 1.96 \times 10^{-30} s^{-1}, k_{Pt}^{diff} = 7.51 \times 10^{-22} s^{-1}, k_{Pd}^{diff} = 8.93 \times 10^{2} s^{-1}$). Once captured at 100 K, it remains immobilized on the dopant site for the remainder time of the simulation. Under these conditions, CO* has comparable likelihood of being captured by Rh or by the secondary dopant, implying that the steady CO* coverage on the primary dopant should be

approximately equal to that on the secondary dopant (Fig. 5.7).

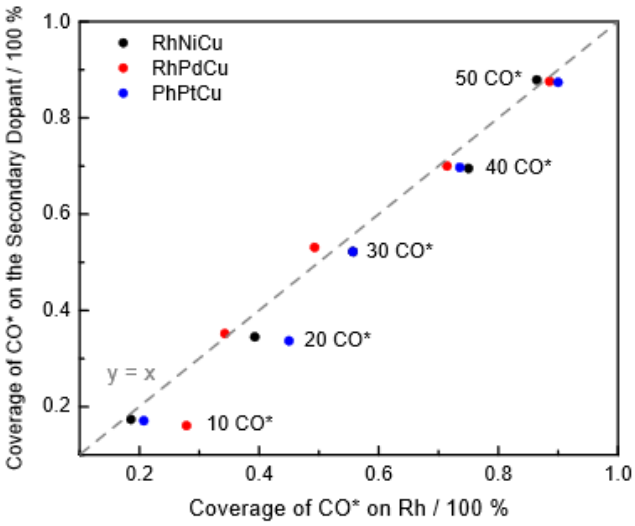


Figure 5. 7 Parity plot of the coverage of CO* on Rh versus coverage of CO* on the secondary dopant at 100 K after 86,400 s. The black, red, and blue dot represent RhNiCu, RhPdCu, and RhPtCu respectively. The black labels indicate the numbers of CO* adsorbate molecules on Cu at the beginning of the simulations. The coverage is normalized with respect to number of surface Rh and secondary dopant atoms, respectively.

Raising the temperature to 150 K leads to qualitatively different CO* redistribution behavior, most notably for RhPdCu (Fig. 5.5C-D). In the RhPdCu case, CO* begins to preferentially accumulate on Rh shortly after the simulation starts, and after 24 h essentially all Rh sites become CO-covered, indicating substantial poisoning. By contrast, for RhPtCu and RhNiCu, the dopant-site populations remain effectively unchanged over the full simulation window, showing that Rh does not experience progressive blocking under the same conditions (Fig. 5.5C-D). This divergence can be attributed to the comparatively weak CO* trapping ability of Pd on the TD-SAA. The event statistics reveal

frequent back-diffusion from Pd to Cu host sites over the course of the run (Fig. 5.6B), indicating Pd releases CO* more readily than the Pt or Ni dopants. Once liberated onto the host lattice, CO* can again diffuse between Cu sites and ultimately be captured by Rh, thereby poisoning the Rh active sites, which then are no longer available for HCOO** dissociation.

Taken together, the DFT energetics and KMC trajectories show that site distribution of CO* at the low temperature is governed primarily by kinetic trapping rather than by thermodynamic equilibration. Once a CO* reaches and adsorbs on a dopant site, the return (dopant to host) diffusion barrier is effectively prohibitive at ~100 K, especially on RhNiCu and RhPtCu. In this case, the molecule remains immobilized on that dopant for long times. Therefore, CO* does not necessarily end up exclusively on Rh even though Rh binds CO* most strongly; instead, CO* becomes partitioned among all the available dopant traps.

Because the lattice contains many more secondary dopant atoms than Rh atoms, a larger fraction of CO* is captured by the secondary dopant simply by statistical availability. The “numbers advantage”, combined with suppressed back-diffusion at low temperature, lead to substantial CO* population on the secondary dopant and result in comparable CO* coverages across the different dopant species under low temperature (~100 K) conditions.

5.3.4 The Temperature of CO Diffusion on each TD-SAA Surface

Experimentally, the appearance of a double CO_2 TPD peak tracks closely with the temperature regime in which CO* becomes mobile on the TD-SAA surface. Motivated by this correlation, we analyze the CO* transport behavior on the three TD-SAA compositions examined here with the temperature ramp. In addition, our earlier study (Project 4, Section 4.3.5)[2] showed that residual H* generated from HCOOH* dehydrogenation can occupy mixed hollow sites around Rh and effectively form a local “hydrogen wall,” which can impede species migration toward Rh. To evaluate whether such H*-induced blocking alters the onset of CO* diffusion, we carried out KMC simulations to determine the temperature at which CO* redistribution occurs on each TD-SAA in the absence of H* versus with pre-existing H* present on the surface.

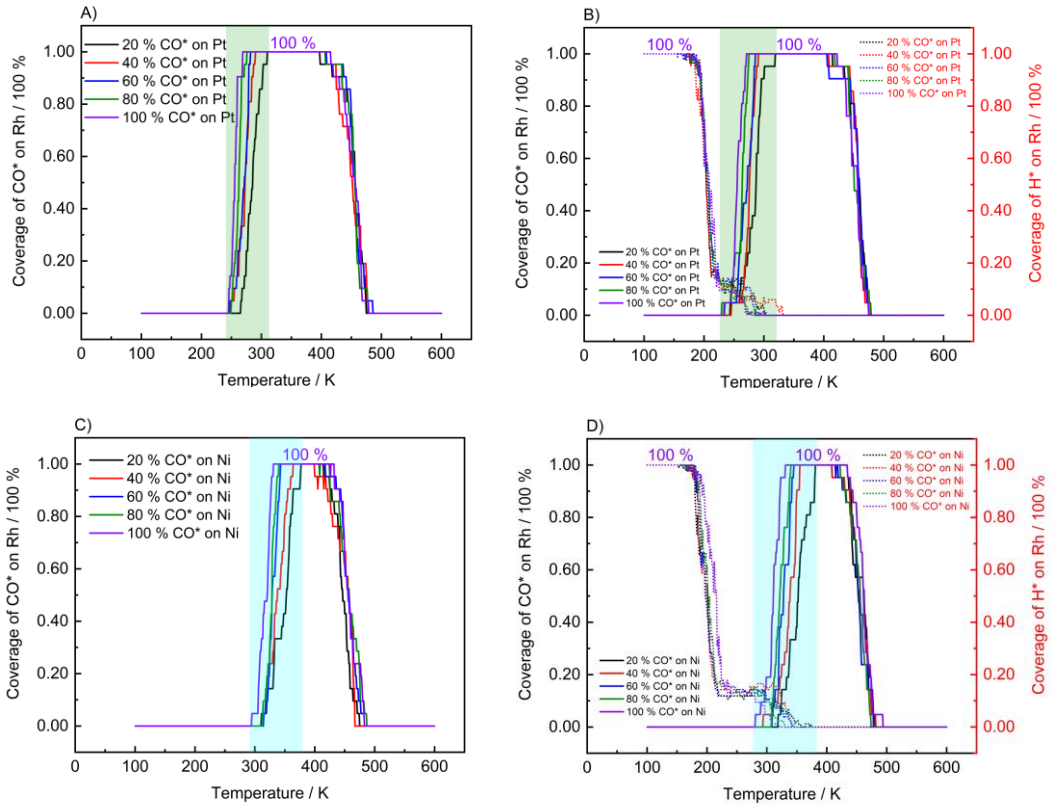


Figure 5. 8 CO* (solid) and H* (dot) coverages (normalized with respect to number of top and mixed hollow Rh sites, respectively) on Rh site profiles with respect to temperature without (A) and with (B) 1000 pre-existing H* on RhPtCu; and without (C) and with (D) 1000 pre-existing H* on RhNiCu. The black, red, blue, green, and purple dash and dot lines represent, respectively, the results with 20 %, 40 %, 60 %, 80 %, and 100 % CO* occupancies (normalized with respect to Pt/Ni sites) set on the Pt/Ni sites before simulations start. The green region indicates the time window when the CO* starts to diffuse from Pt site to Rh site. Each trajectory is the average of three KMC runs to simulate diffusion and desorption of H* and CO*.

To incorporate the experimental coverage conditions into the KMC model, we set the initial H* coverage based on the HCOOH* uptake. Experimentally, the HCOOH* coverage is ~10%, corresponding to 1,000 adsorbed HCOOH* on a 10,000-site lattice. Assuming that O–H activation occurs readily at low temperature and that these species generate surface hydrogen before the onset of extensive CO* migration, we initialized the simulations with 1,000 pre-

adsorbed H* atoms. To clearly track the subsequent CO* redistribution dynamics, CO* was initially placed exclusively on the secondary dopant sites, with the secondary site CO* coverage varied between 20% and 100% (namely introducing 10, 20, 30, 40, and 50 CO* molecules on the TD-SAA).

For RhPtCu, the KMC simulations reveal a clear coverage dependence. For higher initial CO* coverages on Pt sites, the temperature at which CO* redistribution toward Rh occurs shifts to lower values. In addition, H* has only a minor influence on CO* migration on RhPtCu (Figs. 5.8A and B). This is because H_2* formation and removal are efficient on Pt-containing surfaces, so the H* population around ~300 K (the regime where CO* begins to transfer from Pt to the Cu host) is relatively small, limiting H* blocking effects (dotted lines in Fig. 5.8B). Consequently, at temperatures below ~300 K, CO* remains largely confined to Pt sites and does not rapidly repopulate Rh, helping to keep Rh ensembles available for other reactions.

RhNiCu exhibits the same qualitative behavior, but the redistribution window shifts to higher temperature (~300–400 K) (Fig. 5.8C and D). This shift is consistent with the stronger stabilization of CO* on Ni compared with Pt, as indicated by the DFT formation energies (Fig. 5.8C). Given that Rh catalyzed HCOO** dissociation begins at approximately ~270 K, both RhPtCu and RhNiCu are predicted to maintain a sufficiently CO*-free Rh population in the

relatively low temperature regime to enable HCOO** C–H activation on Rh before CO* fully migrates back to poison the Rh sites.

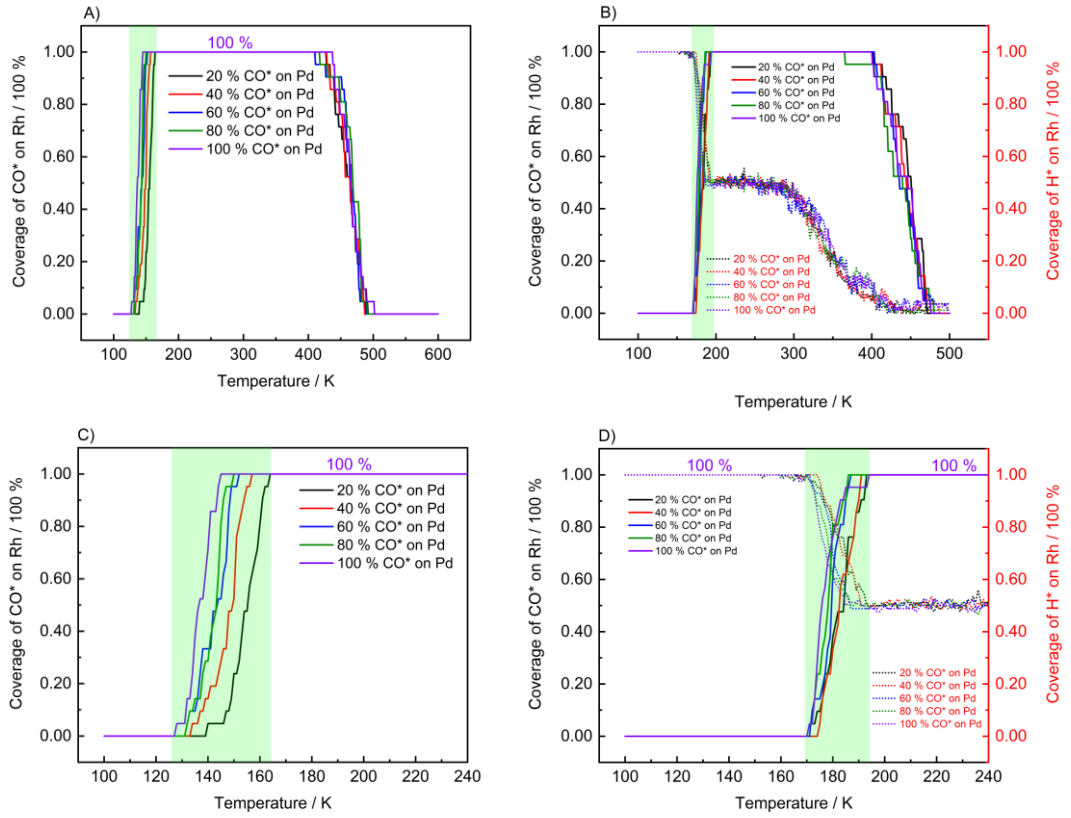


Figure 5. 9 CO* (solid) and H* (dot) coverages (normalized with respect to number of top and mixed hollow Rh sites, respectively) on Rh site profiles with respect to temperature without (A) and with (B) 1000 pre-exist H* on RhPdCu. Panels (C) and (D) are enlarged views of the temperature ranges highlighted in (A) and (B), respectively. The black, red, blue, green, and purple dash and dot lines represent the 20 %, 40 %, 60 %, 80 %, and 100 % CO* (normalized with respect to Pd sites) are set on Pd site before simulations start, respectively. The green region indicates the time window when the CO* adsorbates start to diffuse from Pd site to Rh site. Each trajectory is the average of three KMC runs to simulate diffusion and desorption of H* and CO*.

Although the temperature dependent CO* coverage on Rh in RhPdCu follows the same overall pattern as in RhPtCu and RhNiCu, several features highlight its distinct behavior (Fig. 5.9). First, Rh becomes blocked by CO* at a much

lower temperature. Complete Rh site coverage occurs at approximately 160 K (without pre-adsorbed H*) and around 200 K (with pre-existing H*), substantially earlier than in the other two TD-SAAs (Fig. 5.9). This early poisoning is consistent with the relatively weak stabilization of CO* on Pd ($E_F = -0.30\ eV$), compared with the much stronger CO* binding on Ni ($E_F = -0.82\ eV$) (Fig. 5.3A). In this case, CO* more readily leaves Pd sites, and diffuses onto the Cu host, followed by either desorption from the surface or being captured by Rh at low temperature, accelerating Rh site poisoning.

Second, unlike RhPtCu and RhNiCu, the redistribution temperature in RhPdCu is sensitive to the amount of pre-existing H* used to initialize the simulations, since H* occupancy on mixed hollow sites remains significant when CO* diffusion begins. In Chapter 4, we have calculated the H_2 desorption temperature from Pd and Cu sites to be around 260 K.[2] Note that Fig. 5.9B shows the number of H* on Rh instead of H* on whole lattice. As H* trapped by Rh must overcome an energy barrier of around 0.3 eV to migrate back to Cu, the change in the amount of H* on Rh lags behind that on Cu. In this case, at these comparatively low temperatures, H* removal is inefficient on RhPdCu surfaces, so H* coverage tends to accumulate and reach a plateau once Rh has already been fully blocked (Fig. 5.9B). Overall, the simulations indicate that premature Rh deactivation is the key factor explaining why RhPdCu lacks low-temperature (<300 K) HCOO** decomposition activity.

5.3.5 HCOO Dissociation on TD-SAA Surfaces with Pre-existing CO

Having investigated the behavior of CO* and H* on the TD-SAA surfaces, we carried out KMC simulations for HCOO** decomposition on the different TD-SAA models with pre-existing CO*. Each TD-SAA (100) lattice comprised 9,943 Cu atoms, 50 secondary-dopant atoms (0.5%), and 7 Rh atoms (0.07%). To match the experimental preparation conditions, the simulations were initialized with 1,000 HCOO** and 1,000 H* placed randomly on the surface, corresponding to an overall 10% coverage HCOOH*. In addition, to probe the impact of CO poisoning, 10–50 CO* species were introduced initially on the secondary dopant sites.

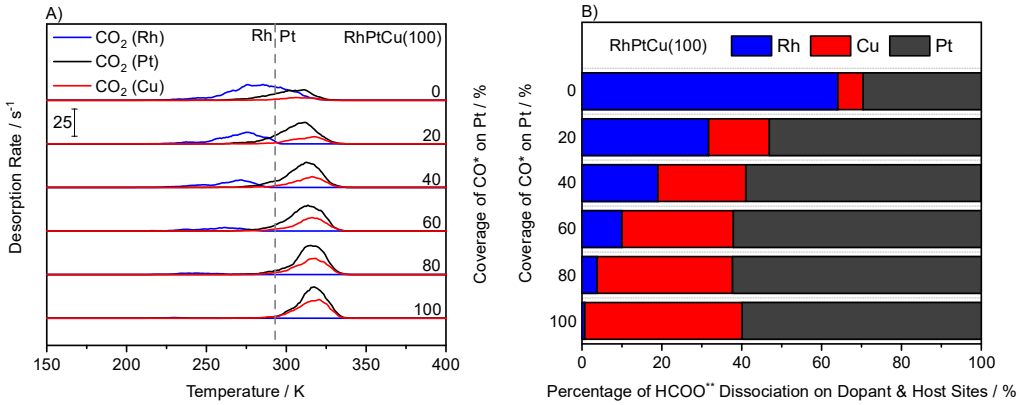


Figure 5. 10 KMC simulated HCOO** dissociation processes starting with coverage of HCOO** and H* equals to 10 % (coverage respective to total 10,000 sites) on RhPtCu surfaces with different coverage of CO*, including 0 %, 20 %, 40 %, 60 %, 80 %, and 100 % (coverage respective to 70 Pt sites), initially set on the secondary dopants. (A) Simulated TPD spectra of CO_2 desorption on Rh (blue line), Pt (black line), and Cu (red line) desorption on lattices. Dashed vertical lines differentiate the temperature regimes where CO* desorption is dominated by the primary dopant (Rh) vs. the other sites (Pt and Cu). (B) Bar chart showing the percentage of HCOO** dissociation on Rh (blue), Pt (black), and Cu (red) sites. Each trajectory is the average of three KMC runs to simulate HCOO** dissociation and desorption of CO_2*.

Fig. 5.10A presents CO_2 TPD spectra obtained from the KMC simulations of HCOO** decomposition on RhPtCu, with the color indicating the site type responsible for CO_2 formation. CO_2* is assumed to desorb immediately after it is produced rather than diffusing across the surface, consistent with the DFT finding in Chapter 4 that CO_2* does not form a stable chemisorbed state on Cu(100) and therefore remains weakly bound.

For higher initial CO* loadings on Pt, the Rh contribution (blue bars in Fig. 5.10A) becomes smaller and the CO_2 TPD peak shifts to lower temperature (blue lines in Fig. 5.10A). This behavior reflects earlier Rh site shutdown. Higher CO* coverage on Pt promotes earlier CO* transfer to Rh, which poisons Rh sooner and terminates HCOO** dissociation on Rh earlier in the temperature ramp. Accordingly, the Rh-derived CO_2 signal decays earlier and the corresponding peak moves to lower temperatures. In parallel, as the Pt/host contribution grows, the black signal strengthens and its maximum moves slightly to higher temperatures. At low CO* coverage, too little HCOO** decomposes on Pt to produce a well-defined Pt-related CO_2 peak. At higher CO* initial coverage, for which Rh becomes inactive earlier, a larger fraction of HCOO** dissociates on Pt, allowing the Pt-related CO_2 peak to emerge clearly. In addition, the Cu-derived component (red) also increases with CO loading.

This interpretation is further supported by a detailed quantitative analysis of the

event statistics (Fig. 5.10B), which reveals how many HCOO** molecules undergo C–H scission on each site type. Increasing the initial CO* loading on Pt reduces the number of Rh-derived C–H activations, because Rh becomes poisoned earlier and its contribution shuts down sooner.

At CO* coverages below ~60%, raising the CO* level increases the fraction of HCOO** decomposition occurring on both Pt and Cu, reflecting the progressive diversion of reactivity away from Rh. When the initial CO* coverage exceeds 60%, the Pt contribution reaches a plateau. The fraction of HCOO** dissociation occurring on Pt remains essentially constant at 60%, while additional loss of Rh activity is compensated mainly by increased decomposition on Cu. This behavior is consistent with our earlier findings in Chapter 4, that the intrinsic barriers for HCOO** dissociation on Pt and on Cu are relatively close (difference on the order of <0.2 eV). Consequently, even in a PtCu SAA (0.7% Pt) without CO*, a substantial share of HCOO** conversion occurs on Pt (≈65%), with the remainder taking place on Cu (more details can be found in Chapter 4, Section 4.3.2). The TD-SAA results indicates that, once Rh is deactivated, the Pt:Cu partitioning of HCOO** dissociation resembles that of the corresponding PtCu bimetallic SAA.

A broadly similar dependence is also observed for RhNiCu (Fig. 5.11). However, in that system, when the CO* coverage rises beyond ~60%, the fraction of

HCOO** dissociation occurring on Ni decreases, indicating a stronger sensitivity of Ni site participation to high CO* loading compared with Pt. We will discuss the details on this phenomenon in the following section.

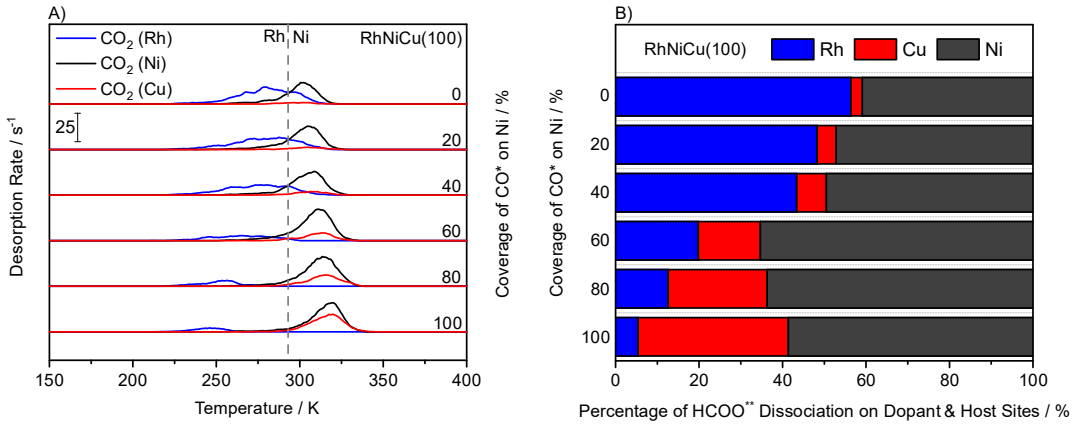


Figure 5. 11 KMC simulated HCOO** dissociation processes starting with coverage of HCOO** and H* equals to 10 % (coverage respective to total 10,000 sites) on RhNiCu surfaces with different coverage of CO*, including 0 %, 20 %, 40 %, 60 %, 80 %, and 100 % (coverage respective to 70 Ni sites), initially set on the secondary dopants. (A) Simulated TPD spectra of CO_2 desorption on Rh (blue line), Ni (black line), and Cu (red line) desorption on lattices. Dashed vertical lines differentiate the temperature regimes where CO* desorption is dominated by the primary dopant (Rh) vs. the other sites (Ni and Cu). (B) Bar chart showing the percentage of HCOO** dissociation on Rh (blue), Ni (black), and Cu (red) sites. Each trajectory is the average of three KMC runs to simulate HCOO** dissociation and desorption of CO_2*.

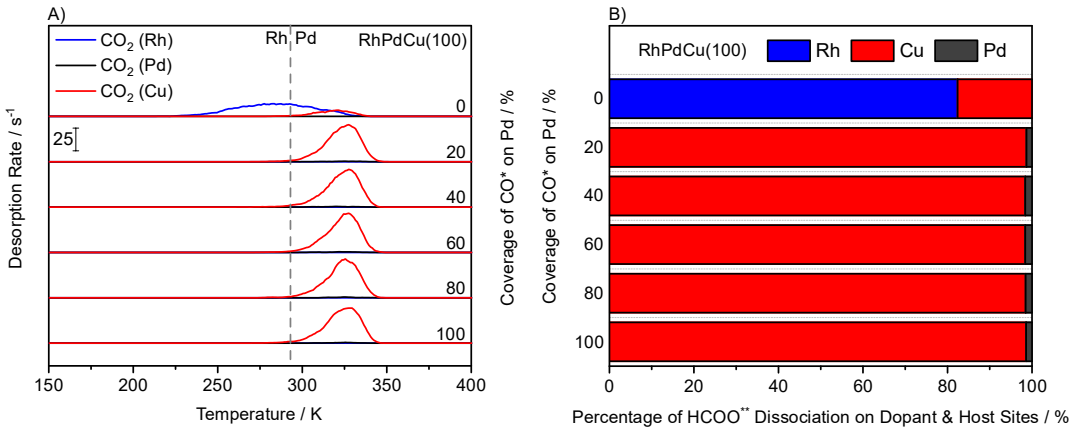


Figure 5. 12 KMC simulated HCOO** dissociation processes starting with coverage of HCOO** and H* equals to 10 % (coverage respective to total 10,000 sites) on RhPdCu surfaces with different coverage of CO*, including 0 %, 20 %, 40 %, 60 %, 80 %, and 100 % (coverage respective to 70 Pd sites), initially set on the secondary dopants. (A) Simulated TPD spectra of CO_2 desorption on Rh (blue line), Pd (black line), and Cu (red line) desorption on lattices. Dashed vertical lines differentiate the temperature regimes where CO* desorption is dominated by the primary dopant (Rh) vs. the other sites (Pd and Cu). (B) Bar chart showing the percentage of HCOO** dissociation on Rh (blue), Pd (black), and Cu (red) sites. Each trajectory is the average of three KMC runs to simulate HCOO** dissociation and desorption of CO_2*.

RhPdCu behaves differently from the other TD-SAAs. As shown in Fig. 5.12, a Rh-derived CO_2 signal is only present when the surface starts with no CO*. Introducing even a modest CO* loading, like 20% CO* coverage on Pd sites in our setup, is sufficient to occupy all 7 Rh atoms before ~200 K, thereby shutting down Rh-derived HCOO** decomposition. Once Rh is poisoned this early in the temperature ramp, it can no longer contribute the low-barrier pathway for HCOO** C–H activation.

The HCOO** dissociation counting analysis in Fig. 5.12B supports this interpretation. Without pre-adsorbed CO*, approximately 80% of HCOO**

dissociation events occur at Rh on RhPdCu. This fraction is slightly larger than in RhPtCu (~60%) and RhNiCu (~55%), because Pd sites are intrinsically less active for HCOO** decomposition than Pt or Ni, making Rh comparatively more favorable when it is accessible. In contrast, once CO* is present and Rh is blocked at low temperatures, most of the remaining C-H scission activity is redistributed to the host. Since the HCOO** dissociation barriers on Pd and Cu are similar, decomposition occurs predominantly on Cu sites, which vastly outnumber Pd sites (9,943 Cu vs 50 Pd). This outcome is consistent with prior results in Chapter 4.[2] For a 0.7% PdCu SAA without CO*, only about 2.5% of HCOO** dissociation takes place on Pd and the remainder occurs on Cu, mirroring the RhPdCu behavior under CO* pre-covered conditions.

Overall, our analysis shows that the temperature at which CO* redistributes between Rh and the secondary dopant in TD-SAAs is governed primarily by how strongly the secondary dopant stabilizes CO*. This conclusion is consistent with the experimental observations and is further corroborated by the HCOO** reactivity simulations, which together identify CO* diffusion as the mechanistic origin of the double-peak feature reported in the experimental TPD.

5.3.6 Effect of Residual CO on HCOO Dissociation

The KMC analysis further reveals a behavior specific to RhNiCu that is not observed for RhPtCu. When the initial CO* loading rises above 60%, the

reaction is increasingly diverted to the Cu host rather than proceeding on Ni sites on RhNiCu. This shift is evident from the reduced Ni-site contribution (red bars in Fig. 5.11B). As a result, the ratio of number of HCOO** converted between Ni and Cu drops to roughly 55% on Ni (Fig. 5.11B), which is noticeably smaller than the Ni-site fraction predicted for a NiCu bimetallic SAA without pre-adsorbed CO (≈70%) (Fig. 5.11B in Chapter 4).

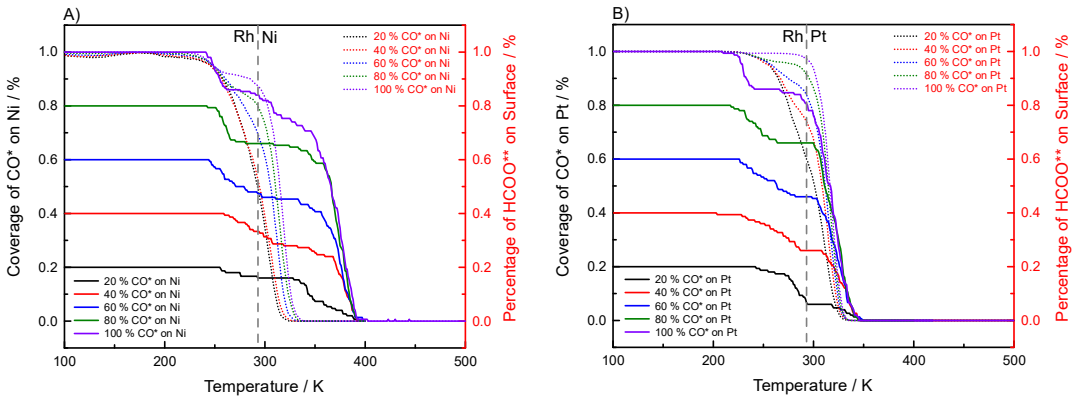


Figure 5. 13 CO* (solid) coverages (normalized with respect to number of top and mixed hollow Rh sites, respectively) on Rh site and percentage of HCOO** (dot) on the surface profiles with respect to temperature on (A) RhNiCu and (B) RhPtCu. The black, red, blue, green, and purple dash and dot lines represent the 20 %, 40 %, 60 %, 80 %, and 100 % CO* (normalized with respect to secondary dopant top sites) are set on secondary dopant sites before simulations start, respectively. Dashed vertical lines differentiate the temperature regimes where CO* desorption is dominated by the primary dopant (Rh) vs. the other sites (Pd and Cu). Each trajectory is the average of three KMC runs to simulate HCOO** dissociation.

To rationalize this Ni-specific shift, we compare the temperature evolution of CO* coverage and the fraction of unreacted HCOO** on RhNiCu and RhPtCu in Fig. 5.13. For RhNiCu, Fig. 5.13A shows that when the temperature reaches ~300 K, when Rh is largely CO-blocked, the residual CO* remains strongly retained on the secondary Ni dopant and persists until roughly ~400 K. As an

illustrative case, when Ni is initialized with 100% CO* coverage, the surface still retains >80% CO* on Ni* even after HCOO** conversion has essentially completed (Fig. 5.13A, purple curve). This result is consistent with the fact that increasing the initial CO* coverage level suppresses the number of HCOO** molecules that can react on both Rh and Ni, so fewer reaction events occur to unblocked Ni sites during the simulation.

In contrast, on RhPtCu the CO* population does not remain trapped on the secondary dopant once Rh has become fully blocked. After Rh poisoning, CO* is released more readily from Pt, allowing Pt sites to become accessible again; these vacant Pt sites can then contribute to HCOO** dissociation at higher temperature (Fig. 5.13B). These results are consistent with the two distinct peaks observed in the TPD spectra for Ni- and Pt-doped samples, we attribute the lower-temperature peak to the HCOO** dissociation on Rh, followed by the CO* transfer from Ni/Pt to Rh sites along with the increasing temperature. These newly available Pt sites can then participate in HCOO** dissociation, particularly at elevated temperature (Fig. 5.1). Whereas Pd, as a weaker trap, enables early CO* migration that prematurely poisons Rh, suppressing low-temperature activity (Fig. 5.1).

5.4 Conclusion

In this project, we established a DFT + GT-KMC framework to explain how CO*

poisoning and redistribution control the activity of TD-SAAs during HCOO** dissociation to CO_2. DFT energy profiles show that CO* diffusion on Cu-based SAAs is facile on the host lattice but CO* becomes kinetically trapped at dopant sites at low temperature, with its stability following the trend: Rh > Ni > Pt > Pd. KMC simulations further demonstrate that CO* removal is typically diffusion-limited, involving CO* migration from dopant sites onto Cu host sites and desorption therefrom, rather than directly from the dopant sites.

KMC simulations of CO* diffusion on TD-SAAs show that, at low temperature ~100 K, CO* has an approximately equal probability of being trapped by each single dopant sites. Because Rh atoms are much less abundant than the secondary dopant atoms, a larger fraction of CO* is initially captured on the secondary dopant sites. As the temperature increases, CO* gradually redistributes and migrates toward Rh, eventually blocking the Rh active sites.

Building on these insights, KMC models of the HCOO** decomposition chemistry on these materials reveal that the experimentally observed double-peak CO_2 TPD on RhPtCu and RhNiCu originates from HCOO** dissociation on Rh and on the secondary dopant. Only a fraction of HCOO** can be activated on Rh as the CO* bound to Pt and Ni can diffuse to the Rh site as temperature increases. Stronger CO* traps, such as Ni and Pt, delay CO* transfer to Rh and preserve a low-temperature window where Rh can catalyze

HCOO** decomposition, whereas Pd, as a weaker trap, enables early CO* migration that prematurely poisons Rh, suppressing low-temperature activity. Overall, our results indicate that introducing an appropriate secondary dopant can act as a CO* scavenger to mitigate SAA deactivation and maintain active-site availability.

Closing Statement and Future Perspectives

This thesis developed and applied a multi-scale modelling framework to understand and design SAA catalysts for H_2 production from liquid oxygenates. Motivated by the need for scalable, low-carbon energy carriers and by the practical appeal of CH_3OH and HCOOH as hydrogen carriers, the work combined DFT to resolve adsorption thermodynamics and elementary reaction barriers with GT-KMC simulations to connect microscopic energetics to measurable macroscopic observables under temperature-programmed conditions. The work carried out in this thesis provides a coherent mechanistic picture of how isolated dopants in coinage-metal hosts reshape reactivity, how those effects manifest under realistic coverages and site competitions, and how poisoning phenomena can be mitigated through rational alloy design. The key highlights of this work are summarized below.

(1) Establishing transferable reactivity trends for oxygenate chemistry on SAAs.

Chapter 3 systematically examined adsorption configurations and energetics for a set of oxygenated intermediates relevant to biomass-derived feedstocks for H_2 production on Ni/Pd/Pt/Rh-doped Cu(111), Ag(111), and Au(111) SAAs. It was shown that, for many adsorbates, formation (adsorption) energies on SAAs fall between those of their monometallic components and that adsorption geometries can often be rationalized through simple valency rules for pure

metals. Importantly, kinetic barriers were calculated for key bond-breaking and bond-forming events in CH_3OH dehydrogenation and C–O coupling. By constructing and interpreting TCS and BEP relations, we clarified when SAAs follow monometallic trends and when they deviate in a catalytically advantageous way, in which SAAs combine relatively weak product binding with reduced activation barriers. It was thus demonstrated that SAAs can offer an improved compromise between activity and selectivity compared with pure host metals.

(2) Resolving the mechanistic origin of dopant-dependent activity trends for HCOOH decomposition on Cu-based SAAs.

Chapter 4 focused on the experimentally relevant, CO-free channel for HCOO decomposition in which bidentate HCOO** C–H scission governs CO_2 formation and ultimately H_2 evolution. DFT mapped minimum energy pathways on Cu(100) and Cu-based SAAs (Rh, Ni, Pt, Pd dopants) and revealed dopant-related transition state configurations that rationalize the intrinsic barrier ordering (RhCu < NiCu < PtCu < PdCu < Cu). Our results indicate that, because reactive initial states for C–H activation are largely host-like proximal configurations, dopant effects are expressed primarily through stabilization of later states, including the energetics of H* and coupled intermediate configurations. In this regime, the CO* formation energy on the dopant emerges as a practical descriptor for the HCOO** C–H activation barrier across the SAA

series, while the same descriptor is not generally transferable in an equivalent way across monometallic surfaces.

The on-lattice KMC models represent large Cu(100) lattices with dilute dopant populations, include elementary steps relevant to HCOO** decomposition and hydrogen evolution, and explicitly treat site availability, diffusion-driven competition, short-range lateral interactions, and coverage evolution. The DFT parameterized KMC simulations enabled mechanistic understanding that cannot be obtained from DFT barriers alone. First, apparent peak temperatures reflect not only intrinsic barriers but also the evolving accessibility of active dopant sites; Second, coverage-dependent inhibition by residual H* can become a controlling factor. Overall, experimentally observed activity orderings can be rationalized as emergent properties of coupled event networks rather than single-barrier comparisons.

(3) Introducing a design principle for mitigating CO poisoning using secondary dopant sites.

Chapter 5 addressed a persistent limitation for SAA catalysis: CO poisoning via strong binding to reactive dopant top sites. The thesis quantified CO* diffusion and desorption landscapes on Cu-based SAAs and demonstrated, through coupled DFT+KMC analysis on two-dopant (100) SAAs surfaces (RhNiCu, RhPtCu, RhPdCu), that CO* removal is mediated by diffusion. CO* migrates

from dopants to host sites and desorbs predominantly from Cu rather than directly from dopant sites. This mechanistic insight enabled the concept of secondary dopants as CO* scavengers: appropriately chosen secondary single-atom sites can preferentially trap CO* at low temperature, delaying its migration to the primary active dopant (e.g., Rh), thereby preserving a kinetic window in which HCOO** can dehydrogenate before the primary site becomes blocked. The framework explains the characteristic double-peak CO_2 TPD features of RhNiCu and RhPtCu and provides a concrete alloy design strategy to regulate active site availability under CO* poisoning conditions.

In summary, this thesis advances the mechanistic understanding and design principles for hydrogen production from liquid oxygenates on SAA catalysts. By unifying DFT calculated energetics with explicit lattice kinetics, it clarifies how isolated dopants control elementary steps, how these effects emerge under realistic coverages and site competitions, and how poisoning can be mitigated through multi dopant design. The resulting insights and modelling tools provide a rigorous foundation for predictive SAA catalyst development in renewable hydrogen and broader oxygenate conversion to H_2 production chemistries.

While this thesis has established a robust multi-scale framework for analyzing oxygenate conversion on SAA catalysts, several important directions remain open for future work. A particularly promising next step is to extend the

DFT+GT-KMC methodology developed here to CH_3OH decomposition on a carefully selected Ag-based SAA, with Rh/Ag representing a logical first prototype. Such a study would enable a direct connection between the transferable adsorption and activation trends identified in Chapter 3 and the explicit coverage-dependent reaction kinetics already demonstrated for HCOOH decomposition in Chapters 4 and 5. In particular, a lattice KMC treatment of CH_3OH conversion could resolve how competition among CH_3OH*, CH_3O*, CH_2O*, H*, CO*, and other dehydrogenation intermediates governs the temperature-dependent lattice of H_2 formation, the accumulation of poisoning species, and the accessibility of isolated dopant sites under realistic reaction conditions.

A further important direction is the screening of TD-SAA motifs to assess whether the secondary-dopant design principle introduced in this thesis can be generalized beyond CO poisoning. In addition to CO*, other strongly bound spectator or poisoning species, such as HCOO-derived fragments, CH_x intermediates, or carbon residues formed during methanol decomposition, may also limit active-site availability and alter overall reactivity. Systematic DFT screening combined with lattice KMC modelling could therefore be used to identify TD-SAA combinations in which the secondary dopant selectively scavenges poisoning species away from the primary active site, thereby preserving a wider kinetic window for the desired dehydrogenation pathway. In

this way, TD-SAA design may evolve from a case-specific strategy for CO management into a broader framework for controlling poisoning in oxygenate reforming chemistry.

Appendix A

Table A 1 Optimized lattice constants from DFT using OptB86b-vdW for FCC Cu, Ag, Au, Ni, Pd, Pt and Rh. The lattice constants are found by performing total energy minimization at various FCC unit cell volumes (a=b=c, α=β=γ=90°), fitting the resulting energies and volumes to the Murnaghan equation of state and finding the minimum thereof.

Metal	DFT Lattice Constant (Å)
Ag	4.077
Au	4.127
Cu	3.608
Ni	3.478
Pd	3.909
Pt	3.961
Rh	3.829

Table A 2 Formation energies (E_F) of fragments adsorbed to the most favored (lowest energy) adsorption site on pure metal and SAA (111) surfaces, as computed by DFT. Values of E_F are relative to CH_4(g), H_2(g), and CO_2(g) as given by Eq. (2.51) in the main text.

	Formation Energy, E_F (eV)							
Surface	CH_3	OH	CH_3O	CH_2OH	CH_3OCH_2	H_2O	CH_3OH	CH_3OCH_3
Ag(111)	1.21	-0.72	0.25	1.02	1.79	-1.33	-0.33	0.55
Au(111)	0.87	-0.14	0.74	0.54	1.32	-1.33	-0.36	0.52
Cu(111)	0.67	-1.28	-0.32	0.64	1.41	-1.41	-0.43	0.44
Ni(111)	0.15	-1.50	-0.66	0.02	0.84	-1.53	-0.57	0.29
Pd(111)	0.35	-0.72	0.11	-0.18	0.69	-1.52	-0.57	0.25
Pt(111)	0.03	-0.44	0.29	-0.45	0.43	-1.56	-0.66	0.21
Rh(111)	0.17	-1.19	-0.41	-0.33	0.50	-1.63	-0.71	0.15
Ni/Ag(111)	0.54	-1.23	-0.27	0.27	1.11	-1.52	-0.55	0.40
Ni/Au(111)	0.63	-0.81	0.09	0.25	1.10	-1.69	-0.73	0.23
Ni/Cu(111)	0.47	-1.37	-0.46	0.22	1.03	-1.52	-0.55	0.35
Pd/Ag(111)	0.77	-0.67	0.29	0.46	1.31	-1.35	-0.36	0.50
Pd/Au(111)	0.72	-0.26	0.63	0.26	1.09	-1.48	-0.51	0.35
Pd/Cu(111)	0.73	-1.02	-0.10	0.41	1.24	-1.41	-0.43	0.43
Pt/Ag(111)	0.42	-0.55	0.37	0.08	0.95	-1.39	-0.40	0.49
Pt/Au(111)	0.28	-0.36	0.53	-0.12	0.73	-1.43	-0.48	0.38
Pt/Cu(111)	0.42	-0.80	0.10	0.09	0.93	-1.43	-0.46	0.44
Rh/Ag(111)	0.37	-0.89	0.03	-0.05	0.84	-1.52	-0.54	0.35
Rh/Au(111)	0.32	-0.66	0.18	-0.17	0.71	-1.70	-0.75	0.15
Rh/Cu(111)	0.46	-1.11	-0.21	0.02	0.87	-1.56	-0.59	0.27

Table A 3 TCS for species 1 (x-axis) and species 2 (y-axis) adsorbed in their most favored adsorption sites on pure metals and SAAs (Fig. 3.5 in main text). Linear Regression parameters (slope, a, and intercept, b in eV) are given in addition to coefficients of determination (R^2) and mean absolute errors in eV (MAE). Results of Student's T-test (to determine if the slopes and intercepts of pure metal and SAA TCS relations are different) are given for 90 % and 99 % confidence intervals as "Yes" or "No" for different and not different, respectively. Details of calculation methods can be found in the work of Darby et al.[59]

			Linear Regression							
Species 1 (x)	Species 2 (y)		a	b (eV)	R^2	MAE (eV)	T-test (90% Confidence) Diff'nt Slope	T-test (90% Confidence) Diff'nt Intercept	T-test (99% Confidence) Diff'nt Slope	T-test (99% Confidence) Diff'nt Intercept
OH	CH_3O	Pure	0.984 ± 0.081	0.843 ± 0.078	0.967	0.073	No	No	No	No
		SAA	0.966 ± 0.029	0.881 ± 0.025	0.991	0.022				
		Global	0.979 ± 0.039	0.867 ± 0.035	0.974	0.046				
CH_2OH	CH_3OCH_2	Pure	0.928 ± 0.014	0.833 ± 0.007	0.999	0.015	No	Yes	No	No
		SAA	0.928 ± 0.030	0.861 ± 0.007	0.990	0.015				
		Global	0.839 ± 0.006	0.926 ± 0.015	0.995	0.017				
H_2O	CH_3OH	Pure	1.241 ± 0.065	1.313 ± 0.096	0.986	0.014	Yes	Yes	No	No
		SAA	1.088 ± 0.026	1.105 ± 0.039	0.995	0.006				
		Global	1.135 ± 0.038	1.163 ± 0.057	0.981	0.013				
CH_3OH	CH_3OCH_3	Pure	1.073 ± 0.053	0.899 ± 0.028	0.988	0.012	No	No	No	No
		SAA	0.842 ± 0.026	0.929 ± 0.050	0.977	0.014				
		Global	0.932 ± 0.060	0.845 ± 0.032	0.934	0.023				
H_2O	CH_3OCH_3	Pure	1.336 ± 0.078	2.315 ± 0.115	0.983	0.018	Yes	Yes	Yes	Yes
		SAA	0.898 ± 0.088	1.710 ± 0.133	0.912	0.024				
		Global	1.038 ± 0.092	1.893 ± 0.137	0.882	0.031				

Table A 4 Activation energies (Ea) and reaction energies (ΔE_{Rxn}) for the h-CH_3OH and the d-CH_3OH C-H dissociation reaction pathways on pure metal (blue) and SAA (red) surfaces. Preferable pathway in the table is defined as the pathway with lower absolute energy of the transition state. The energy differences of ΔE_{Tot}^{IS} and ΔE_{Tot}^{TS} are calculated by the activation energy of h-pathway minus that of the d-pathway and the reaction energy of h-CH_3OH pathway minus that of the d-CH_3OH pathway, respectively. Double dash means that we were not able to find a transition state for the corresponding pathway.

	$CH_3OH^* \rightarrow CH_2OH^* + H^*$						
Surface	h-CH_3OH pathway		d-CH_3OH pathway		Preferable	Energy difference	
	E_a (eV)	E_{Rxn} (eV)	E_a (eV)	E_{Rxn} (eV)	pathway	ΔE_{Tot}^{IS} (eV)	ΔE_{Tot}^{TS} (eV)
Ag(111)	1.91	1.67	--	--	--	--	--
Au(111)	1.52	1.20	--	--	--	--	--
Cu(111)	1.40	0.81	--	--	--	--	--
Ni(111)	0.78	0.07	--	--	--	--	--
Pd(111)	0.64	0.03	--	--	--	--	--
Pt(111)	0.63	-0.25	--	--	--	--	--
Rh(111)	0.67	0.01	--	--	--	--	--
Ni/Ag(111)	1.51	0.54	0.94	0.85	d-CH_3OH	0.21	0.79
Ni/Au(111)	1.34	0.80	1.06	1.00	d-CH_3OH	0.40	0.68
Ni/Cu(111)	1.25	0.63	0.88	0.55	d-CH_3OH	0.12	0.49
Pd/Ag(111)	1.63	1.42	1.10	0.93	d-CH_3OH	0.00	0.52
Pd/Au(111)	1.33	0.91	1.07	0.85	d-CH_3OH	0.17	0.43
Pd/Cu(111)	1.38	0.82	1.09	0.73	d-CH_3OH	-0.03	0.27
Pt/Ag(111)	1.49	1.14	0.81	0.44	d-CH_3OH	-0.12	0.56
Pt/Au(111)	1.25	0.55	0.78	0.39	d-CH_3OH	0.11	0.59
Pt/Cu(111)	1.35	0.81	0.88	0.39	d-CH_3OH	-0.13	0.35
Rh/Ag(111)	1.37	0.00	0.59	0.32	d-CH_3OH	0.20	0.98
Rh/Au(111)	1.19	0.58	0.70	0.45	d-CH_3OH	0.42	0.92
Rh/Cu(111)	1.22	0.58	0.69	0.33	d-CH_3OH	0.18	0.71

Table A 5 Activation energies (Ea) and reaction energies (ΔE_{Rxn}) for the h-CH_3OH and the d-CH_3OH O-H dissociation reaction pathways on pure metal (blue) and SAA (red) surfaces. The “preferable pathway” in this table is defined as the pathway with the lower absolute energy of the transition state. Energy differences of ΔE_{Tot}^{IS} and ΔE_{Tot}^{TS} are calculated by the activation energy of h-pathway minus that of the d-pathway and the reaction energy of h-CH_3OH pathway minus that of the d-CH_3OH pathway, respectively. Double dash means that we were not able to find a transition state for the corresponding pathway.

	$CH_3OH^* \rightarrow CH_3O^* + H^*$						
Surface	h-CH_3OH pathway		d-CH_3OH pathway		Preferable	Energy difference	
	E_a (eV)	E_{Rxn} (eV)	E_a (eV)	E_{Rxn} (eV)	pathway	ΔE_{Tot}^{IS} (eV)	ΔE_{Tot}^{TS} (eV)
Ag(111)	1.53	0.84	--	--	--	--	--
Au(111)	1.72	1.31	--	--	--	--	--
Cu(111)	1.05	-0.11	--	--	--	--	--
Ni(111)	0.84	-0.50	--	--	--	--	--
Pd(111)	0.96	0.15	--	--	--	--	--
Pt(111)	0.73	0.47	--	--	--	--	--
Rh(111)	0.81	-0.08	--	--	--	--	--
Ni/Ag(111)	1.05	0.35	0.96	0.19	d-CH_3OH	0.21	0.29
Ni/Au(111)	1.43	0.43	1.21	0.70	d-CH_3OH	0.40	0.62
Ni/Cu(111)	0.87	-0.26	0.96	-0.23	d-CH_3OH	0.12	0.04
Pd/Ag(111)	1.16	0.54	1.43	0.64	h-CH_3OH	0.00	-0.28
Pd/Au(111)	1.57	1.05	1.58	1.21	d-CH_3OH	0.17	0.16
Pd/Cu(111)	0.86	-0.07	1.39	-0.15	h-CH_3OH	-0.03	-0.56
Pt/Ag(111)	0.87	0.41	1.24	0.54	h-CH_3OH	-0.12	-0.49
Pt/Au(111)	1.15	1.02	1.34	1.09	h-CH_3OH	0.11	-0.08
Pt/Cu(111)	0.72	-0.07	1.30	-0.19	h-CH_3OH	-0.13	-0.71
Rh/Ag(111)	0.84	0.28	0.96	0.20	d-CH_3OH	0.20	0.08
Rh/Au(111)	1.27	0.44	1.15	0.85	d-CH_3OH	0.42	0.54
Rh/Cu(111)	0.68	-0.27	1.05	-0.01	h-CH_3OH	0.18	-0.19

Table A 6 Activation energies (Ea) and reaction energies (ΔE_{Rxn}) for the h-CH_3O and the d-CH_3O C-H dissociation reaction pathways on pure metal (blue) and SAA (red) surfaces. Preferable pathway in the table is defined as the pathway with lower absolute energy of the transition state. The energy differences of ΔE_{Tot}^{IS} and ΔE_{Tot}^{TS} are calculated by the activation energy of h-pathway minus that of the d-pathway and the reaction energy of h-CH_3OH pathway minus that of the d-CH_3OH pathway, respectively. Double dash means that we were not able to find a transition state for the corresponding pathway.

	$CH_3O^* \rightarrow CH_2O^* + H^*$						
Surface	h-CH_3O pathway		d-CH_3O pathway		Preferable	Energy difference	
	E_a (eV)	E_{Rxn} (eV)	E_a (eV)	E_{Rxn} (eV)	pathway	ΔE_{Tot}^{IS} (eV)	ΔE_{Tot}^{TS} (eV)
Ag(111)	1.16	0.99	--	--	--	--	--
Au(111)	0.76	0.45	--	--	--	--	--
Cu(111)	1.22	0.89	--	--	--	--	--
Ni(111)	0.86	0.38	--	--	--	--	--
Pd(111)	0.60	-0.23	--	--	--	--	--
Pt(111)	0.18	-0.48	--	--	--	--	--
Rh(111)	0.57	-0.10	--	--	--	--	--
Ni/Ag(111)	1.24	1.07	0.74	0.56	d-CH_3O	--	0.51
Ni/Au(111)	0.69	0.63	0.79	0.57	d-CH_3O	0.14	0.04
Ni/Cu(111)	1.22	0.55	0.76	0.47	d-CH_3O	--	0.46
Pd/Ag(111)	1.11	0.87	0.78	0.45	d-CH_3O	--	0.33
Pd/Au(111)	--	--	0.72	0.34	d-CH_3O	0.19	--
Pd/Cu(111)	1.06	0.80	1.00	0.46	d-CH_3O	--	0.06
Pt/Ag(111)	0.98	0.77	0.45	0.33	d-CH_3O	0.12	0.65
Pt/Au(111)	0.75	0.44	--	--	h-CH_3O	-0.11	--
Pt/Cu(111)	1.05	0.75	0.73	0.15	d-CH_3O	--	0.32
Rh/Ag(111)	--	--	0.42	-0.05	d-CH_3O	0.06	--
Rh/Au(111)	0.77	0.38	--	--	h-CH_3O	-0.23	--
Rh/Cu(111)	1.04	0.74	0.56	-0.02	d-CH_3O	--	0.48

Table A 7 Activation energies (Ea) and reaction energies (ΔE_{Rxn}) for the h-CH_2OH and the d-CH_2OH O-H dissociation reaction pathways on pure metal (blue) and SAA (red) surfaces. Preferable pathway in the table is defined as the pathway with lower absolute energy of the transition state. The energy differences of ΔE_{Tot}^{IS} and ΔE_{Tot}^{TS} are calculated by the activation energy of h-pathway minus that of the d-pathway and the reaction energy of h-CH_3OH pathway minus that of the d-CH_3OH pathway, respectively. Double dash means that we were not able to find a transition state for the corresponding pathway.

	$CH_2OH^* \rightarrow CH_2O^* + H^*$						
Surface	h-CH_2OH pathway		d-CH_2OH pathway		Preferable	Energy difference	
	E_a (eV)	E_{Rxn} (eV)	E_a (eV)	E_{Rxn} (eV)	pathway	ΔE_{Tot}^{IS} (eV)	ΔE_{Tot}^{TS} (eV)
Ag(111)	0.98	0.22	--	--	--	--	--
Au(111)	0.87	0.65	--	--	--	--	--
Cu(111)	0.94	0.00	--	--	--	--	--
Ni(111)	0.65	-0.32	--	--	--	--	--
Pd(111)	0.72	0.03	--	--	--	--	--
Pt(111)	0.64	0.34	--	--	--	--	--
Rh(111)	0.71	-0.15	--	--	--	--	--
Ni/Ag(111)	0.55	-0.30	1.38	0.24	h-CH_2OH	0.74	-0.09
Ni/Au(111)	0.82	0.29	1.05	0.49	d-CH_2OH	0.30	0.06
Ni/Cu(111)	0.78	-0.16	0.99	-0.10	d-CH_2OH	0.44	0.24
Pd/Ag(111)	0.57	-0.13	1.26	0.45	h-CH_2OH	0.54	-0.15
Pd/Au(111)	0.75	0.35	--	--	h-CH_2OH	0.29	--
Pd/Cu(111)	0.86	0.05	0.90	0.08	d-CH_2OH	0.23	0.18
Pt/Ag(111)	0.29	-0.32	1.48	0.75	h-CH_2OH	0.90	-0.28
Pt/Au(111)	0.44	0.07	1.43	1.12	h-CH_2OH	0.65	-0.34
Pt/Cu(111)	0.61	0.03	1.05	0.30	d-CH_2OH	0.55	0.11
Rh/Ag(111)	0.32	-0.46	1.42	0.45	h-CH_2OH	1.08	-0.02
Rh/Au(111)	0.54	0.12	--	--	h-CH_2OH	0.73	--
Rh/Cu(111)	0.62	-0.77	1.00	0.11	d-CH_2OH	0.68	0.29

Table A 8 Activation energies (Ea) and reaction energies (ΔE_{Rxn}) for the h-CH_3O and the d-CH_3O C-O coupling reaction pathways on Group 1 pure metal (blue) and SAA (red) surfaces. Preferable pathway in the table is defined as the pathway with lower absolute energy of the transition state. Energy differences of ΔE_{Tot}^{IS} and ΔE_{Tot}^{TS} are calculated by the activation energy of h-pathway minus that of the d-pathway and the reaction energy of h-CH_3OH pathway minus that of the d-CH_3OH pathway, respectively. Double dash means that we were not able to find a transition state for the corresponding pathway.

CH_3O*(dopant) + CH_3* → CH_3OCH_3* / CH_3O*(host) + CH_3* → CH_3OCH_2* + H*							
Group 1	h-CH_3OH pathway		d-CH_3OH pathway		Preferable	Energy difference	
surface	E_a (eV)	E_{Rxn} (eV)	E_a (eV)	E_{Rxn} (eV)	pathway	ΔE_{Tot}^{IS} (eV)	ΔE_{Tot}^{TS} (eV)
Ag(111)	1.21	-0.86	--	--	--	--	--
Au(111)	1.18	-1.08	--	--	--	--	--
Cu(111)	1.90	0.11	--	--	--	--	--
Pd(111)	1.55	-0.23	--	--	--	--	--
Pd/Ag(111)	1.36	-0.52	1.11	-1.19	h-CH_3OH	-0.46	-0.23
Pd/Au(111)	1.06	-0.98	1.80	-0.14	h-CH_3OH	-0.07	-0.11
Pd/Cu(111)	1.69	-0.02	1.11	-1.08	h-CH_3OH	-0.14	-0.24
Pt/Cu(111)	2.00	0.31	1.73	-0.35	h-CH_3OH	-0.59	-0.33

Table A 9 Activation energies (Ea) and reaction energies (ΔE_{Rxn}) for the h-CH_3O and the d-CH_3O C-O coupling reaction pathways on Group 2 pure metal (blue) and SAA (red) surfaces. Preferable pathway in the table is defined as the pathway with lower absolute energy of the transition state. The energy differences of ΔE_{Tot}^{IS} and ΔE_{Tot}^{TS} are calculated by the activation energy of h-pathway minus that of the d-pathway and the reaction energy of h-CH_3OH pathway minus that of the d-CH_3OH pathway, respectively. Double dash means that we were not able to find a transition state for the corresponding pathway.

CH_3O*(dopant/host) + CH_3* → CH_3OCH_3*							
Group 2	h-CH_3OH pathway		d-CH_3OH pathway		Preferable	Energy difference	
surface	E_a (eV)	E_{Rxn} (eV)	E_a (eV)	E_{Rxn} (eV)	pathway	ΔE_{Tot}^{IS} (eV)	ΔE_{Tot}^{TS} (eV)
Ni(111)	2.22	0.83	--	--	--	--	--
Pt(111)	1.48	-0.32	--	--	--	--	--
Rh(111)	1.57	0.14	--	--	--	--	--
Ni/Ag(111)	1.24	0.29	1.28	-0.50	h-CH_3OH	-0.15	-0.18
Ni/Au(111)	1.01	-0.02	1.23	-0.73	d-CH_3OH	0.39	0.16
Ni/Cu(111)	1.73	0.68	1.88	0.12	h-CH_3OH	-0.09	-0.25
Pt/Ag(111)	1.66	0.30	1.11	-1.08	h-CH_3OH	-0.89	-0.34
Pt/Au(111)	1.45	-0.14	1.22	-0.96	h-CH_3OH	-0.30	-0.07
Rh/Ag(111)	1.08	-0.10	1.12	-0.90	h-CH_3OH	-0.59	-0.62
Rh/Au(111)	1.00	-0.40	1.28	-0.86	h-CH_3OH	0.10	-0.18
Rh/Cu(111)	1.39	0.27	1.76	-0.23	h-CH_3OH	-0.27	-0.64

Table A 10 Formation energies of initial states ($E_{F,ini}$), transition states ($E_{F,tra}$), and final states ($E_{F,fin}$) of C-O coupling on pure metal and SAA (111) surfaces, as computed by DFT. Values of E_F are relative to CH_4(g), H_2(g), and CO_2(g) as given by Eq. (2.51) in the main text. Double dash means that we were not able to find a transition state for the corresponding pathway.

Surface	**Formation energy: $CH_3O^* + CH_3^* \rightarrow CH_3OCH_3^*$ / $CH_3O^* + CH_3^* \rightarrow CH_3OCH_2^* + H^*$**					
	h-CH_2OH pathway			d-CH_2OH pathway		
	$E_{F,ini}$ (eV)	$E_{F,tra}$ (eV)	$E_{F,fin}$ (eV)	$E_{F,ini}$ (eV)	$E_{F,tra}$ (eV)	$E_{F,fin}$ (eV)
Ag(111)	1.41	2.62	0.55	--	--	--
Au(111)	1.60	2.78	0.52	--	--	--
Cu(111)	0.33	2.23	0.44	--	--	--
Ni(111)	-0.45	1.77	0.38	--	--	--
Pd(111)	0.49	2.04	0.25	--	--	--
Pt(111)	0.34	1.82	0.02	--	--	--
Rh(111)	-0.17	1.41	-0.03	--	--	--
Ni/Ag(111)	0.75	2.00	1.04	0.90	2.17	0.40
Ni/Au(111)	1.35	2.36	1.32	0.96	2.19	0.23
Ni/Cu(111)	0.14	1.86	0.81	0.23	2.11	0.35
Pd/Ag(111)	1.01	2.37	0.49	1.47	2.60	0.50
Pd/Au(111)	1.47	2.54	0.50	1.54	2.65	0.35
Pd/Cu(111)	0.45	2.14	0.43	0.59	2.38	0.44
Pt/Ag(111)	0.67	2.34	0.97	1.57	2.67	0.49
Pt/Au(111)	1.05	2.50	0.91	1.35	2.56	0.38
Pt/Cu(111)	0.20	2.20	0.51	0.79	2.53	0.44
Rh/Ag(111)	0.66	1.75	0.56	1.25	2.37	0.35
Rh/Au(111)	1.11	2.11	0.71	1.01	2.29	0.15
Rh/Cu(111)	0.24	1.62	0.51	0.50	2.26	0.27

Table A 11 Formation energies of initial states ($E_{F,ini}$), transition states ($E_{F,tra}$), and final states ($E_{F,fin}$) of CH_2OH O-H activation on pure metal and SAA (111) surfaces, as computed by DFT. Values of E_F are relative to $CH_4(g)$, $H_2(g)$, and $CO_2(g)$ as given by Eq. (2.51) in the main text. Double dash means that we were not able to find a transition state for the corresponding pathway.

	Formation energy: $CH_2OH^* \rightarrow CH_2O^* + H^*$					
Surface	h-CH_2OH pathway			d-CH_2OH pathway		
	$E_{F,ini}$ (eV)	$E_{F,tra}$ (eV)	$E_{F,fin}$ (eV)	$E_{F,ini}$ (eV)	$E_{F,tra}$ (eV)	$E_{F,fin}$ (eV)
Ag(111)	1.01	1.99	1.23	--	--	--
Au(111)	0.53	1.40	1.18	--	--	--
Cu(111)	0.63	1.57	0.63	--	--	--
Ni(111)	0.01	0.66	-0.31	--	--	--
Pd(111)	-0.18	0.54	-0.14	--	--	--
Pt(111)	-0.45	0.19	-0.11	--	--	--
Rh(111)	-0.34	0.37	-0.49	--	--	--
Ni/Ag(111)	1.00	1.54	0.69	0.26	1.63	0.50
Ni/Au(111)	0.54	1.35	0.82	0.24	1.29	0.72
Ni/Cu(111)	0.65	1.44	0.49	0.21	1.20	0.11
Pd/Ag(111)	0.99	1.56	0.85	0.45	1.71	0.90
Pd/Au(111)	0.53	1.29	0.89	0.25	--	--
Pd/Cu(111)	0.62	1.48	0.68	0.40	1.30	0.47
Pt/Ag(111)	0.97	1.26	0.64	0.07	1.54	0.82
Pt/Au(111)	0.52	0.96	0.59	-0.13	1.29	0.98
Pt/Cu(111)	0.62	1.23	0.66	0.07	1.12	0.38
Rh/Ag(111)	1.02	1.34	0.55	-0.06	1.36	0.39
Rh/Au(111)	0.55	1.09	0.66	-0.19	--	--
Rh/Cu(111)	0.69	1.31	-0.08	0.01	1.01	0.12

Table A 12 Linear regression slopes (a), intercepts (b, in eV), R^2 and MAE in eV for the BEP relationship for six reactions; C-H and O-H activation of CH_3OH, C-H activation of CH_3O, C-H activation of CH_2OH, C-O coupling between CH_3 and CH_3O. Data is given for these reactions on pure metal (111) surfaces (blue), SAA (111) surfaces (red) and globally (black). Results of Student's T-test (to determine if the slopes and intercepts of pure metal and SAA BEP relations are different) are given for 90 % confidence intervals as "Yes" or "No" for different and not different, respectively.

		Linear Regression					
Reaction	Surface	a	b (eV)	R^2	MAE (eV)	T-test (90% Confidence) Diff'nt Slope	Diff'nt Intercept
$CH_3OH^* \rightarrow CH_2OH^* + H^*$	Pure	0.712 ± 0.047	0.720 ± 0.039	0.979	0.066	No	Yes
	SAA	0.614 ± 0.103	0.509 ± 0.067	0.780	0.060		
	Global	0.664 ± 0.080	0.577 ± 0.058	0.800	0.130		
$CH_3OH^* \rightarrow CH_3O^* + H^*$	Pure	0.499 ± 0.161	0.943 ± 0.104	0.658	0.090	No	No
	SAA	0.443 ± 0.068	0.850 ± 0.041	0.809	0.172		
	Global	0.462 ± 0.075	0.884 ± 0.046	0.693	0.124		
$CH_3O^* \rightarrow CH_2O^* + H^*$	Pure	0.621 ± 0.078	0.595 ± 0.046	0.928	0.080	No	No
	SAA	0.521 ± 0.182	0.530 ± 0.072	0.452	0.080		
	Global	0.589 ± 0.080	0.543 ± 0.038	0.762	0.093		
$CH_2OH^* \rightarrow CH_2O^* + H^*$	Pure	0.163 ± 0.180	0.770 ± 0.058	0.141	0.099	No	No
	SAA	0.698 ± 0.222	0.694 ± 0.062	0.497	0.024		
	Global	0.491 ± 0.158	0.711 ± 0.046	0.363	0.164		
$CH_3O^* + CH_3^* \rightarrow CH_3OCH_3^*$	Pure	0.599 ± 0.096	1.768 ± 0.067	0.951	0.063	No	No
	SAA	0.667 ± 0.056	1.797 ± 0.040	0.910	0.080		
	Global	0.652 ± 0.047	1.791 ± 0.033	0.916	0.076		
$CH_3O^* + CH_3^* \rightarrow CH_3OCH_2^* + H^*$	Pure	0.666 ± 0.203	1.615 ± 0.105	0.915	0.090	No	Yes
	SAA	0.644 ± 0.022	1.250 ± 0.074	0.587	0.140		
	Global	0.710 ± 0.203	1.341 ± 0.080	0.576	0.201		

Table A 13 Distance between the lowest H atom in CH_3 and the dopant atom ($D_{H\text{-}dopant}$) and distance between the C atom in CH_3 and the dopant atom ($D_{C\text{-}dopant}$) on the slab for Group 1 SAAs (blue) and Group 2 SAAs (red) in transition states of C-O coupling h-CH_3O pathway.

Surface	$D_{H\text{-}dopant}$ (Å)	$D_{C\text{-}dopant}$ (Å)
Group 1 Pure metal and SAA		
Ag(111)	2.42	2.61
Au(111)	2.38	2.54
Cu(111)	2.27	2.52
Pd(111)	1.99	2.33
Pd/Ag(111)	2.04	2.27
Pd/Au(111)	2.09	2.27
Pd/Cu(111)	2.09	2.41
Pt/Cu(111)	2.08	2.43
Group 2 Pure metal and SAA		
Ni(111)	1.64	1.96
Pt(111)	1.79	2.06
Rh(111)	1.75	2.02
Ni/Ag(111)	1.64	1.92
Ni/Au(111)	1.74	1.95
Ni/Cu(111)	1.63	1.93
Pt/Ag(111)	1.87	2.15
Pt/Au(111)	1.95	2.18
Rh/Ag(111)	1.75	2.01
Rh/Au(111)	1.81	2.03
Rh/Cu(111)	1.73	2.04

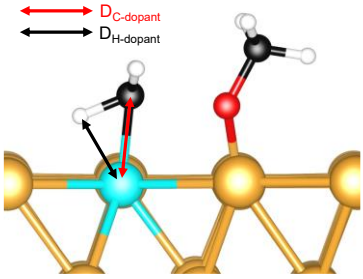


Figure A 1 Transition state of C-O coupling h-CH_3O pathway on Ni/Au(111). Distance between the lowest H atom in CH_3 and the dopant atom ($D_{H\text{-}dopant}$) and distance between the C atom in CH_3 and the dopant atom ($D_{C\text{-}dopant}$) are shown in the black and the red arrow, respectively.

Appendix B

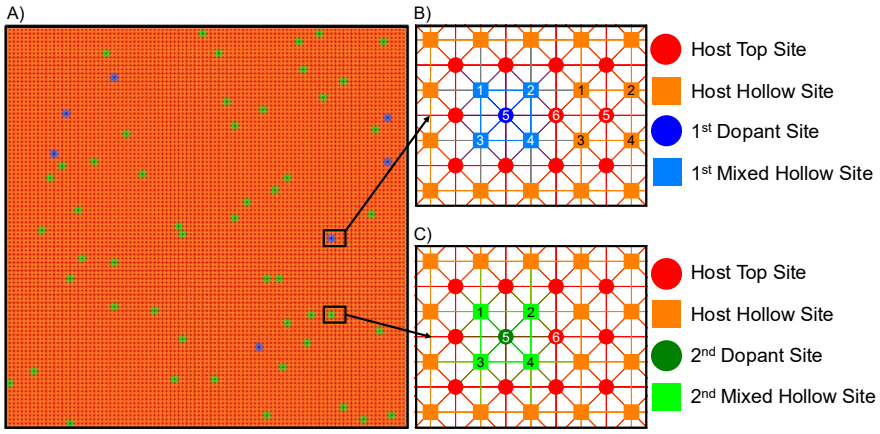


Figure B 1 (A) A typical TD-SAA fcc(100) surface used for KMC simulation in this work, including two parts of TD-SAA for the 1st (B) and 2nd (C) dopant region. Host, 1st and 2nd dopant top sites are represented by red, blue, and blue dots, respectively. Host hollow sites and 1st and 2nd dopant-host-mixed hollow sites are shown in orange, light blue, and light green squares, respectively. The numbers in this figure are used to define energy patterns in Table B1 in Appendix B.

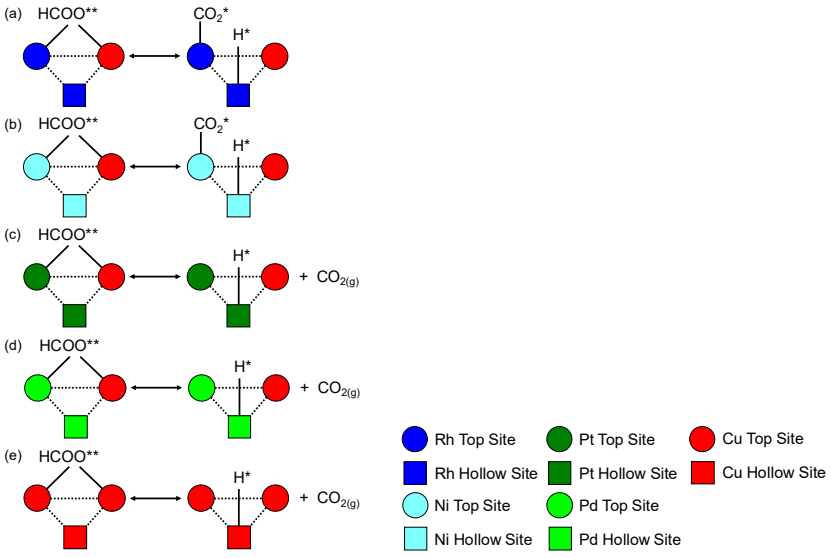


Figure B 2 Microscopic processes that could occur on the main lattice during the KMC simulation in Chapter 4 and Chapter 5. Top sites of Rh, Ni, Pt, Pd, and Cu atoms of TD-SAA(100) are shown as blue, light blue, green, light green, and red circles, respectively. Hollow sites of Rh, Ni, Pt, Pd, and Cu atoms of TD-SAA(100) are shown as blue, light blue, green, light green, and red squires, respectively. Events (a) and (b) are HCOO** dissociations to CO* adsorbates, events (c) - (e) are HCOO** dissociations to CO gas molecules.

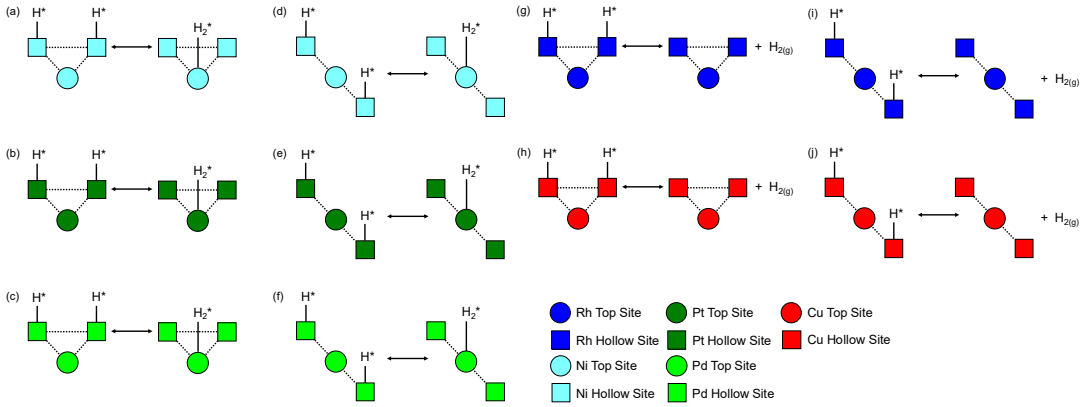


Figure B 3 Microscopic processes that could occur on the main lattice during the KMC simulation. Top sites of Rh, Ni, Pt, Pd, and Cu atoms of TD-SAA(100) are shown as blue, light blue, green, light green, and red circles, respectively. Hollow sites of Rh, Ni, Pt, Pd, and Cu atoms of TD-SAA(100) are shown as blue, light blue, green, light green, and red squires, respectively. Events (a) - (c) are H_2* formations via neighboring hollow sites, events (c) - (e) are H_2* formations via diagonal hollow sites. Events (g) and (h) are gas phase H_2 formations via neighboring hollow sites, events (i) and (j) are gas phase H_2 formations via diagonal hollow sites.

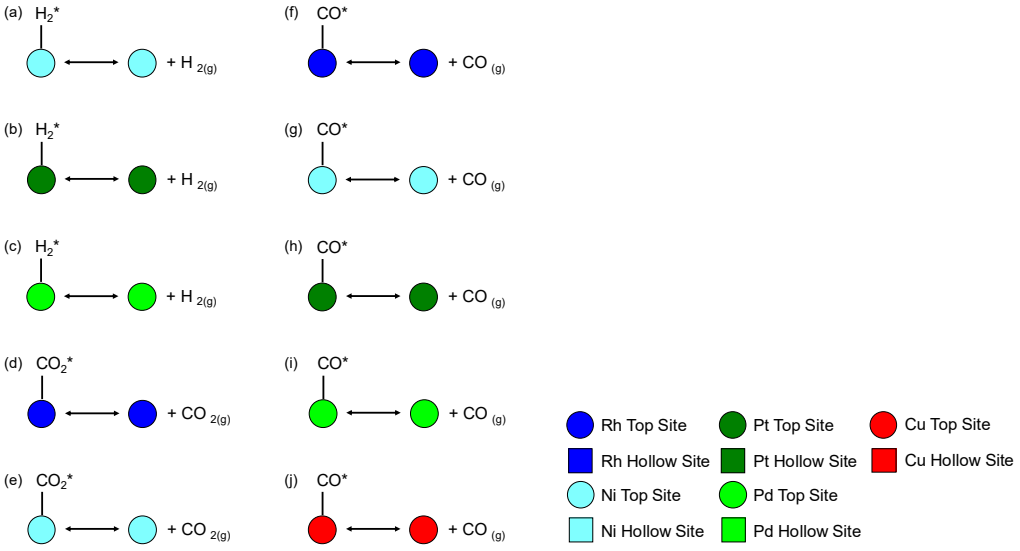


Figure B 4 Microscopic processes that could occur on the main lattice during the KMC simulation. Top sites of Rh, Ni, Pt, Pd, and Cu atoms of TD-SAA(100) are shown as blue, light blue, green, light green, and red circles, respectively. Hollow sites of Rh, Ni, Pt, Pd, and Cu atoms of TD-SAA(100) are shown as blue, light blue, green, light green, and red squires, respectively. Events (a) - (c) are H_2* desorption. Events (d) and (e) are CO_2* desorption. Events (f) - (j) are CO* desorption.

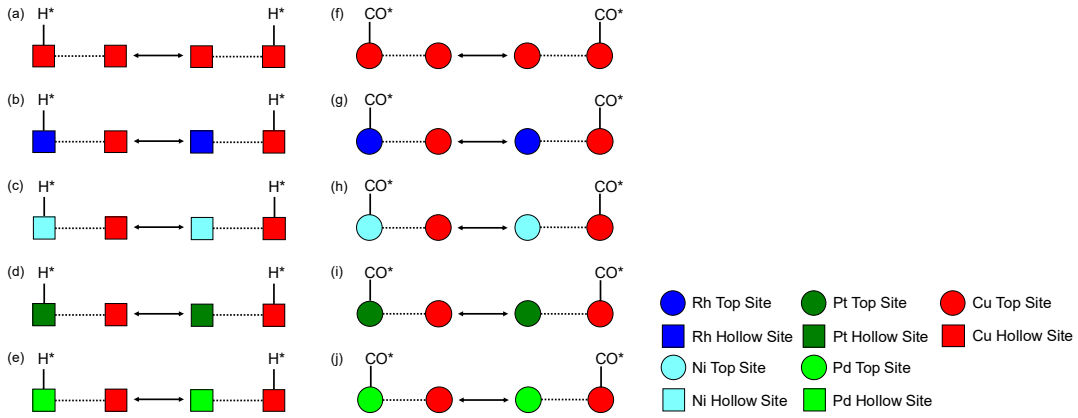


Figure B 5 Microscopic processes that could occur on the main lattice during the KMC simulation. Top sites of Rh, Ni, Pt, Pd, and Cu atoms of TD-SAA(100) are shown as blue, light blue, green, light green, and red circles, respectively. Hollow sites of Rh, Ni, Pt, Pd, and Cu atoms of TD-SAA(100) are shown as blue, light blue, green, light green, and red squires, respectively. Events (a) - (e) are H* diffusions. Events (f) - (j) are CO* diffusions.

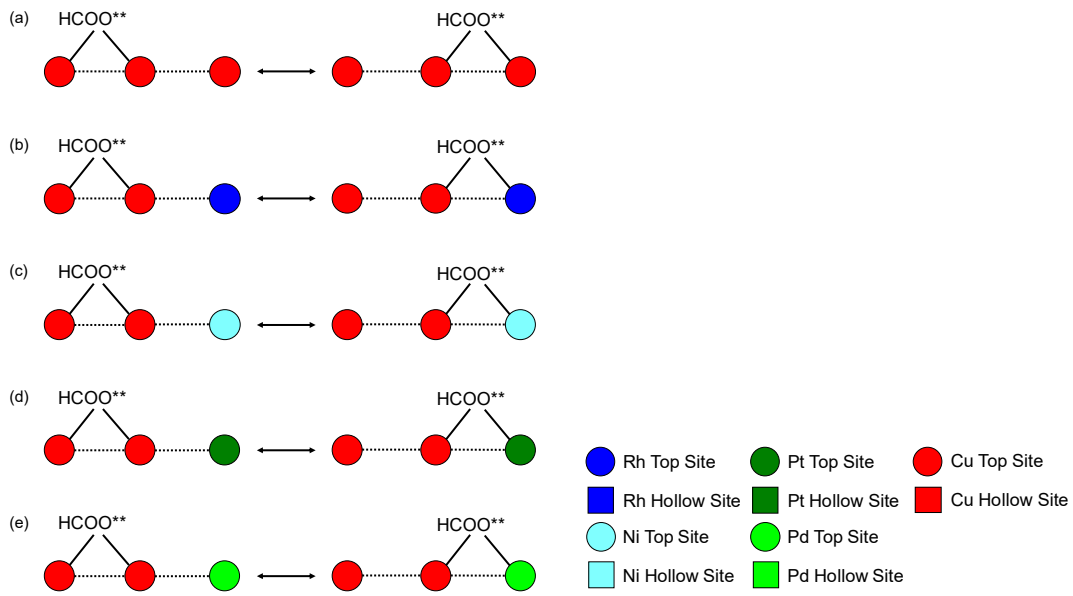


Figure B 6 Microscopic processes that could occur on the main lattice during the KMC simulation. Top sites of Rh, Ni, Pt, Pd, and Cu atoms of TD-SAA(100) are shown as blue, light blue, green, light green, and red circles, respectively. Hollow sites of Rh, Ni, Pt, Pd, and Cu atoms of TD-SAA(100) are shown as blue, light blue, green, light green, and red squires, respectively. Events (a) - (e) are HCOO** translation diffusions.

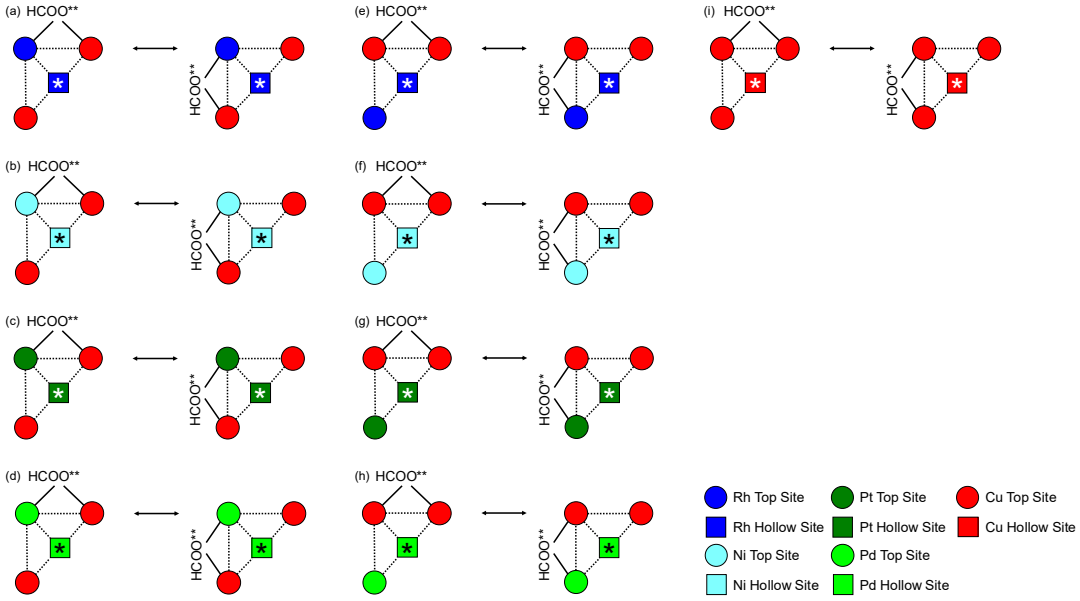


Figure B 7 Microscopic processes that could occur on the main lattice during the KMC simulation. Top sites of Rh, Ni, Pt, Pd, and Cu atoms of TD-SAA(100) are shown as blue, light blue, green, light green, and red circles, respectively. Asterisk indicates the sites must be empty for the diffusion step to occur. Hollow sites of Rh, Ni, Pt, Pd, and Cu atoms of TD-SAA(100) are shown as blue, light blue, green, light green, and red squires, respectively. Events (a) - (i) are HCOO** rotation diffusions.

Table B 1 ECI parameters and their graph multiplicities (GM). This table shows which clusters were used in the cluster expansion of each investigated alloy, along with the corresponding ECI and GM. The positions of occupied adsorption sites are shown in Figure B1. The double dashes indicate that the specific cluster was not used in this case. 'N/A' indicates that the given configuration is unstable, so large ECIs (3.0 eV) are used to avoid the occurrence of that configuration. The ECIs are given in eV and include zero-point energy corrections.

Energy Patterns for Simulation											
Pattern index	Adsorption Site					Effective cluster interaction (eV)					Graph Multiplicity
	H^*	H_2^*	$HCOO^{**}$	CO_2^*	CO^*	Rh Region	Ni Region	Pt Region	Pd Region	Cu Region	
1	1	--	--	--	--	-0.3	-0.23	-0.17	-0.10	-0.02	1
2	1 2	--	--	--	--	0.03	0.04	0.04	0.01	0.01	2
3	1 4	--	--	--	--	0.05	0.04	0.19	0.00	0.02	2
4	1 2 3	--	--	--	--	0.00	0.00	0.10	0.02	0.03	2
5	1 2 3 4	--	--	--	--	-0.02	-0.09	-0.31	0.05	-0.01	8
6	--	5	--	--	--	-0.32	-0.08	0.08	0.08	N/A	1
7	1	5	--	--	--	0.11	0.10	0.21	0.06	N/A	1
8	1 2	5	--	--	--	-0.04	-0.03	N/A	N/A	N/A	2
9	1 4	5	--	--	--	0.02	0.05	-0.11	N/A	N/A	2
10	1 2 3	5	--	--	--	0.02	0.01	N/A	N/A	N/A	2
11	1 2 3 4	5	--	--	--	0.10	-0.02	N/A	N/A	N/A	8
12	--	--	5 6	--	--	-0.20	-0.29	0.16	0.10	-0.14	1
13	1	--	5 6	--	--	0.14	0.16	0.17	0.04	0.03	1
14	2	--	5 6	--	--	0.24	0.24	0.28	0.14	0.10	1
15	1 3	--	5 6	--	--	-0.02	-0.02	-0.02	0.02	0.00	2
16	2 4	--	5 6	--	--	0.10	0.04	0.1	0.07	0.04	2
17	1 2	--	5 6	--	--	-0.05	-0.01	-0.04	-0.02	0.06	1

18	1 4	--	5 6	--	--	0.00	-0.05	-0.02	-0.02	-0.03	1
19	1 2 4	--	5 6	--	--	-0.05	-0.02	-0.01	-0.01	0.00	1
20	1 2 3	--	5 6	--	--	-0.02	0.01	0.04	-0.02	-0.02	1
21	1 2 3 4	--	5 6	--	--	0.05	-0.27	0.02	0.03	0.00	24
22	--	--	--	5	--	0.08	0.24	N/A	N/A	N/A	1
23	1	--	--	5	--	0.11	0.14	N/A	N/A	N/A	1
24	1 2	--	--	5	--	-0.03	-0.13	N/A	N/A	N/A	2
25	1 4	--	--	5	--	-0.04	0.11	N/A	N/A	N/A	2
26	1 2 3	--	--	5	--	N/A	N/A	N/A	N/A	N/A	2
27	1 2 3 4	--	--	5	--	N/A	N/A	N/A	N/A	N/A	8
28	--	--	--	--	5	-0.13	0.21	0.38	0.73	1.03	1
29	1	--	--	--	5	0.16	0.14	0.28	0.21	0.08	1
30	1 2	--	--	--	5	-0.01	-0.04	-0.03	-0.03	0.01	2
31	1 4	--	--	--	5	0.13	0.17	-0.03	0.14	0.12	2
32	1 2 3	--	--	--	5	-0.04	0.02	-0.06	0.02	-0.03	2
33	1 2 3 4	--	--	--	5	0.09	-0.11	0.22	-0.11	-0.06	8

Table B 2 Key elementary steps related to the HCOO dissociation mechanism on TD-SAA lattices. The frequency of initial, transition, and final states for each step are shown in the table, and blue frequencies indicate gas phase molecules. Forward energy barrier represents the reaction energy of a given elementary step from co-adsorbates. The energies are given in eV and include zero-point energy corrections. Since the partial pressures of CO_2 and H_2 are 0 bar during the reaction, no adsorption of these species will occur.

Elementary Steps in Simulation				
Reaction index	Initial Frequency	Transition Frequency	Final Frequency	Forward Energy Barrier (eV)
Fig.B2a	[2939 1505 1330 1289 976 731 311 294 247 100 93 71]	[1728 1361 1016 722 673 628 250 210 166 103 66]	[1698 1116 661 513 276 133 101 60 25] [1292 605 133]	0.55
Fig.B2b	[2938 1503 1332 1294 979 731 302 291 255 98 83 79]	[1752 1533 1132 657 600 565 240 192 125 111 48]	[1713 1124 640 487 247 121 81 75 27] [1183 457 285]	0.68
Fig.B2c	[2923 1503 1328 1290 982 732 307 261 236 88 72 61]	[1921 1566 1111 827 698 257 235 194 80 61 25]	[1663 704 270] [2337 1304 627 625]	0.79
Fig.B2d	[2915 1508 1329 1295 988 728 281 264 224 73 59 39]	[1847 1254 1110 834 709 512 209 128 102 66 46]	[867 572 211] [2337 1304 627 625]	0.94
Fig.B2e	[2923 1511 1339 1304 993 733 284 266 249 89 78 65]	[1976 1264 1005 802 777 480 184 149 76 56 33]	[622 520 487] [2337 1304 627 625]	0.95
Fig.B3a	[1183 457 285] [1183 457 285]	[1876 1661 390 354 172]	[2878 1470 840 299 270 187]	0.45
Fig.B3b	[1663 704 270] [1663 704 270]	[1997 1904 292 194 190]	[2548 1502 691 284 245 126]	0.38

Fig.B3c	[867 572 211] [867 572 211]	[1843 1625 374 304 184]	[3622 812 413 240 216 102]	0.68
Fig.B3d	[1183 457 285] [1183 457 285]	[1876 1661 390 354 172]	[2878 1470 840 299 270 187]	0.45
Fig.B3e	[1663 704 270] [1663 704 270]	[1997 1904 292 194 190]	[2548 1502 691 284 245 126]	0.23
Fig.B3f	[867 572 211] [867 572 211]	[1843 1625 374 304 184]	[3622 812 413 240 216 102]	0.68
Fig.B3g	[1292 605 133] [1292 605 133]	Non-activated Desorption	[4334]	0.57
Fig.B3h	[622 520 487] [622 520 487]	[1322 1223 690 438 355]	[4334]	0.77
Fig.B3i	[1292 605 133] [1292 605 133]	Non-activated Desorption	[4334]	0.55
Fig.B3j	[622 520 487] [622 520 487]	[1322 1223 690 438 355]	[4334]	0.76
Fig.B4a	[2878 1470 840 299 270 187]	Non-activated Desorption	[4334]	0.08
Fig.B4b	[2548 1502 691 284 245 126]	Non-activated Desorption	[4334]	0.00
Fig.B4c	[3622 812 413 240 216 102]	Non-activated Desorption	[4334]	0.00
Fig.B4d	[1698 1116 661 513 276 133 101 60 25]	Non-activated Desorption	[2337 1304 627 625]	0.00

Fig.B4e	[1713 1124 640 487 247 121 81 75 27]	Non-activated Desorption	[2337 1304 627 625]	0.00
Fig.B4f	[1940 436 349 348 56 52]	[2091 49 42][1]	[2100]	0.00
Fig.B4g	[1951 404 330 329 63 56]	[2086 55 46][1]	[2100]	0.01
Fig.B4h	[1972 431 326 326 63 59]	[2081 56 41][1]	[2100]	0.04
Fig.B4i	[1982 350 250 249 58 56]	[2096 54 28][1]	[2100]	0.01
Fig.B4j	[1987 308 264 263 55 41]	[2087 49 43][1]	[2100]	0.03
Fig.B5a	[622 520 487]	[1190 1173]	[622 520 487]	0.14
Fig.B5b	[1292 605 133]	[1174 1104]	[622 520 487]	0.14
Fig.B5c	[1183 457 285]	[1172 1117]	[622 520 487]	0.13
Fig.B5d	[1663 704 270]	[1184 1142]	[622 520 487]	0.18
Fig.B5e	[867 572 211]	[1187 1159]	[622 520 487]	0.16
Fig.B5f	[1987 308 264 263 55 41]	[1907 298 271 149 67]	[1987 308 264 263 55 41]	0.07
Fig.B5g	[1940 436 349 348 56 52]	[1930 305 262 164 53]	[1987 308 264 263 55 41]	0.01
Fig.B5h	[1951 404 330 329 63 56]	[1987 308 264 263 55][2]	[1987 308 264 263 55 41]	0.01
Fig.B5i	[1972 431 326 326 63 59]	[1987 308 264 263 55][2]	[1987 308 264 263 55 41]	0.01
Fig.B5j	[1982 350 250 249 58 56]	[1987 308 264 263 55][2]	[1987 308 264 263 55 41]	0.01
Fig.B6a[3]	[2923 1511 1339 1304 993 733 284 266 249 89 78 65]	[2909 1481 1301 1298 983 705 239 178 54 50 45]	[2923 1511 1339 1304 993 733 284 266 249 89 78 65]	0.35
Fig.B6b[3]	[2923 1511 1339 1304 993 733 284 266 249 89 78 65]	[2904 1474 1302 1291 976 695 243 175 61 60 49]	[2939 1505 1330 1289 976 731 311 294 247 100 93 71]	0.37

Fig.B6c[3]	[2923 1511 1339 1304 993 733 284 266 249 89 78 65]	[2909 1474 1300 1295 982 704 246 178 60 55 43]	[2938 1503 1332 1294 979 731 302 291 255 98 83 79]	0.30
Fig.B6d[3]	[2923 1511 1339 1304 993 733 284 266 249 89 78 65]	[2884 1575 1307 1185 975 711 263 206 89 43 20]	[2923 1503 1328 1290 982 732 307 261 236 88 72 61]	0.47
Fig.B6e[3]	[2923 1511 1339 1304 993 733 284 266 249 89 78 65]	[2904 1516 1305 1261 978 703 222 190 52 51 23]	[2915 1508 1329 1295 988 728 281 264 224 73 59 39]	0.41
Fig.B7a	[2939 1505 1330 1289 976 731 311 294 247 100 93 71]	[2936 179 1329 1279 969 715 281 272 184 96 89]	[2939 1505 1330 1289 976 731 311 294 247 100 93 71]	0.00
Fig.B7b	[2938 1503 1332 1294 979 731 302 291 255 98 83 79]	[2930 1481 1337 1283 975 714 279 252 183 105 91]	[2938 1503 1332 1294 979 731 302 291 255 98 83 79]	0.00
Fig.B7c	[2923 1503 1328 1290 982 732 307 261 236 88 72 61]	[2916 1482 1329 1278 975 714 255 222 184 74 57]	[2923 1503 1328 1290 982 732 307 261 236 88 72 61]	0.00
Fig.B7d	[2915 1508 1329 1295 988 728 281 264 224 73 59 39]	[2906 1498 1332 1272 982 711 243 210 194 71 56]	[2915 1508 1329 1295 988 728 281 264 224 73 59 39]	0.00
Fig.B7e	[2923 1511 1339 1304 993 733 284 266 249 89 78 65]	[2913 1484 1337 1289 981 712 236 217 182 83 71]	[2939 1505 1330 1289 976 731 311 294 247 100 93 71]	0.15
Fig.B7f	[2923 1511 1339 1304 993 733 284 266 249 89 78 65]	[2912 1491 1337 1289 985 714 244 226 191 85 74]	[2938 1503 1332 1294 979 731 302 291 255 98 83 79]	0.00
Fig.B7g	[2923 1511 1339 1304 993 733 284 266 249 89 78 65]	[2912 1479 1328 1281 982 717 231 227 142 67 52]	[2923 1503 1328 1290 982 732 307 261 236 88 72 61]	0.30

Fig.B7h	[2923 1511 1339 1304 993 733 284 266 249 89 78 65]	[2912 1482 1329 1285 984 718 237 221 144 77 66]	[2915 1508 1329 1295 988 728 281 264 224 73 59 39]	0.17
Fig.B7i	[2923 1511 1339 1304 993 733 284 266 249 89 78 65]	[2912 1491 1338 1290 984 713 246 224 189 87 69]	[2923 1511 1339 1304 993 733 284 266 249 89 78 65]	0.01

1. Two vibrational modes are missing and correspond to rotations. In this work, we treat these modes using a free-rotor model.
2. The transition-state barrier is too small (< 0.01 eV) to resolve, indicating an initial-state–like transition state. Therefore, the transition-state frequencies are taken to be those of the initial state, with the ideal diffusion mode removed.
3. Lateral diffusion of HCOO** may, in principle, involve a sizable energy barrier. However, we treat it as fast diffusion, because the rotational diffusion barrier is low (see Figure B7), enabling rapid surface diffusion of HCOO**.

Table B 3 Peak temperatures of HCOO** dissociation TPD spectra obtained from simulations (before and after modifying the C-H activation barriers), experiments, and their deviations. The temperature begins at 100 K with 1000 H* and 1000 HCOO** on the lattice and ends at 550 K, with a ramp rate of 2 K/s. Positive deviations are indicated in blue and negative deviations in red.

	TPD Peak (K)									
Surface	Experimental Peak		Simulation Peak		Deviation Model 1 from Experiment		Simulation Peak (with E_a + 0.2 eV)		Deviation Model 2 from Experiment	
	H_2	CO_2	H_2	CO_2	H_2	CO_2	H_2	CO_2	H_2	CO_2
RhCu(100)	215	283	204	254	-11	-29	204	318	-11	+35
NiCu(100)	202	377	172	306	-30	-71	174	378	-28	+1
PtCu(100)	223	379	198	312	-25	-67	199	374	-24	-5
PdCu(100)	231	405	260	328	+29	-77	260	390	+29	-15
Cu(100)	252	409	288	328	+36	-81	290	390	+38	-19

References

(1) Li, W.; Madan, S. E.; Réocreux, R.; Stamatakis, M. Elucidating the Reactivity of Oxygenates on Single-Atom Alloy Catalysts. *ACS Catalysis* **2023**, *13* (24), 15851–15868.

(2) Wang, Y.; Li., W; Lam, H; Schumann, J; Réocreux, R; Hannagan, R. T.; Çınar, V; Daniels, A. S.; Swearer, D. F.; Michaelides, A.; Deshlahra, P.; Eagan, N. M.; Stamatakis, M.; Sykes, E. C. H. Breaking Established Reactivity Trends with Single-Atom Alloys. Submitted.

(3) Wang, Y.; Li, W.; Schumann, J.; Réocreux, R.; Daniels, A. S.; Rajabi, N.; Michaelides, A.; Stamatakis, M.; Sykes, E. C. H. Secondary Single-Atom Sites in Single-Atom Alloy Surfaces Enhance Reactivity by Scavenging CO. *Nature Chemistry* **2025**. In preparation.

(4) Energy, I. *Statistical Review of World Energy 2025*; Energy Institute, London, 2025. https://www.energyinst.org/statistical-review.

(5) International Energy, A. *Global Hydrogen Review 2025: Demand*; International Energy Agency, 2025. https://www.iea.org/reports/global-hydrogen-review-2025/demand.

(6) Grasemann, M.; Laurenczy, G. Formic acid as a hydrogen source – recent developments and future trends. *Energy & Environmental Science* **2012**, *5* (8), 8171–8181.

(7) Usman, M.; Yamada, T. Methanol Reforming for Hydrogen Production: Advances in Catalysts, Nanomaterials, Reactor Design, and Fuel Cell Integration. *ACS Engineering Au* **2025**, *5* (4), 314–346.

(8) Group, I. *Global Industrial Catalyst Market Statistics*; 2024. https://www.imarcgroup.com/industrial-catalyst-market-statistics.

(9) Johnson, M. PGM chemicals and catalysts.

(10) Survey, U. S. G. Platinum-Group Metals Statistics and Information.

(11) Arends, I. W. C. E.; Sheldon, R. A. Activities and stabilities of heterogeneous catalysts in selective liquid phase oxidations: recent developments. *Applied Catalysis A: General* **2001**, *212* (1), 175–187.

(12) Cole-Hamilton, D. J. Homogeneous Catalysis--New Approaches to Catalyst Separation, Recovery, and Recycling. *Science* **2003**, *299* (5613), 1702–1706.

(13) Vural Gürsel, I.; Noël, T.; Wang, Q.; Hessel, V. Separation/recycling methods for homogeneous transition metal catalysts in continuous flow. *Green Chemistry* **2015**, *17* (4), 2012–2026.

(14) Réocreux, R.; Stamatakis, M. One Decade of Computational Studies on Single-Atom Alloys: Is In Silico Design within Reach? *Accounts of Chemical Research* **2022**, *55* (1), 87–97.

(15) Hannagan, R. T.; Giannakakis, G.; Flytzani-Stephanopoulos, M.; Sykes, E. C. H. Single-Atom Alloy Catalysis. *Chemical Reviews* **2020**, *120* (21), 12044–12088.

(16) Qin, F.; Chen, W. Copper-based single-atom alloys for heterogeneous catalysis. *Chemical Communications* **2021**, *57* (22), 2710–2723.

(17) Kresse, G.; Hafner, J. Ab initio molecular dynamics for liquid metals. *Physical Review B* **1993**, *47* (1), 558–561.

(18) Kresse, G.; Furthmüller, J. Efficient iterative schemes for ab initio total-energy calculations using a plane-wave basis set. *Physical Review B* **1996**, *54* (16), 11169–11186.

(19) Dong, W.; Kresse, G.; Furthmüller, J.; Hafner, J. Chemisorption of H on Pd(111): An ab initio approach with ultrasoft pseudopotentials. *Physical Review B* **1996**, *54* (3), 2157–2166.

(20) Gillespie, D. T. Exact stochastic simulation of coupled chemical reactions. *The Journal of Physical Chemistry* **1977**, *81* (25), 2340–2361.

(21) Bortz, A. B.; Kalos, M. H.; Lebowitz, J. L. A new algorithm for Monte Carlo simulation of Ising spin systems. *Journal of Computational Physics* **1975**, *17* (1), 10–18.

(22) Fichthorn, K. A.; Weinberg, W. H. Theoretical foundations of dynamical Monte Carlo simulations. *The Journal of Chemical Physics* **1991**, *95* (2), 1090–1096.

(23) Voter, A. F. INTRODUCTION TO THE KINETIC MONTE CARLO METHOD. In *Radiation Effects in Solids*, Dordrecht, 2007//, 2007; Sickafus, K. E., Kotomin, E. A., Uberuaga, B. P., Eds.; Springer Netherlands: pp 1–23.

(24) Ziff, R. M.; Gulari, E.; Barshad, Y. Kinetic Phase Transitions in an Irreversible Surface-Reaction Model. *Physical Review Letters* **1986**, *56* (24), 2553–2556.

(25) Reuter, K.; Scheffler, M. First-principles kinetic Monte Carlo simulations for heterogeneous catalysis: Application to the CO oxidation at RuO_2(110). *Physical Review B* **2006**, *73* (4), 045433.

(26) Stamatakis, M.; Vlachos, D. G. A graph-theoretical kinetic Monte Carlo framework for on-lattice chemical kinetics. *The Journal of Chemical Physics* **2011**, *134* (21), 214115.

(27) Garcia, G.; Arriola, E.; Chen, W.-H.; De Luna, M. D. A comprehensive review of hydrogen production from methanol thermochemical conversion for sustainability. *Energy* **2021**, *217*, 119384.

(28) B. S, T.; Asapu, R. State of the Art of Methanol Reforming for Hydrogen Generation. *ChemBioEng Reviews* **2024**, *11* (3), 543–554.

(29) Olah, G. A. Beyond Oil and Gas: The Methanol Economy. *Angewandte Chemie International Edition* **2005**, *44* (18), 2636–2639.

(30) Schorn, F.; Breuer, J. L.; Samsun, R. C.; Schnorbus, T.; Heuser, B.; Peters, R.; Stolten, D. Methanol as a renewable energy carrier: An assessment of production and transportation costs for selected global locations. *Advances in Applied Energy* **2021**, *3*, 100050.

(31) Makepeace, J. W.; He, T.; Weidenthaler, C.; Jensen, T. R.; Chang, F.; Vegge, T.; Ngene, P.; Kojima, Y.; de Jongh, P. E.; Chen, P.; et al. Reversible ammonia-based and liquid organic hydrogen carriers for high-density hydrogen storage: Recent progress. *International Journal of Hydrogen Energy* **2019**, *44* (15), 7746–7767.

(32) Eppinger, J.; Huang, K.-W. Formic Acid as a Hydrogen Energy Carrier. *ACS Energy Letters* **2017**, *2* (1), 188–195.

(33) Wang, X.; Meng, Q.; Gao, L.; Jin, Z.; Ge, J.; Liu, C.; Xing, W. Recent progress in hydrogen production from formic acid decomposition. *International Journal of Hydrogen Energy* **2018**, *43* (14), 7055–7071.

(34) Bartholomew, C. H. Mechanisms of catalyst deactivation. *Applied Catalysis A: General* **2001**, *212* (1), 17–60.

(35) Xu, S.; Chansai, S.; Xu, S.; Stere, C. E.; Jiao, Y.; Yang, S.; Hardacre, C.; Fan, X. CO Poisoning of Ru Catalysts in CO2 Hydrogenation under Thermal and Plasma Conditions: A Combined Kinetic and Diffuse Reflectance Infrared Fourier Transform Spectroscopy–Mass Spectrometry Study. *ACS Catalysis* **2020**, *10* (21), 12828–12840.

(36) de Vries, J. G.; Jackson, S. D. Homogeneous and heterogeneous catalysis in industry. *Catalysis Science & Technology* **2012**, *2* (10), 2009–2009.

(37) Fechete, I.; Wang, Y.; Védrine, J. C. The past, present and future of heterogeneous catalysis. *Catalysis Today* **2012**, *189* (1), 2–27.

(38) Bell, A. T. The Impact of Nanoscience on Heterogeneous Catalysis. *Science* **2003**, *299* (5613), 1688–1691.

(39) Schlögl, R. Heterogeneous Catalysis. *Angewandte Chemie International Edition* **2015**, *54* (11), 3465–3520.

(40) Ertl, G. Reactions at Surfaces: From Atoms to Complexity (Nobel Lecture). *Angewandte Chemie International Edition* **2008**, *47* (19), 3524–3535.

(41) Stamatakis, M.; Vlachos, D. G. Unraveling the Complexity of Catalytic Reactions via Kinetic Monte Carlo Simulation: Current Status and Frontiers. *ACS Catalysis* **2012**, *2* (12), 2648–2663.

(42) Nørskov, J. K.; Bligaard, T.; Rossmeisl, J.; Christensen, C. H. Towards the computational design of solid catalysts. *Nature Chemistry* **2009**, *1* (1), 37–46.

(43) Sabatier, P. *La catalyse en chimie organique*; C. Béranger, 1913.

(44) Medford, A. J.; Vojvodic, A.; Hummelshøj, J. S.; Voss, J.; Abild-Pedersen, F.; Studt, F.; Bligaard, T.; Nilsson, A.; Nørskov, J. K. From the Sabatier principle to a predictive theory of transition-metal heterogeneous catalysis. *Journal of Catalysis* **2015**, *328*, 36–42.

(45) Balandin, A. A. Modern State of the Multiplet Theor of Heterogeneous Catalysis *Advances in Catalysis*, Eley, D. D., Pines, H., Weisz, P. B. Eds.; Vol. 19; Academic Press, 1969; pp 1–210.

(46) Hammer, B.; Nørskov, J. K. Theoretical surface science and catalysis—calculations and concepts. In *Advances in Catalysis*, Vol. 45; Academic Press, 2000; pp 71–129.

(47) Evans, M. G.; Polanyi, M. Inertia and driving force of chemical reactions. *Transactions of the Faraday Society* **1938**, *34* (0), 11–24.

(48) Logadottir, A.; Rod, T. H.; Nørskov, J. K.; Hammer, B.; Dahl, S.; Jacobsen, C. J. H. The Brønsted–Evans–Polanyi Relation and the Volcano Plot for Ammonia Synthesis over Transition Metal Catalysts. *Journal of Catalysis* **2001**, *197* (2), 229–231.

(49) Michaelides, A.; Liu, Z. P.; Zhang, C. J.; Alavi, A.; King, D. A.; Hu, P. Identification of General Linear Relationships between Activation Energies and Enthalpy Changes for Dissociation Reactions at Surfaces. *Journal of the American Chemical Society* **2003**, *125* (13), 3704–3705.

(50) Bligaard, T.; Nørskov, J. K.; Dahl, S.; Matthiesen, J.; Christensen, C. H.; Sehested, J. The Brønsted–Evans–Polanyi relation and the volcano curve in heterogeneous catalysis. *Journal of Catalysis* **2004**, *224* (1), 206–217.

(51) Abild-Pedersen, F.; Greeley, J.; Studt, F.; Rossmeisl, J.; Munter, T. R.; Moses, P. G.; Skúlason, E.; Bligaard, T.; Nørskov, J. K. Scaling Properties of Adsorption Energies for Hydrogen-Containing Molecules on Transition-Metal Surfaces. *Physical Review Letters* **2007**, *99* (1), 016105.

(52) Boucher, M. B.; Zugic, B.; Cladaras, G.; Kammert, J.; Marcinkowski, M. D.; Lawton, T. J.; Sykes, E. C. H.; Flytzani-Stephanopoulos, M. Single atom alloy surface analogs in Pd0.18Cu15 nanoparticles for selective hydrogenation reactions. *Physical Chemistry Chemical Physics* **2013**, *15* (29), 12187–12196.

(53) Kyriakou, G.; Boucher, M. B.; Jewell, A. D.; Lewis, E. A.; Lawton, T. J.; Baber, A. E.; Tierney, H. L.; Flytzani-Stephanopoulos, M.; Sykes, E. C. H. Isolated Metal Atom Geometries as a Strategy for Selective Heterogeneous Hydrogenations. *Science* **2012**, *335* (6073), 1209–1212.

(54) Lucci, F. R.; Liu, J.; Marcinkowski, M. D.; Yang, M.; Allard, L. F.; Flytzani-Stephanopoulos, M.; Sykes, E. C. H. Selective hydrogenation of 1,3-butadiene on platinum–copper alloys at the single-atom limit. *Nature Communications* **2015**, *6* (1), 8550.

(55) Shan, J.; Liu, J.; Li, M.; Lustig, S.; Lee, S.; Flytzani-Stephanopoulos, M. NiCu single atom alloys catalyze the CH bond activation in the selective non-oxidative ethanol dehydrogenation reaction. *Applied Catalysis B: Environmental* **2018**, *226*, 534–543.

(56) Marcinkowski, M. D.; Liu, J.; Murphy, C. J.; Liriano, M. L.; Wasio, N. A.; Lucci, F. R.; Flytzani-Stephanopoulos, M.; Sykes, E. C. H. Selective Formic Acid Dehydrogenation on Pt-Cu Single-Atom Alloys. *ACS Catalysis* **2017**, *7* (1), 413–420.

(57) Liu, J.; Lucci, F. R.; Yang, M.; Lee, S.; Marcinkowski, M. D.; Therrien, A. J.; Williams, C. T.; Sykes, E. C. H.; Flytzani-Stephanopoulos, M. Tackling CO Poisoning with Single-Atom Alloy Catalysts. *Journal of the American Chemical Society* **2016**, *138* (20), 6396–6399.

(58) Marcinkowski, M. D.; Jewell, A. D.; Stamatakis, M.; Boucher, M. B.; Lewis, E. A.; Murphy, C. J.; Kyriakou, G.; Sykes, E. C. H. Controlling a spillover pathway with the molecular cork effect. *Nature Materials* **2013**, *12* (6), 523–528.

(59) Darby, M. T.; Réocreux, R.; Sykes, E. C. H.; Michaelides, A.; Stamatakis, M. Elucidating the Stability and Reactivity of Surface Intermediates on Single-Atom Alloy Catalysts. *ACS Catalysis* **2018**, *8* (6), 5038–5050.

(60) Darby, M. T.; Stamatakis, M.; Michaelides, A.; Sykes, E. C. H. Lonely Atoms with Special Gifts: Breaking Linear Scaling Relationships in Heterogeneous Catalysis with Single-Atom Alloys. *The Journal of Physical Chemistry Letters* **2018**, *9* (18), 5636–5646.

(61) Köuppel, H.; Domcke, W.; Cederbaum, L. S. Multimode Molecular Dynamics Beyond the Born-Oppenheimer Approximation. In *Advances in Chemical Physics*, Advances in Chemical Physics, 1984; pp 59–246.

(62) Slater, J. C. A Simplification of the Hartree-Fock Method. *Physical Review* **1951**, *81* (3), 385–390.

(63) Pauli, W. Über den Zusammenhang des Abschlusses der Elektronengruppen im Atom mit der Komplexstruktur der Spektren. *Zeitschrift für Physik* **1925**, *31* (1), 765–783.

(64) Hartree, D. R. The Wave Mechanics of an Atom with a Non-Coulomb Central Field. Part I. Theory and Methods. *Mathematical Proceedings of the Cambridge Philosophical Society* **1928**, *24* (1), 89–110.

(65) Fock, V. „Selfconsistent field“ mit Austausch für Natrium. *Zeitschrift für Physik* **1930**, *62* (11), 795–805.

(66) Pulay, P. Convergence acceleration of iterative sequences. the case of scf iteration. *Chemical Physics Letters* **1980**, *73* (2), 393–398.

(67) Roothaan, C. C. J. New Developments in Molecular Orbital Theory. *Reviews of Modern Physics* **1951**, *23* (2), 69–89.

(68) Møller, C.; Plesset, M. S. Note on an Approximation Treatment for Many-Electron Systems. *Physical Review* **1934**, *46* (7), 618–622.

(69) Kohn, W.; Sham, L. J. Self-Consistent Equations Including Exchange and Correlation Effects. *Physical Review* **1965**, *140* (4A), A1133–A1138.

(70) Hohenberg, P.; Kohn, W. Inhomogeneous Electron Gas. *Physical Review* **1964**, *136* (3B), B864–B871.

(71) Levy, M. Universal variational functionals of electron densities, first-order density matrices, and natural spin-orbitals and solution of the v-representability problem. *Proceedings of the National Academy of Sciences* **1979**, *76* (12), 6062–6065.

(72) Lieb, E. H. Density functionals for coulomb systems. *International Journal of Quantum Chemistry* **1983**, *24* (3), 243–277.

(73) What is Density Functional Theory? In *Density Functional Theory*, 2009; pp 1–33.

(74) Perdew, J. P.; Schmidt, K. Jacob's ladder of density functional approximations for the exchange-correlation energy. *AIP Conference Proceedings* **2001**, *577* (1), 1–20.

(75) Vosko, S. H.; Wilk, L. A comparison of self-interaction-corrected local correlation energy functionals. *Journal of Physics B: Atomic and Molecular Physics* **1983**, *16* (20), 3687.

(76) Perdew, J. P.; Zunger, A. Self-interaction correction to density-functional approximations for many-electron systems. *Physical Review B* **1981**, *23* (10), 5048–5079.

(77) Langreth, D. C.; Perdew, J. P. Theory of nonuniform electronic systems. I. Analysis of the gradient approximation and a generalization that works. *Physical Review B* **1980**, *21* (12), 5469–5493.

(78) Becke, A. D. Density-functional exchange-energy approximation with correct asymptotic behavior. *Physical Review A* **1988**, *38* (6), 3098–3100.

(79) Kohn, W.; Becke, A. D.; Parr, R. G. Density Functional Theory of Electronic Structure. *The Journal of Physical Chemistry* **1996**, *100* (31), 12974–12980.

(80) Perdew, J. P.; Yue, W. Accurate and simple density functional for the electronic exchange energy: Generalized gradient approximation. *Physical Review B* **1986**, *33* (12), 8800–8802.

(81) Lacks, D. J.; Gordon, R. G. Pair interactions of rare-gas atoms as a test of exchange-energy-density functionals in regions of large density gradients. *Physical Review A* **1993**, *47* (6), 4681–4690.

(82) Tao, J.; Perdew, J. P.; Staroverov, V. N.; Scuseria, G. E. Climbing the Density Functional Ladder: Nonempirical Meta--Generalized Gradient Approximation Designed for Molecules and Solids. *Physical Review Letters* **2003**, *91* (14), 146401.

(83) Becke, A. D. Density-functional thermochemistry. III. The role of exact exchange. *The Journal of Chemical Physics* **1993**, *98* (7), 5648–5652.

(84) Klimeš, J.; Bowler, D. R.; Michaelides, A. Van der Waals density functionals applied to solids. *Physical Review B* **2011**, *83* (19), 195131.

(85) Hammer, B.; Hansen, L. B.; Nørskov, J. K. Improved adsorption energetics within density-functional theory using revised Perdew-Burke-Ernzerhof functionals. *Physical Review B* **1999**, *59* (11), 7413–7421.

(86) Becke, A. D. On the large-gradient behavior of the density functional exchange energy. *The Journal of Chemical Physics* **1986**, *85* (12), 7184–7187.

(87) Dion, M.; Rydberg, H.; Schröder, E.; Langreth, D. C.; Lundqvist, B. I. Van der Waals Density Functional for General Geometries. *Physical Review Letters* **2004**, *92* (24), 246401.

(88) Perdew, J. P.; Burke, K.; Ernzerhof, M. Generalized Gradient Approximation Made Simple. *Physical Review Letters* **1996**, *77* (18), 3865–3868.

(89) Payne, M. C.; Teter, M. P.; Allan, D. C.; Arias, T. A.; Joannopoulos, J. D. Iterative minimization techniques for ab initio total-energy calculations: molecular dynamics and conjugate gradients. *Reviews of Modern Physics* **1992**, *64* (4),

1045–1097.

(90) Neugebauer, J.; Scheffler, M. Adsorbate-substrate and adsorbate-adsorbate interactions of Na and K adlayers on Al(111). *Physical Review B* **1992**, *46* (24), 16067–16080.

(91) Bengtsson, L. Dipole correction for surface supercell calculations. *Physical Review B* **1999**, *59* (19), 12301–12304.

(92) Bloch, F. Über die Quantenmechanik der Elektronen in Kristallgittern. *Zeitschrift für Physik* **1929**, *52* (7), 555–600.

(93) Vanderbilt, D. Soft self-consistent pseudopotentials in a generalized eigenvalue formalism. *Physical Review B* **1990**, *41* (11), 7892–7895.

(94) Troullier, N.; Martins, J. L. Efficient pseudopotentials for plane-wave calculations. *Physical Review B* **1991**, *43* (3), 1993–2006.

(95) Phillips, J. C.; Kleinman, L. New Method for Calculating Wave Functions in Crystals and Molecules. *Physical Review* **1959**, *116* (2), 287–294.

(96) Kresse, G.; Joubert, D. From ultrasoft pseudopotentials to the projector augmented-wave method. *Physical Review B* **1999**, *59* (3), 1758–1775.

(97) Kresse, G.; Furthmüller, J. Efficiency of ab-initio total energy calculations for metals and semiconductors using a plane-wave basis set. *Computational Materials Science* **1996**, *6* (1), 15–50.

(98) Ashcroft, N. W. a. M., N.D. *Solid State Physics*; Saunders, Philadelphia, 1976.

(99) Monkhorst, H. J.; Pack, J. D. Special points for Brillouin-zone integrations. *Physical Review B* **1976**, *13* (12), 5188–5192.

(100) Methfessel, M.; Paxton, A. T. High-precision sampling for Brillouin-zone integration in metals. *Physical Review B* **1989**, *40* (6), 3616–3621.

(101) Blöchl, P. E.; Jepsen, O.; Andersen, O. K. Improved tetrahedron method for Brillouin-zone integrations. *Physical Review B* **1994**, *49* (23), 16223–16233.

(102) Blöchl, P. E. Projector augmented-wave method. *Physical Review B* **1994**, *50* (24), 17953–17979.

(103) Sanchez-Portal, D.; Artacho, E.; Soler, J. M. Projection of plane-wave calculations into atomic orbitals. *Solid State Communications* **1995**, *95* (10), 685–690.

(104) Hughbanks, T.; Hoffmann, R. Chains of trans-edge-sharing molybdenum octahedra: metal-metal bonding in extended systems. *Journal of the American Chemical Society* **1983**, *105* (11), 3528–3537.

(105) Dronskowski, R.; Bloechl, P. E. Crystal orbital Hamilton populations (COHP): energy-resolved visualization of chemical bonding in solids based on density-functional calculations. *The Journal of Physical Chemistry* **1993**, *97* (33), 8617–8624.

(106) Henkelman, G.; Jónsson, H. Improved tangent estimate in the nudged elastic band method for finding minimum energy paths and saddle points. *The Journal of Chemical Physics* **2000**, *113* (22), 9978–9985.

(107) Henkelman, G.; Uberuaga, B. P.; Jónsson, H. A climbing image nudged elastic band method for finding saddle points and minimum energy paths. *The Journal of Chemical Physics* **2000**, *113* (22), 9901–9904.

(108) Henkelman, G.; Jónsson, H. A dimer method for finding saddle points on high dimensional potential surfaces using only first derivatives. *The Journal of Chemical Physics* **1999**, *111* (15), 7010–7022.

(109) Schlegel, H. B. Optimization of equilibrium geometries and transition structures. *Journal of Computational Chemistry* **1982**, *3* (2), 214–218.

(110) Conjugate Gradient Methods. In *Numerical Optimization*, Nocedal, J., Wright, S. J. Eds.; Springer New York, 2006; pp 101–134.

(111) Pulay, P. Ab initio calculation of force constants and equilibrium geometries in polyatomic molecules. *Molecular Physics* **1969**, *17* (2), 197–204.

(112) Fletcher, R.; Powell, M. J. D. A Rapidly Convergent Descent Method for Minimization. *The Computer Journal* **1963**, *6* (2), 163–168.

(113) Broyden, C. G. The convergence of single-rank quasi-Newton methods. *Mathematics of Computation* **1970**, *24* (110), 365–382.

(114) Fletcher, R.; Reeves, C. M. Function minimization by conjugate gradients. *The Computer Journal* **1964**, *7* (2), 149–154.

(115) Wolfe, P. Convergence Conditions for Ascent Methods. *SIAM Review* **1969**, *11* (2), 226–235.

(116) Polak, E.; Ribiere, G. Note sur la convergence de méthodes de directions conjuguées. *Revue française d'informatique et de recherche opérationnelle. Série rouge* **1969**, *3* (R1), 35–43.

(117) Schlegel, H. B. Geometry optimization. *WIREs Computational Molecular Science* **2011**, *1* (5), 790–809.

(118) Miller, W. H.; Handy, N. C.; Adams, J. E. Reaction path Hamiltonian for polyatomic molecules. *The Journal of Chemical Physics* **1980**, *72* (1), 99–112.

(119) Mills, G.; Jónsson, H.; Schenter, G. K. Reversible work transition state theory: application to dissociative adsorption of hydrogen. *Surface Science* **1995**, *324* (2), 305–337.

(120) Togo, A.; Tanaka, I. First principles phonon calculations in materials science. *Scripta Materialia* **2015**, *108*, 1–5.

(121) Parlinski, K.; Li, Z. Q.; Kawazoe, Y. First-Principles Determination of the Soft Mode in Cubic ZrO_2. *Physical Review Letters* **1997**, *78* (21), 4063–4066.

(122) Maintz, S.; Deringer, V. L.; Tchougréeff, A. L.; Dronskowski, R. LOBSTER: A tool to extract chemical bonding from plane-wave based DFT. *Journal of Computational Chemistry* **2016**, *37* (11), 1030–1035.

(123) Deringer, V. L.; Tchougréeff, A. L.; Dronskowski, R. Crystal Orbital Hamilton Population (COHP) Analysis As Projected from Plane-Wave Basis Sets. *The Journal of Physical Chemistry A* **2011**, *115* (21), 5461–5466.

(124) Hjorth Larsen, A.; Jørgen Mortensen, J.; Blomqvist, J.; Castelli, I. E.; Christensen, R.; Dułak, M.; Friis, J.; Groves, M. N.; Hammer, B.; Hargus, C.; et al. The atomic simulation environment—a Python library for working with atoms. *Journal of Physics: Condensed Matter* **2017**, *29* (27), 273002.

(125) Momma, K.; Izumi, F. VESTA 3 for three-dimensional visualization of crystal, volumetric and morphology data. *Journal of Applied Crystallography* **2011**, *44* (6), 1272–1276.

(126) Hanson, R. Jmol - a paradigm shift in crystallographic visualization. *Journal*

of Applied Crystallography **2010**, *43* (5 Part 2), 1250–1260.

(127) Arrhenius, S. Über die Reaktionsgeschwindigkeit bei der Inversion von Rohrzucker durch Säuren. **1889**, *4U* (1), 226–248.

(128) Eyring, H. The Activated Complex in Chemical Reactions. *The Journal of Chemical Physics* **1935**, *3* (2), 107–115.

(129) Campbell, C. T. Finding the Rate-Determining Step in a Mechanism: Comparing DeDonder Relations with the “Degree of Rate Control”. *Journal of Catalysis* **2001**, *204* (2), 520–524.

(130) Stegelmann, C.; Andreasen, A.; Campbell, C. T. Degree of Rate Control: How Much the Energies of Intermediates and Transition States Control Rates. *Journal of the American Chemical Society* **2009**, *131* (23), 8077–8082.

(131) Campbell, C. T. The Degree of Rate Control: A Powerful Tool for Catalysis Research. *ACS Catalysis* **2017**, *7* (4), 2770–2779.

(132) Chen, B. W. J.; Xu, L.; Mavrikakis, M. Computational Methods in Heterogeneous Catalysis. *Chemical Reviews* **2020**, *121* (2), 1007–1048.

(133) Nørskov, J. K.; Abild-Pedersen, F.; Studt, F.; Bligaard, T. Density functional theory in surface chemistry and catalysis. *Proceedings of the National Academy of Sciences* **2011**, *108* (3), 937–943.

(134) Frenkel, D.; Smit, B. Chapter 1 - Introduction. In *Understanding Molecular Simulation (Second Edition)*, Frenkel, D., Smit, B. Eds.; Academic Press, 2002; pp 1–6.

(135) Voter, A. F. Hyperdynamics: Accelerated Molecular Dynamics of Infrequent Events. *Physical Review Letters* **1997**, *78* (20), 3908–3911.

(136) Xu, L.; Henkelman, G. Adaptive kinetic Monte Carlo for first-principles accelerated dynamics. *The Journal of Chemical Physics* **2008**, *129* (11).

(137) Pineda, M.; Stamatakis, M. Kinetic Monte Carlo simulations for heterogeneous catalysis: Fundamentals, current status, and challenges. *The Journal of Chemical Physics* **2022**, *156* (12).

(138) Prats, H.; Illas, F.; Sayós, R. General concepts, assumptions, drawbacks, and misuses in kinetic Monte Carlo and microkinetic modeling simulations applied

to computational heterogeneous catalysis. *International Journal of Quantum Chemistry* **2017**, *118* (9).

(139) Stillinger, F. H.; Weber, T. A. Hidden structure in liquids. *Physical Review A* **1982**, *25* (2), 978–989.

(140) Stillinger, F. H. A Topographic View of Supercooled Liquids and Glass Formation. *Science* **1995**, *267* (5206), 1935–1939.

(141) Stillinger, F. H.; Weber, T. A. Dynamics of structural transitions in liquids. *Physical Review A* **1983**, *28* (4), 2408–2416.

(142) Gillespie, D. T. A general method for numerically simulating the stochastic time evolution of coupled chemical reactions. *Journal of Computational Physics* **1976**, *22* (4), 403–434.

(143) Langmuir, I. THE ADSORPTION OF GASES ON PLANE SURFACES OF GLASS, MICA AND PLATINUM. *Journal of the American Chemical Society* **1918**, *40* (9), 1361–1403.

(144) Andersen, M.; Panosetti, C.; Reuter, K. A Practical Guide to Surface Kinetic Monte Carlo Simulations. *Frontiers in Chemistry* **2019**, *Volume 7 - 2019*.

(145) Van Kampen, N. G. Chapter V - THE MASTER EQUATION. In *Stochastic Processes in Physics and Chemistry (Third Edition)*, Van Kampen, N. G. Ed.; Elsevier, 2007; pp 96–133.

(146) Gardiner, C. W. Handbook of Stochastic Methods for Physics, Chemistry and the Natural Sciences. In *Springer Series in Synergetics*, Springer Berlin Heidelberg: 1985.

(147) Hänggi, P.; Talkner, P.; Borkovec, M. Reaction-rate theory: fifty years after Kramers. *Reviews of Modern Physics* **1990**, *62* (2), 251–341.

(148) Kramers, H. A. Brownian motion in a field of force and the diffusion model of chemical reactions. *Physica* **1940**, *7* (4), 284–304.

(149) Gillespie, D. T. A rigorous derivation of the chemical master equation. *Physica A: Statistical Mechanics and its Applications* **1992**, *188* (1), 404–425.

(150) Metropolis, N.; Rosenbluth, A. W.; Rosenbluth, M. N.; Teller, A. H.; Teller, E. Equation of State Calculations by Fast Computing Machines. *The Journal of*

Chemical Physics **1953**, *21* (6), 1087–1092.

(151) Hastings, W. K. Monte Carlo sampling methods using Markov chains and their applications. *Biometrika* **1970**, *57* (1), 97–109.

(152) Kelly, F. P. *Reversibility and stochastic networks*; Cambridge Univ. Press, 2011.

(153) Anderson, D. F. A modified next reaction method for simulating chemical systems with time dependent propensities and delays. *The Journal of Chemical Physics* **2007**, *127* (21), 214107.

(154) Gillespie, D. T. Stochastic Simulation of Chemical Kinetics. *Annual Review of Physical Chemistry* **2007**, *58* (Volume 58, 2007), 35–55.

(155) Gibson, M. A.; Bruck, J. Efficient Exact Stochastic Simulation of Chemical Systems with Many Species and Many Channels. *The Journal of Physical Chemistry A* **2000**, *104* (9), 1876–1889.

(156) Vineyard, G. H. Frequency factors and isotope effects in solid state rate processes. *Journal of Physics and Chemistry of Solids* **1957**, *3* (1), 121–127.

(157) Truhlar, D. G.; Garrett, B. C.; Klippenstein, S. J. Current Status of Transition-State Theory. *The Journal of Physical Chemistry* **1996**, *100* (31), 12771–12800.

(158) McQuarrie, D. A. *Statistical Mechanics*; University Science Books, 2000.

(159) Kolasinski, K. W. *Surface Science: Foundations of Catalysis and Nanoscience*; John Wiley & Sons, Ltd., 2012.

(160) Nielsen, J.; d'Avezac, M.; Hetherington, J.; Stamatakis, M. Parallel kinetic Monte Carlo simulation framework incorporating accurate models of adsorbate lateral interactions. *The Journal of Chemical Physics* **2013**, *139* (22), 224706.

(161) Lausche, A. C.; Medford, A. J.; Khan, T. S.; Xu, Y.; Bligaard, T.; Abild-Pedersen, F.; Nørskov, J. K.; Studt, F. On the effect of coverage-dependent adsorbate–adsorbate interactions for CO methanation on transition metal surfaces. *Journal of Catalysis* **2013**, *307*, 275–282.

(162) Goswami, A.; Ma, H.; Schneider, W. F. Consequences of adsorbate-adsorbate interactions for apparent kinetics of surface catalytic reactions. *Journal of Catalysis* **2022**, *405*, 410–418.

(163) Sanchez, J. M.; Ducastelle, F.; Gratias, D. Generalized cluster description of multicomponent systems. *Physica A: Statistical Mechanics and its Applications* **1984**, *128* (1), 334–350.

(164) van de Walle, A.; Ceder, G. Automating first-principles phase diagram calculations. *Journal of Phase Equilibria* **2002**, *23* (4), 348.

(165) Connolly, J. W. D.; Williams, A. R. Density-functional theory applied to phase transformations in transition-metal alloys. *Physical Review B* **1983**, *27* (8), 5169–5172.

(166) Cordella, L. P.; Foggia, P.; Sansone, C.; Vento, M. A (sub)graph isomorphism algorithm for matching large graphs. *IEEE Transactions on Pattern Analysis and Machine Intelligence* **2004**, *26* (10), 1367–1372.

(167) Benson, R. L.; Yadavalli, S. S.; Stamatakis, M. Speeding up the Detection of Adsorbate Lateral Interactions in Graph-Theoretical Kinetic Monte Carlo Simulations. *The Journal of Physical Chemistry A* **2023**, *127* (48), 10307–10319.

(168) McKay, B. D.; Piperno, A. Practical graph isomorphism, II. *Journal of Symbolic Computation* **2014**, *60*, 94–112.

(169) Chatterjee, A.; Vlachos, D. G. An overview of spatial microscopic and accelerated kinetic Monte Carlo methods. *Journal of Computer-Aided Materials Design* **2007**, *14* (2), 253–308.

(170) Cao, Y.; Li, H.; Petzold, L. Efficient formulation of the stochastic simulation algorithm for chemically reacting systems. *The Journal of Chemical Physics* **2004**, *121* (9), 4059–4067.

(171) Ravipati, S.; d'Avezac, M.; Nielsen, J.; Hetherington, J.; Stamatakis, M. A Caching Scheme To Accelerate Kinetic Monte Carlo Simulations of Catalytic Reactions. *The Journal of Physical Chemistry A* **2020**, *124* (35), 7140–7154.

(172) Savva, G. D.; Stamatakis, M. Comparison of Queueing Data-Structures for Kinetic Monte Carlo Simulations of Heterogeneous Catalysts. *The Journal of Physical Chemistry A* **2020**, *124* (38), 7843–7856.

(173) Ravipati, S.; Savva, G. D.; Christidi, I.-A.; Guichard, R.; Nielsen, J.; Réocreux, R.; Stamatakis, M. Coupling the time-warp algorithm with the graph-theoretical kinetic Monte Carlo framework for distributed simulations of heterogeneous

catalysts. *Computer Physics Communications* **2022**, *270*, 108148.

(174) Snyder, M. A.; Chatterjee, A.; Vlachos, D. G. Net-event kinetic Monte Carlo for overcoming stiffness in spatially homogeneous and distributed systems. *Computers & Chemical Engineering* **2005**, *29* (4), 701–712.

(175) Chatterjee, A.; Vlachos, D. G. Temporal acceleration of spatially distributed kinetic Monte Carlo simulations. *Journal of Computational Physics* **2006**, *211* (2), 596–615.

(176) Gillespie, D. T. Approximate accelerated stochastic simulation of chemically reacting systems. *The Journal of Chemical Physics* **2001**, *115* (4), 1716–1733.

(177) Cao, Y.; Gillespie, D. T.; Petzold, L. R. Efficient step size selection for the tau-leaping simulation method. *The Journal of Chemical Physics* **2006**, *124* (4), 044109.

(178) Haseltine, E. L.; Rawlings, J. B. Approximate simulation of coupled fast and slow reactions for stochastic chemical kinetics. *The Journal of Chemical Physics* **2002**, *117* (15), 6959–6969.

(179) Rao, C. V.; Arkin, A. P. Stochastic chemical kinetics and the quasi-steady-state assumption: Application to the Gillespie algorithm. *The Journal of Chemical Physics* **2003**, *118* (11), 4999–5010.

(180) Cao, Y.; Gillespie, D. T.; Petzold, L. R. The slow-scale stochastic simulation algorithm. *The Journal of Chemical Physics* **2004**, *122* (1), 014116.

(181) E, W.; Liu, D.; Vanden-Eijnden, E. Nested stochastic simulation algorithm for chemical kinetic systems with disparate rates. *The Journal of Chemical Physics* **2005**, *123* (19), 194107.

(182) Dybeck, E. C.; Plaisance, C. P.; Neurock, M. Generalized Temporal Acceleration Scheme for Kinetic Monte Carlo Simulations of Surface Catalytic Processes by Scaling the Rates of Fast Reactions. *Journal of Chemical Theory and Computation* **2017**, *13* (4), 1525–1538.

(183) Savva, G. D.; Stamatakis, M. Tackling the Temporal Stiffness of Kinetic Monte Carlo Simulations of Well-Mixed Chemical Systems via On-the-Fly Scaling and Cost-Error Optimization. *The Journal of Physical Chemistry A* **2025**, *129* (6), 1726–1740.

(184) Chatterjee, A.; Voter, A. F. Accurate acceleration of kinetic Monte Carlo simulations through the modification of rate constants. *The Journal of Chemical Physics* **2010**, *132* (19), 194101.

(185) Kaiser, W.; Gößwein, M.; Gagliardi, A. Acceleration scheme for particle transport in kinetic Monte Carlo methods. *The Journal of Chemical Physics* **2020**, *152* (17), 174106.

(186) Prats, H.; Li, W.; Stamatakis, M. A General Stiffness-Scaling Framework for Accelerating Graph-Theoretical Kinetic Monte Carlo Simulations. *Journal of Chemical Theory and Computation* **2025**, *21* (23), 12262–12277.

(187) Montemore, M. M.; Medlin, J. W. Scaling relations between adsorption energies for computational screening and design of catalysts. *Catalysis Science & Technology* **2014**, *4* (11), 3748–3761.

(188) Greeley, J. Theoretical Heterogeneous Catalysis: Scaling Relationships and Computational Catalyst Design. *Annual Review of Chemical and Biomolecular Engineering* **2016**, *7* (1), 605–635.

(189) Klimeš, J.; Michaelides, A. Perspective: Advances and challenges in treating van der Waals dispersion forces in density functional theory. *The Journal of Chemical Physics* **2012**, *137* (12), 120901.

(190) Klimeš, J.; Bowler, D. R.; Michaelides, A. Chemical accuracy for the van der Waals density functional. *Journal of Physics: Condensed Matter* **2010**, *22* (2), 022201.

(191) Lucci, F. R.; Lawton, T. J.; Pronschinske, A.; Sykes, E. C. H. Atomic Scale Surface Structure of Pt/Cu(111) Surface Alloys. *The Journal of Physical Chemistry C* **2014**, *118* (6), 3015–3022.

(192) Chen, W.-K.; Liu, S.-H.; Cao, M.-J.; Yan, Q.-G.; Lu, C.-H. Adsorption and dissociation of methanol on Au(1 1 1) surface: A first-principles periodic density functional study. *Journal of Molecular Structure: THEOCHEM* **2006**, *770* (1-3), 87–91.

(193) Montoya, A.; Haynes, B. S. DFT Analysis of the Reaction Paths of Formaldehyde Decomposition on Silver. *The Journal of Physical Chemistry A* **2009**, *113* (28), 8125–8131.

(194) Minglong, Q.; Barbier, C.; Subra, R. Ethylene and formaldehyde

chemisorption on small nickel(III) and nickel aluminium clusters: extended Hückel calculations. *Journal of Molecular Catalysis* **1989**, *57* (2), 165–176.

(195) Desai, S. K.; Neurock, M.; Kourtakis, K. A Periodic Density Functional Theory Study of the Dehydrogenation of Methanol over Pt(111). *The Journal of Physical Chemistry B* **2002**, *106* (10), 2559–2568.

(196) Greeley, J.; Mavrikakis, M. Methanol Decomposition on Cu(111): A DFT Study. *Journal of Catalysis* **2002**, *208* (2), 291–300.

(197) Jiang, R.; Guo, W.; Li, M.; Fu, D.; Shan, H. Density Functional Investigation of Methanol Dehydrogenation on Pd(111). *The Journal of Physical Chemistry C* **2009**, *113* (10), 4188–4197.

(198) García-Muelas, R.; Li, Q.; López, N. Density Functional Theory Comparison of Methanol Decomposition and Reverse Reactions on Metal Surfaces. *ACS Catalysis* **2015**, *5* (2), 1027–1036.

(199) Réocreux, R.; Sykes, E. C. H.; Michaelides, A.; Stamatakis, M. Stick or Spill? Scaling Relationships for the Binding Energies of Adsorbates on Single-Atom Alloy Catalysts. *The Journal of Physical Chemistry Letters* **2022**, *13* (31), 7314–7319.

(200) Michaelides, A.; Hu, P. Insight into Microscopic Reaction Pathways in Heterogeneous Catalysis. *Journal of the American Chemical Society* **2000**, *122* (40), 9866–9867.

(201) Schumann, J.; Medford, A. J.; Yoo, J. S.; Zhao, Z.-J.; Bothra, P.; Cao, A.; Studt, F.; Abild-Pedersen, F.; Nørskov, J. K. Selectivity of Synthesis Gas Conversion to C^{2+} Oxygenates on fcc(111) Transition-Metal Surfaces. *ACS Catalysis* **2018**, *8* (4), 3447–3453.

(202) Réocreux, R.; Fampiou, I.; Stamatakis, M. The role of oxygenated species in the catalytic self-coupling of MeOH on O pre-covered Au(111). *Faraday Discussions* **2021**, *229* (0), 251–266.

(203) Inderwildi, O. R.; Jenkins, S. J.; King, D. A. When adding an unreactive metal enhances catalytic activity: NOx decomposition over silver–rhodium bimetallic surfaces. *Surface Science* **2007**, *601* (17), L103–L108.

(204) Greiner, M. T.; Jones, T. E.; Beeg, S.; Zwiener, L.; Scherzer, M.; Girgsdies, F.; Piccinin, S.; Armbrüster, M.; Knop-Gericke, A.; Schlögl, R. Free-atom-like d

states in single-atom alloy catalysts. *Nature Chemistry* **2018**, *10* (10), 1008–1015.

(205) Thirumalai, H.; Kitchin, J. R. Investigating the Reactivity of Single Atom Alloys Using Density Functional Theory. *Topics in Catalysis* **2018**, *61* (5-6), 462–474.

(206) Marcinkowski, M. D.; Darby, M. T.; Liu, J.; Wimble, J. M.; Lucci, F. R.; Lee, S.; Michaelides, A.; Flytzani-Stephanopoulos, M.; Stamatakis, M.; Sykes, E. C. H. Pt/Cu single-atom alloys as coke-resistant catalysts for efficient C–H activation. *Nature Chemistry* **2018**, *10* (3), 325–332.

(207) Hannagan, R. T.; Giannakakis, G.; Réocreux, R.; Schumann, J.; Finzel, J.; Wang, Y.; Michaelides, A.; Deshlahra, P.; Christopher, P.; Flytzani-Stephanopoulos, M.; et al. First-principles design of a single-atom–alloy propane dehydrogenation catalyst. *Science* **2021**, *372* (6549), 1444–1447.

(208) Loges, B.; Boddien, A.; Gärtner, F.; Junge, H.; Beller, M. Catalytic Generation of Hydrogen from Formic acid and its Derivatives: Useful Hydrogen Storage Materials. *Topics in Catalysis* **2010**, *53* (13), 902–914.

(209) Boddien, A.; Loges, B.; Gärtner, F.; Torborg, C.; Fumino, K.; Junge, H.; Ludwig, R.; Beller, M. Iron-Catalyzed Hydrogen Production from Formic Acid. *Journal of the American Chemical Society* **2010**, *132* (26), 8924–8934.

(210) Herron, J. A.; Scaranto, J.; Ferrin, P.; Li, S.; Mavrikakis, M. Trends in Formic Acid Decomposition on Model Transition Metal Surfaces: A Density Functional Theory study. *ACS Catalysis* **2014**, *4* (12), 4434–4445.

(211) Marcinkowski, M. D.; Murphy, C. J.; Liriano, M. L.; Wasio, N. A.; Lucci, F. R.; Sykes, E. C. H. Microscopic View of the Active Sites for Selective Dehydrogenation of Formic Acid on Cu(111). *ACS Catalysis* **2015**, *5* (12), 7371–7378.

(212) Jiang, Z.; Qin, P.; Fang, T. Decomposition mechanism of formic acid on Cu (111) surface: A theoretical study. *Applied Surface Science* **2017**, *396*, 857–864.

(213) Wang, Y.-F.; Li, K.; Wang, G.-C. Formic acid decomposition on Pt1/Cu (111) single platinum atom catalyst: Insights from DFT calculations and energetic span model analysis. *Applied Surface Science* **2018**, *436*, 631–638.

(214) Li, S.; Scaranto, J.; Mavrikakis, M. On the Structure Sensitivity of Formic Acid Decomposition on Cu Catalysts. *Topics in Catalysis* **2016**, *59* (17), 1580–1588.

(215) Li, G.; Guo, W.; Zhou, X.; Yu, X.; Zhu, J. Formic acid adsorption and decomposition on clean and atomic oxygen pre-covered Cu(100) surfaces. *The Journal of Chemical Physics* **2020**, *152* (11), 114703.

(216) Wang, Y.; Schumann, J.; Happel, E. E.; Çınar, V.; Sykes, E. C. H.; Stamatakis, M.; Michaelides, A.; Hannagan, R. T. Observation and Characterization of Dicarbonyls on a RhCu Single-Atom Alloy. *The Journal of Physical Chemistry Letters* **2022**, *13* (27), 6316–6322.

(217) Han, Z.-K.; Sarker, D.; Ouyang, R.; Mazheika, A.; Gao, Y.; Levchenko, S. V. Single-atom alloy catalysts designed by first-principles calculations and artificial intelligence. *Nature Communications* **2021**, *12* (1), 1833.

(218) Stamatakis, M.; Chen, Y.; Vlachos, D. G. First-Principles-Based Kinetic Monte Carlo Simulation of the Structure Sensitivity of the Water–Gas Shift Reaction on Platinum Surfaces. *The Journal of Physical Chemistry C* **2011**, *115* (50), 24750–24762.

(219) Niemantsverdriet, J. W.; Markert, K.; Wandelt, K. The compensation effect and the manifestation of lateral interactions in thermal desorption spectroscopy. *Applied Surface Science* **1988**, *31* (2), 211–219.

(220) Schmid, M.; Parkinson, G. S.; Diebold, U. Analysis of Temperature-Programmed Desorption via Equilibrium Thermodynamics. *ACS Physical Chemistry Au* **2023**, *3* (1), 44–62.

(221) Maintz, S.; Deringer, V. L.; Tchougréeff, A. L.; Dronskowski, R. Analytic projection from plane-wave and PAW wavefunctions and application to chemical-bonding analysis in solids. *Journal of Computational Chemistry* **2013**, *34* (29), 2557–2567.

(222) Jacobsen, S. N.; Helmersson, U.; Erlandsson, R.; Skårman, B.; Wallenberg, L. R. Sharp microfaceting of (001)-oriented cerium dioxide thin films and the effect of annealing on surface morphology. *Surface Science* **1999**, *429* (1), 22–33.

(223) Schumann, J.; Bao, Y.; Hannagan, R. T.; Sykes, E. C. H.; Stamatakis, M.; Michaelides, A. Periodic Trends in Adsorption Energies around Single-Atom Alloy Active Sites. *The Journal of Physical Chemistry Letters* **2021**, *12* (41), 10060–10067.

(224) Inoue, A. Stabilization of metallic supercooled liquid and bulk amorphous alloys. *Acta Materialia* **2000**, *48* (1), 279–306.

(225) Calle-Vallejo, F.; Martínez, J. I.; García-Lastra, J. M.; Rossmeisl, J.; Koper, M. T. M. Physical and Chemical Nature of the Scaling Relations between Adsorption Energies of Atoms on Metal Surfaces. *Physical Review Letters* **2012**, *108* (11), 116103.

(226) Vijay, S.; Kastlunger, G.; Chan, K.; Nørskov, J. K. Limits to scaling relations between adsorption energies? *The Journal of Chemical Physics* **2022**, *156* (23), 231102.

(227) Mori-Sánchez, P.; Cohen, A. J.; Yang, W. Localization and Delocalization Errors in Density Functional Theory and Implications for Band-Gap Prediction. *Physical Review Letters* **2008**, *100* (14), 146401.

(228) Cai, Y.; Michiels, R.; De Luca, F.; Neyts, E.; Tu, X.; Bogaerts, A.; Gerrits, N. Improving Molecule–Metal Surface Reaction Networks Using the Meta-Generalized Gradient Approximation: CO2 Hydrogenation. *The Journal of Physical Chemistry C* **2024**, *128* (21), 8611–8620.